Tailored Structural Material Solutions for Large-Scale Superconducting Magnets

operating at the most extreme cryogenic conditions

Stefanie Langeslag

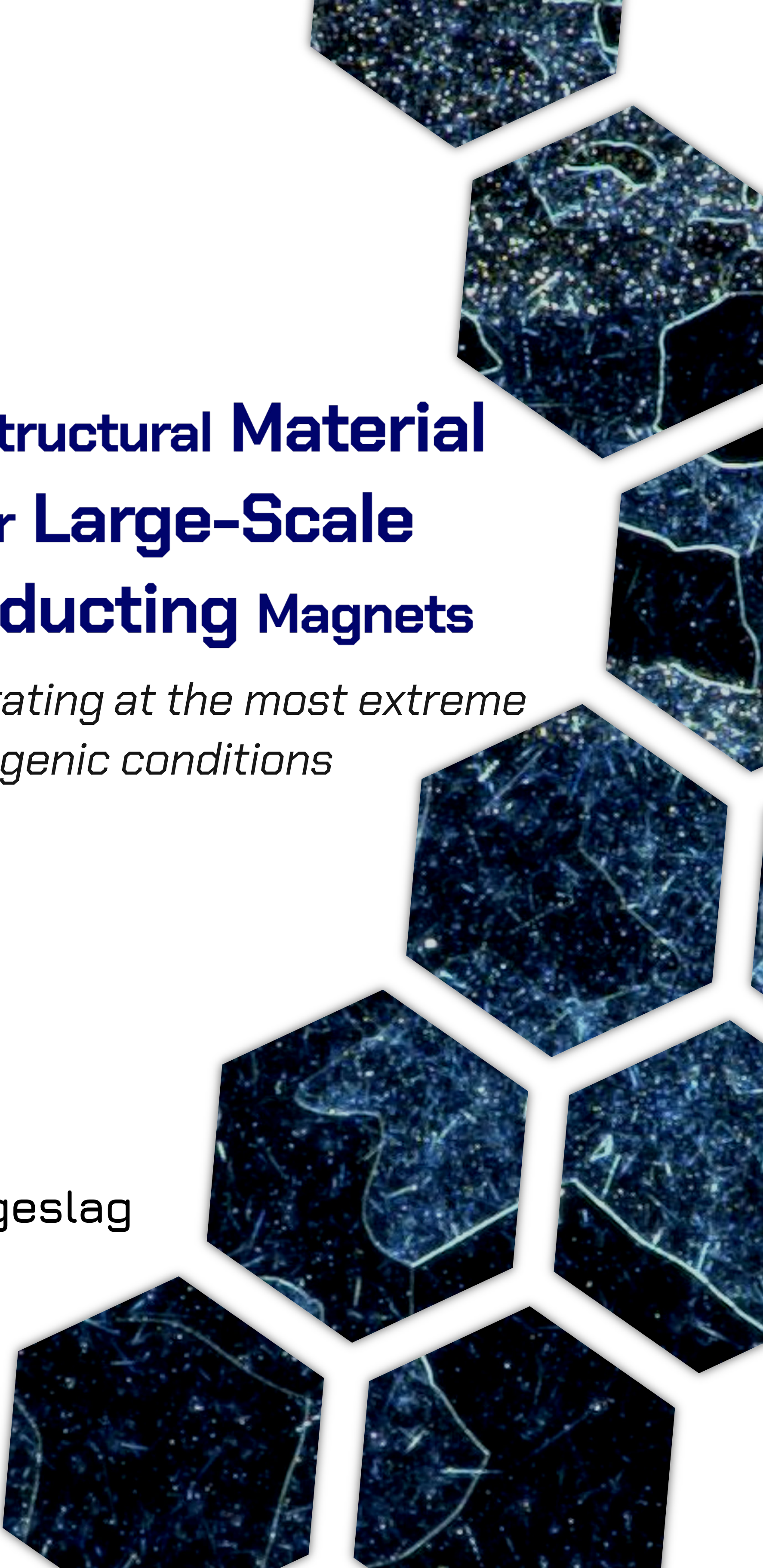

Tailored Structural Material Solutions for Large-Scale Superconducting Magnets

---

Stefanie A. E. Langeslag

Dissertation graduation committee:

Chairman:	Prof. dr. J. L. Herek	University of Twente, TNW
Promotor:	Prof. dr. ir. H. H. J. ten Kate	University of Twente, TNW
Co-promotor:	Dr. M. M. J. Dhallé	University of Twente, TNW
Co-promotor:	Dr. S. Sgobba	CERN, Genève, EN-MME
Members:	Prof. dr. ir. R. Akkerman	University of Twente, ET
	Prof. dr. ir. H. J. M. ter Brake	University of Twente, TNW
	Dr. A. Kario	University of Twente, TNW
	Prof. dr. ir. A. van Keulen	Delft University of Technology
	Dr. K-P. Weiss	Karlsruhe Institute of Technology

The research presented in this thesis was carried out at CERN, Genève, Switzerland.

Disclaimer: Whereas the current study has been carried out with all players in mind, and in cordial collaboration, the statements made in this work could be contradicting those of others. Even though objectivity has been one of the main pillars during my work, I would like to note that the views and opinions expressed in this thesis do not necessarily reflect those of neither CERN nor the ITER Organisation.

Stefanie A. E. Langeslag
Tailored Structural Material Solutions for Large-Scale Superconducting Magnets;
operating at the most extreme cryogenic conditions
Ph. D. thesis, 28th May, 2020, University of Twente, The Netherlands
ISBN: 978-94-028-2052-2

Cover by: S. A. E. Langeslag
Printed by: Ipskamp Printing, The Netherlands
This dissertation is printed on 100% recycled paper

University of Twente
Faculty of Science and Technology (TNW),
Chair of Industrial Application of Superconductivity (ITS),
and Chair of Energy, Materials and Systems (EMS)
Drienerlolaan 5
7522 NB Enschede, The Netherlands

TAILORED STRUCTURAL MATERIAL SOLUTIONS FOR LARGE-SCALE SUPERCONDUCTING MAGNETS

OPERATING AT THE MOST EXTREME CRYOGENIC CONDITIONS

DISSERTATION

to obtain
the degree of doctor at the University of Twente,
on the authority of the rector magnificus,
Prof. dr. T. T. M. Palstra,
on account of the decision of the Doctorate Board,
to be publicly defended
on Thursday, 28^{th} of May 2020 at 14:45.

by

Stefanie Agnes Elisabeth Langeslag

born on the 17^{th} of April 1985
in Eelde-Paterswolde, The Netherlands

This dissertation has been approved by supervisor and co-supervisors

Prof. dr. ir. H. H. J. ten Kate
Dr. S. Sgobba
Dr. M. M. J. Dhallé

Preface

The work presented here is resulting from a fruitful collaboration between three institutes. The work commenced as a quest for conductor material development for superconducting detector magnets between the University of Twente, in particular the Chair for Industrial Applications of Superconductivity and the Experimental Physics department at CERN (European Organisation for Nuclear Research), also representing the ATLAS Collaboration.

As the thesis advanced a third player was introduced with interest specifically in the topic of mechanical characterisation of structural materials for superconducting magnets. An involvement of the international ITER organisation (International Thermonuclear Experimental Reactor) resulted in an extended scope of the thesis hereby presented.

Omdat je altijd naast me staat, luistert naar alle zorgen,
wijzend op de positieve dingen en de kansen van morgen.

Summary

Superconducting high-field magnets have become indispensable in applications requiring the magnetic confinement of charged particles in fusion devices or their identification in particle physics detectors. Current state-of-the-art magnetic confinement systems for plasma fusion physics achieve magnetic-field values of some 13 tesla in bore-sizes exceeding 4 meter, while for future high-energy physics detector magnets magnetic fields of 4 to 6 tesla in a bore diameter of 10 to 12 meter are envisaged. Such ambitious magnets are needed for the further probing of the standard model or to exploit the physics and feasibility of nuclear fusion. A scale-up, however, implies the development of superconductors and magnet structures that can handle the combination of current density, magnetic field and bore size thereby generating static and dynamic forces and resulting stress in the materials, while still subjected to a large set of additional requirements.

For the design of such structures, customised material solutions are essential. In this dissertation the research on three tailored material solutions is presented, each with a unique set of requirements and ensuing challenges. Common to all is the quest for a load-bearing solution that does not overly compromise other essential characteristics. All were designed and selected with the full production sequence in mind, from conception of the raw material until operation in the magnetic environment.

I. F XM-19 special steel as a tailor-made material for heavy gauge forgings.

The ITER Central Solenoid in the ITER tokamak contributes to the magnetic confinement and heating of the plasma. The 13-meter-high solenoid consists of a vertical stack of 6 independently driven modules that are dynamically activated, leading to opposing currents, which on their turn can lead to high separation forces. A pre-compression structure counteracts these forces, furnishing a continuous 180 MN coil-to-coil contact pressure. Preloading is applied by mechanical fastening via 9 subunits along the coil stack, each consisting of 2 outer and 1 inner tie plates. These plates need to feature outstanding mechanical properties over a large temperature range.

A high strength, tailored Nitronic®-50 type F XM-19 austenitic stainless steel has been selected as candidate material. The linearised stress distribution reaches some 250 MPa, which translates to a required yield strength exceeding 380 MPa at room temperature.

Two different manufacturing methods are considered for the production of the 15 meter long tie plates. With a welded structure, individual head- and

slab-forgings are connected by Gas Metal Arc Welding (GMAW). In parallel, a heavy single-piece forged structure is examined by applying successive open-die forging steps, followed by final machining.

To assess these two customised solutions, the tailored F XM-19 material has been extensively reviewed in a production-based setting. Since the maximum internal stress occurs during cool-down to 4.2 K, due to a large difference in thermal contraction between support structure and coils, measurements also focus on these environmental conditions. A custom-made tensile measurement set-up is hence employed to determine representative mechanical material properties at 4.2 K.

The present study confirms that F XM-19, even under the most extreme conditions, has tensile properties that well exceed those of 316LN, the stainless steel typically used in high-energy magnets.

Since real-life materials are rarely without flaws, material toughness under the presence of a flaw needs to be considered under application-relevant conditions. *Whereas an inferior toughness is observed for a heavy F XM-19 forging with respect to a general 316LN, also in this respect, the large-size F XM-19 forgings more than meet the application requirements.* It is nevertheless found that the deformation involved in the extreme forging leads to a marked anisotropy, having its effect on the mechanical behaviour.

The varying currents in the independently driven coils introduce cyclic loading, introducing the necessity of both manufacturing solutions to be assessed in terms of dynamic mechanical behaviour at operating conditions. *Hereby suitability of the heavy forged F XM-19 structures subject to the varying magnetic fields is demonstrated, however, the weld in its current form provides insufficient performance for the application.*

Where one primarily targets optimal mechanical performance, a structural steel in a high-field magnet environment also needs to be non-magnetic. Its chemical composition can in first instance be adjusted to achieve a fully austenitic microstructure, however, thermo-mechanical work during subsequent processing steps may compromise its ferromagnetic properties.

Magnetic measurements were performed to confirm the suitability of this tailor-made material in its final processed state. *The large-size single-piece forging maintains the desired fully austenitic structure,* with a magnetic susceptibility close to zero, *however, in the welded structure some δ-ferrite bands are observed.* This illustrates how, even though F XM-19 has a clear potential for high-field magnets, a finely targeted chemical composition remains essential.

II. Explosion-welding of high-conductivity structures.

The implementation of unit lengths of superconducting cable-in-conduit conductors in the ITER coils impose the use of electrical joints, e.g. at inter-pancake couplings. Such twin-box lap-type joints, produced by compacting each cable end into a copper - stainless steel bimetallic box, simultaneously need to meet stringent electrical and mechanical requirements.

Achieving a fitting bond between two highly varying materials via a liquid fusion process leads to difficulties for which explosion welding is suggested as a solution. Solid-state fusion is achieved through detonating an explosive on the top-plate forcing it onto the base-plate, leading to large local deformation. Ideally an interlocked weld interface is thereby created, accompanied by atomic diffusion.

A large set of copper - stainless steel bimetals were explosion-bonded with varying welding parameters and parent metal characteristics. Validation of the bonded interface is determined in terms of tensile, shear and microstructural characteristics at the envisaged operating temperature of 4.2 K. The data confirm that *explosion-bonded copper-clad plates are suitable for joint application, but also illustrate how parametrisation during the welding process is of major importance.*

Certain welding parameters result in a favourable Von Kármán vortex formation at the bonded interface, with solid-state diffusion often resulting in the formation of intermetallics. However, other parameters may lead to the less beneficial Kelvin-Helmholtz instability or even to local material failure.

Extensive results are presented on the suitability of certain copper purity grades for various joint types. For DC joint applications a highly-pure copper can be of interest, while for AC joints one can aim for a lower-conductivity copper alloy to limit AC losses. Here a non-trivial trade-off needs to be made between DC resistance and AC loss. The data show that *independent of the initial alloy or temper, the welding process renders the material in an H02 temper state.* This treatment strongly reduces the conductivity of highly pure copper, but for less pure copper like C12200, little difference is observed. A beneficial temper gradient is observed over the thickness of the sole, where the welding process leads to increased structural strength at the weld interface but relatively high conductivity at the end where current needs to be transferred. The stability of the temper is nevertheless limited. Thermal processing involved in the final joint manufacturing annuls most of the acquired mechanical properties, causing the material to revert to an annealed state. Hence, *whereas the at present investigated copper grades are suitable for the application, a more thermally stable alloy may further enhance its performance.*

III. High-strength, high-conductivity tailored dilute aluminium.

Future high-resolution particle experiments involve a scale-up towards a 60 kA-class conductor that operates at 5 T, 4.2 K. The required peak magnetic field results in high stress levels at the highly radiation-transparent conductor of the large bore magnet. The suitability of a dilute Al-Ni alloy is examined for use as a large-size superconductor stabiliser, targeting both the required conductive as well as mechanical characteristics of the conductor. Al-0.1wt.%Ni is custom-made for a full application-relevant production sequence involving co-extrusion with a large, 40-strand Nb-Ti/Cu Rutherford type superconducting cable. Due to low solid solubility, dilute alloying of high-purity aluminium with nickel enhances its strength but avoids significant degradation of its transport properties, as characterised by its residual resistivity ratio (RRR).

Even though the RRR value generally decreases with impurity content, *with a dispersed alloying addition of 0.1wt.% nickel an as-extruded RRR value of about 1200 can be maintained.* This value offers a safe margin with respect to the desired RRR 500 limit, even though the necessary mechanical properties are not yet met.

To confirm the material's workability and to determine the beneficial effects of the as-extruded temper, sections of the conductor are work-hardened. Mechanical strength and electrical resistivity are assessed as function of the amount and method of work-hardening, both at room temperature and at 4.2 K. Extended processing in a range of 0% to 30% cold reduction results in a significant improvement of the 0.2% yield strength ($R_{p0.2}$) with respect to the as-extruded temper, demonstrating a fair workability of the diluted alloy. Even though the mechanically advantageous dislocation pinning sites introduced by the cold work also form extra scattering sites for electrical transport, the drop in RRR value remains well within acceptable limits.

With a 4.2 K over room temperature ratio in the $R_{p0.2}$ value surpassing 2, *a co-extruded Al-0.1wt.%Ni alloy achieves the required $R_{p0.2}$ value higher than 120 MPa at 4.2 K while maintaining a RRR value over 500, at an 18% reduced temper.*

Additional thermal treatments, such as resin-curing after coil winding, can cause partial annealing of the cold-worked material, reversing the strengthening effect. On the other hand, targeted thermal treatments at relatively low temperature can also result in precipitation-hardening. The depletion of nickel in the aluminium-rich matrix around the precipitates can result in increased strength and reduced thermal and electrical resistivity. Conductor sections were subjected to a wide range of thermal treatments to assess the Al-0.1wt.%Ni alloy's thermal stability.

For the currently employed Al-0.1wt.%Ni alloy no precipitation-hardening is observed, but its thermal stability is confirmed. While the copper in the explosion-bonded joint material returns fully to its original annealed state, in the Al-0.1wt.%Ni alloy the formed intermetallics retain some of the mechanical properties. The work presented here thus *confirms the suitability of an Al-0.1wt.%Ni alloy for future co-extruded aluminium stabilized superconductors.* Furthermore, it helps to identify an optimal work-hardening sequence and optimal thermal treatment, possibly coinciding with coil resin-curing, for an Al-Ni stabilised superconductor.

All tailored materials that were designed and studied in this work illustrate that for low-temperature high-magnetic-field applications, three strongly interrelated factors need to be considered: composition, workability and thermal stability. Simultaneously taking all three into account throughout a fully scalable chain of production processes is by no means a trivial task, but can nonetheless be accomplished by adopting customised material solutions fully adapted to the application.

Samenvatting (Summary in Dutch)

Supergeleidende magneten voor het opwekken van hoge magneetvelden zijn onmisbaar geworden om geladen deeltjes magnetisch op te sluiten in een fusiereactor, of om deze te identificeren in een detector voor hoge energie fysica. In de huidige magneetsystemen voor opsluiting van plasmas in fusiereactoren worden magneetvelden opgewekt van ongeveer 13 tesla in een boring van meer dan 4 meter, terwijl voor toekomstige deeltjesdetectoren voor hoge-energie fysica magneetvelden van 4 tot 6 tesla moeten worden opgewekt in een boring van 10 tot 12 meter. Zulke ambitieuze magneetsystemen zijn essentieel voor het verdere onderzoek naar het standaardmodel of voor de ontwikkeling van plasmafysica en haalbaarheidsstudies voor kernfusieenergie. Een dergelijke opschaling impliceert echter een verdere ontwikkeling van supergeleiders en structurele elementen van de magneten om de bijbehorende statische en dynamische krachten ten gevolge van de combinatie van magneetveld, stroomdichtheid en afmetingen van de boring te kunnen opvangen waarbij ook nog eens aan vele andere stringente voorwaarden moet worden voldaan.

Bij het ontwerpen van de structurele elementen ligt de essentie voor succes in maatwerk voor materiaaloplossingen. In dit proefschift worden het onderzoek en de resultaten voor drie structurele materiaaloplossingen gepresenteerd, eenieder met de bijbehorende eisen en uitdagingen. Ze zijn alle drie geselecteerd en ontworpen met inachtneming van de volledige productielijn, van grondstof tot uiteindelijk toepassing.

I. F XM-19 speciaal staal voor specifieke zware smeedstukken.

De centrale solenoide in de ITER tokamak draagt bij aan de magnetische opsluiting en verwarming van het hoog-energetisch plasma. De 13 meter hoge solenoide op de centrale as van de tokamak is opgebouwd uit 6 tot een eenheid opgestapelde spoelmodulen en deze worden onafhankelijk van elkaar aangestuurd. De hoge individuele magneetvelden van de modules veroorzaken aanzienlijke uiteendrijvende krachten die opgevangen worden door een structuur die voorspanning op de spoelmodules aanbrengt. Een contactkracht van 180 MN wordt gerealiseerd door middel van 9 onderdelen die elk bestaan uit 2 externe en 1 intern geplaatste trekplaten. Deze trekplaten moeten uitstekende mechanische eigenschappen hebben over een groot temperatuurbereik gelet op de toepasing in de tokamak.

Een speciaal ontwikkelde Nitronic®-50 type F XM-19 roestvrijstaal is geselecteerd als kandidaat vanwege zijn austenitische aard en superieure mechanische eigenschappen. De gelineariseerde spanningsverdeling in dit materiaal laat ongeveer

250 MPa zien wat overeenkomst met een rekgrens van meer dan 380 MPa bij kamertemperatuur.

Twee methoden zijn onderzocht voor de productie van de zware 15-meter lange trekplaten. De eerste methode is het smeden van de 2 kopstukken en 1 staartstuk, om deze 3 delen vervolgens aan elkaar te lassen met een diepe MIG (Metaal Inert Gas) lasverbinding. De tweede methode is de hele trekplaat uit één stuk smeden en vervolgens op maat brengen met een eindbewerking.

De door maatwerk gemaakte proefstukken zijn uitgebreid onderzocht bij lage temperaturen aangezien de mechanische piekspanning plaatsvindt tijdens de afkoeling naar 4.2 K als gevolg van de grote verschillen in thermische contractie. Een trek-rek meting is hiervoor ontwikkeld om de representatieve mechanische eigenschappen van het materiaal te bepalen bij 4.2 K.

De huidige studie bevestigd dat F XM-19, zelfs onder meest extreme omstandigheden, trek-rek eigenschappen bezit die verder gaan dan die van roestvrijstaal 316LN, een staal die vaak in hoogveldmagneten wordt gebruikt.

Aangezien in de praktijk materialen zelden geen gebreken hebben, zijn de breukmechanica eigenschappen onder de omgevingsrelevante conditie van 4.2 K nader onderzocht. *Ondanks dat de taaiheid van zware F XM-19 smeedstukken licht achterblijft bij die van een reguliere 316LN, voldoet het gesmede materiaal gemakkelijk aan de eisen.* Echter, een anisotropie is ontdekt in het materiaal ten gevolge van de grote vervormingen gedurende het smeedproces, waarbij de richtingsafhankelijkheid van het materiaal grote effecten heeft op het mechanische gedrag.

De wisselende magneetvelden van de individuele modules introduceren een extra vermoeiingsbelasting. De materialen die aan beide productiemethoden zijn blootgesteld zijn daarom ook onderzocht op de invloed van een dynamische belasting op de mechanische eigenschappen bij 4.2 K. *F XM-19 in zwaar gesmede componenten is hierbij geschikt bevonden ook in wisselend magnetisch bedrijf, echter de lasverbinding laat enigzins te wensen over.*

Waar men normaal voor een staal in structurele componenten de nadruk volledig legt op de mechanische eigenschappen, moeten we hier ook rekening houden met de magnetische eigenschappen. Met de initiële samenstelling kan een roestvrijstaal volledig austenitisch zijn, echter met thermisch-mechanische behandelingen kunnen ferromagnetische fasen ontstaan.

Om de bruikbaarheid van het materiaal te bevestigen zijn er metingen gedaan aan de magnetische eigenschappen van het materiaal in de volledig bewerkte staat. *Het zware smeedstuk ontstaan uit één deel behoudt zijn volledige austenitische structuur gedurende het gehele productieproces*, met een magnetische susceptibiliteit dicht bij nul. *In de toegevoegde lasverbinding echter, zijn enkele sporen van δ-ferriet gevonden.* Dit laat maar weer eens zien dat voor een materiaal als F XM-19 met een duidelijke potentie voor toepassing in hoogveldmagneten, men toch waakzaam moet zijn voor faseveranderingen ten gevolge van de chemische samenstelling en de toegepaste thermisch-mechanische behandelingen.

II. Explosielassen van hooggeleidende materialen

Het implementeren van gelimiteerde lengtes van cable-in-conduit geleiders in de ITER spoelen maakt het noodzakelijk om elektrische verbindingen te gebruiken. De zogenaamde twin-box verbindingen, die gemaakt worden door de eindstukken van de twee geleiders onder druk ieder in een bimetalen doos te plaatsen, en vervolgens de dozen samen te solderen, is onderhevig aan zware elektrische en mechanische eisen.

Om een goeie verbinding te realiseren tussen de roestvrijstalen en koperen delen van de bimetalen doos, is explosielassen voorgesteld. Met explosielassen maakt men een lasverbinding gebaseerd op een vertand lasvlak met gebruik van atomaire diffusie. Met een explosief wordt de ene plaat met hoge druk op de andere plaat geperst, waarbij grote vervormingen plaatsvinden op het lasvlak.

Een brede selectie bimetalen van koper en roestvrijstaal zijn onderworpen aan explosielassen met een uiteenlopende set van lasparameters en verschillende eigenschappen van het basismateriaal. De validatie van de lasverbinding is gedaan met gebruik van trek- en afschuiftesten, gevolgd door een analyze van de microstructuur. De meetgegevens laten zien dat *het explosielassen van koper op roestvrijstaal platen goed toepasbaar is voor het maken van de elektrische verbindingen tussen de spoelen in magneten.* Echter de meetgegevens laten ook zien dat *het bepalen van de juiste lasparameters van essentieel belang is voor de kwalificatie van de verbinding.*

Bepaalde lasparameters resulteren in een gewenste Von Kármán vortex formatie op de lasnaad dat vaak samen gaat met de formatie van een intermetallische verbinding. Andere lasparameters veroorzaken een minder sterke Kelvin-Helmholtz instabiliteit op het lasvlak of soms zelfs scheuren in het basismateriaal.

Uitgebreide resultaten worden gepresenteerd over de toepasbaarheid van verschillende koperlegeringen gebruikt voor de bimetalen. Voor elektrische verbindingen voor gelijkstroom kan een hoge puurheid koper interessant zijn, terwijl voor een wisselstroomverbinding men zou kunnen kiezen voor een minder goed geleidende koper om AC-verliezen te reduceren. De meetresultaten laten zien dat het explosielasproces een kopergeleider oplevert in een H02 temper, onafhankelijk van de initiële legering of temper. Dit reduceert het geleidingsvermogen van een hoge puurheid koper in extreme mate, echter voor een minder pure legering zoals C12200 resulteert dit in maar marginale verschillen. Een bevorderlijke tempergradiënt is aangetroffen als gevolg van het explosielasproces, waarbij een hogere mechanische prestatie aanwezig is aan de kant van de lasverbinding, terwijl aan de kant waar de elektrische geleiding plaats moet vinden het hogere geleidingsvermogen is aangetroffen. De stabiliteit van de temper, en daarmee de tempergradiënt is echter beperkt. De thermische behandeling die nodig is voor de eindproductie van de elektrische verbinding, maakt dat de koperlegering terugkeert naar de originele onverharde staat. *De koperlegeringen onderzocht in deze studie zijn geschikt bevonden voor de toepassing, echter een meer thermisch stabiele legering zou een extra voordeel kunnen bieden.*

III. Maatwerk voor een sterke en goed geleidende aluminiumlegering.

Voor de opschaling van hoge-energie fysica experimenten in de toekomst zijn nieuwe geleiders voor 60 kA bij 5 T in een 4.2 K-omgeving nodig. Een dergelijke opschaling resulteert in een hoge mechanische spanning in de spoelen met grote boring, die toch in hoge mate transparant voor straling moeten zijn. De bruikbaarheid van een op maatwerk gebaseerde laag Ni-gehalte aluminiumlegering is onderzocht voor gebruik als stabilisatiemateriaal van de NbTi/Cu supergeleider, die daarbij zowel een mechanische als een thermisch-elektrisch geleidende functie heeft. De geschiktheid van Al-0.1wt.%Ni voor deze toepassing is onderzocht door het materiaal te extruderen samen met een 40-aderige NbTi/Cu supergeleidende Rutherford kabel. Als gevolg van de lage oplosbaarheid van nikkel in aluminium is deze zeer geschikt om de geleider mechanisch te versterken zonder te veel concessies te doen aan de elektrische geleidbaarheid, uitgedrukt in de restweerstandverhouding (RRR).

Hoewel de RRR-waarde drastisch afneemt met de introductie van onzuiverheden in puur aluminium kan *met een dosering van 0.1 gewichtsprocent Ni in de vorm van precipitatie een RRR-waarde van ongeveer 1200 na extrusie worden gerealizeerd.* Deze waarde biedt een veilige marge ten opzichte van het doel van RRR > 500 voor de opschaling, waarbij aangetekend wordt dat de beoogde mechanische eigenschap betreffende de rekgrens nog niet is behaald.

Om de verwerkbaarheid, en daarmee de beoogde versterking van het materiaal door middel van verharding te toetsen, zijn korte monsters van de geleider gewalst. Vloeigrens en geleidingseigenschappen zijn daarna onderzocht als functie van de walsmethode en doorsnedereductie, zowel bij kamertemperatuur als bij 4.2 K. *Een significante stijging van de mechanische eigenschappen, in het bijzonder de vloeigrens van het materiaal, kan worden bereikt met het walsen tot een doorsnedereductie tot 30%.* Dit duidt op een geschikte verwerkbaarheid van het materiaal. Daarnaast blijft het verlies van de RRR-waarde binnen redelijke proporties, terwijl het walsen onvermijdelijk ook extra weerstand voor de elektrische geleiding veroorzaakt.

Met een waargenomen 4.2 K over kamertemperatuur verhouding van de vloeigrens van meer dan een factor 2 kunnen we constateren dat *de Al-0.1wt.%Ni-legering de beoogde vloeigrens van 120 MPa bij 4.2 K kan bereiken bij een doorsnedereductie van zo'n 18%, met een resulterende RRR-waarde van ver boven de benodigde 500.*

Extra thermische bewerkingen, zoals die voor het uitharding van hars in de laatste fase van de spoelproductie, kunnen het versterkende effect van het voorafgaande walsproces deels tenietdoen. Aan de andere kant, als de keuze van temperatuur en looptijd goed worden gedaan dan kan ook het proces van precipitatieverharding in gang worden gezet, waarbij de onttrekking van Ni aan de Al-rijke matrix kan resulteren in een hogere mechanische sterkte en lagere thermische en elektrische weerstand. Delen van de geextrudeerde en gewalste geleider zijn daarom onderworpen aan een breed scala van thermische behandelingen om de thermische stabiliteit te beoordelen.

Voor deze specifieke Al-0.1wt.%Ni-legering zijn geen sporen van verdere precipitatie gevonden, echter een brede thermische stabiliteit is bevestigd. Waar, bij een hoge puurheid koper in een bimetaal van koper en roestvrijstaal een thermische behandeling een nagenoeg volledige annulering van de winst van vooraf gedaan mechanische werk in het materiaal ten gevolge had, zien we hier een handhaving van een deel van het werk ten gevolge van de aanwezige intermetallische fasen. Dit bevestigt de geschiktheid van een Al-0.1wt.%Ni-legering voor toekomstige gecoextrudeerde supergeleiders. Daarnaast heeft deze studie geholpen met het ontwerpen en bepalen van de optimale walsprocedure en de daaropvolgende thermische behandelingen voor de beoogde toepassing.

Alle op maatwerk gebaseerde materialen die in dit werk zijn bestudeerd illustreren dat voor toepassingen in hoge magnetische velden bij lage temperatuur rekening moet worden gehouden met drie sterk met elkaar verbonden factoren: chemische samenstelling, verwerkbaarheid en thermische stabiliteit. Het in acht nemen van alle drie aspecten in de volledige productieketen is niet triviaal, maar kan toch worden bereikt door maatwerk te leveren voor materiaaloplossingen die volledig zijn toegespitst op het gebruik.

Contents

1 **Introduction** 1
1.1 Future in Large-Size Superconducting Magnets 2
1.1.1 Large-size magnets for fusion experiments 2
1.1.2 Large-bore magnets for particle physics experiments 5
1.2 Structural Components for Large-Scale Magnets 7
1.2.1 Forces to be counteracted 7
1.2.2 Specific structures for tokamak magnet systems 11
1.2.3 Specific structures for detector magnets 14
1.2.4 Environmental implications 15
1.3 Motivation and Scope 19

I F XM-19, a forged austenitic stainless steel for large load-bearing structures 25

2 **The complexity of large-size austenitic stainless steel forgings** 27
2.1 Introduction 28
2.1.1 Tie plate production; fit for purpose 28
2.2 State-of-the-art austenitic stainless steels 33
2.2.1 The iron-carbon system 33
2.2.2 Nitrogen-strengthened austenitic stainless steel 36

3 **Effect of nitrogen strengthening on low-temperature mechanical properties** 41
3.1 F XM-19 for heavy-gauge structural components 42
3.2 Research methodology 45
3.2.1 Experimental technique for static mechanical measurement at 4.2 K 46
3.2.2 Optimal measurement parameters 50
3.2.3 Measurement uncertainty 51
3.3 Structural benefits of nitrogen strengthening 51
3.3.1 Microstructural characteristics as an explanation for mechanical behaviour 55

4 **F XM-19 as bearer of low-temperature fatigue and fracture toughness** 57
4.1 Research methodology 58
4.1.1 Effect of a flaw on mechanical behaviour 58
4.1.2 Fracture toughness testing at liquid helium temperature 61

4.1.3 Fatigue crack growth rate testing at 4.2 K . . . 66
4.1.4 Experimental characteristics . . . 68
4.1.5 Measurement uncertainty . . . 70
4.2 Low-temperature continuum fatigue behaviour of F XM-19 under the presence of a crack . . . 71
4.3 F XM-19 sustaining fair static loads under the presence of a crack . . . 73
4.3.1 Anisotropy in sizeable F XM-19 forgings . . . 74
4.3.2 Impressive mechanical performance of F XM-19 when loaded in a static manner . . . 80

5 Magnetic performance of F XM-19 83
5.1 Research methodology . . . 84
5.1.1 Low-temperature magnetisation measurements . . . 85
5.2 Magnetic properties of large F XM-19 forgings . . . 86

6 Prospect of F XM-19 for heavy-gauge forgings 93
6.1 Conclusion of F XM-19's performance under stringent conditions . . . 94
6.2 Recommendations for the optimisation of F XM-19 forgings . . . 95

II Explosion-welded connections in ITER-type load-bearing electrical joints 97

7 Issues with copper to stainless steel connections 99
7.1 Introduction . . . 100
7.1.1 Copper selection . . . 100
7.1.2 Stainless steel selection . . . 103
7.2 Achieving a fitting bond between two highly varying materials . . . 104
7.2.1 The process of explosion bonding . . . 105
7.2.2 Materials in function of the welding process . . . 108

8 Structural characteristics of a copper-clad steel plate 111
8.1 Research methodology . . . 112
8.1.1 Mechanical performance measurements . . . 112
8.2 Mechanical behaviour of a Cu-SS explosion weld . . . 117
8.2.1 Structural observations at the weld interface . . . 121

9 Conductive properties of the copper following joint formation 125
9.1 Research methodology . . . 126
9.1.1 Method for RRR measurements at 4.2 K . . . 126
9.1.2 Method for hardness testing . . . 129
9.1.3 Thermal treatments simulating joint formation . . . 129
9.2 Transport performance of an explosion welded copper sole . . . 132

10 Suitability of explosion welding in electrical joints 137
10.1 Conclusion regarding explosion welding for bi-metal joint fabrication 138
10.2 Recommendations for bi-metal improvement . . . 141

III Customised high-purity aluminium as a structurally fit superconductor stabiliser 143

11 Challenging structural strength of a high-purity aluminium stabiliser 145
11.1 Introduction . . . 146
11.2 Lattice imperfections for mechanical strength . . . 148
  11.2.1 Dislocations . . . 149
  11.2.2 Interface imperfections . . . 150
  11.2.3 Volume imperfections . . . 151
11.3 Introducing impurities . . . 153
  11.3.1 Metal matrix composites . . . 153
  11.3.2 Mechanical alloying . . . 154
11.4 Reduced transport properties due to lattice imperfections . . . 155
  11.4.1 Mean free path concession . . . 155
  11.4.2 Adapting solubility to application . . . 156

12 Effect of mechanical alloying on 5N-Al characteristics 161
12.1 Precipitation-type alloy as workhorse for superconducting solenoids . 162
12.2 Research methodology . . . 162
  12.2.1 Billet-on-billet co-extrusion process . . . 163
12.3 Transport characteristics vs. mechanical strength of diluted alloys . . 166
  12.3.1 Microstructural effects clarifying additional strengthening effects 169
  12.3.2 Mechanical characteristics at 4.2 K . . . 171

13 Effect of work-hardening on an Al-0.1wt.%Ni-stabilised conductor 173
13.1 Work-hardening of a conductor section . . . 174
13.2 Workability of the Al-0.1wt.%Ni-alloy . . . 175
  13.2.1 Changes in the microstructure . . . 178
  13.2.2 Al-0.1wt.%Ni's workability: comparison with literature . . . 178
13.3 Properties of Al-0.1wt.%Ni following production-scale work-hardening 181
  13.3.1 Impact on quality of bonding . . . 183
  13.3.2 Mechanical characteristics at 4.2 K . . . 185
  13.3.3 Scaling electrical resistivity with dislocation density . . . 189
13.4 Thermal stability against coil curing . . . 189
  13.4.1 Thermal treatment methodology . . . 190
  13.4.2 Work-hardening dependent recovery . . . 191

14 Al-0.1wt.%Ni candidate material for a high-energy magnet stabiliser 193
14.1 Conclusion based on the Al-Ni alloy's performance . . . 194
14.2 Optimising the co-extruded Al-0.1wt.%Ni-stabilised conductor . . . 195

15 Conclusion 197
15.1 Compositional challenges . . . 198
15.2 Mechanical work and its effect on material behaviour . . . 199
15.3 Influence of thermal processing . . . 201

Bibliography 203

1

Introduction

> ***Engineering is the art of modelling materials we do not wholly understand, into shapes we cannot precisely analyse so as to withstand forces we cannot properly assess, in such a way that the public has no reason to suspect the extent of our ignorance.***
>
> — **A.R. Dykes**
> (American Academic)

Where high magnetic fields are created, following from high currents, large magnetic forces are introduced. These large magnetic forces are required to be counteracted by structures, both heavy and slim, depending on their position and use in a magnet. Stainless-steel structures can be deployed when the item is assigned a pure structural task. Copper or aluminium on the other hand can, despite their reduced mechanical strength, be the answer when additionally specific transport properties are required.

In this first chapter the framework of the thesis is presented. Addressed is the need for mechanical structures in a magnetic environment with elevated stored energies. The mechanical structures serve a wide variety of purposes, depending on their position in the high-energy environment. An overview is given of a threefold of structural components employed in large-size superconducting magnet systems, subject of the present thesis. Per component the reader will find in this introductory chapter environmental challenges and issues when designing such a structure, and in particular its selection and development of material.

As the research considers three structural components and their selected materials, the subsequent thesis is comprising three parts. Each part is consequently further introduced, where the state of the art material solutions are presented. The introductory chapter hereafter thus merely gives the reader a frame of reference. Figure 1.1 shows a brief thesis outline.

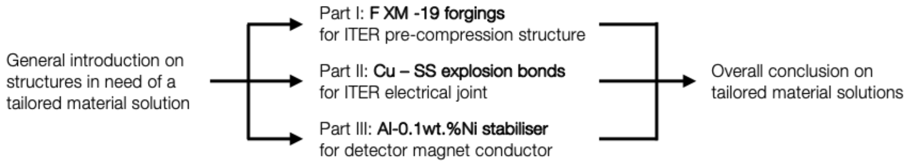

Figure 1.1: Brief outline of the thesis.

Magnet technology has taken flight with the introduction of superconductivity. The introduction of superconducting wires into the world of electromagnets has remarkably increased static magnetic fields up to some 32 T [Weijers et al., 2016], while maintaining sufficient bore diameter for functional use.

Resulting from the corresponding high stored energies are eminent forces in the magnet's structure. Forces arising from energised coils need to be counteracted by large constructive elements in the magnets, constructive elements that need to serve at the same low temperature as required for superconducting coil operation. The focus in this thesis lies on the challenges arising with design and fabrication of aforementioned constructive elements, and in particular their materials and material connections in the state as they are produced for the application. In other words; application based materials and their mechanical properties as needed for their constructive role under extreme environmental conditions.

1.1 Future in Large-Size Superconducting Magnets

For future high-resolution particle physics experiments, as well as state of the art particle fusion experiments, large size superconducting magnets are being developed. Large bore, multi-stack coils are being designed and constructed to generate the required magnetic field to ensure the right particle trajectory.

1.1.1 Large-size magnets for fusion experiments

With ITER, the International Thermonuclear Experimental Reactor, a global international collaboration is building one of the world's most powerful electromagnets to provide plasma handling in the ITER tokamak. A state of the art structure is designed to drive and control the plasma needed to harvest energy from nuclear fusion.

Where the ITER project is trying to demonstrate a crucial step in the feasibility of nuclear fusion to meet the future energy needs, its magnetic structure is designed, produced and tested to demonstrate its suitability and safety. With the aim of producing ten times the amount of energy that it takes to run the process of nuclear fusion, the magnet system will be extensively reviewed for its reliability. The large international project is not only focussing on the net gain of energy by nuclear fusion, but is foremost about the affirmation of the technology required for such a process.

With nuclear fusion only taking place in an extremely high-temperature environment, involving highly energetic particles at high density, which have the tendency to expand, the necessity for a magnetic confinement system is evident. Since no material would be able to confine, shape and drive the plasma in a passive manner just magnetic confinement may prove feasible.

Taking into account the production of some 500 MW of fusion power, the plasma volume will comprise some 830 m^3, for which the tokamak will require some 50 GJ of stored magnetic energy [International Atomic Energy Agency, 2001]. The tokamak principle relies on a steady toroidal magnetic field and a transient axial magnetic field with respect to the torus. The plasma is confined to a doughnut-like volume by the resulting toroidal magnetic field and is heated and stabilised by the plasma current, which is persuaded to flow in a primarily toroidal direction by the changing axial field [Ambrosino, 2009].

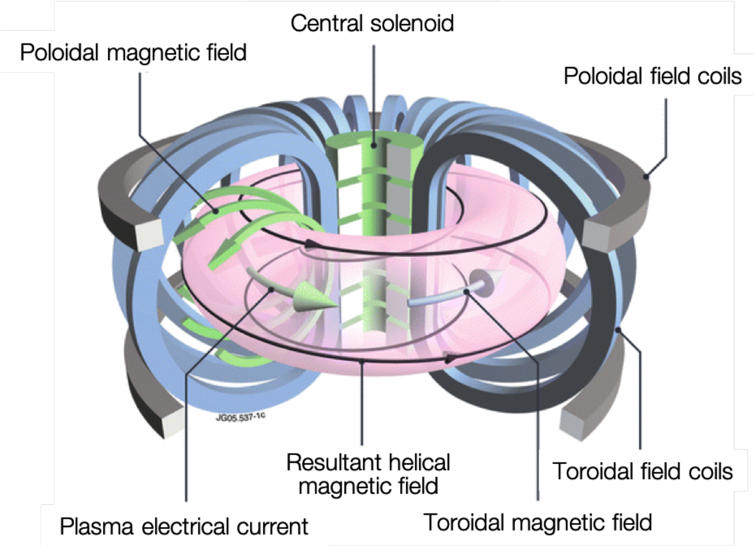

Figure 1.2: Schematic depicting the magnetic control system to form, contain and drive the highly energetic plasma required for nuclear fusion. The image displays only the primary magnet system, which is accompanied by correction coils to absorb any deviations from the required resulting magnetic field [De Tommasi, 2018].

Where one would normally confine matter with a solenoidal shaped coil leaving the ends open for escape, here the quest to fully encapsulate the matter has led to the employment of a type of solenoidal (pipe-like) shape where the ends meet. The resultant so-called toroidal confinement can consist of a helix-like coil stretching over the entire 360° of its circle. Or, more conveniently, in the case of the ITER tokamak, it consists of a number of individual toroidal-field coils placed along this circle as can be observed in figure 1.2. With magnetic field strength decreasing in a coil from the inside-out, additional convergence towards the centre of the toroid is necessary.

A poloidal magnetic field, induced primarily by the internally positioned central solenoid (figure 1.2), causes the particles, now already having a toroidal movement, to spin in a helical direction, with that staying away from the physical walls. Heating of the plasma current is also performed by this central solenoid structure, consisting of a vertical stack of six individually powered coils. By energising the coils in a transient manner they induce plasma currents, much like in a transformer. Here the solenoidal coils can be seen as the primary windings and the plasma as the secondary winding. Heat generation in the plasma is implied by ohmic heating.

Additional coil systems include the externally positioned poloidal-field coils which aid in the shaping of the plasma with a static field. And the correction coils (not shown in figure 1.2), intended to reduce the error fields created by the magnetic system as a whole.

Completely built-up out of the low temperature superconductors NbTi and Nb_3Sn, the ITER tokamak is currently the largest tokamak system under construction. To arrive at a confinement of 830 m^3 of plasma volume, the aforementioned magnets are large-scale, with the toroidal magnet system being the heaviest of the lot. In table 1.1 the magnet system of the ITER tokamak and their main parameters are summarised [Libeyre et al., 2003; Libeyre et al., 2015; Lim et al., 2010; ITER Organisation, 2013a; Foussat et al., 2010].

Table 1.1: Main parameters of the superconducting coils of the ITER tokamak magnet structure.

	CS	**TF**	**PF**	**CC**
Superconductor	Nb_3Sn	Nb_3Sn	NbTi	NbTi
No. of coils	6	18	6	3 x 6
Max. coil dimensions	⌀ 4.3 m	14 x 9 m^2	⌀ 24 m	7.2 x 8.4 m^2
Total mass	947 t	6540 t	2163 t	85 t
Nominal peak field	13.5 T [a]/12.8 T [b]	11.8 T	up to 6.4 T	up to 5.0 T
Operating current	41.8 kA [a]/46 kA[b]	68 kA	up to 52 kA	10 kA
Stored magnetic energy	6.4 GJ	41 GJ	4 GJ	-

[a] at initial magnetisation
[b] at end of burn

1.1.2 Large-bore magnets for particle physics experiments

Following the discovery of the Higgs boson at the Large Hadron Collider (LHC), a new era of elementary particle physics has commenced. Where the current state-of-the-art accelerator complex, conjointly with its high-precision particle detectors have allowed to demonstrate the presence of such a particle, higher precision measurement of its mass and couplings in all details remains to be done. The properties of the Higgs boson leaves the physics community with many questions concerning its complexity. With the current set-up of the LHC and its upgrade to the high-luminosity LHC (HL-LHC) only part of the questions may be answered, leaving the community with the quest for an evolved set-up to explore further.

New generation particle accelerator complexes are being designed to drive particles upto a final collision energy of 100 TeV (FCC-hh; future circular hadron collider), seven times the amount currently achieved in the LHC [Abada et al., 2019]. The increase in particle energy during collision results in an increase in bending force, required to push particle trajectories apart at the collision point, thereby guaranteeing discrimination of the elementary particles emitted.

The bending force is generated with use of a solenoidal magnet field positioned symmetrically around the collision point. Under the influence of the magnetic field produced by the solenoid, charged elementary particles take on a charge- and mass-specific trajectory. Tracking of the charged particles therefore takes place within the bore of the solenoid magnet. Neutral particles, unaffected by the magnetic field, can be partially tracked outside the magnet structure. The solenoid is thus placed at the centre of the detector, and is required to be virtually particle transparent to accommodate for particle tracking also outside the magnet structure. An example of such a solenoid is the central solenoid present at the core of the ATLAS detector (figure 1.3), which is, together with CMS, a universal detector at the LHC accelerator complex. In the case of ATLAS, a coil composed of a 12-strand Rutherford cable embedded in a 4.3 mm wide by 30 mm high purity nickel-doped aluminium stabiliser surrounds the interaction point. The NbTi (Nb-50wt.%Ti) strands, each containing 2050 filaments, accommodate the 7.6 kA current required to generate a 2.0 T central magnetic field in operation. A single layer of conductor is wound with 222 turns per meter to achieve the aforementioned required magnetic field (4.5 mm width per turn including insulation) [CERN, 1997a].

New generation solenoids are designed with large bores and are required to produce enhanced magnetic fields to guarantee particle tracking over a large distance.

Amongst the new-generation solenoids for particle detectors is the solenoid being designed for CLIC, CERNs possible future compact linear electron-positron collider. The conceptual design of the CLIC detector magnet system is based on the experience gained on these types of magnet systems with the last generation detector

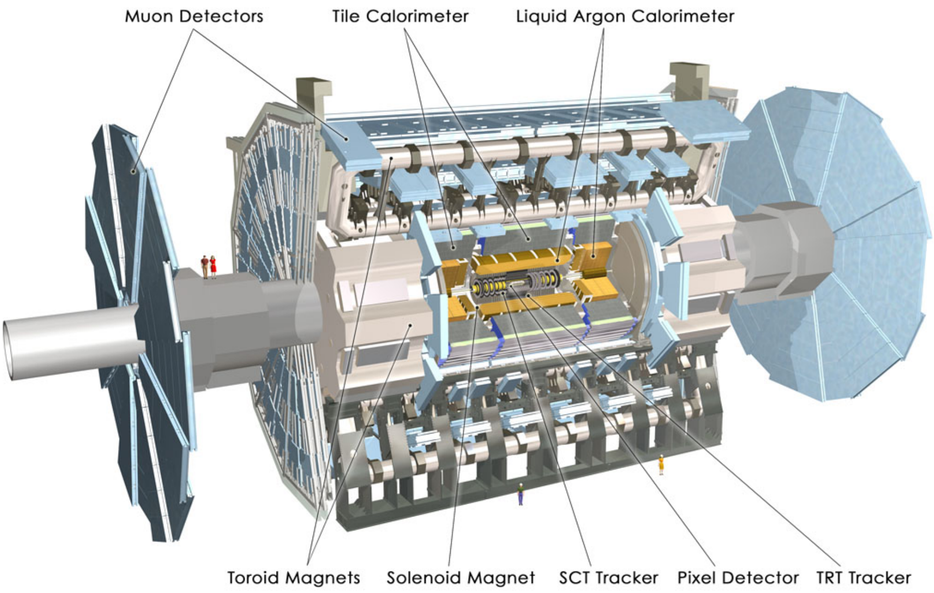

Figure 1.3: Schematic representation of the ATLAS detector, indicating besides the main particle tracking systems also the main magnet systems. Note the position of the solenoid magnet around the inner tracker, leaving particles to pass through the conductor prior to arriving in the calorimeters [Pequenao, 2008].

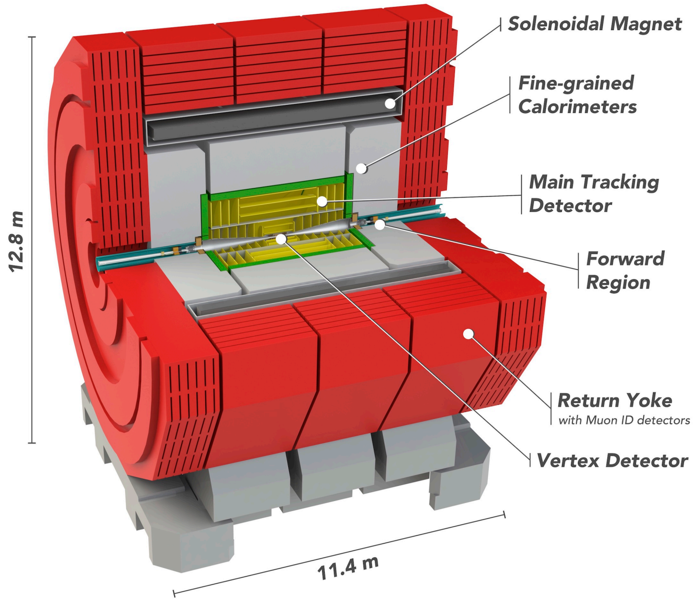

Figure 1.4: Schematic representation of the foreseen CLIC detector, denoting its main particle-tracking systems, but moreover the positioning of its solenoid. Note the increase in bore diameter with this new-generation detector magnets [CERN, 2019].

magnets embedded in the ATLAS and CMS detectors. A five-layer, multi-module solenoid coil with an external support cylinder will be placed in the heart of the detector. Within the CLIC detector, in contrary to the ATLAS detector, additional calorimeters are included within the bore of the magnet, which eminently increases magnet bore size. An increase in distance to the coil axis, and thus the distance to the interaction point, follows. High-precision tracking devices are concentrated in the central part of the detector for which a stable nominal field is required. Combined with the quest for an increase in collision energy results in the need for enhanced conductor performance.

Table 1.2 shows some of the main parameters for the of the ATLAS detector solenoid, versus the design of the CLIC solenoid, showing the scale-up. Moreover figure 1.3 and figure 1.4 show the differences in detector layout between the two, related to the difference in parameters.

Table 1.2: Main parameters of the superconducting central solenoid of ATLAS vs. CLIC_SiD.

	ATLAS	**CLIC_SiD**[a]
Free bore diameter	2.4 m	5.5 m
Nominal magnetic field at IP[b]	2.0 T	5.0 T
Peak magnetic field at the conductor	2.6 T	5.8 T
Operating current	7.6 kA	18 kA
Ampere·turns	8.9 MA·turns	34 MA·turns
Stored magnetic energy	38 MJ	2.3 GJ

[a] compact all-silicon tracking detector concept, chosen as reference here
[b] interaction point

1.2 Structural Components for Large-Scale Magnets

The presented magnet systems require high currents to reach the essential magnetic field, which imperatively means that elevated forces are generated during magnet operation. The main resultant forces are radially oriented hoop forces and axially oriented compressive or separation forces. Each magnet system is required to deal with these forces in a different manner. In magnets, employed for fusion energy, heavy structures are allowed and in most cases vital. Whereas in magnets for particle physics, detector particle radiation transparency is leading, demanding the lightest possible construction, although sufficiently counteractive.

1.2.1 Forces to be counteracted

The magnetic field exercises a force on the current carrying conductor resulting from the cross-product of the two vectors. In the case of a superconducting magnet these forces can be substantial; resulting from the high current density and its resulting magnetic field. The Laplace forces, originating from the Lorentz force law, need to be counteracted either by the coil itself or by its support structure.

Effect of hoop force

The strongest component of magnetic field in a solenoid is in the axial direction, thus exerting, according to the Lorentz force law, an outward radial force on the conductor. This outward radial force is known as the hoop force, resulting in a circumferential hoop stress in the coil windings.

The most straightforward way of determining such a hoop stress in a winding is simply visualising the magnetic field as a two-dimensional gas exerting a pressure on its container, based on Faraday's vision to envisage the magnetic field as a collection of lines under tension, which mutually repel each other. The magnetic pressure can be deduced from the stored energy in axial direction:

$$P_r = \frac{B_z^2}{2\mu_0} \ , \tag{1.1}$$

where B_z is the axial component of the magnetic field and μ_0 is the magnetic permeability of free space. The hoop stress, which is maximum at the coil center, is now given by:

$$\sigma_\theta = \frac{r \cdot P_r}{t} \ , \tag{1.2}$$

where r denotes the radius until coil center, and t the mechanically effective coil thickness. If we consider the hoop stress for the ATLAS central solenoid a quick calculation yields a magnetic pressure of 1.6 MPa based on a 2.0 T axial field. This leads to a maximum hoop stress of some 64 MPa, considering a mechanically effective coil thickness of 30 mm, in other words just the stabilised superconductor (section 1.2.3). The single layer of aluminium stabilised superconductor is, in the case of the ATLAS central solenoid, encapsulated by a 5083-H32 aluminium alloy support cylinder. With the cylinder adding to the mechanically effective coil thickness, we obtain a resulting estimated hoop stress at the coil center of 47 MPa.

For the CLIC_SiD solenoid, with a radial magnetic pressure measuring some 10 MPa, the hoop stress in the center of the outer winding, solely considering this outer winding, arrives at some 320 MPa. Even though this does not fully represent the designed case of the CLIC_SiD solenoid, as the mechanically effective coil thickness differs and the effect of the other windings is not taken into account, it provides an idea of the scaling of hoop stress with increasing field and bore diameter.

Suggested conductor design is such that hoop strain does not exceed 0.15 % and hoop stress does not surpass $^2/_3$ of the effective yield strength. The hoop stress, hoop strain and effective yield strength follows from the aluminium alloy used. A useful representation is in terms of the ratio of structural aluminium, as is shown in figure 1.5, where the ratio of structural aluminium is plotted against the average hoop strain in the conductor. Here the plot is presented for a range of E over M, denoting the energy over mass ratio, linking the stored energy to the volume of cold mass [Herve et al., 2008].

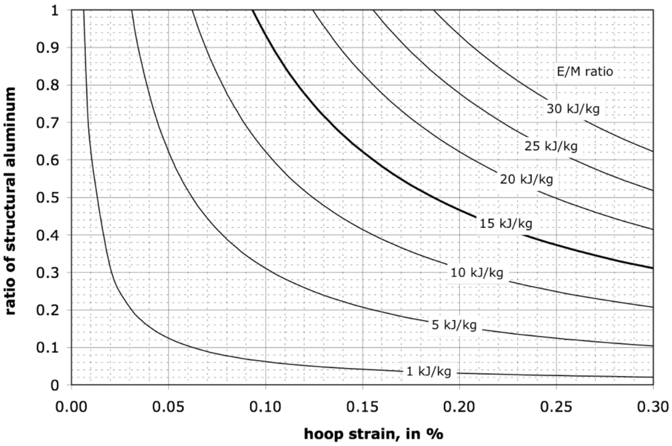

Figure 1.5: Ratio of structural aluminium in the proposed conductor versus hoop strain for a range of $^E/_M$ ratios [Curé, 2010].

From figure 1.5 one can denote hoop strain increasing exponentially with decreasing structural aluminium ratio. In the design of the CLIC_SiD solenoid, a structural ratio of 0.5 to 1.0 is therefore suggested, linking the design to either a hybrid or fully alloyed solution (see section 11.1). To sustain the 0.15 % hoop strain limit, the design must not exceed an $^E/_M$ ratio of 15 kJ/kg. Calculations have shown that for the CLIC_SiD solenoid, a multi-module, 5-layer coil, with an equally adopted external support cylinder, average hoop stress in the conductor reaches at least 116 MPa and 61 MPa for a structural aluminium ratio of 0.5 and 1.0, respectively[Curé, 2010]. As a reference; high purity aluminium, with a purity of at least 99.9998 wt.% Al, holds a yield strength of only 30 MPa to 40 MPa at 4.2 K.

Effect of axial force

Close to the axial ends of a solenoid the magnetic field has a strong radial component, making the force, being perpendicular to the field direction, tending in axial direction, thereby compressing the windings. This stress does not interact with either radial or hoop stress, and their resulting stress at first approximation can be calculated by summing them up over the elements of the winding along its axial direction. Maximum stress is seen at the mid-plane of the coil, and are generally endured by the coil structure itself [Wilson, 1987].

This, however, is not the only force directed in axial direction that a coil stack can exhibit. In the case of individually powered coils, like in the central solenoid stack designed for the ITER tokamak, opposing currents can lead to the forceful separation of the different coil modules.

The Central Solenoid (CS), providing a dynamic magnetic field that inductively drives the plasma, occupying the bore of the ITER tokamak, consists of a vertical stack of six individually driven coils [Mitchell et al., 2012]. As a result of transient varying electrical currents in the individual modules during magnet operation large cyclic forces are introduced, not only radially but also axially [Freudenberg et al., 2011].

The magnetic field curvature at the ends of the individual central solenoid modules create vertical forces. At the initial magnetisation the forces are directed towards the mid-plane of the stack, whereas during ramp-down the end modules carry opposite currents to the central ones, as can be noted from figure 1.6, and are separated with a force up to 75 MN [ITER Organisation, 2013a].

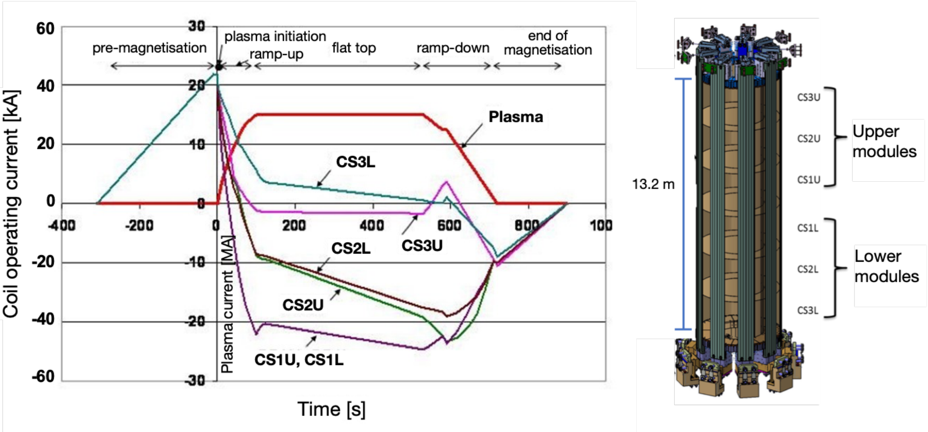

Figure 1.6: Operating current in the 6 CS modules throughout the 15 MA plasma scenario foreseen to be the primary operating scenario of the ITER tokamak. The six modules are magnetised together until plasma initiation, and are subsequently discharged according to individual current profiles to sustain the plasma [Dulon, K., 2010].

The current study responds to the need for specifically designed structures to counterbalance the aforementioned considerable forces of radial and axial nature. The structural components, having often a multitude of purposes besides their structural assignment, can reach increased complexity. Following are structural components, for which their material solutions are the specific topic of the present thesis, briefly explained.

1.2.2 Specific structures for tokamak magnet systems

In the present study the focus lies on two specific components in need of a large counteracting ability of the presented axial and hoop forces in tokamak magnets. Both of which are in need of distinct material solutions to reach the stringent requirements set.

Pre-compression structure

To guarantee structural integrity and consequently magnet stability, the cyclic forces in the CS coils are balanced by a specially designed support structure. To prevent axial movement of the modules during magnet operation, a large pre-compression structure is present, consisting of 27 tie plates. Via 18 outer tie plates, and 9 placed inside the CS modules, pre-load is applied on the coil stack to pre-compress the magnets prior to cool-down, and retain the compressive stress at cold and during the varying operation conditions.

The tie plate configuration consists of a long 'slab' part, and two enlarged 'head' parts at either end, measuring together up to a considerable 15 m in length. The inner tie plates are located in the bore of the CS. Outer tie plates (left- and right-hand) are in mirror symmetry located at the outside diameter of the CS (figure 1.7).

Cyclic loading of the coils emphasises the need for enhanced dynamic properties of this pre-compression structure, besides the apparent static requirements. This is increasing it's complexity, and with that the material's requirements. Furthermore, the pre-compression structure needs to reach the mechanical properties both prior to, as well as subsequent to cool-down, for which the material needs to be achieving both at the pre-load temperature of 293 K, as well as the operating temperature of 4.2 K.

Joint boxes for electrical connection

The magnet system of the ITER experiment includes several sets of superconducting coils composed of the typical CICCs [Mitchell et al., 2012]. The CICCs allow for the transport of high currents required to produce the high magnetic fields needed to confine the plasma [Ciazynski et al., 2001]. Connection of the terminations of these high current carrying coils, and their connection to current feeders, is realised by highly performing, electrical joints (figure 1.8). The joints, necessary for the current distribution between the unit lengths of superconductors, are amongst the coils' critical components. Where the joints are required to transfer high currents at low DC resistance [Martovetsky et al., 1998], they are simultaneously submitted to fast varying high magnetic field, imposing large radial and axial forces. In essence mainly hoop forces, however, also repelling forces between two current carrying cables.

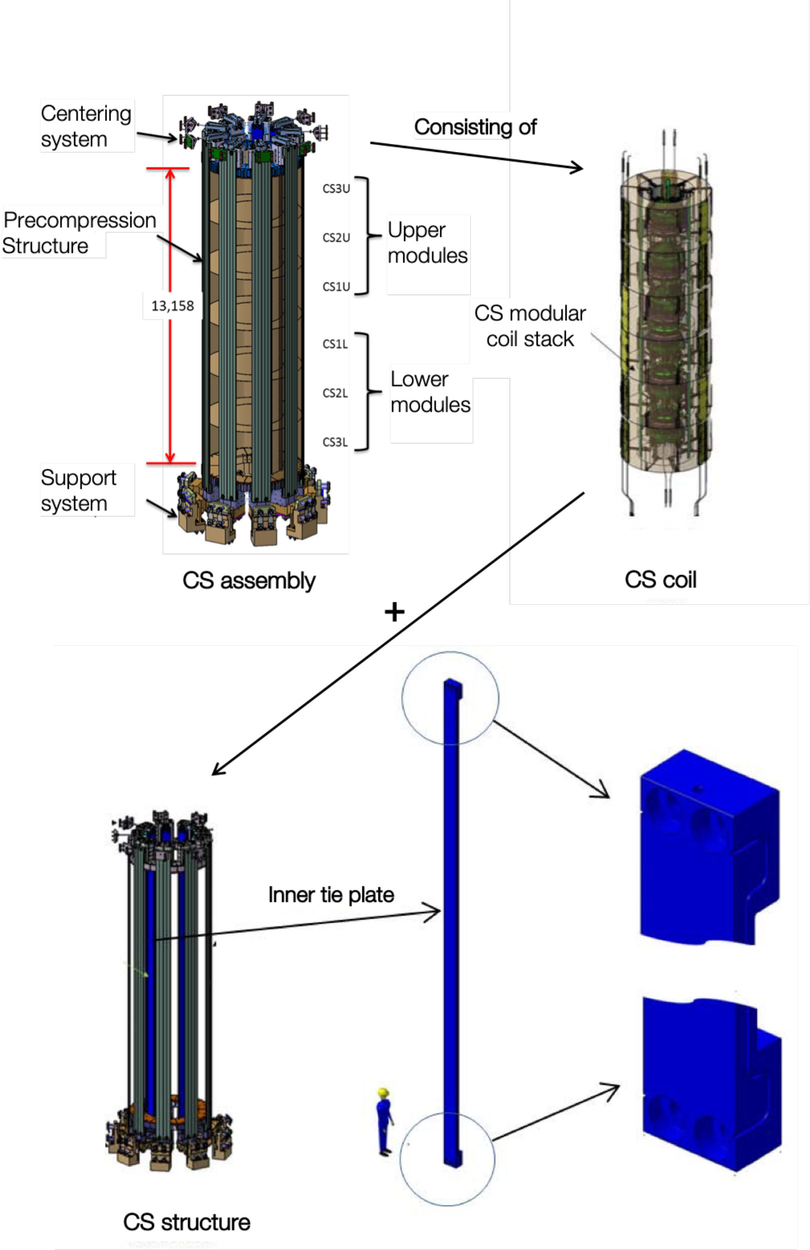

Figure 1.7: Schematic image showing the ITER central solenoid, consisting of its six (6) modules, and its related pre-compression structure. The tie plates are the vertical elements containing the central solenoid module stack, and measure some 15 m in height [ITER Organisation, 2013b; ITER Organisation, 2017].

As a result of being one of the main resistive components, the joints are complex components. Not only the mechanical characteristics, for the resistance against local deformation, but also its electrical behaviour have to be addressed to obtain satisfactory joint operation while avoiding conductor performance degradation.

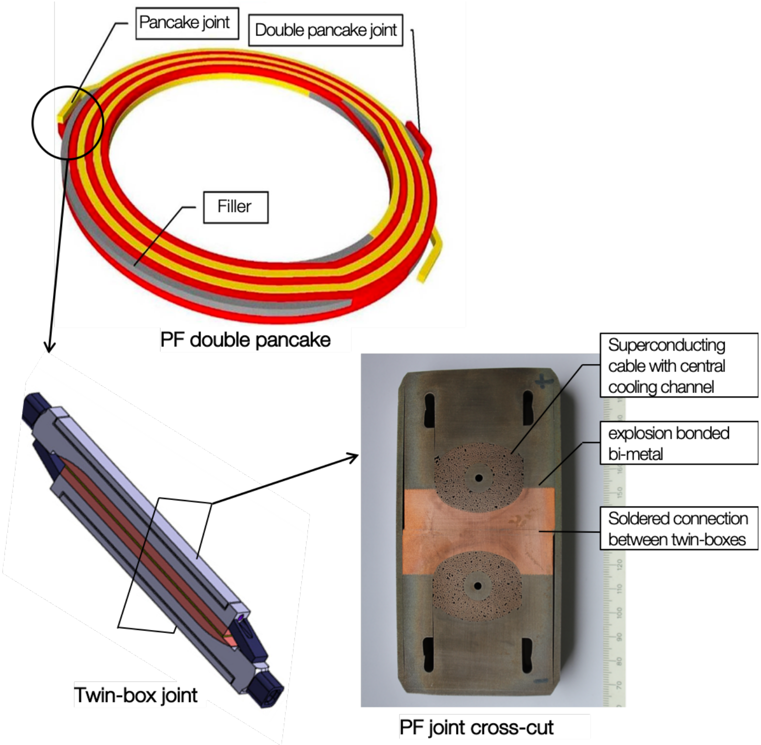

Figure 1.8: Image representing an electrical joint and its positioning in the PF coils. Inter-pancake connection requires the use of an electrical joint, here in the form of a twin-box joint, consisting of two cables compacted into a bimetallic box and subsequently soldered [Rolando et al., 2013; Lim et al., 2010].

The design is based on a twin-box lap type joint. By fabrication of twin terminals at both conductor ends, soldered together, the concept allows for the joints to be dismountable. Each terminal is manufactured by compacting the stripped cable end into a bimetallic box, machined from a copper-clad plate, bonded by the explosive technique [Ciazynski et al., 1996]. Figure 1.8 shows the design and composition of such a twin-box joint, with as a main structural as well as electrical component the bimetallic box where both the superconducting cable ends are embedded in, as well as employed to deliver the current transfer.

The terminal joint relies on both the structural as well as the conductive properties of this bimetallic box, for which it requires a tight mechanical link between the conductive copper-cladding and the structural stainless steel. Sufficient mechanical stability of the copper-cladding needs to be ensured in order to avoid strand movement under electromagnetic load, while guaranteeing efficient current transfer.

1.2.3 Specific structures for detector magnets

In the case of a solenoid, occupying the bore of a particle detector, the self-supporting magnet structure needs to sustain the large electromagnetic force as a result of the high peak magnetic field. The location of the solenoidal coil, see figure 1.9, excludes the implementation of a rigid support structure. The conductor is, itself, required to exhibit high mechanical properties, not only globally, where the alloyed aluminium support cylinder can aid, but also locally where high hoop stress could arise in the vicinity of the superconducting cable.

Reinforced aluminium stabilised superconductor

To ensure superconductor stability and quench protection, the superconducting Rutherford cable is embedded in high-purity aluminium, exhibiting high thermal conductivity and low electrical resistivity. Besides excellent transport properties, the high-purity aluminium also provides a high transparency to particles, essential at its employed location. High local stress needs to be sustained by the high-purity aluminium stabiliser, a material not particularly known for its structural properties.

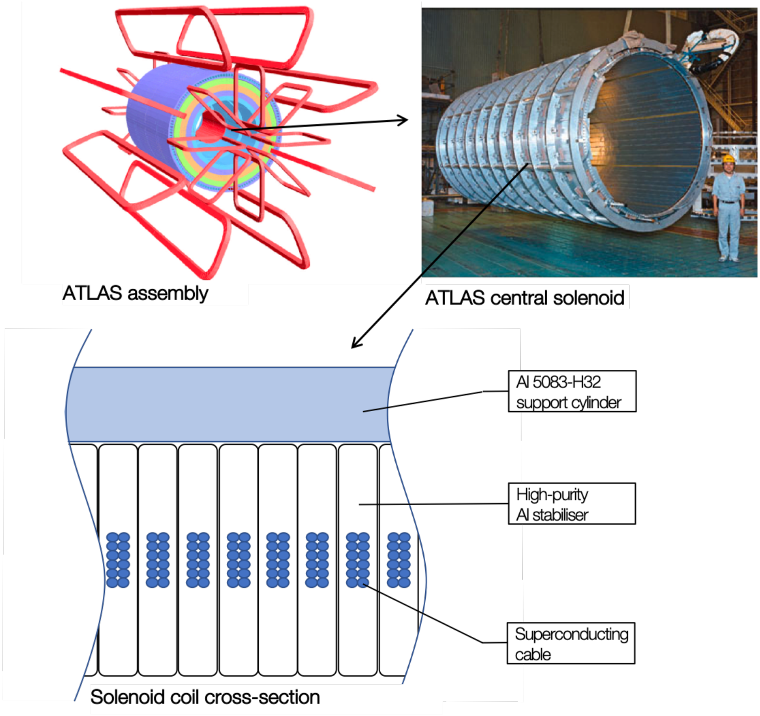

Figure 1.9: Image demonstrating the function and positioning of the aluminium stabilised superconductor, requiring to exhibit besides excellent conductive properties also decent mechanical properties as the structure is enforced to be self-supportive [CERN, 1997a; CERN, 1997b; Larbalestier, 2011].

For the ATLAS central solenoid extensive research and development has led to the realisation of a thermo-electrically capable stabiliser (extensively discussed in section 11.4.2), simultaneously exhibiting sufficient mechanical strength to cope with the forces it is subjected to [Yamamoto et al., 1999]. For future detector magnets, where magnetic field and bore size are envisaged to increase, conductor scale-up is vital. A specifically designed stabiliser needs to meet the extreme conductive, structural and radiation transparency requirements.

1.2.4 Environmental implications

The superconducting cables make use of commercially available low-temperature superconductors, niobium-titanium, NbTi, and niobium-tin, Nb_3Sn. For these materials the superconducting state appears very abruptly when the material is cooled down below a transition point. Below this critical temperature T_c the material becomes a perfect conductor of electrical current, without energy loss, neither thermal nor kinetic. A return of the material to its normal resistive state, however, not only depends on T_c, but it was found that superconductivity is bound by a critical surface depending on the critical temperature T_c, the critical magnetic field B_{c2} and the critical current density J_c (figure 1.10).

With an increase in current density, resulting eminently in an increased magnetic field, one must lower the operation temperature to guarantee superconductivity. With helium being a stable gas boiling at the lowest temperature of 4.2 K, it provides a good cooling medium to achieve the largest margin for superconductivity. In fact, liquid helium can even be pumped down to a temperature of 0.8 K [Sharma, 2015]. The applied temperatures of liquid helium being exploited for superconducting magnet cooling are 1.8 K and 4.2 K. Whilst operating a magnet at such temperatures we can see that a margin remains for NbTi and Nb_3Sn, with their T_c (at $B = 0$ and $J = 0$) of 9.2 K and 18.3 K, respectively. The difference in T_c between the two (NbTi and Nb_3Sn) implicates that for the latter higher magnetic-fields can be reached at the same operating temperature.

While Nb_3Sn holds advantages in terms of superconducting performance over the traditionally used NbTi, its formability is more challenging. NbTi, in its various compositions is being produced in filamentary form since long. As a result of its ductility, a continuous range of solution NbTi-alloys, can be drawn in copper tubes to hair-like thickness for the most efficient superconducting wires. The drawing process is alternated with heat-treatments to improve its mechanical characteristics. This is the basis for a very successful employment of NbTi filamentary wires in superconducting coils for large magnet systems over the past 40 years.

On the contrary, Nb_3Sn, with its specific composition exists as highly-brittle, ceramic compound. As a result, drawing Nb_3Sn filaments is not possible. The structure of Nb_3Sn, with Nb atoms approaching each other more closely than is the case in elemental niobium, is thought to be the reason for its excellent superconducting properties. However, even though its final properties are promising, its applicability to wires is not possible. The first Nb_3Sn conductors were made in the form of thin tapes, by chemical vapour deposition or surface diffusion. The usability of these

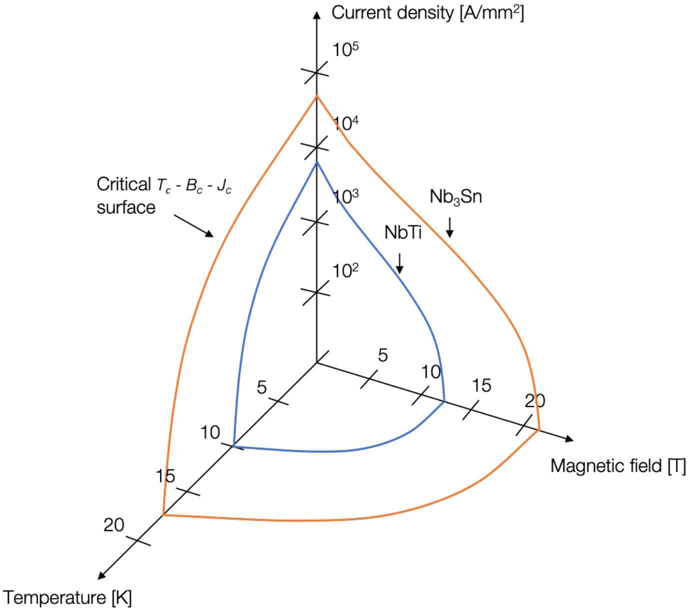

Figure 1.10: Critical current density J_c of two commercial superconductors, NbTi and Nb_3Sn, as a function of magnetic field B and temperature T. A critical surface exists above which the superconductor returns to its 'normal' resistive state.

tapes was limited as with manipulation, and therefore also winding the material could easily break, thus resulting in superconducting current degradation.

Filamentary production of Nb_3Sn became possible when one became aware of the possibility of Nb_3Sn formation by a solid-state process. With a bronze process, filaments of pure niobium are drawn into a matrix of copper/tin bronze, which, after reaching optimal size, are heat-treated at elevated temperature for a substantial duration in order for tin diffusion to take place, resulting in the formation of the superconducting intermetallic compound Nb_3Sn [Wilson, 1987]. These reaction heat-treatments take place in excess of 200 h at a temperature range of 650°C - 700°C (section 9.1.3).

While the specifics of the two superconductors NbTi and Nb_3Sn vary, they both create once wound high magnetic-fields and are in need of a liquid-helium temperature environment for operation. Materials operating in the vicinity of low-temperature superconductors are subjected to the same environmental implications. Superconducting cables are generally submerged in a bath of liquid helium, often of the superfluidic or supercritical kind. A stationary bath can be subsequently cooled by a flow of liquid helium, or in the case of a cable-in-conduit conductor (CICC) employed for the ITER magnet system, the bath itself can be circulative. The CICCs consist of various types of stainless steel jackets, densely filled with superconducting strands in a cable based on either Nb_3Sn or NbTi, and subsequently compacted [Turck et al., 1993]. Cooling of the cables, is realised by direct passage through the conduits, where a void fraction of some 0.15 to 0.3 remains for helium flow, thereby directly mitigating heat at the superconducting strands (figure 1.11). This concept provides a highly efficient cooling scheme by a concentrated liquid helium supply from the cryogenic circuit to the superconducting strands [Bottura et al., 1999], but it requires for the entire surrounding structure to be confined in a cryogenic environment.

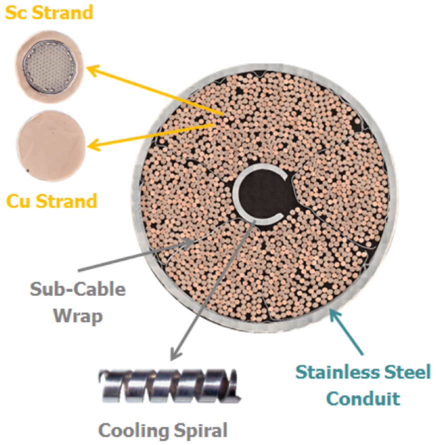

Figure 1.11: Cross sectional image of the Cable In Conduit Conductor for the Toroidal Field coil of the ITER magnet system, and its components explained [Devred et al., 2012].

Where a low temperature is beneficial for the electrical features of a superconductor, they can be highly detrimental for the neighbouring materials, often of a structural type. Metals, generally employed for the structural elements, can exhibit a ductile-to-brittle transformation at sub-zero temperature, thereby not only influencing toughness upon impact, but also in the presence of flaws.

A phenomenon observed in metals when loaded at cryogenic temperature, here liquid helium temperature, is discontinuous yielding. A mode of plastic deformation of a discontinuous nature observed in the plastic domain when loading a metal to failure by tensile forces at cryogenic temperatures. At a temperature below a characteristic threshold, the mode of dislocations transform from a screw to an edge type (see section 11.2.1), resulting from the low thermal energy induced inhibition of screw dislocation motion [Obst et al., 1991].

This phenomenon is highly material dependent, for which threshold temperatures are specific, as well as deformation speed as a result of strain rate sensitivity. Too slow deformation has to be avoided as it would result in the absence of accumulation barriers, as well as excessive local heating resulting from a high rate of deformation. The phenomenon in materials as stainless steel, copper and aluminium, the materials investigated in the present study, typically presents itself in the form of oscillations in the plastic domain (figure 1.12). Sudden drops in stress are observed in the stress strain curve, after which the material retains load, back to its original curve via an inclination parallel to the initial elastic behaviour of the material. The drops in monitored stress is thought to be related to the stress locally surpassing the resistance of the dislocation pile-up, resulting in a sudden release of this dislocation pile-up along a slip plane [Marcinek, 2016].

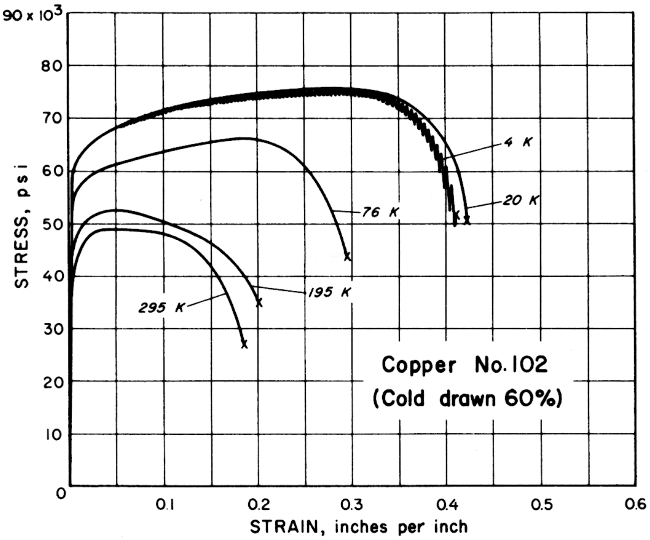

Figure 1.12: Characteristic stress - strain curve of a C10200 copper, extensively studied in Part II. Measurements performed in tension are presented for a wide range of temperatures, where one can note the discontinuous yielding to be present solely at a temperature as low as 4.2 K [Reed et al., 1967].

Discontinuous yielding, or serrated yielding, does not influence the optima such as yield point and ultimate strength; values of importance for this study. Their presence, however, does generally denote a local temperature of the material below the threshold. Additionally, the sudden energy release should be taken into account when designing a material solution where it operates close to its yield point, as thermal transfer to superconducting structures could be highly detrimental for the application.

1.3 Motivation and Scope

The necessity for tailor-made material solutions for future large-scale magnets is eminent, whether the material serves a mere structural task or is required to exhibit additional features. In view of the latter, R & D programs have been set-up at CERN and between CERN and ITER to develop material solutions complying to the most stringent requirements as set by the application.

The aim of this study is to extensively examine a threefold of tailored material solutions for large-scale magnets, and optimise where needed. This comprises a full characterisation of the materials following an application based manufacturing route, and at the environmental conditions the materials will be subjected to in operation. Sample measurement of the mere parent material is generally adopted in a research program, whereas material examination following fabrication in this initial stage is often neglected. The three proposed material solutions, for the application in the ITER pre-compression structure, ITER CICC type electrical joints and at CERN for future detector magnet superconductor stabiliser, are here systematically studied in a production type setting. The relevance of their manufacturing route is thereby included in the outcome.

Specific experimental methods and test configurations have been developed to assess the material under real operating conditions. The outcome of the study adds data to the cryogenic materials database for materials operating under the most stringent conditions in high-magnetic, low-temperature environments; a database currently deficient of a large set of materials essential for low temperature application. Moreover, it will provide the reader with a useful set of data, directly relevant to the specific employment.

As the presented study consists of a threefold of research topics, the thesis is structured accordingly:

Part I: A tailor-made solution is investigated for the large load bearing tie plate structures of the ITER pre-compression system. F-XM-19 is proposed as a material candidate.

- In *Chapter 2* the complexity of large size stainless steel forgings is described. It shows the complexity of the forging operation, and its effect on material behaviour. Furthermore stainless steel candidates are presented, amongst which F XM-19, with its expected benefits.

- In *Chapter 3* the first measurement results are presented. An introduction to the specifics of the selected F XM-19 material is given, and the methodology of testing, involving a custom-built cryogenic set-up. Cryogenic temperature tensile characteristics in an application based setting are presented here, followed by the explanation of the observed behaviour in a optical manner.

- In *Chapter 4* the study on low temperature fatigue behaviour is presented, followed by the characteristics of application driven manufactured F XM-19 under the presence of a flaw. Resulting from characteristic features observed in the microstructure, a suggestion is made for the alteration of the calculation method following the standard. An experimental as well as a numerical justification is given.

- In *Chapter 5* the magnetic response of the material following the two manufacturing routes is presented. Here not only magnetic susceptibility is examined, but also its retentivity.

- In *Chapter 6* a conclusion is presented, comprising a review of the main experimental findings of F XM-19 under operating conditions, aiming at identifying its suitability for the foreseen application. The conclusion is followed by recommendations for further development and optimisation.

Part II: A material arrangement is presented. Both a joining process, essential for the appropriate fabrication of the material solution for the application, and the material itself are assessed. The quality of an explosion weld between copper and stainless steel components is investigated, while trying to establish its effect on the copper half, having an electrical as well as structural role in the application of an electrical joint for current connection in magnets for fusion devices.

- In *Chapter 7* the issues generally observed with copper to stainless steel connections are described, and a solution is suggested in the form of an explosion bond. The selected materials for this bond are presented, together with the consideration for their selection.

- In *Chapter 8* the features and mainly quality of the subsequently obtained explosion bonds are discussed. Mechanical as well as optical characteristics of a large variety of bonded plates are presented, established with use of specially developed measurement processes and equipment. Variations between the different plates are presented, while assessing input parameters.

- In *Chapter 9* the effect of the bimetallic weld on the parent materials is assessed. With use of measurements displaying the materials electrical and mechanical characteristics, material selection versus welding technique is determined. Additionally the thermal stability of the different copper claddings is determined in view of the post-welding treatments, necessary for the application.

- *Chapter 10* holds the conclusion of Part II in which the welding process and material choice is reviewed, followed by recommendations for further improvement.

Part III: A tailored material solution is presented for solenoid conductors for high-energy physics detectors. A material solution is presented, not only based on pure chemical composition, but also on material enhancing treatments. A structurally fit stabiliser is proposed, maintaining sufficient conductivity, thermally as well as electrically, and remaining radiation transparent.

- In *Chapter 11* the various methods of mechanical enhancement of a typical low-strength material are presented, while denoting their risks for its transport properties.

- In *Chapter 12* a discussion on the use of mechanical alloying on highly pure aluminium is presented. Application based manufacturing, and its subsequent measurement, mechanically and electrically, leads to the determination of low-temperature mechanical and transport behaviour of a dilute-alloyed aluminium, Al-0.1wt.%Ni, presented here.

- In *Chapter 13* additional strengthening is proposed in the form of work-hardening. The process of work-hardening is described, followed by its beneficial effect on the mechanical characteristics of the aluminium-alloy stabiliser while being in an application type environment. Detrimental effects of work-hardening are likewise discussed, followed by a discussion on the thermal stability of Al-0.1wt.%Ni; anticipating post-manufacturing material treatments.

- In *Chapter 14* a conclusion on the performance of Al-0.1wt.%Ni is presented, followed by a discussion on room for improvement in terms of dilute-alloying for future applications.

Chapter 15, comprising the overall conclusions and recommendations, concerns a recapitulation on the success and optimisation of design and development of tailored material solutions for large-scale superconducting magnet applications.

Figure 1.13 provides the reader with a brief schematic overview of the thesis structure.

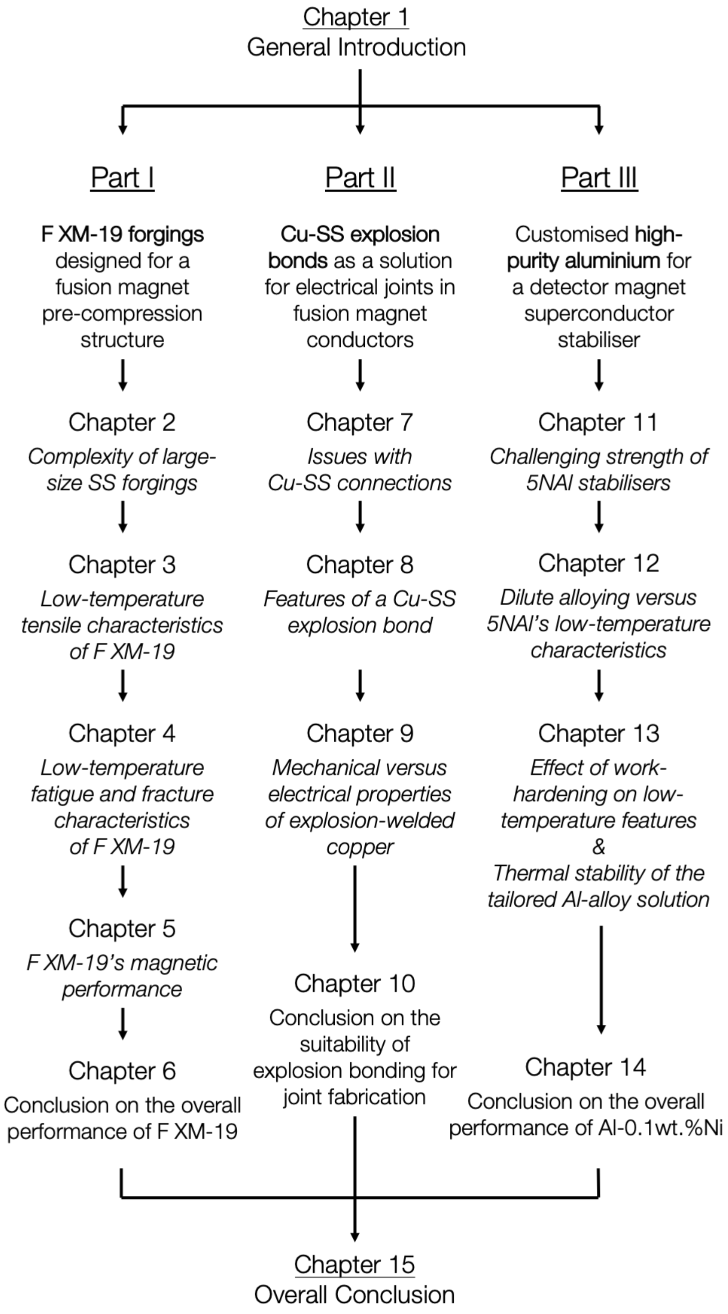

Figure 1.13: Schematic representation of the thesis build-up.

Part I

F XM-19, a forged austenitic stainless steel for large load-bearing structures

2

The complexity of large-size austenitic stainless steel forgings

> ***Men are like steel. When they loose their temper, they loose their worth.***
>
> — **Chuck Norris**
> (American martial artist & actor)

This chapter holds the introduction into the selection of a tailored material solution for the ITER pre-compression tie plates as described in section 1.2.2. The challenges when manufacturing large-size forgings is treated; where from the fabrication process or in this case multiple suggested processes the urge for a carefully selected material is described.

Following from the fabrication challenges, an outline is provided of the stringent material requirements and desired behaviour to realise a tie plate, fit for purpose. Subsequently, a sum-up is provided of the state-of-the-art structural materials as employed in a high magnetic field, cryogenic temperature environment. The candidate forged XM-19 material is introduced, followed by an extensive description of its compositional advantages.

2.1 Introduction

Austenitic stainless steel is widely used for magnet structural components at cryogenic temperatures as a result of their favourable 4.2 K mechanical and magnetic properties. The austenite phase of a steel denotes the presence of its gamma structure, generally targeted with the use of composition-specific thermal treatments. A stainless steel is considered austenitic, when the metal maintains this structure down to ambient temperature.

Stainless steels are categorised by their crystalline structure, where the main classifications are: austenitic, ferritic, martensitic, duplex or precipitation hardenable steels. With the face centred cubic (FCC) austenitic structure being the primary crystalline phase of an austenitic stainless steel, it renders the material essentially non-magnetic, a material property crucial for its application in a highly magnetic environment [Davis, 1994].

This does not imperatively turn all austenitic stainless steels suitable for the purpose of large size structural magnet components like the tie plates described in section 1.2.2. As a result of the challenging production process of these sizeable components, a tailor-made material solution is fundamental.

2.1.1 Tie plate production; fit for purpose

The generally adopted production process for a large-size stainless steel structural component is forging. For the fabrication of the 15 m long tie plates, holding a large length-to-width ratio (section 1.2.2), the mere process of forging, however, holds challenges. Challenges in terms of weight, reheating, material flow and the resultant micro-structural characteristics and mechanical properties. As a result of these challenges, for ITER, two manufacturing routes were explored. Besides a fully forged structure, an alternative was investigated composed from a multitude of smaller forgings subsequently welded together:

1. Single Piece Forged structure (SPF), produced by applying successive forging steps, followed by final machining.

2. Welded Structure (WS), originating from head- and slab-forgings, joined via Gas Metal Arc Welding (GMAW) using an adapted filler material.

A brief introduction into the two production processes and their individual complexity is given.

Single piece forged structure

The single piece forged structure is, as its name suggests, an item forged in a single piece (figure 2.1). A three-phase, multi-step forging process is required to create the 15 m long tie plate, followed by a two step machining process to acquire the final item with its corresponding tight tolerances.

Pre-forging commences from a refined ingot, subsequently electro-slag remelted (ESR), to further remelt and refine the steel.

Forging of the 15 t ingot is performed on a 30 MN digitally controlled hydraulic press with a capacity of 35 MN for small time-span upsetting operations. Upset forging provides vast plastic deformation under high pressure, and is employed to decrease the length of the work piece while increasing its diameter, resulting in an improved material flow and thus better micro-structural characteristics of the end piece.

Figure 2.1: Photograph showing the 15 m tie plate forging from a single piece. Note that this image is taken during an intermediate forging step, is indicative, and thus not contain the full length of the end-piece. The image illustrates the manipulation of the piece on the one end, and the challenges to maintain dimensions and straightness [Degitz, 2013].

The required material homogeneity, within 1 equivalent grain size number around the prescribed average of 3 [ITER Organisation, 2017], is solicited with the use of a preheated ingot to the temperature of some 1200°C, followed by upset forging. Pre-forging results in the intermediate product containing a cross-sectional area of 1.1 m times 1.1 m at equal height. The pre-forging process is used to reduce the cross-sectional surface, and obtaining a workable block for further elongation of the piece, while with upsetting the micro-structural homogeneity is retained.

Pre-forging, intermediate forging and final forging are alternated with intermediate reheating and quench steps to set the metal to its final metallurgical properties. To guarantee the integrity of the piece throughout the forging process, the forging phases are followed by a descaling process, succeeded by an ultrasonic contact control. With the ultrasonic testing procedure irregularities in the bulk of the material can be observed. Mechanical cleaning in the form of intermediate machining and/or grinding can eliminate surface or sub-surface irregularities, which might cause defects in the further forging phases.

The intermediate forging follows a reheating of some 14 h of the pre-forged quenched piece, to realise a homogeneous temperature of the item, resulting in a homogeneous material flow during successive forging. This way, residual stresses are reduced to a minimum. The intermediate forging operation is performed in four successive steps, interspersed with intermediate reheating to reduce the probability of crack formation resulting from poor material flow. The four steps can be divided into two processes, where the first three steps are aimed at reducing the cross-section, and achieving elongation, whereas the last step includes defining the head and slab parts of the tie plate while realising additional elongation. Intermediate forging causes an elongation of the piece to a final 11.7 m, while avoiding sharp corners and edges where material flaws could emerge.

With an annealing furnace capacity in length of only 13 m, the final reduction, and thus final forging operation is required to be done in a single step. Some intermediate reheating of either end of the tie plate is adopted to maintain a forgeable material. A final length is realised of some 15.7 m, containing final elongation and remodelling of the head and slab parts of the item. Build-up of residual stress in the material induced by the size of the forging results in some torsion and bending of the piece. Straightening, in this case, was realised with use of local and global reheatings of the piece prior to cool-down by water quenching. An attempt to retain grain structure was done by performing a solution annealing at 1100°C for 2 h, adopted to the specific steel grade.

The tie plate forging is subsequently machined to final configuration (figure 2.1), with tight tolerances down to 0.1 mm (flatness head section) [US ITER project, 2013].

Welded structure

The welded structure consists of three parts, individually forged, subsequently joined by welding. Advantageous in this production method is the apparent handling during forging, resulting in a better control of material flow and thus grain structure. Items can furthermore be forged near to final size, reducing post-milling activities. However, the main advantage is the potential availability of forging shops equipped and willing to produce such smaller forgings, while only a few companies worldwide can be solicited for the production of the single piece forged structure.

Forging pieces for the welded structure consist of two head forgings (figure 2.2a), and a single slab forging (figure 2.2b). The size reduction of the forged pieces results in apparent advantages in terms of reduced number of forging steps, reheating times and handling. On the contrary, realisation of welds of such dimensions is cumbersome, and the welds need to sustain the same 75 MN load endured by the pre-compression structure (figure 1.2.1), as the welds are inevitably in the load line of the tie plate. Welds are therefore required to hold an equal or better mechanical performance than the base material, where the base material needs to comply with a tensile strength of 690 MPa or superior at room temperature [ITER Organisation, 2017].

To reduce issues at high-stress regions, welds were designed to be performed in the slab region (figure 2.2c), i.e. not at the transition from slab to head section. Figure 2.2d shows a close-up of the weld area, demonstrating the heaviness of the GMAW double-V bevel weld, realised by 16 weld passes from either side.

(a) WS head forging.

(b) WS slab forging.

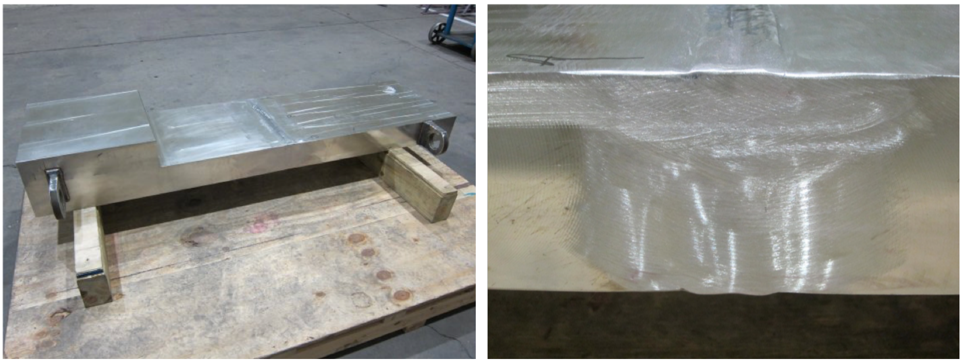

(c) WS prototype containing a machined WS slab joined by GMAW to a WS head forging.

(d) Close-up of the GMAW weldment positioned between the head and slab forgings.

Figure 2.2: Pictures denoting the build-up of the tie plate welded structure, consisting of three smaller but still sizeable forgings; two head forgings (a) and one slab forging (b), joined by three heavy double-V bevel welds (c). The weld close-up in image (d) provides some perception of the complexity and heaviness of the weldment [Degitz, 2013].

2.2 State-of-the-art austenitic stainless steels

The selection of the correct material for the forged productions of the 15 m long tie plates is essential. Where its necessity is apparent not only in terms of achievable properties following a full manufacturing route, but almost just of as much importance, the behaviour of the material during the production process. A tailor-made material is essential, highly performing under the stringent conditions needed [ITER Organisation, 2017]:

- Excellent ductility to assure exceptional forgeability under a large temperature range.

- Static mechanical properties in as-produced form of ≥ 690 MPa in tensile strength with an 0.2% yield point of ≥ 380 MPa; leading to a static mechanical performance of some 1600 MPa and 1200 MPa in ultimate tensile strength and 0.2% yield strength at 4.2 K, respectively.

- Mechanical properties under the presence of a flaw, $\mathrm{K}_Q(J)$, in as-produced form at 4.2 K of $\geq 130\ \mathrm{MPa}\cdot\sqrt{\mathrm{m}}$.

- Magnetic characteristics with a magnetic permeability ≤ 1.03 to avoid magnetisation in a high magnetic field environment.

The feebly magnetic, austenitic stainless steel provides a good basis for the quest for a suitable structural material.

2.2.1 The iron-carbon system

The austenite, or γ phase of iron, when alloyed with carbon alone, is not stable below 727°C, while the maximum solubility of carbon in austenite is only 2.14 wt.%, at a temperature of 1147°C (figure 2.3). The maximum solubility is approximately 100 times larger than for ferrite, or α-iron, for the reason that the former has an FCC structure with larger interstitial positions than the BCC structure of the latter (α-ferrite), resulting in a lower strain on the surrounding iron atoms [Callister et al., 2009]. However, ferrite, prone to magnetisation, exists a second time in the phase diagram, under the name of δ-ferrite, i.e. its δ phase; virtually the same as α-iron, apart from the range of temperatures where it exists [Peckner et al., 1977].

To maintain the austenite phase system, phase transformations involving heat treatments are of great importance, thus so is the tie plate forging and welding process. The importance cannot be overestimated as these transformations yield a wide variety in micro-structures and their accompanied mechanical properties. A steel's crystallographic form is not only defined by its heat treatments, but also

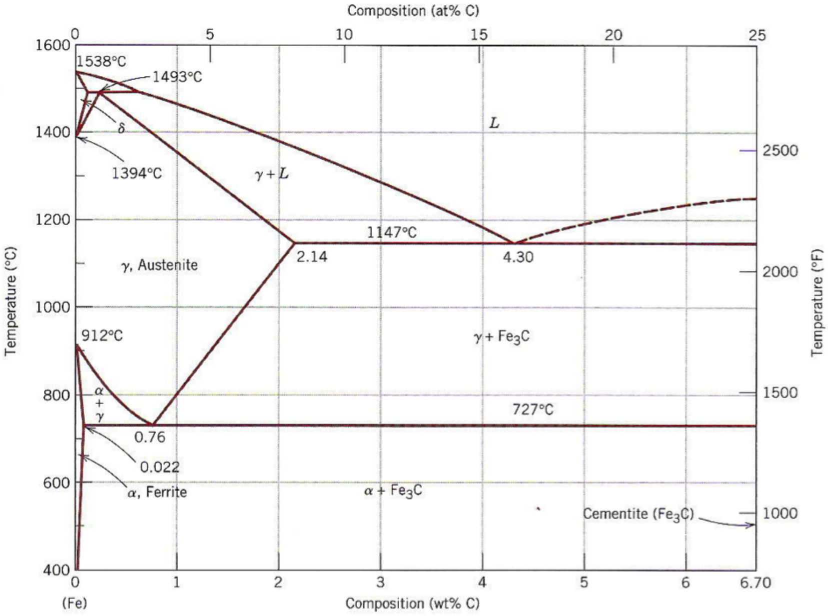

Figure 2.3: Iron-carbon binary phase diagram, showing already its complexity with temperature without the addition of other alloying elements, known for their promotion or inhibition of austenite, i.e. the γ-phase. *From:* [Vander Voort, 1991].

largely by its composition, where minor compositional changes can result in a major change in characteristics.

Stainless steels, or in other words rust-resistant steels have as a major alloying element chromium. A concentration of at least 10.5 wt.% is required to be named stainless. Corrosion resistance of these steels spreads over a large temperature spectrum, making them an interesting type of steel for a wide range of applications.

Additional solutes and their contribution to the Fe-C system

With chromium being a so-called α-stabiliser, in a system where we require a predominantly γ structure (austenite) for the benefit of its negligible magnetic characteristics, additional alloying elements are required for γ stabilisation. A typical γ-stabiliser, used frequently in austenitic stainless steel, is nickel. In view of the latter, Cr and Ni generally form the reference to which the influence of other solutes is classified (the so-called chromium and nickel equivalent). The Cr- and Ni-equivalent denote conjointly an empirical formula for either of the equivalents based on the quantitative composition, from which phase-transition borders are obtained when the Ni-equivalent is placed as function of the Cr-equivalent. A diagram denoting phase transitions, taking into account the main alloying elements, is the Schaeffler constitution diagram in figure 2.4 [Schaeffler, 1947]. Note that these diagrams were introduced for the solidification of welds, making them a mere representation of the microstructure in a specific cooling condition. They can, however, be useful to gain a first insight in the tendency of phase transformations in the microstructure when targeting a certain composition. Another element used to stabilise the austenite is carbon, at limited content when welds or other hot-working processes are in play. An excessive carbon content can introduce sensitisation, where precipitated carbides can form a brittle network, detrimentally affecting toughness and corrosion resistance.

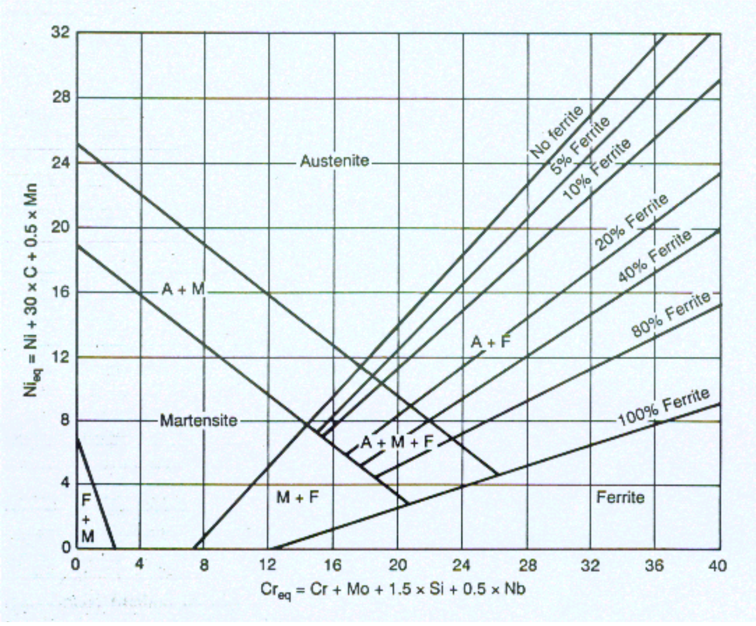

Figure 2.4: Original Schaeffler constitution diagram for the prediction of ferrite formation in austenitic stainless steel welds [Schaeffler, 1947].

Where the nickel solute in austenitic stainless steel has the capability of increasing toughness, other solutes are introduced for their own specific reasons. Manganese can equally increase toughness and ductility, which has resulted in the research of low nickel content austenitic stainless steels with use of manganese, being a similar austenite promoter. The stabilisation of the austenitic phase is in this case done by simultaneous high manganese and nitrogen additions, since manganese increases nitrogen solubility and the reduction of nickel is otherwise impossible for a stable/metastable austenitic stainless steel.

Nickel and manganese coexist very well in a high nitrogen content austenitic stainless steel. Nitrogen is regularly used as a solid-solution strengthener; preserving strength with stress relieving heat treatments. The misfitting nitrogen atoms interfere statically with moving dislocations as drag is generated when dislocations carry nitrogen atoms along through the metal's lattice [Rawers et al., 1996]. The strength of nitrogen-strengthened steels makes them suitable for niche applications like superconducting magnet casings, like the various CICC jackets (section 1.2.4). An additional advantage of an increased nitrogen content in the steel is its hindrance of secondary phase formation, which could otherwise result in global brittleness.

An additional specific which comes with metals susceptible to phase changes with temperature, is the fact that an austenitic stainless steel is not in the least prone to age hardening. Age hardening results from precipitation due to diffusion of elements taking place while keeping the metal for an increased interval at elevated temperatures (for a better understanding see section 11.2.3). Hardening of the metal is therefore realised by cold work (for a better understanding see section 11.2.1). Care should be taken with the work hardening of an austenitic stainless steel for this specific application, as plastic deformation induced martensite could form even though M_S (*martensite start*) temperatures are generally well below 0°C, impairing its magnetic properties [Tobler et al., 1997].

Figure 2.5 holds a schematic overview of the current state-of-the-art austenitic stainless steels, and thereby the ones frequently used in a cryogenic high magnetic field environment. Per grade and family the alloying additions and reductions, and their effect on specific material properties are indicated.

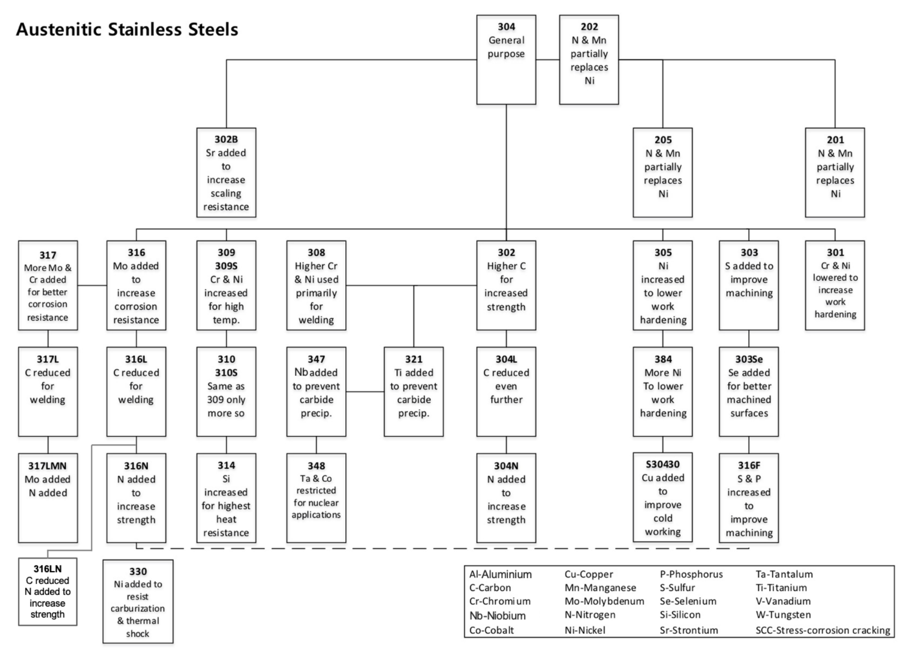

Figure 2.5: Schematic representation of austenitic stainless steel grades and families [Unified Alloys, 2017].

2.2.2 Nitrogen-strengthened austenitic stainless steel

The 300-series austenitic stainless steel serves when looking for a low carbon grade, nitrogen-strengthened, stable steel over a wide range of temperatures. In particular the AISI grade 316LN austenitic stainless steel, a steel commonly selected for cryogenic structures for its high strength and toughness at low temperatures, combined with its adequate weldability [Morris, 1993]. The type 316 alloys are the better corrosion resistant brothers of the 304 alloys. A regular 316 steel can be prone to sensitisation, whereas a low carbon variant, 316L, reduces this problem although at extended exposure to high temperatures some sensitisation can still occur. The nitrogen-strengthened version 316LN on its turn, adds additional resistance to this effect, while realising some solid-solution hardening, raising its minimum specified yield strength (here 0.2%, i.e. $R_{p0.2}$).

In the recent years additional interest has arisen to develop stronger and tougher alloys for cryogenic structural components. Extensive research on structural stainless steels for magnet applications was recently performed for the development of the conductor jackets for the CICCs of the ITER magnet system. Thereby targeting requirements approaching the ones currently set for the tie plates (jacket requirements: $R_{p0.2} \geq$ 1000 MPa & $\mathrm{K}_Q(J) \geq$ 130 MPa$\cdot\sqrt{\mathrm{m}}$ at 4.2 K [ITER Organisation, 2016]). Two options were considered, a lightly modified AISI 316LN (extra-low carbon $\leq$ 0.015%), and a high-manganese austenitic stainless steel, JK2LB. The JK2LB alloy was designed specifically for the application primarily to minimise the thermal contraction mismatch between the conductor jacket and the Nb_3Sn superconducting cables it encases [Nakajima et al., 2004].

Both high-strength alloys have an excellent combination of strength, toughness and a reduced vaporising element content, essential for the low-temperature, high-vacuum application. In table 2.2 a selection of existing data of the latest development in 316LN and JK2LB stainless steels for the ITER magnet system is compiled. A wide variety of material compositions (see table 2.1) and tempers are presented, amongst which the extruded and subsequently compacted state of the CICC jackets, but also profiles and plates either extruded or hot-rolled investigated for coil cases and magnet support structures.

Table 2.1: Chemical composition in wt.% of the different heats presented in table 2.2.

Heat	**Material**	**C**	**Mn**	**P**	**S**	**Si**	**Ni**	**Cr**	**Mo**	**Nb**	**Co**	**N**	**B**
A.	***316LN***	0.024	1.48	-	-	0.44	13.60	16.70	2.58	-	-	0.16	-
B.	***316LN***	0.017- 0.024	1.54- 1.68	0.015- 0.017	0.001- 0.002	0.36- 0.43	12.34- 12.90	16.15- 16.85	2.02- 2.14	0.001- 0.010	0.014- 0.020	0.108- 0.133	0.0001- 0.0010
C.	***316LN***	0.017- 0.024	1.64- 1.69	0.014- 0.019	0.001	0.40- 0.44	13.40- 13.08	16.69- 16.85	2.05- 2.13	<0.010	0.020 0.143	0.118-	0.0010
D.	***316LN***	0.014- 0.017	1.59- 1.62	0.019	0.001	0.42- 0.44	12.39	16.55- 16.67	2.09- 2.11	<0.010	0.020	0.103- 0.117	0.0010
E.	***316LN***	0.015	0.98	0.010	0.001	0.23	12.00	16.25	2.09	-	0.010	0.13	-
F.	***316LN***	0.010	0.98	0.008	0.006	0.25	12.18	16.45	2.06	-	0.011	0.14	-
G.	***316LN***	0.014	0.96	0.009	0.002	0.21	11.25	16.60	2.07	-	0.010	0.14	-
H.	***JK2LB***	0.013	21.80	0.007	0.002	0.26	9.25	12.80	0.98	-	-	0.12	0.0036
I.	***JK2LB***	0.017	21.40	0.010	0.002	0.13	9.37	13.50	1.30	-	0.020	0.14	-
J.	***JK2LB***	0.023	21.02	0.008	0.002	0.25	9.19	12.78	1.18	-	0.010	0.15	-

Table 2.2: Selected 4.2 K mechanical data of recent austenitic stainless steel development.

Material description	**Heat**	**Temper**	$R_{p0.2}$[a] [MPa]	R_m[b] [MPa]	$\mathrm{K}_Q(J)$ [MPa·$\sqrt{\mathrm{m}}$]	**Grain size**[c] [number]	**Reference**
316LN 700 mm section forging	**A.**	F[d]+SA[e]@1057C+ CW[f]12%+SR[g]@600C	889	1430	456	G 0.0-2.5	[Drexler et al., 1994]
316LN 30 mm hot-rolled plate	**B.**	F+HR[h]+SA+P[i]	948	1780	267	G 3.0-5.0	[Sgobba et al., 2017]
316LN 45 mm hot-rolled plate	**B.**	F+HR+SA+P	858	1550	260	G 3.0-4.0	[Sgobba et al., 2017]
316LN L-shape extrusion (t=35 mm)	**C.**	F+HE[j]+SA+P	945	1597	274	G 3.0-4.0	[Sgobba et al., 2017]
316LN R-shape[k] extrusion (t=35 mm)	**D.**	F+HE+SA+P	868	1605	250	G 3.0-5.5	[Sgobba et al., 2017]
316LN conductor jacket	**E.**	SA@1040C	895	1470	264	G 5.5	[Sgobba et al., 2012] [Nyilas, 2010]
	F.	CO[l]	942	1640	-	-	[Sgobba et al., 2012]
	F.	CO+AG[m]	876	1614	-	-	[Sgobba et al., 2012]
	G.	CO+ST[n]2.5%	1026	1584	-	-	[Sgobba et al., 2012]
	G.	CO+ST2.5%+AG	938	1553	272	G 5.5	[Sgobba et al., 2012]
JK2LB conductor jacket	**H.**	SA	787	1322	254	-	[Hamada et al., 2008]
	H.	CO+AG	1006	1376	224	-	[Hamada et al., 2008]
	I.	CO+AG	1156	1478	164	G 4.5-6.0	[Sgobba et al., 2013] [Hamada et al., 2011]
	J.	CO+ST2.5%+AG	1222	1478	112	G 5.0-5.5	[Sgobba et al., 2013] [Nyilas et al., 2011]
JK2LB manifold forging	**-**	F	935	1358	276	G 3.0	[McRae et al., 2017]
316LN 100 mm GMAW (GTL[p])	**-**	AW[o]	1134	1427	218	-	[Langeslag et al., 2014]
316LN 100 mm GMAW (RLT[q])	**-**	AW	1151	1393	168	-	[Langeslag et al., 2014]

---

[a] 0.2% yield strength
[b] maximum tensile strength
[c] according to ASTM E 112
[d] forged
[e] solution-annealed
[f] cold-worked
[g] stress-relieved
[h] hot-rolled
[i] pickled
[j] hot-extruded
[k] rectangular-shape
[l] compacted
[m] aged
[n] stretched
[o] as-welded
[p] measured in groove section, $\mathrm{K}_Q(J)$ in TL-orientation, $R_{p0.2}/R_m$ in T-orientation
[q] measured in root section, $\mathrm{K}_Q(J)$ in LT-orientation, $R_{p0.2}/R_m$ in T-orientation

Note that not only composition, but also material condition as a function of manufacturing route and post-manufacturing treatments play a major role in the obtained mechanical performance. Unfortunately 4.2 K mechanical data on heavy-gauge forged 316LN and JK2LB is scarce. Additionally, some selected data of a 316LN GMAW weld is included for completeness and a reference for the welded structure.

Even though these widely used 316 alloys are fit for cryogenic structural purposes, they do not fully comply with the stringent ITER requirements on the material intended for the large compression structure. The requirements stand at an $R_{p0.2}$ of at least 380 MPa with an R_m of 690 MPa [ITER Organisation, 2017], based on resisting the 250 MPa stress taken up by the tie plates to generate the 180 MN coil-to-coil contact loading. This leads to the target of a 4.2 K yield strength in the vicinity of 1200 MPa, while assuring a toughness to fracture under the presence of a flaw of 130 MPa$\cdot\sqrt{\text{m}}$, which are generally inversely related. From table 2.2 we can note that for heavy-gauge productions these targets are not met.

The candidate material proposed for the ITER pre-compression structure is the less known ASTM A965 type XM-19, in forged form denoted as grade F XM-19. This is a 22-chromium, 13-nickel, 5-manganese grade; a highly pure, low carbon, nitrogen-strengthened austenitic stainless steel (table 2.3). Where in an AISI 316LN alloy nitrogen content does not surpass 0.2 wt.%, this F XM-19 grade can hold a nitrogen content of up to 0.3 wt.%. The increased manganese content is accountable for the increase in uptake of nitrogen in the steel. This high nitrogen content also gives it its trade-name; Nitronic®-50.

Table 2.3: Chemical composition of F XM-19 as per ASTM A182 by weight percent.

Element	C	Mn	P	S	Si	Ni	Cr	Mo	Nb + Ta	N	V
minimum	0	4	0	0	0	11.5	20.5	1.5	0.1	0.2	0.1
maximum	0.06	6	0.04	0.03	1	13.5	23.5	3	0.3	0.4	0.3

With phosphorus and sulphur contributing, via inclusions such as sulphides (e.g. MnS), to a decrease in toughness and fatigue life when hot worked, like is the case with forging, the impurity levels are kept to a minimum. An exceptional state of cleanliness of the material is required to guarantee optimal mechanical properties at cryogenic temperature. Where generally steels encounter a ductile to brittle transition when cooled to cryogenic temperature, austenitic stainless steels remain ductile, resulting in an increased fatigue life and fracture toughness. Fracture mode in these steels is mostly by microvoid coalescence, resulting from voids nucleating at the site of inclusions. Inclusion count is therefore, following production (i.e. hot working), set to an absolute minimum.

F XM-19 has gained interest for cryogenic purpose in the form of structural components as a result of its advantageous chemical composition. The carefully balanced composition leads to an excellent forgeability, weldability and high yield strength at both ambient as well as cryogenic temperatures [McRae et al., 2014].

3

Effect of nitrogen strengthening on low-temperature mechanical properties

In this third chapter the advantages of a heavy-gauge F XM-19 forging operating at liquid helium temperature in terms of static mechanical behaviour is dealt with. An extensive introduction into the F XM-19 heats employed for the study and their compositional advantages is enclosed in the initial part of this chapter, followed by the customised research methodology for the establishment of its 4.2 K tensile properties.

Study outcome demonstrates an advantageous behaviour of the F XM-19 forging material, whereas the weld, realised to link the forgings of the welded structure, shows inferior tensile characteristics. Some material particularities observed during tensile testing are in depth assessed and its effect interpreted in the closing of this chapter.

3.1 F XM-19 for heavy-gauge structural components

F XM-19 provides a combination of corrosion resistance and strength not found in any other commercial material. Excellent mechanical properties are featured within a temperature range from 4.2 K to highly elevated temperatures reaching some 800°C. The high nitrogen addition not only results in room temperature strengthening and the increase of yield strength at cryogenic temperature, but also plays a role in several metal enhancing phenomena. Nitrogen, like molybdenum and the chromium solute added for this purpose, protects against corrosion attacks, like the pitting type. As a result of nitrogen, the nickel content can be reduced, while maintaining a stable austenite phase, resulting in improved resistance against stress corrosion cracking, while remaining non-magnetic. In spite of a high manganese addition to realise the beneficial uptake of nitrogen, the equilibrated composition allows to maintain physical properties similar to 316LN [Sgobba et al., 2016].

Besides being profitable in terms of strength, austenite stability, and corrosion resistance, nitrogen solutes in F XM-19 have a 4^{th} effect; the capacity to inhibit carbon migration, or sensitisation (section 2.2.1). This effect becomes even more pronounced in welded sections, as carbide precipitation in weld heat-affected zones is reduced, resulting in an increase of low temperature toughness.

F XM-19's high-strength properties are, however, directly related to the metal forming process in terms of hot working, which makes the material marginally post-processable in terms of hot work or supplementary heat treatments. Post-processing, and conjointly enhanced mechanical manipulation needs to be performed at ambient temperature, i.e. cold work.

The work-hardening phenomenon associated with austenitic stainless steels is that of austenite transforming to martensite; a hard magnetic phase (section 2.2.1). Here the degree of transformation is related to the stability of the austenite phase and the temperature in place. F XM-19 is found to be resistant against the austentic to martensitic transformation, rendering the material non-magnetic even following extreme processing and at cryogenic temperature.

F XM-19 has therefore been the target material for the present study, where two prototype tie plates, one of each solution (section 2.1.1), have been produced out of the fairly unknown material for cryogenic application. Table 3.1 shows the specific chemical composition of the heats employed for either mock-up.

Table 3.1: Chemical composition of F XM-19 heats employed for this study.

Heat	C	Mn	P	S	Si	Ni	Cr	Mo	Nb + Ta	N	V
SPF	0.022	5.4	0.021	0.001	0.35	12.55	21.1	2.05	0.196	0.294	NA
WS	0.035	5.2	0.024	0.004	0.27	12.09	21.2	2.12	0.160	0.280	0.14

In early evaluations of the nitrogen strengthened Nitronic®-alloys, fusion welds were performed without the use of filler metals [Espy, 1982]. Fused area structure was found comprising a δ-ferrite content of no less than 3% in the austenite matrix, a curious phenomenon as both the Schaeffler constitution diagram (figure 2.4), as well as the DeLong diagram [DeLong et al., 1956], which also allows for nitrogen enhanced materials, predicted 0% ferrite. Further exploration showed that the manganese equivalent as used in the standard Schaeffler and DeLong diagrams did not properly reflect the effect of the solute, which was equally noticed by Hull who studied in detail the effect of manganese on the formation of δ-ferrite, while developing his own constitution diagram [Hull, 1973].

In the case of the Schaeffler diagram, the nickel equivalent on the y-axis changed to accommodate for the effect of manganese, resulting in a new standard for future works; encompassing a wider range of stainless steels with a manganese content up to 15%. An additional modification was proposed based on the observed deviation of calculated and measured values regarding true nitrogen content. The initial multiplication factor of 30, determined empirically, was adapted to 22 for a nitrogen content over 0.2 wt.%, and 20 for a nitrogen content over 0.25 wt.%. The modified Schaeffler diagram [Espy, 1982] now takes into account high manganese, high nitrogen content stainless steels, with possible additional solutes like vanadium, copper and aluminium. Ferrite contents are calculated based on the nickel and chromium equivalent as described in equation 3.1:

$$\begin{aligned} Ni\ equivalent = {} & wt.\%\ Ni + 30 \cdot wt.\%\ C + 0.87 \cdot wt.\%\ Mn \\ & + 0.33 \cdot wt.\%\ Cu + (wt.\%\ N - 0.045) \cdot 30 \text{ when } N\ 0.0/0.20, \\ & or \cdot 22 \text{ when } N\ 0.21/0.25, or \cdot 20 \text{ when } N\ 0.26/0.35, \end{aligned} \tag{3.1a}$$

$$\begin{aligned} Cr\ equivalent = {} & wt.\%\ Cr + wt.\%\ Mo + 1.5 \cdot wt.\%\ Si + 0.5 \cdot wt.\%\ Nb \\ & + 5 \cdot wt.\%\ V + 3 \cdot wt.\%\ Al. \end{aligned} \tag{3.1b}$$

Here the percentage of ferrite, up to some 30%, in a matrix of austenite (A), or austenite + martensite (A + M) can be predicted within roughly 4% [Espy, 1982].The percentage of ferrite is here considered to be equivalent to the WRC Ferrite Number (FN). One should take into account that a faster freezing rate of smaller size welds can give a lower ferrite content than predicted, and the contrary holds for a slow freezing rate in a large size weld, like the one treated in this study.

Figure 3.1 shows this Schaeffler-Espy modified constitution diagram for high manganese, high nitrogen content stainless steels. In the diagram both forging heats, i.e. for the single piece forged and for the welded solution, are drawn in. Note that the F XM-19 heats lie 'dangerously' close to the initial ferrite border. This denotes that, even though the material appears ideal in terms of low temperature mechanical characteristics, one has to take care to maintain a fully austenitic material structure throughout the process of selecting an adapted composition at the level of the steel marker, up until the finalisation of processing.

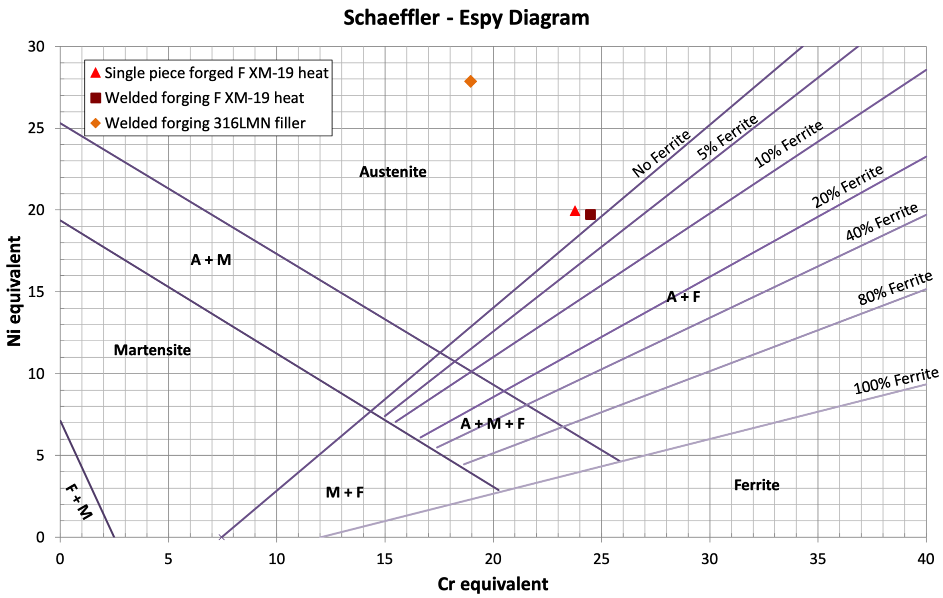

Figure 3.1: Schaeffler-Espy modified constitution diagram for stainless steel (weld) metal, for high manganese, high nitrogen containing heats [Espy, 1982].

For completeness the filler material as employed for the welded structure is indicated in the aforementioned constitution diagram. A logical choice would be a filler metal with base composition matching that of the F-XM-19 material. GMAW (Gas Metal Arc Welding) and GTAW (Gas Tungsten Arc Welding) procedures have shown that even though the static, i.e. tensile requirements were easily met by the welds employing an XM-19 filler metal, fracture toughness in such welds were found insufficient. In addition, the magnetic behaviour of the material post-welding was found to be ferromagnetic; a result from the less stable composition of the XM-19 material [Walsh et al., 2015].

A 316LMN filler material was proposed, following an extensive study of compatible weld filler metals for the weld of a thick section F XM-19 base metal with feebly magnetic and cryogenic service requirements [Nyilas et al., 1982; Walsh et al., 2015]. A manganese-, nitrogen-modified 316LN filler is employed, to approach the XM-19 material by adding 4% to 8% Mn, thereby increasing N_2 solubility. The composition of this material (table 3.2) holds a safe margin with respect to the ferrite transition line, as can be seen from figure 3.1. Welds performed on thick sections of F XM-19 materials, with either welding process, have shown sufficient margin with respect to the requirements in terms of both tensile and toughness properties, even though low-temperature tensile properties were found slightly inferior to those when employing the XM-19 filler metal. Following its favourable composition, the welded material was found to be non-magnetic [Walsh et al., 2015].

Table 3.2: Chemical composition of the 316LMN filler as employed for the welded structure.

Heat	C	Mn	P	S	Si	Ni	Cr	Mo	Nb + Ta	N	V
316LMN	0.020	6.73	0.017	0.003	0.33	20.96	15.38	2.66	0.050	0.180	0.080

3.2 Research methodology

Procurement of the ITER central solenoid, and its pre-compression structure, is the responsibility of the US domestic agency, who ordered the fabrication of the two prototype tie plates. From the welded prototype tie plate, three sub-size samples were made available for the present study, taken from three different positions in the prototype tie plate; one from the head forging, one from the weld region, and one from the slab forging, respectively (figure 3.2a). From the single piece forged prototype tie plate, full-thickness, full-width cross cuts were made available from both head and slab ends (figure 3.2b).

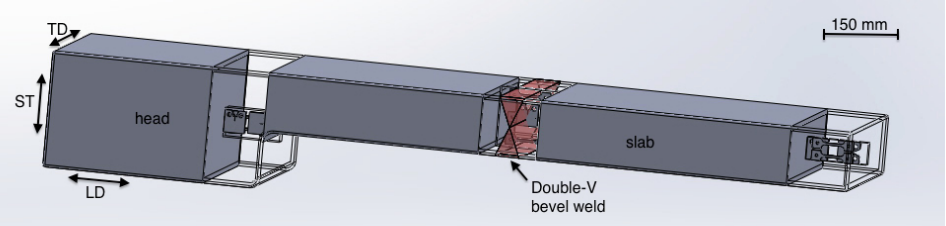

(a) Welded structure.

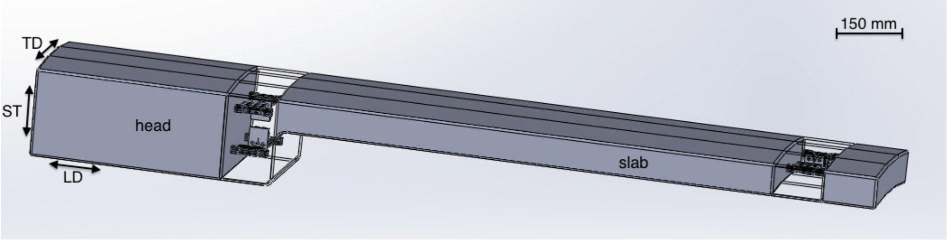

(b) Single piece forged structure.

Figure 3.2: Specimen extraction scheme for the welded solution (a) and the single piece forged solution (b).

3.2.1 Experimental technique for static mechanical measurement at 4.2 K

Application-based measurement limits the experimental techniques used in terms of sizeability. Even though large-size forgings and idem welds account for a fair amount of study material, specimen positioning does not allow for the use of normal sized, standardised specimens. Sub-size specimen testing, still respecting the applicable standards, is here the path to take. The adapted specimen design is presented in figure 3.3. Sub-size testing allows to limit liquid helium consumption. A single traction test, performed at liquid helium temperature, on a standard size specimen, requires a helium consumption of at least 20 l. For a sub-size specimen helium consumption can be limited to some 5 l per test, thereby not only reducing consumption, but also cool-down and warm-up time.

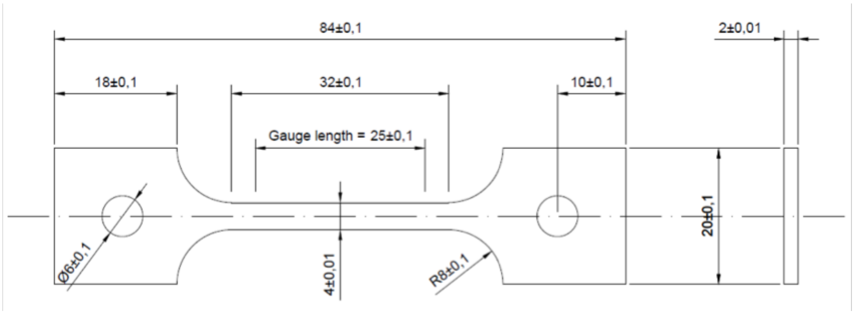

Figure 3.3: Specimen design for both liquid helium and ambient temperature tensile tests.

A tensile set-up for testing at liquid helium temperature has been developed at CERN for testing sub-size specimens, in the research leading up to the Large Hadron Collider [Sgobba et al., 1995].

Room temperature (RT) testing is being performed with specially developed specimen holders, for the fixation of these sub-size specimens, directly attached to the UTS Testsysteme 200 kN traction machine's cross-head. In the case of cryogenic testing a cryostat is employed. High-precision tensile measurements at 4.2 K are performed with this cryostat acting as thermal container as well as load-bearing link; transferring load from the cross-head of the machine via an intermediate load-cell to the specimen.

The 18 kN cryogenic traction set-up consists of a male and a female part, both shown in figure 3.4. The female part contains a double walled envelope, with intermediate insulation partially realised by vacuum for maintaining a 4.2 K helium bath around the specimen, while reducing losses resulting from heat transfer. A threaded connection with the bottom end of the traction machine relates to the load transferring structure. The male part is constructed in such a way that the female part endures tensile stress during operation. The female part is the weak element in the load chain, driving the maximum test tensile force of 18 kN.

Figure 3.4: Photograph of the employed tensile cryostat as developed by CERN in the preparation of the LHC. The cryostat, with its male (right) an female (left) part can house the sub-size specimens of figure 3.3 for cryogenic tensile testing.

The male half, the insert, is the main structural item housing the specimen. It consists of a stainless steel flange, which is directly the upper lid closing the dewar. Three glass-fibre columns are rigidly connected to the upper flange, to which the lower specimen holder is attached. The top specimen holder is directly connected via a traction rod, to the cross-head of the universal traction machine. This pulling rod therefore passes through the upper flange of the insert. A low friction passage is created with use of rubber O-rings. Additional thermal insulation on the top end is realised with use of three copper screens fixed to the fibreglass columns. The construction of the set-up puts the insert in compression during testing, thereby risking buckling of the columns. By adding a stabilising triangle, buckling was calculated to be reduced by a factor 3 [Corthesy, 1995; Bonhomme, 2003].

The top-flange of the set-up not only houses the passage of the pulling rod, but also accounts for the introduction and recuperation of the liquid helium (figure 3.5). Liquid helium measurements are performed in an enclosed environment, ensuring recuperation, thereby reducing helium losses to a minimum. Additional ports in the top flange accommodate electrical connections linking the sensors for test monitoring.

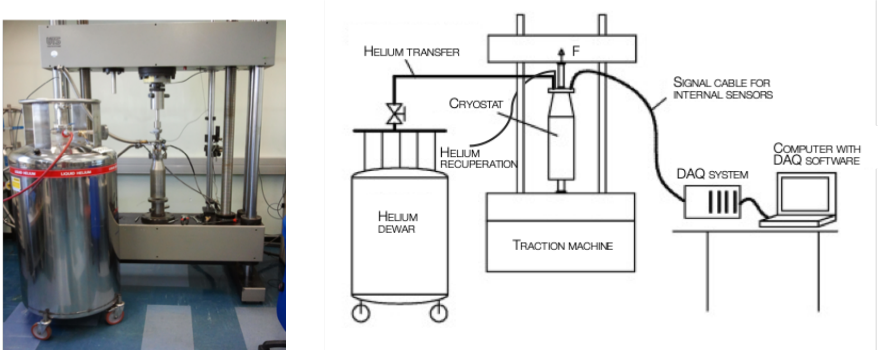

(a) Photograph of the cryogenic tensile set-up. **(b)** Schematics of the cryogenic tensile set-up and its connections.

Figure 3.5: Cryogenic tensile set-up employed for the presented study. Photograph of the set-up (a) and a schematic representation (b).

Necessity of low-temperature monitoring devices

The necessity of the cryogenic dewar to simultaneously host a wide range of sensors becomes apparent when closing the envelope. As a result of the liquid helium container, a closed environment is created, and the specimen is not directly visible. To determine the stress-strain curve of the specimen, a load and displacement measurement system is required to be incorporated in the set-up.

Load registration at the site of the specimen is the evident choice of preference. The limited volume inside the cryostat holds a constraint, together with the added heat load in the cryogenic environment. Sensors are moreover very susceptible for variations with small changes of temperature, therefore an external load cell is chosen. The load cell is directly connected to the pulling rod, thereby limiting compliance picked-up by this system. The Maywood U2000 load-cell imminently functions at ambient temperature at all times, guaranteeing a stable operation with a resolution of 0.27 N up to 25 kN [Sherborne Sensors, 2013](figure 3.6a). A shear web design in a Wheatstone bridge configuration is used to minimise errors resulting from multi-directional forces (out of the main loading axis). Frequent calibration and compliance check with use of a custom-made internal load-cell increases measurement reliability. The stiffness of the load cell, together with the high operating frequency give good results when measuring sharp load peaks as observed with serrated yielding, a phenomenon observed in metals loaded at 4.2 K (section 1.2.4).

Displacement monitoring is performed by a spring-type extensometry system, guaranteeing the monitoring of the material's extension from start until material failure, even in the case of highly ductile materials, where elongation can exceed 50% of the original gauge length. Note that a spring-type extensometer is less suitable for very specific determination of serrated yielding phenomena; a delayed response results from its flexibility.

A Nyilas type W-extensometer is used, designed and fabricated by Dr. A. Nyilas from CEME-KIT (Cryogenic Engineering & Materials Expertise; spin-off from Karlsruhe Institute of Technology), presented in figure 3.6b. Two W-extensometers are employed on either side of the specimen to account for possible bending effects. Sharp knifes on the large legs of the W ascertain proper gripping, combined with a spring holding the two extensometers in place. In rare cases sliding of the extensometers was observed during measurement, indicated by a sudden dive in registered displacement, upon which the concerned data was excluded from interpretation. The extensometers referred to accompany with a gauge length of only 25 mm, a maximum displacement of no less than 15 mm. The extensometry is based on a strain-gauge system measuring the deflection of the extensometer's legs.

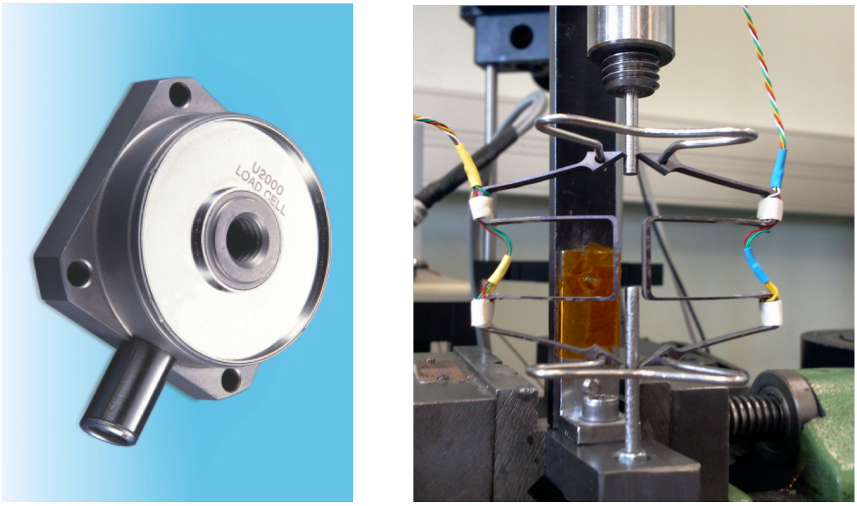

(a) Maywood U2000 load-cell. **(b)** W twin-extensometers.

Figure 3.6: Stress-strain monitoring systems as employed for low temperature tensile tests. Load-cell for accurate measurement of applied load (a) and a spring type extensometry system (here photographed while being calibrated) for the on-specimen measurement of material deformation (b).

Helium liquid level is measured by level-gauges; two resistances coupled, of which one is situated below specimen level, and the second above the specimen level. Level-gauge stability exists when both resistances are fully submerged, indication on its turn a full submersion of the specimen in the helium liquid. Witness samples have been instrumented with Cernox temperature sensors (CX-1050-SD-30 supplied by Lake Shore Cryotronics), with a resolution of 5 mK to confirm 4.2 K specimen temperature throughout the test, from which the testing speed is cross-checked. As a result of serrated yielding and accompanying heat generation due to rapid energy release, small temperature spikes are observed to about 10 K, after which the specimen temperature rapidly decreases again to 4.2 K, denoting a stable testing temperature at this 4.2 K.

3.2.2 Optimal measurement parameters

Room temperature (RT) measurements are conducted on a 200 kN electromechanical universal tensile machine of UTS Testsysteme GmbH, at a constant stress speed of 5 MPa/s up to one half of the specified yield strength, i.e. here $380\ \mathrm{MPa}/2 = 190$ MPa, and subsequently slowed down to a deformation speed of 1.5 mm/min according to ASTM E8/E8M. Specimens, analogous to the RT specimens, immersed in a liquid helium bath, are tested using the same universal tensile machine by measuring at an initial stroke rate of 0.5 mm/min, congruent with a strain rate of some $3.3 \cdot 10^{-4}\ \mathrm{s}^{-1}$. For subsequent specimens, the stroke rate was decreased to 0.15 mm/min, a strain rate of $1 \cdot 10^{-4}\ \mathrm{s}^{-1}$, for a better definition of the stress-strain curve, and if present, to assess variations with strain rate. Both applied rates are fully consistent with ASTM E1450, a standard especially designed for low temperature tensile testing.

Sub-size tensile specimens, comprising a 25 mm gauge-length and 4 mm x 2 mm gauge-section, are machined for both WS and SPF longitudinally with respect to the forging direction, corresponding to the axis of the main stress during pre-load and operation. The sub-size specimen design takes into account various factors, including the available space inside the cryostat, specimen cross-sectional size with respect to the system's load constraint, while realising a shape in accordance with ASTM standard E8M to which the low-temperature standard equally refers. Figure 3.3 demonstrates the specimen design employed for both RT and 4 K testing, in order to limit parameter variation for comparison reasons. To achieve the appropriate tolerances and reduce the chance on stress induced hardening, specimens have been machined by electro-erosion, and have a low pressure mechanical finishing.

As a result of limited availability of material for the WS, for the head- and slab-forging a single series of specimens is extracted (figure 3.2), denoted as MH and MS, for the centre of the head and centre of the slab region, respectively. In the WS GMAW weld, three sets of specimens are extracted, from top weld crown (TW), middle weld root (MW), and bottom weld crown (BW). For the SPF, tensile specimens, extracted from the slab of the forging, were taken in mid-plane position (MS), whereas for its head-forging specimens are machined from two locations; top (TH) and bottom (BH), with respect to the ST direction. All tensile specimens are listed in table 3.3.

Table 3.3: Tensile measurements; sample designation.

Prototype	Position	Location	Specimen orientation	Sample designation
WS	Head	Middle	LD	WS_MH[a]
	Weld	Top[b]	LD	WS_TW
		Middle[c]	LD	WS_MW
		Bottom[b]	LD	WS_BW
	Slab	Middle	LD	WS_MS
SPF	Head	Top	LD	SFS_TH
		Bottom	LD	SPF_BH
	Slab	Middle	LD	SPF_MS

[a] all samples tested both at 293 K and 4 K

[b] weld crown

[c] weld root

3.2.3 Measurement uncertainty

Mechanical properties testing at 4.2 K holds uncertainty in measurement results as any other testing method. Data scatter results from material property variability as well as the experimental procedure; the latter making testing at liquid helium temperature intrinsically complex and variable. The measurement error following from material property variability is included in the graphical representation of the data by means of the spread denoted in the error-bars. The uncertainty following from the experimental method is calculated according to [Gabauer, 2000]. Note that this uncertainty calculation is restricted to ambient and elevated temperatures, for which a translation is made to 4.2 K measurement results.

The uncertainty in the measured R_m values is determined at an approximate 1.1% for the room temperature measurement data, versus 1.2% for the liquid helium temperature measurements, based on a confidence level of 80%. For the measured $R_{p0.2}$ data, room temperature uncertainty is approximated at 1.4%. $R_{p0.2}$ uncertainty, measured at 4.2 K, holds 1.5%. Measurement uncertainty is included in the table listings of the measured data, and are reported according to [Gabauer, 2000].

3.3 Structural benefits of nitrogen strengthening

In table 3.4 all tensile test results obtained for the application based F XM-19 material are listed. Figure 3.7 provides a more graphical representation, with measurement spread denoted by the error-bars. Even though one can not comprise all data in a single representative plot, these graphs provide a global view for visualisation of general trends. The technical requirement at room temperature has been joined for comparison, as described in the ASTM standard A965 for forged XM-19. ASTM technical specification is generally employed as material requirements in application based settings, as is the case for the ITER forged XM-19 tie plates [ITER Organisation, 2017].

Table 3.4: Summary of test results comprising all traction data.

Prototype	Position	Location	Designation	Temperature [K]	$R_{p0.2}$[a] [MPa]	R_m[b] [MPa]
WS	Head	Middle	WS_MH	RT	407 ± 6[c]	717 ± 8
				4.2	1310 ± 20	1666 ± 20
	Weld	Top	WS_TW	RT	451 ± 6	611 ± 7
				4.2	1130 ± 17	1360 ± 16
		Middle	WS_MW	RT	475 ± 7	671 ± 7
				4.2	1240 ± 19	1453 ± 17
		Bottom	WS_BW	RT	455 ± 6	619 ± 7
				4.2	1160 ± 17	1286 ± 15
	Slab	Middle	WS_MS	RT	412 ± 6	748 ± 8
				4.2	1266 ± 19	1743 ± 21
SPF	Head	Top	SPF_TH	RT	404 ± 6	762 ± 8
				4.2	1150 ± 17	1699 ± 20
		Bottom	SPF_BH	RT	394 ± 6	749 ± 8
				4.2	1140 ± 17	1692 ± 20
	Slab	Middle	SPF_MS	RT	419 ± 6	763 ± 8
				4.2	1201 ± 18	1709 ± 21
ASTM A965		Requirement		RT	380	690

---

[a] 0.2% yield strength
[b] maximum tensile strength
[c] measurement uncertainty

The data for the WS and SPF forgings falls in the same range with an ambient temperature R_m of approximately 720 MPa to 760 MPa. This remarkably increases to a 1670 MPa to 1740 MPa range for R_m at 4.2 K (figures 3.7a and 3.7b). The tensile measurements performed on these high-strength forgings indicate tensile properties exceeding the ASTM A965 standard tensile requirements for forged XM-19 at ambient temperature ($R_{p0.2}$ = 380 MPa, R_m = 690 MPa) for all forgings:

- SPF forging: $\mathrm{R}_{p0.2} \approx$ 395 MPa & 420 MPa,
  $\mathrm{R}_m \approx$ 750 MPa & 765 MPa, for the head and slab respectively,

- WS head forging: $R_{p0.2} \approx$ 405 MPa, $R_m \approx$ 720 MPa,

- WS slab forging: $R_{p0.2} \approx$ 410 MPa, $R_m \approx$ 750 MPa.

Note the quite extraordinary performance of this material with respect to a typically employed austenitic stainless steel at 4.2 K like the in section 2.2.2 mentioned AISI 316LN. 316LN generally exhibits an ambient temperature $R_{p0.2}$ and R_m not exceeding by much the 300 MPa and 600 MPa, respectively. Results at 4.2 K for AISI 316LN bulk material show an $R_{p0.2}$ and R_m of approximately 900 MPa and 1500 MPa, respectively, depending on post-processing [Tobler et al., 1997].

The above is congruent when looking more in detail to the tensile data of the weld, connecting the slab of the WS to its head. One can observe that this joint features a tensile strength at ambient temperature, $R_m@RT$, of some 610 MPa to 670 MPa (figure 3.7c). This is in line with what is measured for a 316LN type stainless steel; here the base for the weld-filler. These values however, lie under the ASTM A965 standard requirements, which, even though meant for XM-19 forged material, is the origin of the ITER requirement for qualification, where a performance better than or equal to the base material, thus $R_m > 690$ MPa, is requested. The overall structure is subject to high loads not only during operation, but also prior to cool-down.

A high compression is pre-existing, already at room temperature to realise central solenoid structural stability, prior to, during and following cool-down, when thermal contraction releases some of this pre-compression. Already at room temperature it is therefore of paramount importance that no local yielding occurs, which hold for the forged material as well as for the weld, which is not allowed to be a weak link in the chain.

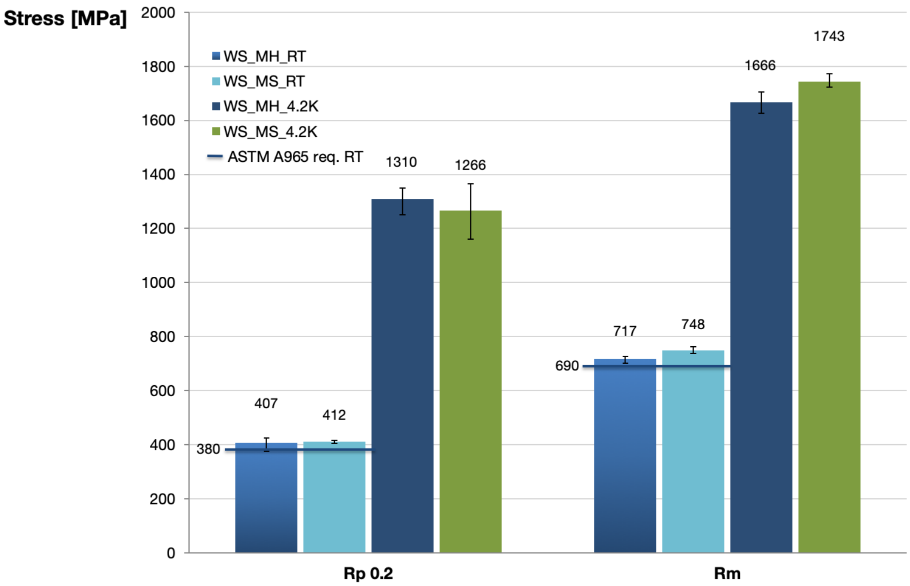

(a) Mechanical properties, $R_{p0.2}$ and R_m, obtained at ambient and 4.2 K for the WS's head and slab forgings. The error-bar in the plot denotes the measurement spread.

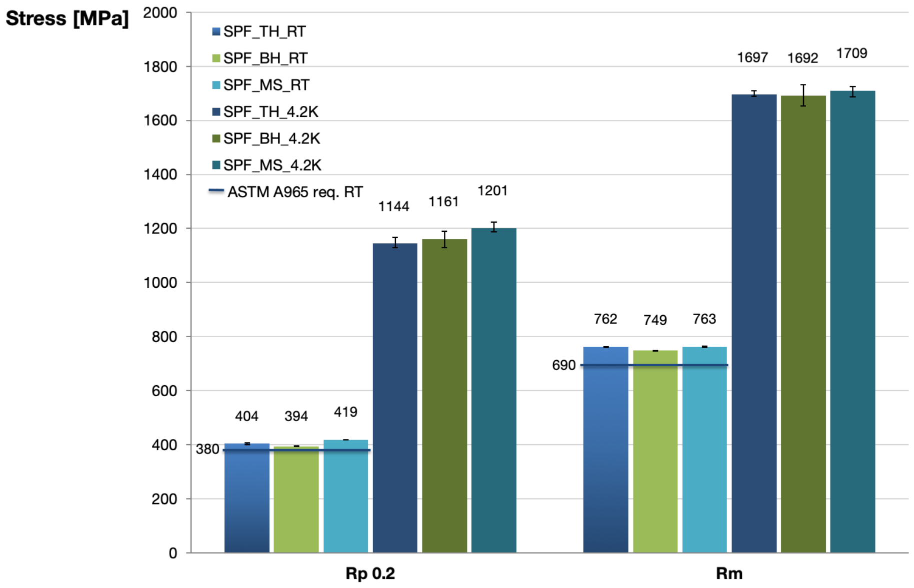

(b) Mechanical properties, $R_{p0.2}$ and R_m, obtained at ambient and 4.2 K for the SPF's head and slab regions.The error-bar in the plot denotes the measurement spread.

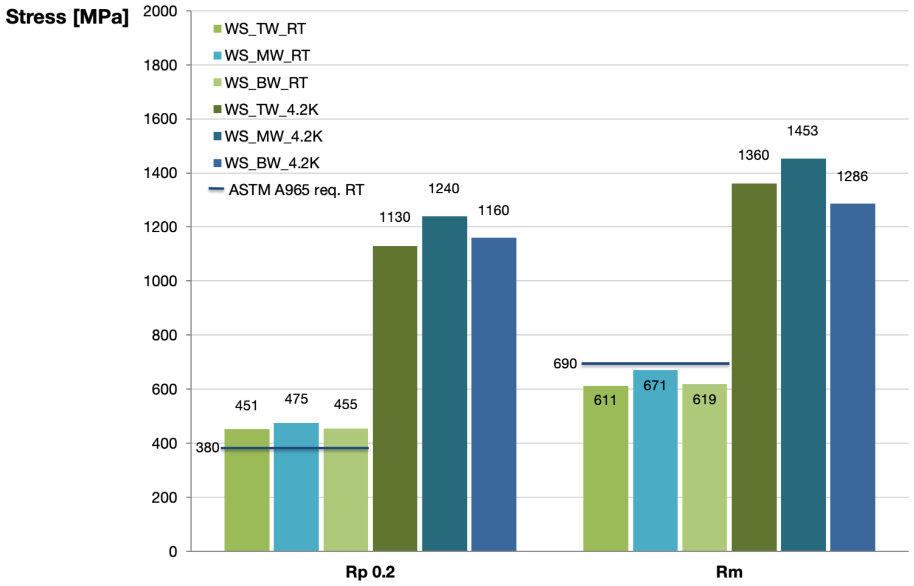

(c) Mechanical properties, $R_{p0.2}$ and R_m, obtained at ambient and 4.2 K for the three weld regions (top crown, middle root and bottom crown) of the WS. Note that this figure does not hold error-bars; each of the individual measurements is presented as each specimen contains a different fraction of weld-metal and should be treated independently.

Figure 3.7: Overview of the prominent tensile properties as obtained for the F XM-19 alloy, forged and in welded state, with respect to the reference technical requirement of ASTM A965 (denoted with the horizontal line). Note the remarkable behaviour of the XM-19 material for a sizeable forged product.

3.3.1 Microstructural characteristics as an explanation for mechanical behaviour

The tensile properties of the slab pieces, in both WS and SPF, prove to be slightly higher with respect to the head pieces, consistent with the observation of a finer grained structure in the slab forgings (figure 3.8). Consider, in this case that the micrograph presented for the head region, i.e. figure 3.8b, is obtained for a central region in the forging's head, to represent an average view of the head's microstructure.

Following the tensile measurements, furthermore a variation is noticed in tensile properties along the cross-section of the SPF head piece. For the top side of the head piece, slightly higher values ($R_{p0.2}$ at RT (4.2 K) $\approx$ 405 (1150 MPa), R_m at RT (4.2 K) $\approx$ 760 (1700 MPa)) are obtained than for the bottom side ($R_{p0.2}$ at RT (4.2 K) $\approx$ 395 (1140 MPa), R_m at RT (4.2 K) $\approx$ 750 (1690 MPa)). This can again be accounted for by the variation in grain structure observed (figure 3.9).

In fact, following grain size measurements, performed on a LEICA MZ16 stereomicroscope, following the 'mean lineal intercept' procedure according to ASTM E112, the variation in grain size was determined to be grain size number G = 3.5 $\div$ 4.5 for the top region of the head piece, while for the bottom a grain size number of G = 1.5 $\div$ 2.5 was found. The grain size number n, is related to the average number of grains per square inch (645 mm^2) at a magnification of 100 x, N, in the following manner (equation 3.2):

$$N = 2^{\,n-1}. \tag{3.2}$$

Thus the grain size number, n, is decreasing with increasing grain size.

Differences in grain structure can very well be related to variations in heat exposure and the extent of work of the different sections during the forging process. One of the phenomena explaining increased mechanical behaviour of the refining grain structure is known as Hall-Petch grain boundary strengthening, discussed in detail in section 11.2.2.

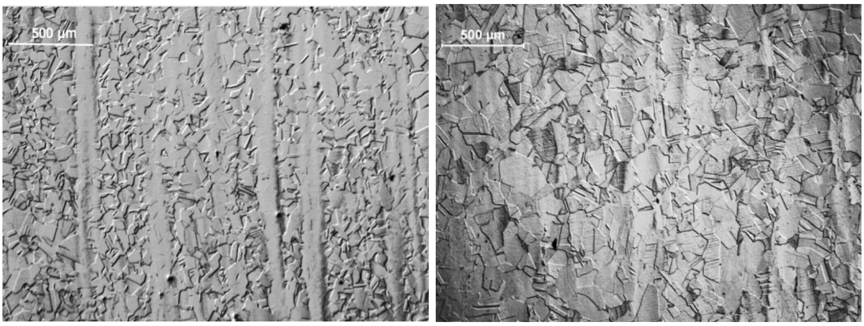

(a) Microstructure of the slab region of the SPF forging.

(b) Microstructure of the head region of the SPF forging.

Figure 3.8: Micrographs obtained at a magnification of 100 x following mechanical polishing succeeded by electrolytic etching at 6 V for 1 minute with a 10 g/100 ml oxalic acid/H_2O solution according to ASTM E407, to reveal the microstructure of the slab (a), and head (b) region of the SPF forging. Direction of maximum flow (i.e. longitudinal direction) is vertical in this view. Notice the difference in grain structure between the slab and head region; a finer structure is observed for the slab region, however containing a greater severity of strain lines.

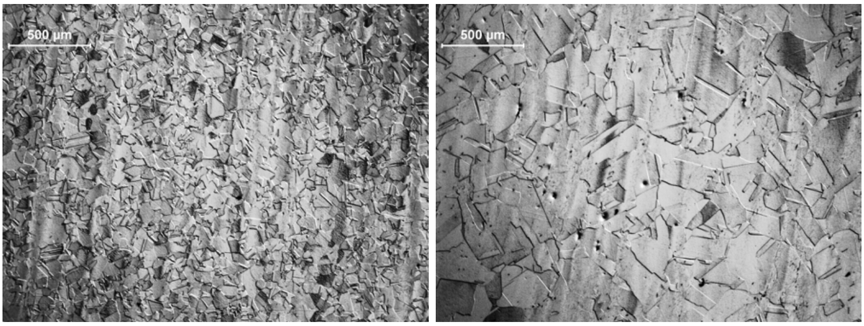

(a) Microstructure of the top head region of the SPF forging.

(b) Microstructure of the bottom head region of the SPF forging.

Figure 3.9: Micrographs obtained at an original magnification of 100 x following mechanical polishing succeeded by electrolytic etching at 6 V for 1 minute with a 10 g/100 ml oxalic acid/H_2O solution according to ASTM E407, to reveal the microstructure of the top (a), and bottom (b) region of forged head of the SPF solution. Direction of maximum flow (i.e. longitudinal direction) is vertical in this view. Notice the finer grain structure observed for the top head region, the region adjacent to the slab, with respect to the bottom head region.

4

F XM-19 as bearer of low-temperature fatigue and fracture toughness

Where studies for structural verification of material solutions comprise the straightforward bulk material strength approach, application based settings often require knowledge of the material's behaviour in a not so perfect state. Strength failure of load-bearing structures can be of the former yielding-dominant type. In the latter case, failure holds a fracture-dominant type, a failure type that depends on macroscopic imperfections. This is where the failure classifications hold their origin. In the case of yielding, general plasticity plays a major role, where controlling features are those resistant against plastic flow, like; interstitials, grain boundaries, secondary phases, and dislocation networks.

In the case of fracture, highly localised plasticity is leading, essentially dictated by macroscopic defects like: weld flaws, porosity, forging laps as well as fatigue and stress corrosion cracks. Fracture-dominant failure leads therefore to general yielding failure and is of great interest in application based studies as the one presented here, where aforementioned macroscopic flaws are likely to exist. In fracture mechanics these fracture-dominant failure modes are studied. Both static loading cases in terms of fracture toughness, as well as a dynamic loading cases in terms of fatigue crack growth rate are included, to which the tie plates of study here, are subjected to.

The manner of establishing as-said dynamic- and static performance under the presence of a flaw is discussed in this chapter, after which their method of testing is introduced. The primarily qualitative fatigue related measurement of fracture mechanics demonstrates a behaviour of all forgings within expectations. The weld nevertheless exhibits a crack growth rate under the presence of fatigue loading, significantly higher than the base forgings. Equally, all forgings exhibit a fracture toughness under static loading exceeding the NIST trendline for austenitic stainless steels, whereas the weld performs inferior. For the formulation of the fracture toughness some alterations are made to the standard compliance equation, necessary for its computation, which is extensively discussed in the prior-to-last section of this chapter.

4.1 Research methodology

Similarly as for the establishment of properties when the material is loaded in pure tension, in the case of the study of the dynamic and semi-static flaw induced behaviour of the F XM-19 material, here referred to the fracture mechanics of the material, specimens are extracted from head, slab and in the case of the WS also weld regions (figure 3.2). The research methodology and theory follows from an extensive literature study, here mainly based on the theories and experimental techniques as described in [Janssen et al., 2004] and [Anderson, 2005]. The ASTM standards in place are: ASTM E1823 for standard terminology, ASTM E647 for fatigue crack growth rate testing and ASTM E1820 for fracture toughness measurements.

4.1.1 Effect of a flaw on mechanical behaviour

In general fracture mechanics it is said that an existing flaw, or crack, will propagate if thereby the total energy of the system is lowered. Here is assumed that there is a simple energy balance, consisting of a decrease in elastic strain energy within the stressed body as the crack extends, counteracted by the energy needed to create new crack surfaces (a combination of the surface energy plus the work done in plastic deformation) [Anderson, 2005].

The aforementioned relates to an ’energy release rate’ or sometimes referred to as a ’crack driving force’, G, which in the case of Linear Elastic Fracture Mechanics (LEFM) can be considered congruent to the stress intensity approach. In the stress intensity, K, approach, fracture occurs when a critical stress distribution in front of the crack tip is reached. This theory of equivalence is however only true when the form of the stress distribution around and close to a crack tip is always the same, as observed in a linear elastic case. The stress intensity factor, K, must be linearly related to stress, as in equation 4.1 formulated by Irwin [Irwin, 1957] in view of the elastic theory:

$$\sigma_{ij} = \frac{K}{\sqrt{2\pi r}} f_{ij}(\theta) + ..., \tag{4.1}$$

where σ_{ij} denotes the stresses in the vicinity of the crack tip, and r and θ are the cylindrical polar coordinates of a point with respect to the crack tip [Janssen et al., 2004].

Even though the stress intensity factor in the LEFM approach is a powerful tool, it is generally solely applicable to stable cracking with blunted crack tips. In the case of sharp crack tips, where the radius tends to zero, a stress singularity at the crack tip is observed. Furthermore, crack growth and fracture are described under essentially elastic loading conditions. Even though the theory for LEFM is much better developed, only some aesthetic alteration can describe plasticity in the crack tip region, and only very limited. In practice a fully elastic behaviour at the crack tip is rarely the case, only in a plain strain situation of very brittle materials like ceramics. Crack tips tend to be very sharp in which case the problem needs to be treated elasto-plastically as in most materials the plastic zone becomes simply too large. The domain of the Elastic-Plastic Fracture Mechanics (EPFM) solves some of these issues, although some of the material's behaviour is still not fully described.

In EPFM the crack opening displacement (COD) approach is one of the most known. This approach focusses on the strain in the crack tip region in stead of the stress as done in the stress intensity approach. In the presence of plasticity a crack tip will blunt when loaded in tension, upon which the crack flank displacement at the tip of this blunting crack can describe the fracture in terms of a crack tip opening displacement (CTOD) parameter. Critical CTOD values corresponding to the onset of fracture can describe the behaviour of even very tough materials. The critical CTOD values are then used to qualify materials according to their requirements.

The disadvantage of the COD approach is that its equation is only valid for an infinite plate with a central crack, and it has proven very difficult to derive such an equation for practical geometries. The COD approach, with its CTOD critical parameter, can only properly describe the onset of crack opening. This is useful to compare at first instance the crack resistance of materials, but limited beyond.

In 1968 Rice considered going a step further, by taking into consideration potential energy changes in crack growth in a non-linear elastic material [Rice, 1968]. This is a method to describe plastic behaviour in a non-linear elastic manner, provided that no unloading occurs in the material. The factor describing this fracture behaviour, J, is in fact a contour integral which can be evaluated along any arbitrary path enclosing the crack tip. Here J is equal to the earlier denoted energy release rate, G, used for linear elastic materials, but then for the non-linear elastic case. The integral has a value equal to the decrease in potential energy per increment of crack extension. It's path independence implies that J can be seen as a measure for the intensity of both stress and strain at the tip of a crack, indicating that it can be seen as both an energy parameter (like G), as well as a stress intensity factor (like K).

Even though the limit of the J-integral approach is that no unloading is allowed in any part of the body, the integral is efficient in describing plastic behaviour with the use of a non-linear elastic approach, and will be employed here. The method and its restrictions is illustrated in the deformation theory of plasticity in figure 4.1. A plastically deformable material when unloading gives a permanent deformation, while for a non-linear elastic material with unloading no permanent deformation is registered. As the J-integral depends on a range of elastic relations, like the elastic relationship between stress and strain, and the principle of virtual work, thus approaching this non-linear elastic case, no permanent deformation is accounted for.

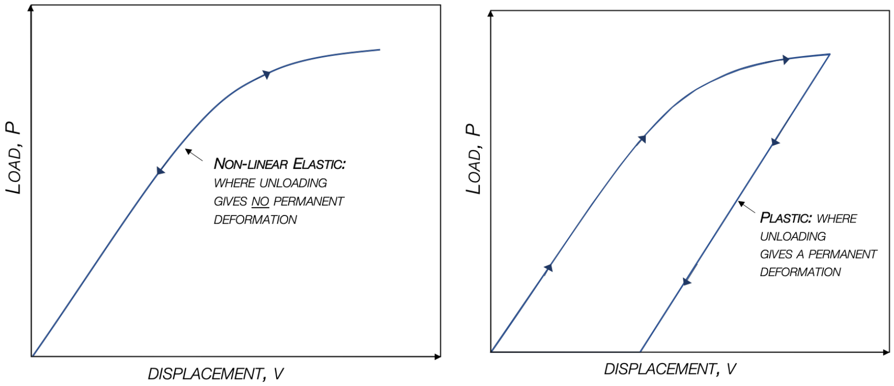

(a) Non-linear elastic deformation.

(b) Plastic deformation.

Figure 4.1: Load-displacement graphs for bodies of a non-linear elastic material (a) and a plastically deformable material (b).

Taking all this into account the J-integral does not only describe fairly well the onset of crack growth, extrapolated to a elasto-plastic case, but also to some extent stable crack growth. It can very well be used as a measure of fracture toughness in a wide range of materials, as is performed in this study.

The stress intensity factor can still be used in certain elasto-plastic cases where crack tip plasticity is fairly low. This is the case in sub-critical crack growth, under the so-called critical stress intensity factor, K_c, or the size independent K_{Ic} (only holding if certain geometrical conditions are met), which can be found for example in fatigue loading. The rate of crack growth as a result of fatigue is defined as the crack extension, Δa, over a small number of cycles, ΔN, from which its limit can be written as the differential ${}^{\mathrm{d}a}/_{\mathrm{d}N}$:

$$\frac{\mathrm{d}a}{\mathrm{d}N} = f(\Delta K, R). \tag{4.2}$$

The change in stress intensity ΔK correlates to fatigue crack growth rates in specimens with differing stress ranges and crack lengths, provided the stress ratio, $R = {}^{\sigma_{min}}/_{\sigma_{max}}$, is the same. Equation 4.2 can be plotted on a log-scale giving an overall estimate of the crack growth behaviour of a material under fatigue, our second area of interest, further described in section 4.1.3.

4.1.2 Fracture toughness testing at liquid helium temperature

The experimental procedure for determining J, or more specifically J_{Ic}, the critical mode I[1] J-value at the onset of crack extension, was first described by Begley and Landes in 1971 [Begley et al., 1972]. The expression, and testing method, has since gone through some optimisations. The original J_{Ic} test standard describes J_{Ic} determination purely based on the plastic deformation, following from the area obtained under a load-displacement, P-v, diagram (figure 4.2), following a loading - unloading sequence as described in equation 4.3:

$$J_{Ic} = \frac{2U_{cr}}{Bb} \cdot f({}^{a}/{}_{W}), \tag{4.3}$$

where B is the thickness of the specimen, b the length of the uncracked ligament in front of the crack and U_{cr} is the area under the P-v curve at the onset of crack extension.

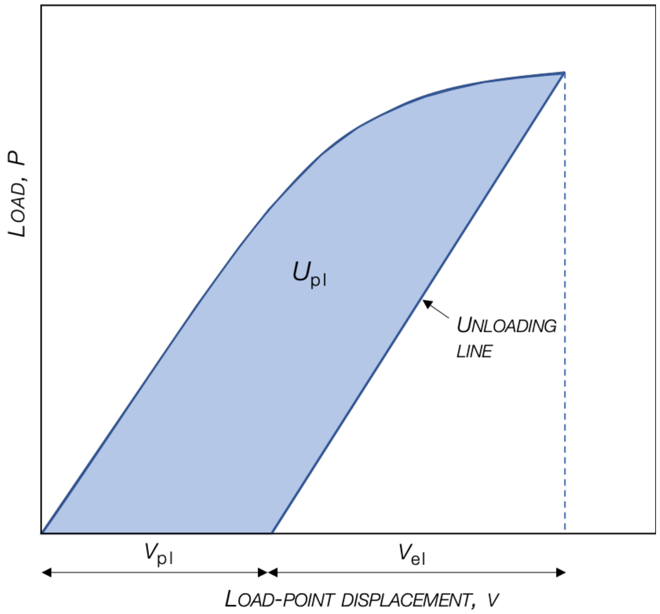

Figure 4.2: P-v curve, showing the plastic work U_{pl}, which at the onset of crack extension is otherwise named U_{cr}. Load-point displacement denotes the displacement observed at the axis where load is applied, from which v_{el} and v_{pl} are its elastic and plastic parts, respectively.

The revised standard divides the load-line displacement into two parts, an elastic and a plastic part, respectively. v_{el}, denoting the elastic part of the displacement,

---

[1] Mode I: loading condition where the crack opening runs perpendicular to the plane of principle stress.

can be expressed in terms of specimen compliance. This leads to the J equation in equation 4.4:

$$J_I = \frac{\eta U_{pl}}{B_N b} \cdot \frac{1-\nu^2}{E} K_I^2. \tag{4.4}$$

Here B_N denotes the net thickness of the specimen, equal to B in the case that there are no side grooves, and η refers to the specimen type.

We recognise the first factor as the plastic part, while the latter represents the elastic energy parameter, G. The elastic stress intensity factor K_I in this elastic energy parameter, when considering a plain strain situation can be described as:

$$K_I = \frac{P \cdot S}{BW^{n/6}} \cdot f(a/W). \tag{4.5}$$

In theory now J_{Ic} can be determined based on a single test in which the specimen is loaded until the onset of crack extension. In practice however, pinpointing the onset of crack growth has proven to be very difficult. This problem has been overcome by loading a set of specimens each to give a small but different crack extension, Δa. Then the values of J are plotted against Δa and extrapolated to $\Delta a = 0$ in order to obtain the critical J at the onset of crack extension. An example can be seen in figure 4.3. These curves are called J resistance curves, and are, equally in the new standard, still employed.

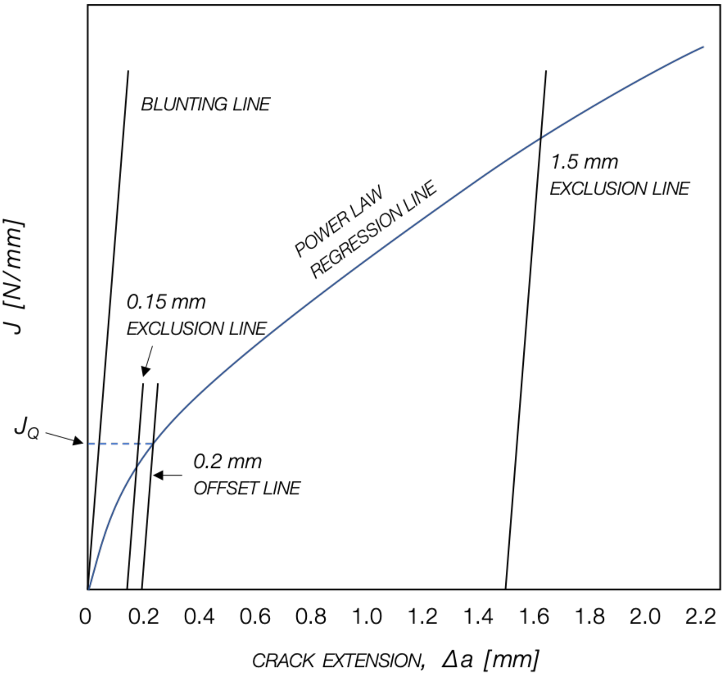

Figure 4.3: Characteristic J resistance curve, determined from J versus Δa data points obtained for different crack extensions for a single material.

In the current standard, the provisional critical value, J_Q, is determined at an offset of 0.2 mm, similar to the 0.2% yield point used in tension. The critical J value at the onset of crack extension gives rise to too much scatter as a result of the transition between the blunting process and actual crack extension not being always distinct. The 0.2 mm offset line is determined based on a blunting line, adopted as a result of an apparent increase in crack length owing to crack tip blunting (resulting in a false crack tip opening displacement reading). The apparent crack extension due to crack blunting can be accounted for by $J = 2\sigma_0 \Delta a$. The 0.2 mm reference point is now taken at the crossing of the power regression line with this blunting line at 0.2 mm crack extension.

For the power regression fit some data points are excluded, namely the ones prior to the 0.15 mm exclusion line, which ensures that Δa is at least 0.15 mm and can be measured accurately enough. And the ones post the 1.5 mm exclusion line, ensuring that Δa is generally less than 6% of the remaining ligament during testing, for which equation 4.4 remains valid.

$f(^a/_W)$ in equation 4.3 through equation 4.5 refer to the specimen type, as does S, p and η. The equations above hold for J testing of three-point notched bending (SENB) specimens as well as the so-called compact tension (CT) specimens. Both are consistent with a mode I crack opening condition. We employ the latter, for increased applicability in a liquid helium environment. In this case, in accordance with the ASTM standard E1820, $f(^a/_W)$ in equation 4.5 becomes:

$$f\left(\frac{a}{W}\right) = \frac{\left(2+\frac{a}{W}\right)\left\{0.886+4.64\left(\frac{a}{W}\right)-13.32\left(\frac{a}{W}\right)^2+14.72\left(\frac{a}{W}\right)^3-5.6\left(\frac{a}{W}\right)^4\right\}}{\left(1-\frac{a}{W}\right)^{3/2}}. \tag{4.6}$$

Furthermore, for CT specimen testing S becomes 1, $n = 3$, and $\eta = 2 + 0.522\ ^b/_W$.

The provisional J_Q, as derived from the constructed power regression line, as shown in figure 4.3 can, according to the standard, only be translated to the geometrically independent J_{Ic} if testing and sampling complies to certain requirements. Unfortunately, following adopted sub-size specimen dimensions, not all validity requirements can be met.

The specimen design is shown in figure 4.4, from which the reduced thickness of the item can be noted. The sub-size specimen design follows from a reduction in thermal load for liquid helium testing, and the maximum tensile load the set-up can endure in the case of a J test. Even though one cannot derive a geometrically independent material property from these specimens, the specimen design was chosen, such that results can be compared with those of a large variety of earlier test campaigns done on welds of ITER components on specimens of comparable geometry. Values will therefore be presented in the form of J_Q to avoid any ambiguity with respect to their purpose and validity.

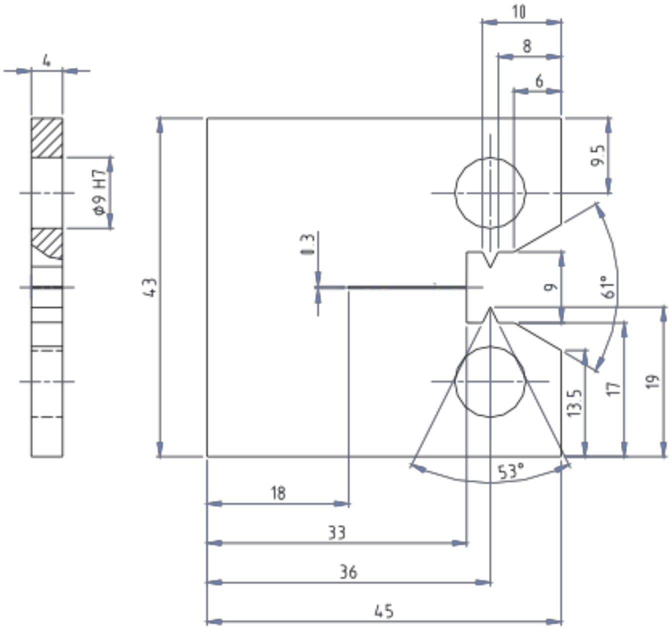

Figure 4.4: CT specimen design as employed for the J_Q tests described in this document. All dimensions are in mm. Specimen design is chosen for comparison reasons; no geometrically independent material property can be deduced from this geometry as a result of its reduced thickness.

Compliance method for cryogenic testing at 4.2 K

One can assume that by testing a batch of specimens, each to a certain specified crack extension to obtain a single J_Q value, is heavy on the labour side, as well as on helium consumption. Therefore the compliance method is adopted. As can be seen in figure 4.5, a single specimen is now loaded and unloaded several times, by which only partial unloading is achieved. In this way a set of data points, at different crack extensions can be obtained for a single specimen as U_{pl} can be determined for each hysteresis cycle. To avoid reversed plasticity having any effect on the test results, the maximum unloading range is set to 50% of the current load, or 20% of plastic collapse, whichever is the smallest. Plastic collapse can be calculated according to $P_L = {}^{B(W-a)^2\sigma_0}/_{(2W+a)}$ for a CT specimen [Janssen et al., 2004].

When employing this resistance curve procedure, dependent on the elastic compliance technique which results in a J resistance curve from a single specimen test, J is calculated from an incremental method. This results in the calculation of $K_{(i)}$ for the elastic part of J according to equation 4.5, by:

$$K_{(i)} = \frac{P_i}{BW^{1/2}} \cdot f({}^{a_i}/_W), \tag{4.7}$$

with $f({}^{a_i}/_W)$ according to equation 4.6.

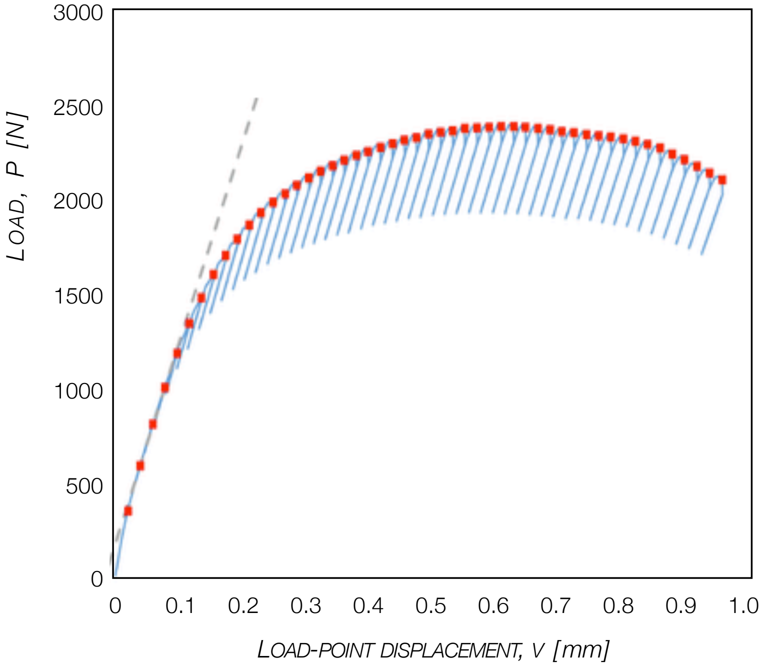

Figure 4.5: Illustration of the unloading compliance method, reducing the amount of tests to be performed.

The calculation of $J_{pl(i)}$, its plastic part, follows from equation 4.8 [Janssen et al., 2004]:

$$J_{pl(i)} = \left[J_{pl(i-1)} + \left(\frac{\eta_{(i-1)}}{b_{(i-1)}} \right) \frac{A_{pl(i)} - A_{pl(i-1)}}{B_N} \right] \left[1 - \gamma_{(i-1)} \frac{a_{(i)} - a_{(i-1)}}{b_{(i-1)}} \right], \quad (4.8)$$

where: $\eta_{(i-1)} = 2.0 + 0.522\, {}^{b_{(i-1)}}/_{W}$ consistent with it's definition for equation 4.4, and $\gamma_{(i-1)} = 1.0 + 0.76\, {}^{b_{(i-1)}}/_{W}$, both implying the CT specimen geometry.

In the plastic part, equation 4.8, $A_{pl(i)} - A_{pl(i-1)}$ refers to the increment in the plastic area under the load to load-line displacement curve figure 4.5. A_{pli} can be calculated from:

$$A_{pl(i)} = A_{pl(i-1)} + \frac{[P_{(i)} + P_{(i-1)}][v_{pl(i)} - v_{pl(i-1)}]}{2}, \quad (4.9)$$

where $v_{pl(i)}$ is known as the plastic part of the load-line displacement, v, or in effect equal to $v_i - (P_{(i)} C_{LL(i)})$. $C_{LL(i)}$ is here the elastic compliance.

The empirically derived function of $C_{LL(i)}$, the so-called ASTM compliance function, denoted in equation 4.10 plays a major role in the determination of the J resistance curve:

$$\begin{aligned} C_{LL(i)} &= \frac{1}{EB_e}\left(\frac{W+a_i}{W-a_i}\right)^2 [2.1630 + 12.219\left(\frac{a_i}{W}\right) - 20.065\left(\frac{a_i}{W}\right)^2 - 0.9925\left(\frac{a_i}{W}\right)^3 \\ &+ 20.609\left(\frac{a_i}{W}\right)^4 - 9.9314\left(\frac{a_i}{W}\right)^5], \end{aligned} \tag{4.10}$$

with:

$$B_e = B - \frac{(B-B_N)^2}{B}. \tag{4.11}$$

In order to obtain a sufficiently sharp crack tip prior to the J_Q-test, a fatigue pre-cracking is performed at room temperature. This is followed by a two step cool-down, initially to liquid nitrogen temperature, i.e. 77 K followed by a supplementary cool-down to the target temperature of 4.2 K using liquid helium. This two-step cool-down is employed to reduce helium consumption. In our case static crack extension for the determination of J_Q is done by increasing the load with a cross-head speed of 0.5 mm/min. After reaching general yielding, the load is manually reversed down to $\sim 10\%$ unloading in a cyclic manner, staying safely away from the maximum allowed unloading range. The loading/unloading process is terminated at the position of maximum load, followed by 3 to 5 extra sequences. The resistance curve is subsequently constructed relating the J-integral to the physical crack extension, from which J_Q is calculated.

Physical crack extension can be determined by flaming the specimen following the J_Q-measurement to 600°C to expose the exact location of the notch by oxidizing the specimen's crack surface. Examination by light microscopy following the specimen's total failure with use of fatigue loading at ambient temperature provides the ability examine the cracked surface and this exact location of the notch and thus final crack extension.

4.1.3 Fatigue crack growth rate testing at 4.2 K

The characteristic curve to determine the fatigue behaviour of a structure under the presence of discontinuities, or the $\mathrm{d}a/\mathrm{d}N$ - ΔK curve, can be seen in figure 4.6. Composed out of three regions, it shows the characteristic behaviour of a metal's fatigue crack growth related to the stress intensity range.

In 'Region I' a threshold value can be noted, ΔK_{th}, below which the crack grows at either extremely low rate or not at all. This is followed by a continuum region, from which characteristic values for the material can be derived. In this 'Region II', the crack growth rate is some power function of ΔK, resulting in a linear relationship between $log(\mathrm{d}a/\mathrm{d}N)$ and $log(\Delta K)$. Subsequently, in the third region, 'Region III', the growth curve tends towards an asymptote again, pushing ΔK towards its critical value ΔK_c, or in other words, final failure.

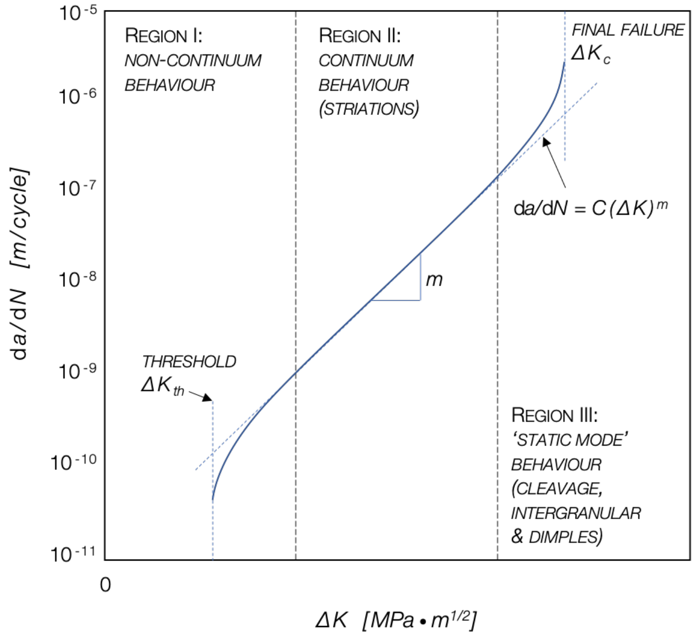

Figure 4.6: Characteristics of a fatigue crack growth rate curve ${}^{\mathrm{d}a}/_{\mathrm{d}N} = f(\Delta K, R)$.

The initial and latter region of the ${}^{\mathrm{d}a}/_{\mathrm{d}N}$ - ΔK relationship are challenging to describe, even though ΔK_{th} could, evidently, give some knowledge about the material's permissible crack length, and/or admissible applied stress in order to avoid crack growth. Where a material exhibits 'Region II' behaviour over a wide range of crack growth rates, the case in high-strength steels, a description of the second region can be made with more significance. By fitting an empirical formula to this range of the data, a set of material characteristic constants can be derived, providing a first estimate of crack growth behaviour.

The empirical formula for 'Region II' behaviour is known as the Paris equation, where two constants, C and m describe the curve, see figure 4.6:

$$\frac{\mathrm{d}a}{\mathrm{d}N} = C(\Delta K)^m. \tag{4.12}$$

In order to determine this ${}^{\mathrm{d}a}/_{\mathrm{d}N}$ - ΔK relationship, the main purpose of testing is to construct the crack growth curve a versus N, from which the growth rate ${}^{\Delta a}/_{\Delta N}$, and its limit ${}^{\mathrm{d}a}/_{\mathrm{d}N}$ can be determined at all times. The stress intensity range then follows from the stress range $\Delta\sigma = \sigma_{max} - \sigma_{min}$, in the form of equation 4.13:

$$\Delta K = K_{max} - K_{min} = \Delta\sqrt{\pi a}. \tag{4.13}$$

For a low-temperature fatigue crack growth rate (FCGR) measurement, a pre-crack is initiated at cryogenic temperature to avoid stress on an already opened crack during cool-down. a versus N for a specified stress range is measured at a 20 Hz constant amplitude fatigue load over the entire test duration at a constant load range ($P_{min}/P_{max} = 0.1$). The crack extension is followed by employing the aforementioned tailor-made extensometer at the specimen's load-line. Crack tip position can then be subsequently calculated using the ASTM E647 compliance function. FCGR tests are here applied from an initial $a = 12$ mm (load-line to notch position) up to a crack position of $a \approx 20$ mm.

In terms of helium consumption efficiency, the FCGR tests are in the current study combined with J_Q measurements. Fatigue loading is not continued into 'Region III' behaviour, but is arrested when sufficient data is gathered for a proper description of the power law. The consecutive J_Q test is performed via the J-integral method by static crack extension, where the load is gradually increased as is described in section 4.1.2, which we will from now on denote as a 'dedicated J-test'.

4.1.4 Experimental characteristics

Measurements are performed on a set-up comparable to the one described for the low-temperature measurements performed in tension. A two column system integrated in a 100 kN Instron servo-hydraulic testing machine is employed (figure 4.7). With a measurement volume, superior to the one used for tensile measurements, this set-up can host the appropriate width of the selected sub-size specimen geometry, while still maintaining space for all sensory equipment.

(a) Full measurement set-up. **(b)** Male part with specimen holders.

Figure 4.7: Dynamic and static fracture mechanics set-up employed for low temperature analysis of fracture toughness and fatigue crack growth rate.

The extensometer, following crack extension, is, analogous to the ones employed for low-temperature tensile testing, a tailor-made solution by Dr. A. Nyilas from CEME-KIT. It uses a strain-gauge system with Wheatstone bridge configuration, to guarantee accurate measurements. The extensometer is of the clip-on type, i.e. the knifes of the extensometer are clipped by pre-compression within the 'mouth' of the specimen. During crack opening extensometer deflection results in an analogous change in strain-gauge resistance.

Two specimens per type and direction were tested to reduce testing load and liquid helium consumption. The compact tension, CT, specimens are machined in accordance with the positions of the aforementioned tensile specimens.

Specimens are machined with different orientations as listed in table 4.1, according to ASTM E1823, where the first letter indicates the applied load direction, and the second the direction of crack extension. One specimen type comprises a long notch, processed by electro-erosion machining for dedicated J_Q tests (figure 4.4). A second holds a shorter notch to account for the ~8 mm travel of the crack tip during fatigue testing in a combined FCGR and J_Q test. All FCGR and J_Q specimens are listed in table 4.1.

Table 4.1: Fracture mechanics; sample designation.

Prototype	Position	Location	Test sequence	Specimen orientation[a]	Sample designation
WS	Head	-	FCGR + J_Q	SL	WS_MH_SL
				LS	WS_MH_LS
	Weld	Middle	FCGR + J_Q	LS	WS_MW_LS
	Slab	-	FCGR + J_Q	SL	WS_MS_SL
				LS	WS_MS_LS
SPF	Head	Top	FCGR + J_Q	LT	SPF_TH_LT
				LS	SPF_TH_LS
		Bottom	dedicated J_Q	LT	SPF_BH_LT$_J$
				LS	SPF_BH_LS$_J$
	Slab	Middle	FCGR + J_Q	LT	SPF_MS_LT
				LS	SPF_MS_LS
			dedicated J_Q	LT	SPF_MS_LT$_J$
				LS	SPF_MS_LS$_J$

---

[a] according to ASTM E1823

4.1.5 Measurement uncertainty

With fatigue crack growth rate, FCGR, data being subject to a large range of scatter, primarily at the low stress intensity range, data interpretation is often subject to a mathematical smoothing technique [Zheng et al., 1997]. Uncertainty in the final Paris law curve following from the measurement operator is therefore elevated. A. Nyilas determined in the onset of the study of F XM-19 for pre-compression purposes that an individual data uncertainty exists of $\pm 1.51 \cdot 10^{-5}$ mm/cycles at a reference ΔK of 25 MPa$\sqrt{\mathrm{m}}$, relating to an uncertainty of almost 35% [Nyilas, 2014]. Note that 25 MPa$\sqrt{\mathrm{m}}$ is at the onset of region II behaviour, and therefore represents the worst-case-scenario in terms of individual uncertainty. The Paris law, being determined by a linear empirical fit to the smoothed data, partially levels out the uncertainty in the individual values, mainly imposed by the operator. Paris law constants remain stable with consistently overestimated (or underestimated) data. The Paris constants, however, are not implemented as a requirement but merely serve for qualitative comparison. They do provide an estimate of crack growth behaviour in a dynamic environment.

Fracture toughness in terms of $K_Q(J)$ is the parameter used for mechanical qualification of the F XM-19 material under the presence of a flaw. The uncertainty in $K_Q(J)$ has been calculated following [Plaza, 2000], with a translation to liquid helium testing. The uncertainty in the measured $K_Q(J)$ values is determined at an approximate 2.1% for the liquid helium temperature measurements, based on a confidence level of 80%. Values presented in the tables and graphs represent the mean value and standard deviation following from the individual measurements. The additional measurement uncertainty presented here is noted below the graphic.

4.2 Low-temperature continuum fatigue behaviour of F XM-19 under the presence of a crack

Where a metal demonstrates a fatigue behaviour in the continuum region as described in figure 4.6, even at cryogenic temperature, the welded material shows a particular phenomenon during the FCGR test, depending on the crack growth path in the double-V bevel (figure 4.9a). A cluster of data points at the onset of the continuum region can be observed.

The crack, starting from the root of the weld, in our case the mid-plane of the tie plate slab (figure 4.8), penetrates the weld towards the weld crown. The initially unusual propagation, denoted by the decreasing trend-line in figure 4.9a, indicates a large influence of the base to weld material ratio, combined with possible residual stresses in the weld root, on the crack growth properties. This, physically improbable, apparently decreasing crack propagation could indicate a virtual crack closure resulting from the release of internal compressive stress from events as weld shrinkage and load deposit. With increasing cycle, a virtual crack closure is picked up by decreasing crack tip opening displacement, monitored by the deflectometer in place.

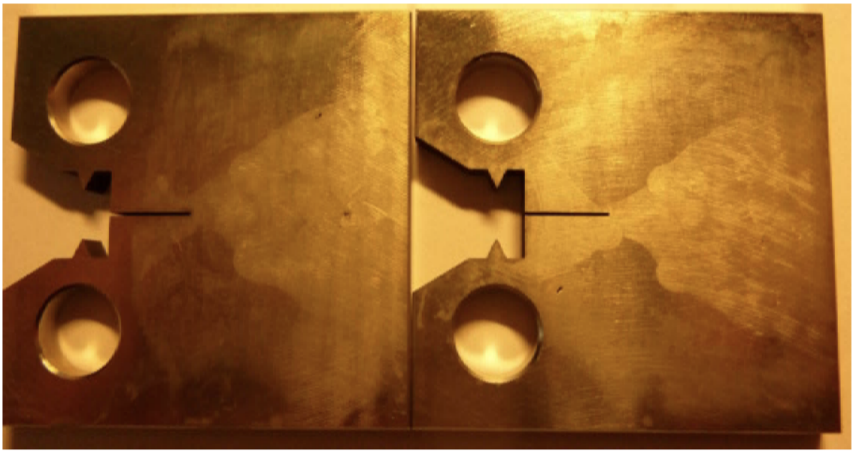

Figure 4.8: Two specimens representing the FCGR + J_Q measurement of the WS weld, denoting the actual position of the notch [Nyilas, 2014]. Note that the onset of crack extension will be highly influenced by the physical position of the notch, the weld to base metal ratio, and additional material effects introduced by the welding process.

In the second stage, when crack propagation is fully in the weld groove, the data shows a usual crack growth similar to what can be observed for a weld with a more regular weld width, and less weld passes. The fatigue crack growth rate in the weld material now increases considerably faster with increasing stress intensity in this second stage, with respect to the base metal forgings (figure 4.9b).

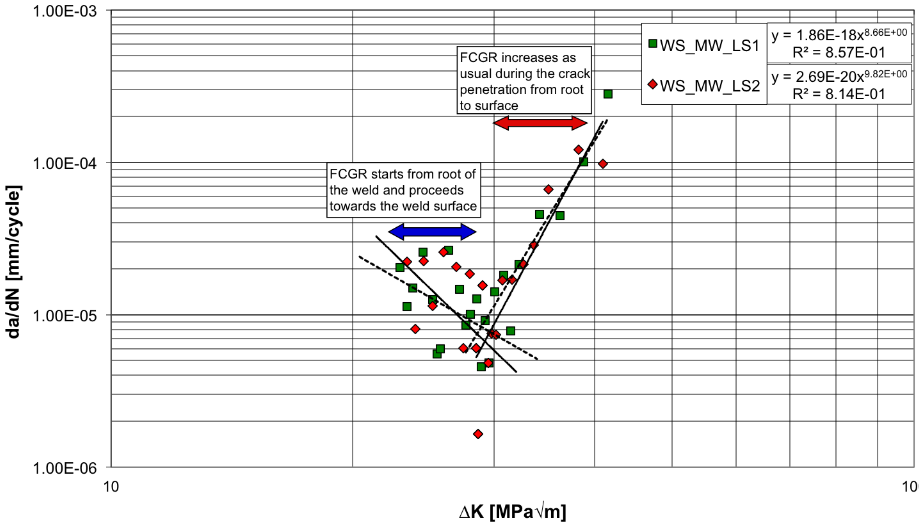

(a) FCGR data for the joint of the welded solution [Nyilas, 2014].

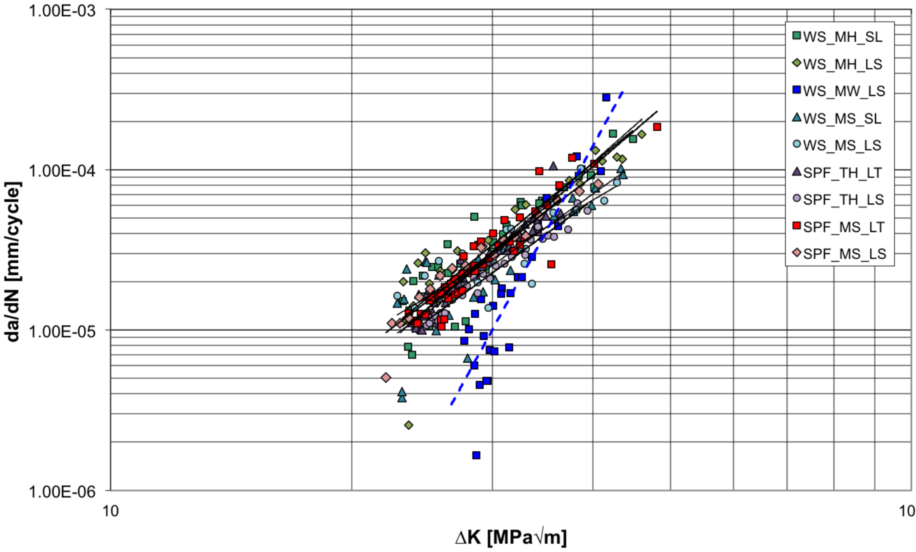

(b) FCGR data compared.

Figure 4.9: Fatigue Crack Growth Rate vs. Stress Intensity at liquid helium temperature for the two tie plate prototypes at various positions and in various crack growth directions.

The FCGR values for the parent metal of the various forgings fall nicely in the same range. The SPF forged material is very consistent with respect to measured values on the WS forged base material (figure 4.9b). The WS slab forging displays a marginally lower growth rate with increasing stress intensity. In the summarising table 4.2 the latter can be observed in further detail, where the Paris constants are given for comparison.

4.3 F XM-19 sustaining fair static loads under the presence of a crack

It is generally not allowed to describe elasto-plastic, non-linear crack propagation with the use of LEFM, in terms of K, where the stress distribution around the crack tip is always the same. The stress intensity factor K, linearly related to stress, or in our case the critical stress intensity factor K_Q, is here added for comparison. K_Q provides us here with a simplified notion of the material's fracture toughness; a value to be related with typical requirements as set up in projects like the one for the ITER tokamak. We need, however, to take into account its validity in a purely elastic range.

In table 4.2, besides the critical elasto-plastic J_Q values, also the elastic K_Q values are presented, both determined from the P-*v* diagram.

Table 4.2: Summary of test results, comprising both tensile and fracture mechanics data.

	Tensile[a]	$R_{p0.2}$	R_m	CT	K_Q	J_Q	Paris constants	
	T [K]	[MPa]	[MPa]	dir.	[MPa$\sqrt{m}$]	[N/mm]	C [$^{m}/_{MPa\ m^{0.2}\ cycle}$]	m
WS_MH	RT	407±6[b]	717±8	SL	122±3	77±2	$3.38\cdot10^{-11}$	4.06
	4.2	1310±20	1666±20	LS[c]	250±5	315±7	$9.47\cdot10^{-11}$	4.41
WS_TW	RT	451±6	611±7	LS	112±2	62±1	$3.32\cdot10^{-19}$	9.13
	4.2	1130±17	1360±16					
WS_MW	RT	475±7	671±7					
	4.2	1240±19	1453±17					
WS_BW	RT	455±6	619±7					
	4.2	1160±17	1286±15					
WS_MS	RT	412±6	748±8	SL	124±3	76±2	$1.43\cdot10^{-10}$	3.55
	4.2	1266±19	1743±21	LS	226±5	231±5	$1.31\cdot10^{-9}$	2.93
SPF_TH	RT	404±6	762±8	LT	170±4	130±3	$2.46\cdot10^{-11}$	4.12
	4.2	1150±17	1699±20	LS	220±5[d]	215±5[c]	$1.01\cdot10^{-10}$	3.62
SPF_BH	RT	394±6	749±8	LT_J	190±4	161±3	-	-
	4.2	1140±17	1692±20	LS_J	197±4	173±4	-	-
SPF_MS	RT	419±6	763±8	LT	188±4	157±3	$1.42\cdot10^{-11}$	4.29
				LS	223±5[c]	237±5[c]	$8.26\cdot10^{-11}$	3.77
	4.2	1201±18	1709±21	LT_J	226±5	239±5	-	-
				LS_J	243±5[c]	289±6[c]	-	-

---

[a] only holds for the tensile measurements, all fracture mechanics measurements are conducted at cryogenic temperature

[b] measurement uncertainty

[c] deduced from a single measurement

[d] anisotropic crack extension - adjusted compliance equation used

What becomes immediately apparent from table 4.2 is the high degree of anisotropy of the forged material, present for both the excessive sized forging of the SPF as well as for both forgings of the WS. WS specimen direction SL with a crack extension along the forging direction L, while load is applied in the short transverse direction S, exhibits a fracture toughness approximately twice as low as when the crack runs perpendicular to the forging direction (specimen direction LS).

One can observe then from the SPF fracture toughness data that crack extension perpendicular to the longitudinal direction of the forging holds the higher values. A crack extension in fact is most prone to occur in this direction perpendicular to the longitudinal direction of the plate, with the crack extending in transverse or short transverse direction. It can be stated therefore, that the values obtained for WS, in SL-direction, are very conservative and that this case is not likely to occur.

4.3.1 Anisotropy in sizeable F XM-19 forgings

The next question to answer is where the anisotropic fracture behaviour shown in section 4.3 has its origin. The directionality of the material following forging becomes most apparent for the SPF tie plate slab, where the crack extension during the J_Q test, occurred in a direction perpendicular to the initial tearing direction for the samples with LS positioning (figure 4.10a).

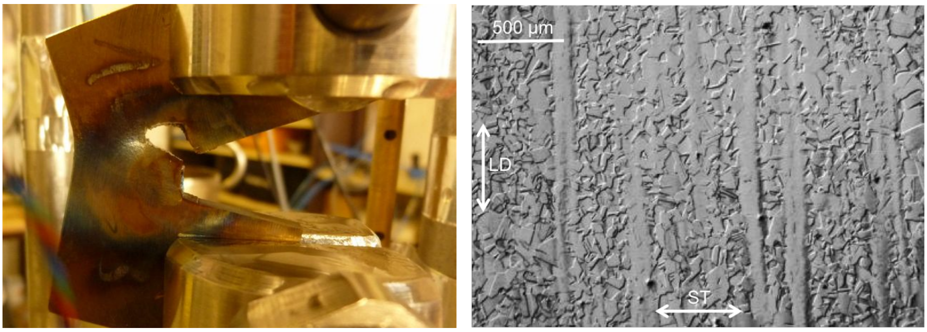

(a) Image of the J_Q test on an LS specimen of the SPF slab.

(b) Micrograph of the SPF slab region, original magnification 100 x.

Figure 4.10: Photograph indicating the 90° crack growth during the J_Q test in specimen LS2 of the SPF tie plates slab piece (a), and a corresponding micrograph showing the fibrous microstructure of the SPF tie plate slab (b).

Following additional microstructural inspection, the crack extension direction is present parallel to the observed planes with strain markings in the microstructure of the slab (figure 4.10b). The crack appears to take the path of least resistance, deviating to a plane parallel to the strain markings. For the SPF tie plate head, this anisotropic behaviour was also observed in the top region, however much less pronounced in the bottom region. This is consistent with the lesser extent of strain lines observed in the bottom of the SPF head, although still present.

The same holds for the WS forgings. Some strain markings were observed in the materials microstructure, as can be observed in figure 4.11, in which micrographs of the WS slab (a) and head (b) regions in the LS plane are presented. The extent of anisotropy was observed to be similar in the case of the WS slab, and lesser in the case of the WS head to the SPF tie plate head bottom region, and found to be limited in its effect on the fracture toughness results.

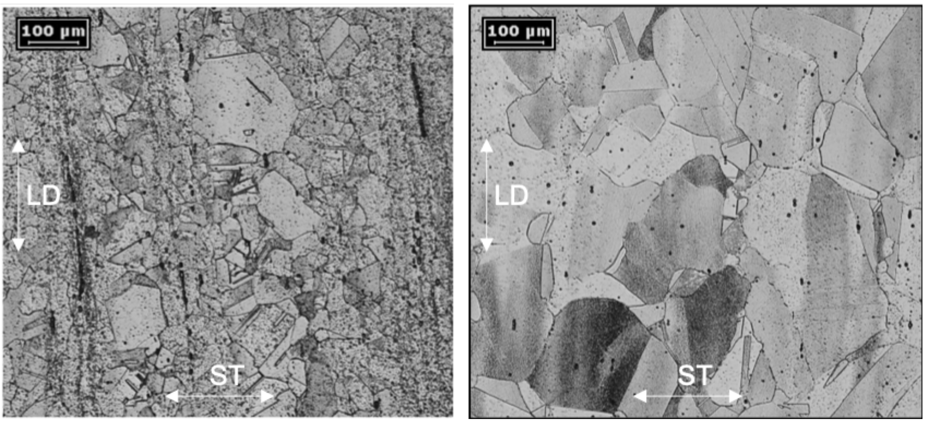

(a) Micrograph of the WS slab region, original magnification 100 x.

(b) Micrograph of the WS head region, original magnification 100 x.

Figure 4.11: Micrographs showing the microstructure of the WS slab (a) and head (b) forging, both containing to some extent micro strain lines as a result from the material processing.

Strain marking in the metal is known for introducing fibrous characteristics. The markings correspond to a pattern of internal planes that were submitted to extensive plastic shear during forming. As such, they can account for material behaviour as is observed in fibre reinforced materials.

The anisotropic material characteristics can be well explained in the case of heavy forgings. Large deformations take place during the tie plate production, in which, for the single piece forged item, deformations are of even larger extent. The same holds for slab versus head forgings, where the head is subject to a smaller reduction in the thickness direction with respect to the slab. In the case of the forging extracted from a single piece of material, the top end of the head, which is in an direct contact with the slab, and therefore simultaneously less exposed to free boundaries for stress relief, contains a higher degree of anisotropy. Which results, microstructurally and mechanically, in a transitional area between head and slab.

Validity of the ASTM compliance function in the case of anisotropic crack growth

In the case of the SPF head top region and its slab region, the evaluation of the J-test using the ASTM E1820 standard could not be applied since the unloading slopes of the load versus displacement record relies on the standard compliance function of a compact tension specimen where the crack extension occurs at a 0° plane.

ASTM E1820 leaves the researcher free to experimentally determine the elastic compliance. This provides us with the possibility of estimating the effect of a 90° crack propagation during a J_Q testing procedure.

Compliance is determined via the inverse of the materials stiffness, where the stiffness depends on various factors like material properties such as the Young's modulus. It is nevertheless also heavily affected by geometrical characteristics, amongst which the crack path. To determine specimen stiffness, or in other words $^{\Delta P}/_{\Delta v}$, one can perform some loading-unloading sequences in the elastic regime. If the former is repeated for a range of crack length to specimen width ratio's, i.e. $^{a}/_{W}$ in equation 4.10, one can determine from it's inverse a compliance function for a certain crack extension range, or in other words $\left(^{\Delta v}/_{\Delta P}\right)_i$.

Compliance in this case was initially determined numerically, with the use of Finite Element Modelling (FEM). Virtual specimens with a variation in crack length and anisotropic crack extension are loaded and unloaded to a 2 kN force, while the load-line displacement v_{LL}, is calculated. For simplification a two-dimensional model is employed for the shear reason that a comparison with a three-dimensional variant resulted in a deviation of less than 0.8%.

Load to load-line displacement is determined for a virtual crack extension between 18 mm and 26 mm, where 18 mm corresponds to the onset of the crack extension in the J_Q tests as presented in figure 4.4. Specimen stiffness for a $0°$ crack plane was determined using a virtual crack extension of 18, 20, 21, 22, and 23 mm, for reference and comparison purposes with the ASTM compliance function equation 4.10. Subsequently crack extension in the $90°$ plane has been studied by employing a virtual crack extension of 20 mm in the $0°$ plane, followed by 1, 2, 4 and 6 mm in the $90°$ plane.

In table 4.3 the variables and related outcomes are listed, where an additional calculated value is presented. EBC is added as the dimensionless value representing specimen properties. E, known as the material characteristic Young's modulus, here taken to be 200 GPa, for reference with the accompanying experimental results, later presented. B known as the specimen's thickness, here 4 mm, and C, here our computed load-line compliance. From EBC we can later derive the compliance function. Subsequently in figure 4.12 the results from table 4.3 are plotted versus the general $0°$ crack extension ASTM compliance function under the same conditions.

Table 4.3: Details and numerical values as obtained for the FEM analysis of 0° crack extension and subsequently 90° crack diversion of CT specimens as employed for this research.

Crack plane	a [mm]	$\frac{a}{W}$	v_{LL}[a] [mm]	S [kN/mm]	C [mm/kN]	EBC[b]
0°	18	0.500	0.095	21.1	$4.75{\cdot}10^{-2}$	38.0
	20	0.556	0.125	16.0	$6.25{\cdot}10^{-2}$	50.0
	21	0.583	0.145	13.8	$7.25{\cdot}10^{-2}$	58.0
	22	0.611	0.170	11.8	$8.50{\cdot}10^{-2}$	68.0
	23	0.639	0.205	9.8	$1.03{\cdot}10^{-2}$	82.0
20 mm @ 0° followed by 1, 2, 4 and 6 mm @ 90°	21	0.583	0.136	14.7	$6.80{\cdot}10^{-2}$	54.4
	22	0.611	0.142	14.1	$7.10{\cdot}10^{-2}$	56.8
	24	0.667	0.156	12.8	$7.80{\cdot}10^{-2}$	62.4
	26	0.722	0.176	11.4	$8.80{\cdot}10^{-2}$	70.4

---

[a] load-line displacement

[b] dimensionless value standing for Young's modulus E (here 200 GPa), specimen thickness B (here 4 mm), and the computed compliance C

Note the proper agreement between the compliance obtained by FEM analysis considering a 0° crack extension, and the ASTM compliance function valid for the same isotropic conditions. On the other hand, one can see that a crack deviation out of the 0° plane results in an apparent decrease in compliance, or increase in stiffness, leaving a calculation of J no longer representative when using the general ASTM compliance function. One can very well anticipate a stiffening of the specimen not directly related to the pure material properties. The imminent decrease in compliance (or compliance increment, as used) will therefore virtually lead to a decrease in J_Q, thus underestimating this material characteristic.

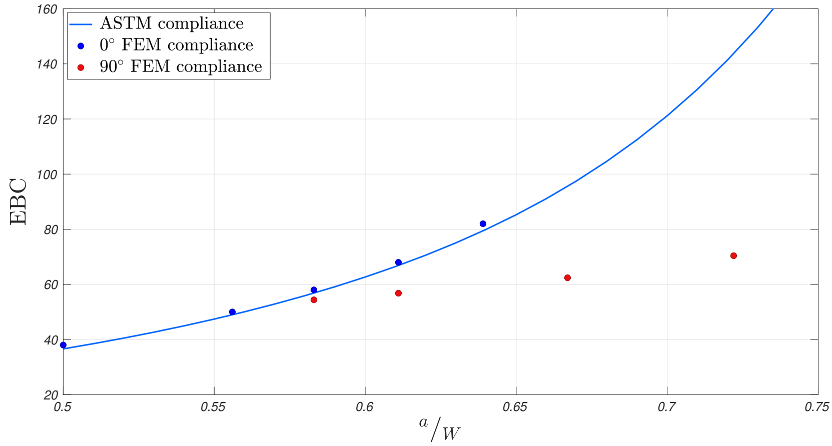

Figure 4.12: Compliance diagram based on the numerically obtained compliance for the 0° and the subsequent 90° crack propagation in an E = 200 GPa type steel, compared to the general ASTM E1820 compliance function at E = 200 GPa. Note the nice agreement between the ASTM compliance function and the numerical compliance for the 0° crack plane, whereas for the 90° crack plane the curve flattens.

A reliability check of the obtained FEM results is done in the form of a physical experiment. A batch of 7 specimens were tested each with a different physical crack extension. For this cross-check the more known 316LN material is employed, exhibiting a Young's modulus of $\sim$ 200 GPa. Specimens were machined in the same manner as for the earlier J_Q tests including an artificial crack, machined by electro-erosion, corresponding to the crack extension under study in figure 4.13. A single specimen amongst this batch has been machined with a 20 mm crack purely in the $0°$ plane, as a reference. All other 6 specimens contained a certain amount of crack extension in the $90°$ plane, following this initial 20 mm in the $0°$ plane (figure 4.14).

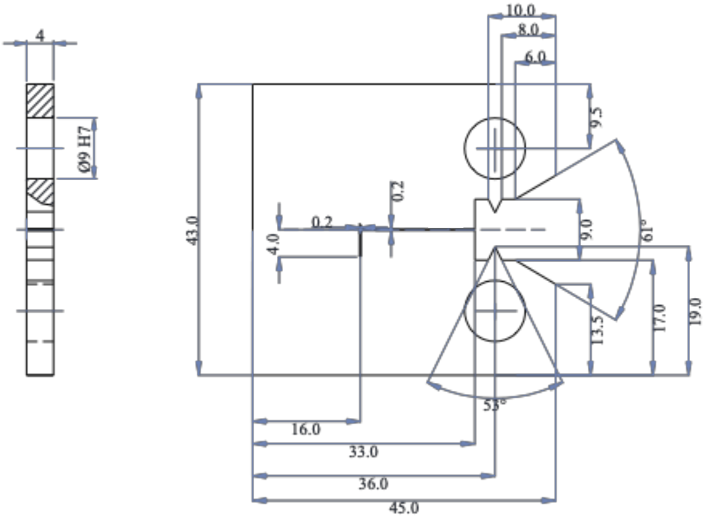

Figure 4.13: Compliance specimen design, here with a 4 mm out of plane machined artificial crack extension, as employed for the measurements in view of determining a valid compliance function. All dimensions are in mm.

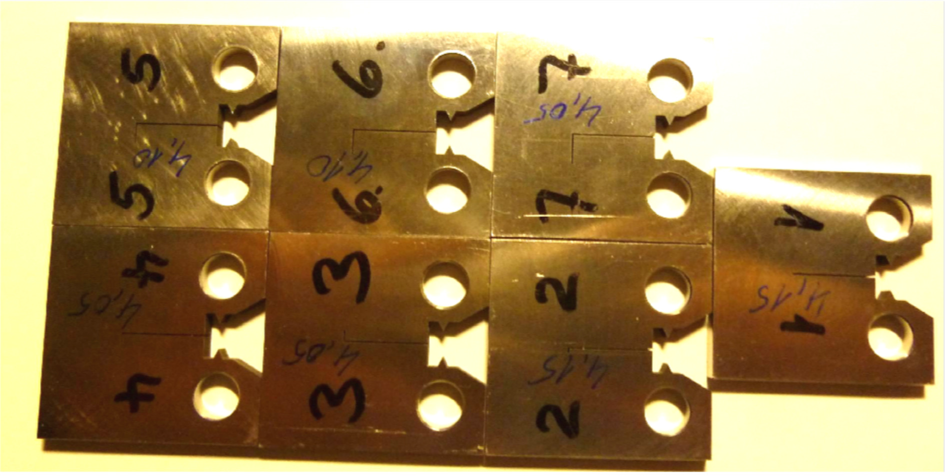

Figure 4.14: Photograph of all produced and measured compliance specimens with different artificial machined out of plane crack extensions for the determination of a correct compliance function for $90°$ crack extension.

In order to reduce chances of plasticity, these specimens were loaded to 1 kN under tension at the load line, while load-line displacement was measured employing the same extensometer as employed for the earlier J_Q and FCGR measurements.

Table 4.4: Details and experimental values obtained for the physical analysis of 0° crack extension and subsequently 90° crack diversion of CT specimens.

Crack plane	a [mm]	$\frac{a}{W}$	B [a] [mm]	S [kN/mm]	C [mm/kN]	EBC
0°	20	0.556	4.15	15.9	$6.28{\cdot}10^{-2}$	52.1
20 mm @ 0° followed by 1, 2, 3, 4, 5 & 6 mm @ 90°	21	0.583	4.15	15.1	$6.66{\cdot}10^{-2}$	55.3
	22	0.611	4.05	14.2	$7.02{\cdot}10^{-2}$	56.9
	23	0.639	4.05	13.3	$7.53{\cdot}10^{-2}$	61.0
	24	0.667	4.10	12.7	$7.90{\cdot}10^{-2}$	64.8
	25	0.694	4.10	11.9	$8.38{\cdot}10^{-2}$	68.7
	26	0.722	4.05	11.1	$8.98{\cdot}10^{-2}$	72.7

---

[a] measured specimen thickness

In table 4.4 the employed parameters and the measured characteristics of the various specimens are listed. The denoted stiffness in the table follows directly from the P-*v* curves obtained for the specimens when loaded to 1 kN and subsequently unloaded.

In the corresponding graph figure 4.15 it becomes apparent that experimental and numerical results agree very well. The minor discrepancy between experimental and FEM results can be accounted for by a small difference of the actual Young's modulus of the tested material. A decrease of 3.8% in Young's modulus in the calculations results in a disappearance of the difference. As the Young's modulus in the numerical analysis is given, consequently the new compliance function is derived from the numerical data. A second degree polynomial was found to fit the data best, with fit parameters:

$$p1 = 340.1, \quad p2 = 329.6 \text{ and } p3 = 131.1\ . \tag{4.14}$$

This results in a form of compliance function as follows:

$$C_{LL} = \frac{1}{EB_e}\left[340.1\left(\frac{a}{W}\right)^2 - 329.6\left(\frac{a}{W}\right) - 131.1\right]\ . \tag{4.15}$$

The adjusted compliance function for the evaluation of fracture toughness at 90° crack extension was then applied for the evaluation of the specimens featuring crack-plane deviation. Consequently data presented for the LS measurement direction of the SPF prototype in table 4.2 were evaluated according to this adjusted compliance function, denoted with tablenote *c*.

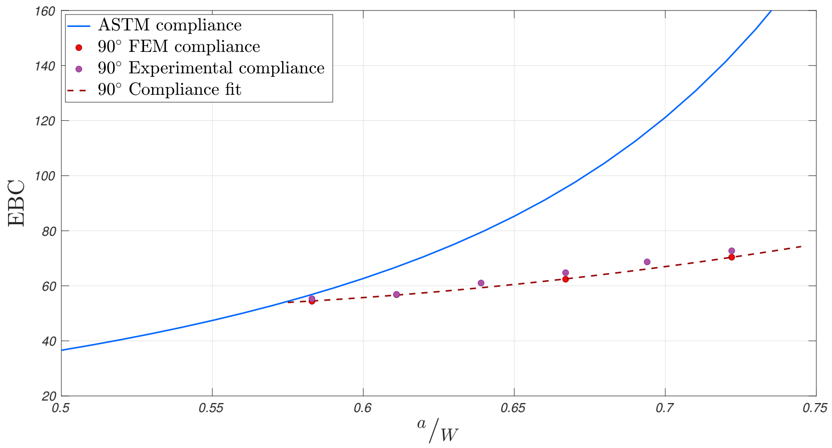

Figure 4.15: Calculated compliance at a 90° crack plane plotted against the compliance obtained for the same crack plane in an experimental manner. The ASTM compliance function is added as a reference. Data is represented for a material exhibiting an E-modulus of 200 GPa. Note that the data for the numerical and experimental cases agree very well. A small deviation could be accounted for by a small discrepancy in E-modulus. The 90° fit line represents the newly adopted compliance function for the tested specimens featuring crack-plane deviation.

4.3.2 Impressive mechanical performance of F XM-19 when loaded in a static manner

Figure 4.16 shows the obtained fracture toughness K_Q data, versus tensile yield strength $R_{p0.2}$ for the WS and SPF prototypes in LS-direction. The graph represents a set of data giving reference as to what the static mechanical performance of this fairly unknown material is at cryogenic temperature, both under the presence of a flaw, and in ’flawless’ state. The obtained data from the current study is compared with an available fracture toughness trend-line of austenitic stainless steel at 4.2 K [Davis, 1994].

The LS-direction, with its critical values, is chosen since this direction corresponds to the most probable tearing direction during operation, and consequently to the tear direction during tensile test. One can observe that the fracture toughness for the F XM-19 forgings as function of R$_{p0.2}$ lies above the trend-line, whereas for the weld the contrary is observed. The fracture toughness measurements reveal a marginally increased fracture toughness of the WS tie plate forged base material with respect to the SPF tie plate material.

In order to assess the performance of the F XM-19 material, under realistic utilisation, the obtained critical values have been equally compared with some selected 'bulk' 316LN material. Data for hot-rolled and extruded 316LN in a fair state, are added as an indication of the performance of either material. We see as previously anticipated, that the F XM-19 material behaviour in a 'flawless' state outperforms by far the 316LN bulk material. 316LN still exhibits superior properties when flaws are present, even though the presented 316LN selected data falls on the trend-line, where F XM-19 lie above.

Note that, with exception of the weld case, all static mechanical characteristics of the F XM-19 material fall well above the ITER requirements for these forgings. This is even valid in the case a flaw is present ($K_Q > 130\ \text{MPa} \cdot \sqrt{\text{m}}$), demonstrating its very interesting mechanical characteristics for this application.

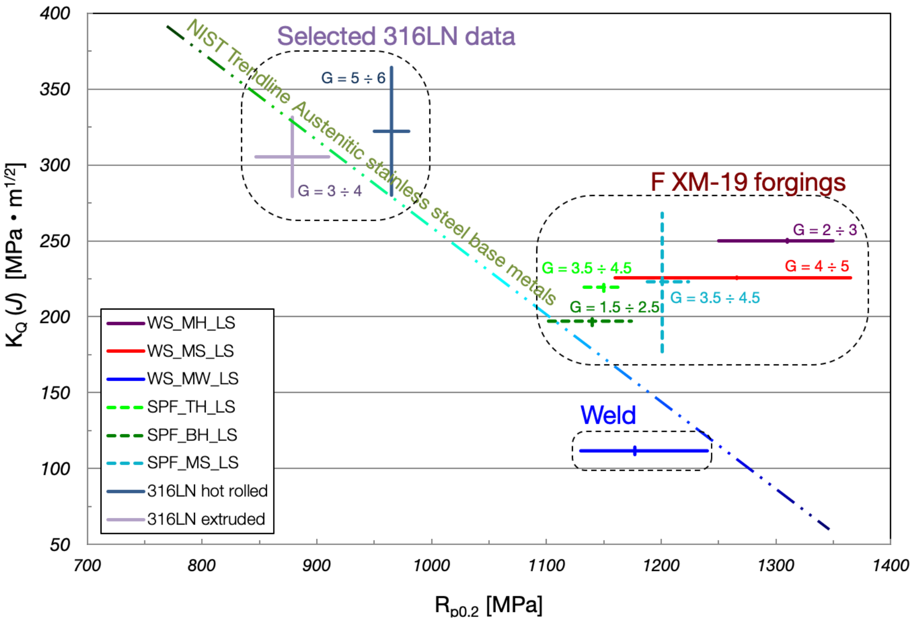

Figure 4.16: Fracture toughness K_Q vs. 0.2% yield strength $R_{p0.2}$ at 4.2 K for the F XM-19 forged material and its weld. For comparison grain size numbers are also displayed.

5

Magnetic performance of F XM-19

After having established F XM-19's potential for large load-bearing structures operating at cryogenic temperatures, both in a static as well as a dynamic manner, next to verify is it's suitability in a magnetic environment. For a magnet application a non-, or feebly magnetic material is essential, which is always a challenge in steel based structures. Any form of ferrite or martensite in the steel's structure can lead to an increase in magnetic permeability. The presence, amount and distribution of the ferromagnetic phases determine the magnetic response or susceptibility of the material. Beneficial for the application here is a low magnetic susceptibility approaching a relative magnetic permeability of 1.0.

Here the employed research methodology is presented, realising the evaluation of the material's magnetic performance over a wide range of temperatures down to liquid helium temperature. A magnetic susceptibility as anticipated is observed for the single piece forged structure, whereas for the forgings of the welded structure some δ-ferrite segregations result in elevated magnetic permeability values, detrimental for its applicability in a high magnetic field structure.

5.1 Research methodology

The magnetic permeability, is defined as the relative change in magnetic flux density B inside a material compared with the magnetising field the material is located in when exposed to the applied magnetising field H:

$$\mu = {}^{B}\!/_{H} = \mu_0 \mu_r. \tag{5.1}$$

Here μ_r denotes the dimensionless relative magnetic permeability, where $\mu_0 = 4\pi \cdot 10^{-7} H/m$ is the magnetic permeability of vacuum.

A second value representing the magnetic behaviour of a material is the amount of it's magnetisation when placed in a magnetic field. Net magnetisation, expressed as the density of induced magnetic dipole moments per unit volume in a magnetic material, results from the response of a material to an external magnetic field, in addition to any unbalanced dipole moments in the material itself, as is the case in ferromagnetic materials.

Magnetisation is expressed with use of a hysteresis curve of magnetisation versus magnetic field, in which magnetic susceptibility, magnetic saturation and retentivity in the case of a non-linear ferromagnetic material can be recognised. The hysteresis curves can be presented by either B-H or M-H curves following:

$$M = \chi H. \tag{5.2}$$

Here the volume magnetic susceptibility χ is a constant in the case of a non-magnetic material, i.e. a linear relationship can be observed from the magnetisation M versus external magnetic field H curve. In the case of a ferromagnetic material, even in light form, the material's magnetisation increases fast with increasing magnetic field until a typical turning-point, followed by a curve flattening to a constant volume magnetic susceptibility, the saturation value, in line with a non-magnetic material. This is due to the limit of flux density generated when all ferromagnetic domains in the material become aligned.

In the case of a ferromagnetic material there is often no one-to-one correspondence of M with χ. In the case of magnetic field reduction, the material retains some of the magnetic flux inside its structure. The randomisation of the magnetic domains is delayed with respect to the removal of external magnetic field. This phenomenon is known as the materials retentivity, and is an expression of the magnetic 'hardness' of the material.

The three main types of materials, as can be read from the M-H hysteresis curve, are graphically represented in figure 5.1. Here the hysteresis curves of the different forgings are determined both at ambient temperature, as well as at 4.2 K.

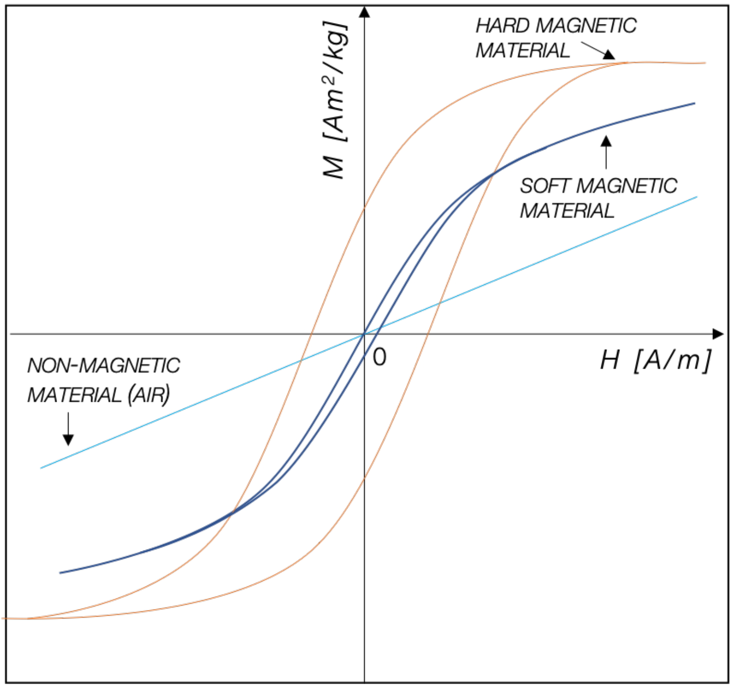

Figure 5.1: Characteristic magnitisation curves, demonstrating magnetisation response for a non-magnetic, soft-magnetic and hard-magnetic material.

5.1.1 Low-temperature magnetisation measurements

The magnetic measurements are performed with use of a Vibrating Sample Magnetometer [Arauzo, 2014]. The magnetic permeability can be calculated from the volume magnetisation following:

$$\mu_r = 1 + \chi = 1 + \frac{M\ [A/m]}{H\ [A/m]}. \tag{5.3}$$

The specimen, extracted by electro-erosion and subsequently mechanically finished, is sinusoidally oscillating at a frequency of 40 Hz and a peak amplitude of 2 mm, while being fixed with cotton in a gelatin capsule enclosed in a short straw sample holder (figure 5.2). The specimens have the overall size of 8 mm x 4 mm x 2 mm. Magnetic field is applied along the (8 mm) longitudinal direction of the sample to retain maximum accuracy, for which also a magnet reset takes place prior to each measurement. Periodic calibration is performed with use of a palladium sample with an accuracy better than 1% of the magnetic moment. Three specimens along the thickness of the slab region of the WS and SPF prototype forgings were measured, as specified in table 5.1. The slab region was chosen, as for the prior mechanical and optical investigations the slab showed most critical as a result of the high degree of work exerted on this region during fabrication.

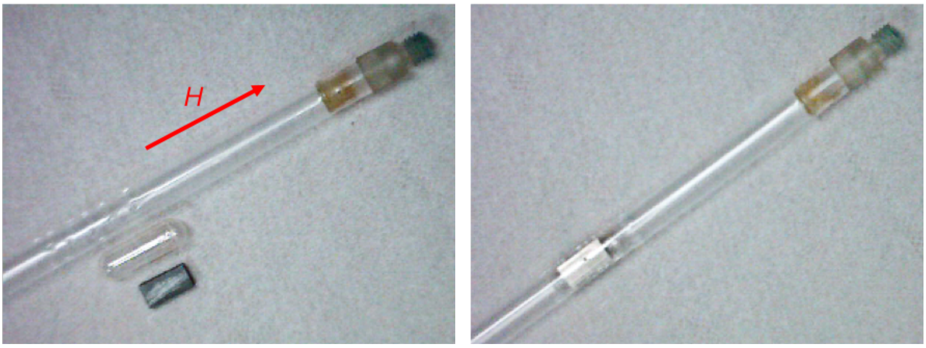

(a) Specimen holder, disjointed. Showing holder, capsule and specimen.

(b) Specimen as mounted in the dedicated specimen holder.

Figure 5.2: Specimen holder for the magnetic measurements performed by VSM technique, in dismounted (a) and mounted (b) state. Magnetic field, H, is indicated in red, to denote applied magnetic field direction with respect to the specimen orientation.

Each specimen is subjected to a magnetisation measurement at 7960 A/m (100 Oe) from 4 K to 300 K, followed by a hysteresis cycle up to 9 T (7162 kA/m) at both 295 K (ambient temperature) and 4.2 K (simulating operating temperature).

Table 5.1: Specimen characteristics as employed for the magnetic measurements, essential for the calculation of the magnetic properties of the F XM-19 material.

Specimen designation	Mass[a] [mg]	Dimensions [mm^3]	Volume [mm^3]
WS_TS	510.14	8.03 x 4.04 x 2.01	65.2
WS_MS	503.58	8.11 x 4.04 x 1.96	64.2
WS_BS	503.08	8.07 x 4.03 x 1.99	64.7
SPF_TS	506.30	7.99 x 4.05 x 2.02	65.4
SPF_MS	505.48	8.02 x 4.05 x 2.01	65.3
SPF_BS	504.18	8.03 x 4.03 x 2.01	65.0

---

[a] measurement accuracy of 20 μg

5.2 Magnetic properties of large F XM-19 forgings

The measured magnetisation curves are shown in figure 5.3. Very nice hysteresis curves at both ambient as well as cryogenic temperatures are obtained. The first three diagrams shown in figure 5.3a, figure 5.3b and figure 5.3c represent in orange and blue the magnetisation curves for the WS prototype forging at ambient and 4.2 K, respectively. Likewise the three diagrams shown in figures 5.3d, 5.3e and 5.3f represent in orange and blue the magnetisation curves for the SPF prototype forging at ambient and 4.2 K, respectively. The curves of the middle slab regions of either prototype are shown side by side to demonstrate the difference between the two prototype forgings, as result of their varying heat.

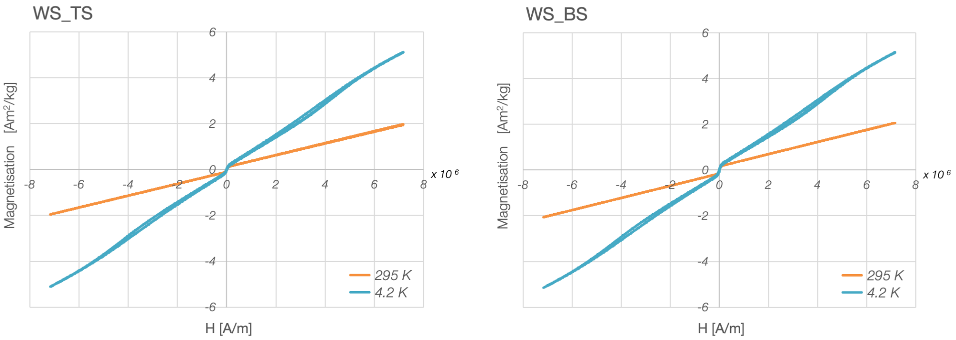

(a) Magnetisation curve for WS_TS.
(b) Magnetisation curve for WS_BS.

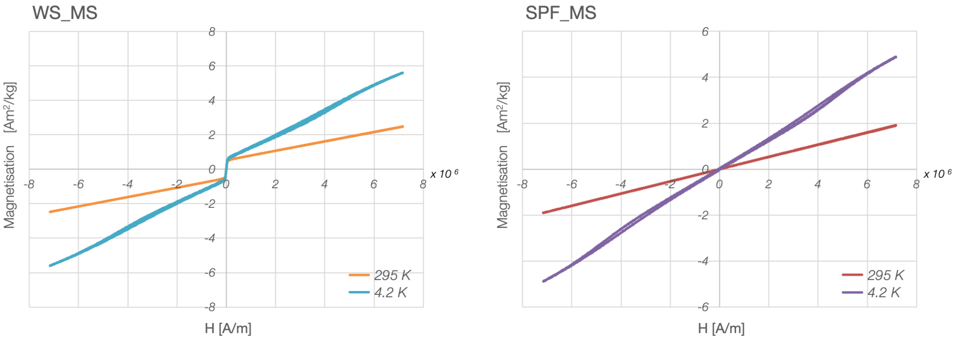

(c) Magnetisation curve for WS_MS.
(d) Magnetisation curve for SPF_MS.

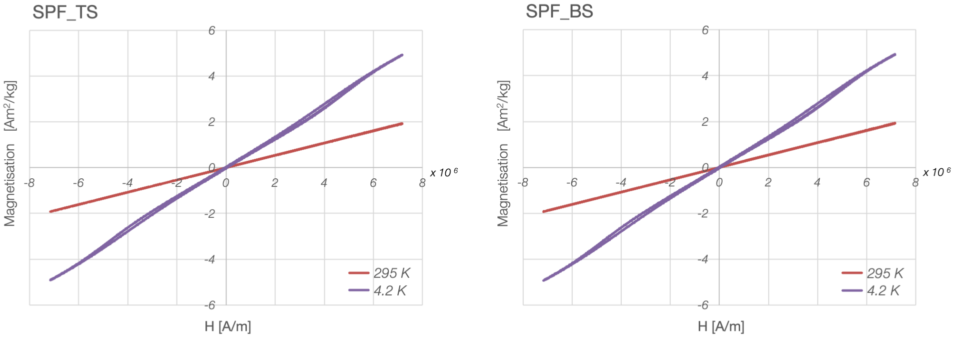

(e) Magnetisation curve for SPF_TS.
(f) Magnetisation curve for SPF_BS.

Figure 5.3: Magnetisation curves. Magnetisation, M, as function of the external field, H, for the three measured zones of the WS and the SPF forgings, respectively.

Where the SPF forging demonstrates a linear magnetisation for all of its tested slab regions (middle, top and bottom), the WS forging shows a magnetic susceptibility which is not constant over the measured range. The linearity observed for the SPF forging samples, is consistent with a fully austenitic stainless steel structure anticipated.

The curves for the WS forging rise some concern. The characteristic shape of the curve, as described in section 5.1, points towards a ferromagnetic material, even though limited. The sudden increase in magnetisation, M, at lower field is remarkable, while subsequently a flattening towards the pronounced linear behaviour similar to the one observed for the SPF forging is seen. We can anticipate the presence of ferromagnetic domains, i.e. ferromagnetic phases, present in the material. Still we can consider the WS forging a soft magnetic material, as no large effect of retentivity is observed.

The origin of the magnetic phases is yet to be determined, with reference to the micrographs in figure 5.4. These micrographs represent the search for secondary phases, performed initially with the use of a Murakami etching procedure, according to ASTM E407. Immersion of the specimens in a fresh, hot solution, stains carbides black, δ-ferrite in yellow and σ-phase in blue. The micrograph, presented in figure 5.4a, shows the presence of δ-ferrite bands in the microstructure, seen from the yellow stringers. A subsequent etching with an oxalic acid solution, initially aimed to determine sensitisation, or in other words carbide formation at grain boundaries rendering the material susceptible for intergranular corrosion and embrittlement, shows even more clearly the segregated lines of δ-ferrite present in the WS microstructure. The origin of the ferromagnetic domains is in the form of δ-ferrite, thus rendering the WS forged structure not fully austenitic.

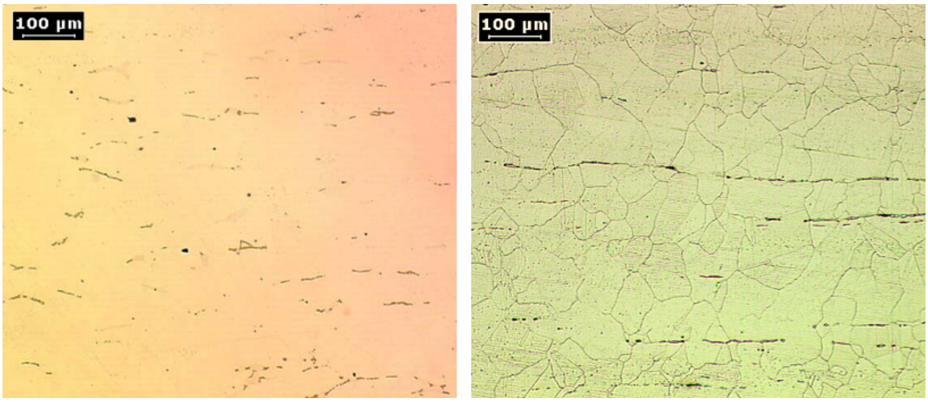

(a) Micrograph of the WS slab after Murakami etching. Direction of maximum flow is here horizontal, original magnification 100 x.

(b) Micrograph of the WS slab after Oxalic acid etching. Direction of maximum flow is here horizontal, original magnification 100 x.

Figure 5.4: Micrographs of the central area M of the WS slab, following Murakami etching (a), staining for the presence of particular secondary phases like δ-ferrite (yellow), and following Oxalic acid etching (b). In both cases δ-ferrite stringers appear to be present in the WS slab's central region.

With reference to the modified Schaeffler-Espy constitution diagram in figure 3.1 in section 3.1 this presence of δ-ferrite can be explained. Even though from this diagram the ferrite formation was not anticipated, its formation is not startling. Where the diagram is in principle developed for a weld, the Espy modified diagram is conservative for a wrought material. One can imagine that as a result of the considerable amount of material to be cooled in the process of large forging operations, ferrite formation for a heat lying so close to the first ferrite line would therefore not be unimaginable. This observation, combined with the fact that a diagram as such is merely an indication of the phase behaviour of a material, leads to the statement that both F XM-19 heat and its processing results in unsought products.

The presence of the δ-ferrite phase in the austenitic microstructure of the WS prototype then evidently also leads to the observed magnetic permeability of the material. Figure 5.5 shows the relative magnetic permeability determined for either prototype, at the top, middle and bottom of the slab, over the full measurement range of 4 K to 300 K. Take note that the results for the WS slab in figure 5.5a are presented on a different scale than the ones for the SPF slab in figure 5.5b. The significantly higher relative magnetic permeability of the WS prototype forging with respect to those of the SPF prototype forging, over the full range of measurement temperature is evident. Where the WS' relative magnetic permeability lies between a hundred to a tenth above the relative magnetic permeability of vacuum, the relatively magnetic permeability of the SPF slab is found to be a factor ten lower.

In addition for the WS slab, even though fairly constant over the full temperature range, a discrepancy is present between the three measurement positions. Where both the bottom as well as the top of the slab region hold a relative magnetic permeability below 1.05, the central region shows a value much higher between 1.15 and 1.20. This is consistent when considering the region most prone to the observed segregated secondary phases as seen in figure 5.4. Segregation is far more likely to occur in the central region of a large forging structure, for the mere reason that cool down time during forming is at a far lower rate then occurring at its surface, leaving time for the necessary diffusion.

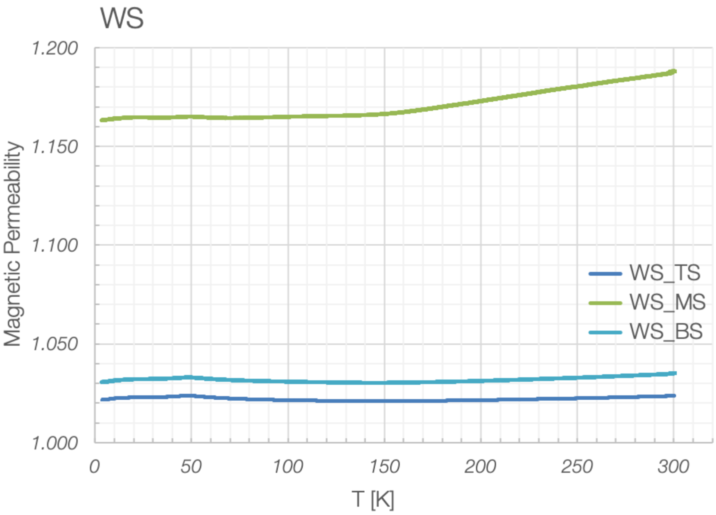

(a) Magnetic permeability curves for all measured locations in the WS prototype.

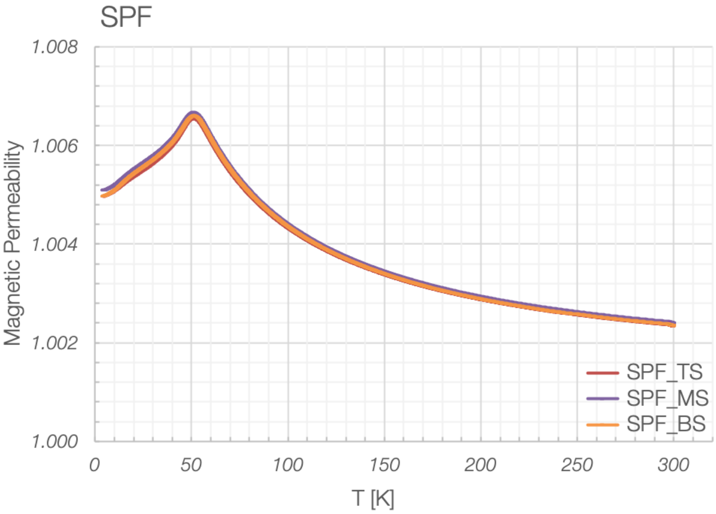

(b) Magnetic permeability curves for all measured locations in the SPF prototype.

Figure 5.5: Magnetic permeability as function of temperature for the WS prototype (a), and the SPF prototype (b). Note that the y-axis values differ, and that where for the SPF prototype values well below the required limit ($\mu_r \leq 1.030$) are measured, for the WS prototype most of the regions present values exceeding this limit.

Where the WS prototype's slab presents values unsolicited for a structural application in high-field magnets, the relative magnetic permeability values not exceeding 1.007, as obtained for the SPF prototype are within expectation. Table 5.2 denotes the expectations for a F XM-19 obtained from literature [Collings, 1980], which is essentially austenitic as can be deduced from the presented values.

Table 5.2: Characteristic relative magnetic permeability for F XM-19 [Collings, 1980].

Temperature [K]	Relative Magnetic Permeability, μ_r
295	1.0021
250	1.0022
200	1.0025
150	1.0028
100	1.0035
50	1.0053
33	1.0073
15	1.0060

In summary, the SPF slab forging represents magnetic properties preferential for the application, while the WS slab forging denotes values exceeding requirements, where ITER requires a relative magnetic permeability not exceeding 1.030 [ITER Organisation, 2017].

6

Prospect of F XM-19 for heavy-gauge forgings

The study presented here yields a complete and practical view of the relatively unknown material F XM-19 for use in a magnetic environment. Following a full-scale production of two tie plate prototypes from two different material heats and two different manufacturing approaches, we can now draw well-founded conclusions regarding the material's potential and anticipate on its performance in heavy magnet structures operating under most stringent conditions.

Considering its theoretical suitability, based on an extraordinary tensile performance while maintaining a valuable behaviour when imposing a flaw, the material holds great possibilities. F XM-19, even under extreme conditions holds up its end of the bargain, presenting mechanical properties generally outreaching the ones of 316LN, currently mostly used for structural elements in a low temperature, high magnetic field environment. When using F-XM-19 great care is nevertheless required regarding the employed heat and pragmatic processing.

The present chapter holds the conclusions drawn from the study on F XM-19's suitability for heavy-gauge forged structures envisaged for high-field magnetic structures. This is followed in the second section of the chapter by some thoughts on how to improve the process of material selection and processing for as-said structures.

6.1 Conclusion of F XM-19's performance under stringent conditions

For the ITER central solenoid pre-compression structure, two full-scale tie plate prototypes were successfully produced out of F XM-19, following two different manufacturing approaches.

F XM-19 forging of such complexity and size was proven feasible without major issues throughout the process. For both prototypes, the forged base material exhibits tensile properties exceeding the reference ambient temperature ASTM A182 specifications of $R_{p0.2} \geq 380$ MPa and $R_m \geq 690$ MPa for forged XM-19 for both head as well as slab forgings. Room temperature tensile properties fall in the range of 390 MPa to 420 MPa, and 720 MPa to 760 MPa for $R_{p0.2}$ and R_m, respectively, with a measurement uncertainty of 1.8% to 1.9%. Tensile properties tend to increase with a significant amount from ambient temperature to 4.2 K, towards 1140 MPa to 1310 MPa, and 1670 MPa to 1740 MPa, for $R_{p0.2}$ and R_m, respectively, with a measurement uncertainty of 1.9% to 2.2%. The mechanical properties reported are unseen to date for bulk austenitic stainless steels operating at low temperatures, where $R_{p0.2}$ does not exceed 950 MPa.

For the slab of the forgings, in both prototypes, tensile properties were found to be some 2% to 5% higher compared to the head of the forgings, consistent with the smaller grain structure observed in this region. A discrepancy of approximately 1% is observed in the tensile properties of the bottom of the single piece forged head with respect to the top of the single piece forged head. Together with the observation of locally large grains in the bottom of the head, this leads to the assumption of locally applied heat during the forging process, from which grain growth occurs, directly affecting mechanical strength.

As a result of the 316LMN filler material selected, of generally lower strength than the F XM-19 base metal, the joint of the welded prototype features a tensile strength value under the minimum requirement for qualification, which requires a performance better than or equal to the base material. ASTM A182 requires an R_m of at least 690 MPa, where the weld features an R_m in the range between 610 MPa and 670 MPa. In addition, the fatigue crack growth rate in the joint of the welded structure increases considerably faster with increasing stress intensity with respect to the base metal forgings, by a factor 2 to 3. Moreover, its fracture toughness as function of $R_{p0.2}$ lies below the NIST trendline for austenitic stainless steel base metals, according to which this weld is certified.

Fracture toughness of the forgings is a characteristic to be taken into account. Materials are rarely without flaws, and a flaw can easily decrease performance to a state where the material turns not applicable. This is not the case for the forged XM-19 prototypes presented in this study. Whereas a difference is observed with respect to 316LN, extensively employed for structural elements, although generally not in alike size, the behaviour of the F XM-19 forgings is still more than sufficient for the application. 4.2 K requirements hold a K_Q of at least $130\ \text{MPa} \cdot \sqrt{\text{m}}$. Even though the elasto-plastic, non-linear crack propagation behaviour studied can not be completely described by K, K_Q values derived from J for the forged structures surpass the 4.2 K requirement. K_Q data holds a range between 200 MPa $\cdot \sqrt{\mathrm{m}}$ and 250 MPa $\cdot \sqrt{\mathrm{m}}$ for the forged material in the most critical LS-direction, thereby exhibiting almost twice the required value.

With the latter one needs to take into account observed directionality of the forgings, resulting in the derivation and application of a new compliance function for the calculation of the fracture toughness of some measurement locations in the form of:

$$C_{LL} = \frac{1}{EB_e}\left[340.1\left(\frac{a}{W}\right)^2 - 329.6\left(\frac{a}{W}\right) - 131.1\right] . \qquad (6.1)$$

The directionality, situated in the preferential direction as it inhibits principal crack propagation, causes no direct threat to the functionality of the item. Such directionality, however, is worrisome and needs to be closely monitored.

Magnetic measurements were performed to confirm the suitability of the material in high magnetic field. Although the heavy-gauge forging of the single piece forged structure showed the preferred fully austenitic structure, in the welded structure some δ-ferrite segregated lines were detected, affecting negatively the magnetic properties. Where for the single piece forging a maximum relative magnetic permeability of 1.007 was obtained over the full measurement range of 4.2 K to 300 K, a maximum relative permeability of 1.19 was obtained for the welded forging. Either forging process, material heat, or both could account for the presence of the secondary phase. This leads to the conclusion that specific designs of material and process are essential in order to avoid low-temperature embrittlement and insufficient magnetic properties. Where the embrittlement is indicated by the low fracture toughness K_Q of 120 MPa $\cdot \sqrt{\mathrm{m}}$ of the welded structure material in the SL direction, denoting crack extension along the longitudinal direction, i.e. along the direction of the observed secondary phase stringers.

This leads to the overall conclusion that, in view of the study presented here, the F XM-19 material provides high potential for large-size structural items in a low-temperature, high-magnetic environment. However, in order for the forged XM-19 item to perform best, specific recipes need to be followed for the steelmaking and subsequent thermo-mechanical processes.

6.2 Recommendations for the optimisation of F XM-19 forgings

When adopting F XM-19 in the complex fabrication of these one-of-a-kind items, operating in an environment a material is not often exposed to, one must, indeed reach for a tailored solution. F XM-19 in its sort does not necessarily indicate suitability, which has become undoubtedly apparent in this study. Where the type F XM-19 allows for a range of grades, with the complexity of forming of idem items one needs to take care of processes resulting in secondary phase formation. Forging steps must allow for quick cool-down, even of core regions, and intermediate cooling or local reheating during hot forging steps needs to be limited.

Material dependability on production process can be reduced by employing a facility with greater competences in both logistics and hard-ware. Consequently, additional intermediate reheating of the entire piece will reduce chances of diffusion and secondary phase formation, followed by the reduction of internal stresses resulting in the strain orientation as observed excessively in the single piece forged structure. Severely deforming the material, at reduced temperatures, results in the introduction of flaws in the material matrix. Flaws introduced of micro or macro sort, pushes the material behaviour towards its lesser performance with respect to a 316LN. A study of mechanical measurements, with the aim of determining internal stress during the forging operation, can shed light on the forging process and possible additional adjustments to the procedure.

Besides optimising steps in the fabrication process that could increase F-XM-19 predictability on a full-scale setting, one must also reach for the optimal composition of the material. We have noted that a material, only marginally on the border of a fully austenitic structure, could lead to issues both in embrittlement, as well as its obvious problems in terms of magnetisation. The design of an F XM-19 heat for heavy-gauge structures must therefore comprise targeting an austenite promoting balance of constituents. One must aim for a tailored manganese and nickel content, towards the upper limit of the standard, with the use of nitrogen, while reducing the chromium equivalent, comprised by mainly chromium, molybdenum and silicon.

While the main focus lies on the suitability of the forged XM-19 material, its translation to the application, and optimal fabrication route plays an equally important role. The overall fabrication of the item; the central solenoid tie plate, is presented by two solutions. Whereas challenges were observed with the fabrication of both currently presented solutions, a preference is directed towards the single piece forged structure. A weld of the magnitude as necessary for the welded structure comprises major challenges. Whereas forging operations for a welded structure are more straight forward, major changes must be implemented in the welding process to render this solution a suitable ’back-up’.

The welding procedure itself is not a direct emphasis in this study, therefore in-depth details are not included here. However, the observed mechanical response of the weld could be largely accounted for by weld defects introduced during the weld process. An extensive welding study, altering weld types, procedures and even filler metals must be performed to determine the feasibility of a welded structure for the fabrication of the 15 m long tie plates. For the current application, however, only minor adjustments, and proper monitoring of heat and process could result in a much more elegant single piece forged structure.

Part II

Explosion-welded connections in ITER-type load-bearing electrical joints

7

Issues with copper to stainless steel connections

> ***Whether you function as welders or inspectors, the laws of physics are impeccable lie-detectors. You may fool men. You will never fool the metal.***
>
> — **Lois McMaster Bujold**
> (American writer)

Where a structure requires a multitude of functions; in the case of a joint both mechanical resistance and electrical conductivity, complications arise when employing a single material. The terminal joint, as presented in section 1.2.2, relies on both structural and conductive properties of a material. For this, use is made of a bimetallic box. A tight mechanical link is essential between the conductive copper terminal cladding and the structurally fit stainless steel base, whilst avoiding degradation of the conductive properties.

We search for a made-to-measure connection between two rather contrasting materials both with their specific function. Even though a full qualification of such a bi-metal would comprise a full study of either metal employed, here the emphasis is primarily on the quality of the connection itself, where the effect of the joining method on the material characteristics of either part of the bimetallic box is dealt with.

In the present chapter the challenges are introduced when targeting two widely varying material requirements. The two main joint functions are described and its related selection of materials. Issues with bonding the two highly varying materials is briefly explained. Explosion welding is suggested and its process and functionality explained. Finally a listing of the bimetallic plates employed for the study is presented.

7.1 Introduction

A joint to connect unit lengths of superconducting coils or to ascertain a link to electrical terminals, as described in section 1.2.2, is required to fulfil both electrical and mechanical requirements not easily found in a single material. Its mechanical function needs to satisfy a performance exhibiting an $R_{p0.2}$ value of $\geq$180 MPa and an R_m of 240 MPa to 300 MPa to withstand axial and radial forces resulting from the produced high-magnetic field. Its electrical function on the other hand requires a current transfer for which a 4.2 K resistivity of the current carrying element is targeted between 2.3 $n\Omega$m and 3.7 $n\Omega$m. This relates to a Residual Resistivity Ratio (RRR) of some 5 to 8 when considering a room temperature electrical resistivity of 18 $n\Omega$m. To ascertain a current transfer as such, the hardness of the element may not surpass 95 HV, for the realisation of a low resistance connection between the cables and the current carrying joint member which is done by compaction. Here the requirements are reported for the joints of the PF coils, introduced in section 1.2.2 which holds the most stringent requirements in terms of mechanical properties [Dalmut, G., 2005]. Magnet systems using joints operating in direct current mode can on the other hand hold resistivity requirements of up to an RRR value of 100 [ITER Organisation, 2014].

As a result of the stringent conditions imposed by the application, a joint fabricated from a bi-metal is suggested. Either part of the bi-metal bears one of the two main functions. Austenitic stainless steel is selected to support the mechanical function of the joint, whereas copper carries its electrical function.

7.1.1 Copper selection

As a result of transient magnetic fields during coil operation, eddy currents are induced in the copper sole of the bimetallic box leading to Joule-heating, hence causing a reduced superconductor stability margin [Ciazynski et al., 2002]. The use of a low-purity copper cladding, featuring a low RRR, can therefore be efficient to increase loop resistance and reduce the induced currents. On the contrary, low-resistance current transport through the copper side of the bimetallic box is essential, for which a high-RRR copper is beneficial. Obviously a compromise is needed between these two conflicting requirements. The copper selection is therefore depending on its application and specific operating mode, primarily alternating or direct. The present study therefore implements both, a range of high-purity copper alloys as well as a low-purity copper as can be used for the application.

OF(E) copper

Commercially available high-purity copper exists up to a pureness of $99.999^{+}\%$, relating to a room temperature resistivity ρ, of a mere $1.68 \cdot 10^{-8}$ Ω m in soft (annealed) state. The high-purity copper is obtained in a final production step by electrolytic purification. In the electrolysis the impure metal obtained by concentration of the copper from the ore, is placed at the site of the anode, while the cathode contains a pure variant of either copper, stainless steel or titanium. With the electrolytic process, assisted by the electrolyte, generally a copper sulphate, a deposition of copper ions on the cathode takes place while impurities remain either in solution or end up as slack [Davis, 2001].

A commercial pure copper making use of this process is Electrolytic Tough Pitch (ETP) copper, which after the electrolytic refining process undergoes an additional remelting and oxidation process, to reach a controlled low-content oxygen 'tough-pitch' condition. ETP copper, or UNS C11000, then contains a minimum of 99.9% Cu, relating to an electrical resistivity of $1.72 \cdot 10^{-8}$ Ω m [Aurubis, 2013].

A minor oxygen concentration though, can result in major issues, mainly when considering weld- and brazeability. Cu-DHP, or C12200 deoxidised, oxygen-free, high phosphorus content copper, is a counterpart of the ETP copper. Where the UNS naming for Cu-DHP is C12200. Use of this material resolves issues with oxygen remnants, equally in terms of oxygen induced hydrogen embrittlement. The high-phosphorus content to deoxidise the material, however, disturbs on a high level the material's conductivity. Phosphorus is an addition which could equally endanger the high-vacuum environment as a result of its volatility.

An expression of the intrinsic resistivity of a metal based on specific assumptions, is the Bloch-Grüneisen formula:

$$\rho_i(T) = \frac{C}{M\theta}\left(\frac{T}{\theta}\right)^5 J_S\left(\frac{\theta}{T}\right), \tag{7.1}$$

where T is the temperature, θ the electrical resistivity Debye temperature (related to the maximum frequency of a crystal's lattice vibrations), M the atomic weight, C a constant and J_S a transport integral as result of a temperature shift.

The intrinsic resistivity tends to zero exponentially as the temperature goes to the absolute zero, related to the 'freezing' of the lattice [Matula, 1979]. With the presence of impurities, however, in the case of C12200 the high phosphorus content, additional scattering points are present, resulting in an increase in resistivity. The different types of impurity atoms will make independent, additive contributions to the resistivity, each increasing with concentration c, of the particular impurity. This residual resistivity, ρ_0, is to first approximation independent of temperature, and the total resistivity can now be written as:

$$\rho(c, T) = \rho_0(c) + \rho_i(T). \tag{7.2}$$

Equation 7.2 is known as Matthiessen's Rule. This equation gives a general idea of the additivity of resistivity contributions from different sources, therefore it can be equally applied to other sources of scattering such as lattice imperfections (for typical types of scattering sources see section 11.2). Note that some deviations from Mathiessen's Rule can exist, which can be seen from non-linearity in a $\rho - \rho_0$ as function of $\log \rho_0$ plot for a single value of T, and is defined as:

$$\Delta(c,T) = [\rho(c,T) - \rho_0] - \rho_i(T). \tag{7.3}$$

Amongst this, magnetoresistance has an effect on the simplified Matthiessen's Rule in equation 7.2, where a transverse magnetic field negatively affects in a quadratic manner the material's resistivity. At low temperatures down to 4.2 K at increased magnetic fields the affect approaches linearity [Launey, 1959]. The absolute effect is nevertheless observed to be again dependent on the metal's purity [Kapiza et al., 1929].

In figure 7.1 the conductivity in $10^6\ S/m$ is given, from which the total resistivity, ρ, can be obtained by taking the inverse (conductivity, $\sigma_{[S/m]}$, equals ${}^1/_{\rho\ [\Omega m]}$) for a range of impurities in copper [Copper Development Association Inc., 2020]. Note from this figure that the additive contribution in Matthiessen's rule with concentration c in equation 7.2, varies for different impurity atoms, where a phosphorus addition implies a major contribution. Furthermore, one can see that with low-impurity additions, whether the impurity addition has a major or minor contribution, relatively, an elevated effect is noted on the electrical conductivity. I.e., even with low phosphorus additions, as in the case of the C12200 alloy (P 0.015 - 0.040), major contributions to the electrical resistivity can be expected.

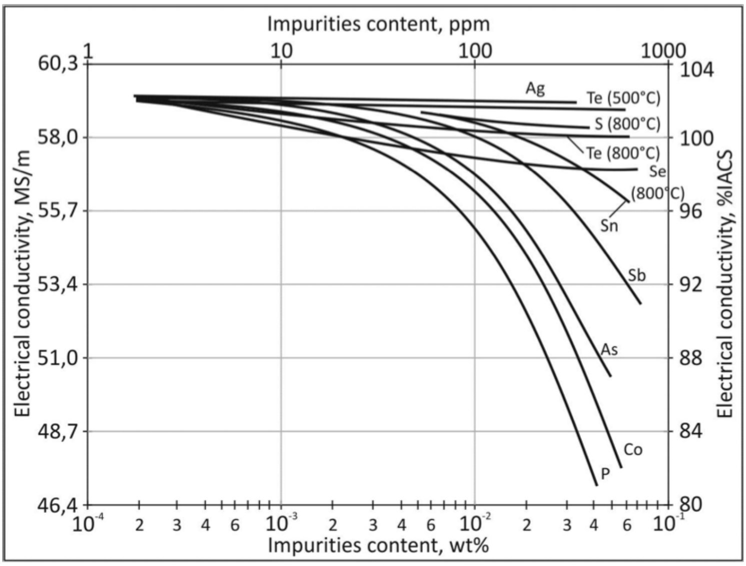

Figure 7.1: Influence of impurity additions on the electrical conductivity of oxygen free electrolytic refined copper. The second y-axis represents the remaining conductivity following impurity additions in IACS[1] [Smart et al., 1943].

---

[1] Relating to a 100% IACS for annealed commercially pure copper with a resistivity of $1.72\ x10^{-8}\ \Omega\ m$ (for an extensive explanation see section 11.4.2).

Oxygen-free, High Conductivity Copper (OF or OFE) or the UNS C10200 - C10100 alloys, with a minimum of 99.95% to 99.99% Cu, respectively, offer the advantages of both the Electrolytic Tough Pitch Copper (ETP) - C11000 and the Phosphor Deoxidized Copper (DHP) – C12200 alloy. The UNS C10100 to C10200 series are high-purity, oxygen-free, non-phosphorus-deoxidised coppers that do not contain in vacuum evaporating elements. They feature a very high electrical and thermal conductivity and exhibit a high ductility accompanied by a high impact strength [Copper Development Association Inc., 2020], essential for electrical joints.

The advantage of high-purity copper grades stretches beyond the apparent low resistivity for which the UNS C10100 is clearly the preferred candidate. Its high ductility and ’softness’ in annealed conditions also leaves for advantages in cable to sole connection. Soft materials, however, hold the disadvantage of possible local yielding at increased stress. The high-current superconducting cables embedded in the bi-metal can introduce high loads on the surrounding component of which the copper is a direct neighbour. Local yielding of the copper can result in strand movement and correspondingly normal zone generation and propagation in the material. Where ’soft’ or low yield strength coppers can be beneficial for the application, they can also form a pitfall.

The suitability of several copper grades is therefore assessed, ranging from the low-purity C12200 to the high-purity C10100 copper grade.

7.1.2 Stainless steel selection

The two austenitic stainless steel grades employed for this study are AISI 316L and AISI 316LN, both suitable in a cryogenic environment and essentially non-magnetic, see section 2.2.1. The stainless steel base is subject to less demanding requirements, which are generally fulfilled by a standard AISI 316L and AISI 316LN. The base metal itself is therefore of reduced interest in this study. The focus regarding the stainless steel side of the bi-metal is concentrated on its weldeability discussed in section 7.2.2.

7.2 Achieving a fitting bond between two highly varying materials

Where a typical metallic connection is made with use of a welding technique, for the here presented case some difficulties arise. The materials selected; low-carbon 316 type austenitic stainless steel 316L and 316LN, and various copper grades, are generally materials which have the ability to be joined by a welding technique. However, as the weld pool contains highly dissimilar materials, the metallurgy of the weld can drastically differ from the base materials, making the welding process more challenging. This can result in differences in the individual material behaviour as well as in the characteristics of the connection.

In essence, a welding process based on liquid fusion, requires for both metals to have similar melting points. This is not the case for stainless steel and copper, where the latter has a melting point 1.3 times higher. Welding energy is required to be a considerably higher for the copper, than needed for the stainless steel. This is resulting from the discrepancy in melting point and furthermore the difference thermal conductivity. The design of the joint must consequently be adapted to the welding process. When welding from the copper side, or simultaneously through both, the high amount of energy will result in a larger than normal heat affected zone, and thermal distortions. As the high energy comes though the stainless steel, its magnitude can cause voids and blow-outs, and large weld shrinkage can result in weld cracking.

Welding through the stainless steel first, proceeding to use a lower amount of energy for the fusion of the stainless steel into the copper, results in using copper as a heat sink. With this process one is essentially creating a stainless steel weld into the copper, resulting in liquefaction problems at the copper side. The resulting material properties of the copper will consequently become highly unreliable. Considering the long and wide connection area in the joint boxes, achieving a high level of super-fluid helium leak tightness is a main issue.

For any dissimilar joint, metallurgical processes arise with low predictability in both the connection itself as well as the parent metals. A way to circumvent this, is to make use of a solid state welding process not relying on the melting of the materials to be joined. A solid state process like explosion bonding, does not require for the materials to have a similar melting point as the bond is created with use of atomic diffusion and mechanical deformation, generally realised by imposing high levels of deformation.

7.2.1 The process of explosion bonding

The process of explosion bonding, or explosion welding, offers the option to deploy a wide range of materials in a single comprehensive design, as required for the twin-box. Dissimilar metal transitions can be used for structural elements where a tight connection is required while reducing transitional regions, detrimentally affecting the materials' properties.

The history of explosion bonding has its origin in the war, where explosions resulted in shrapnel 'welded' together. The process is found to result from atomic diffusion between the base material and its cladding, following from large deformation in the transition region. It was in 1964 commercialised by DuPont, under the name of DetaClad® [Nobelclad, 2020; Blakely, 2010].

The market of the explosion bonding technique depends on the joining of highly dissimilar metals, where cladding materials are for example stainless steel, nickel, copper and aluminium. Even very hard materials like tantalum and titanium can be joined with this process, with use of a 'softer' intermediate metal to guarantee deformeability. Explosion welding is not only a solution for the welding of materials with varying melting points, but also for materials with a difference in thermal expansion and a large variation in hardness. As the process is most instantly no significant bulk heating arises during the process, omitting typical accompanying chemical processes.

In the explosion welding process the harder material, generally of higher thickness is used as a stationary base plate, called the backer. The softer cladding material, the flyer, often under an angle, is driven into the backer with high force by detonation of an explosive (figure 7.2). The high pressure, necessary to realise the atomic bonding of the materials, is developed near the collision point, and is the most important parameter to be controlled.

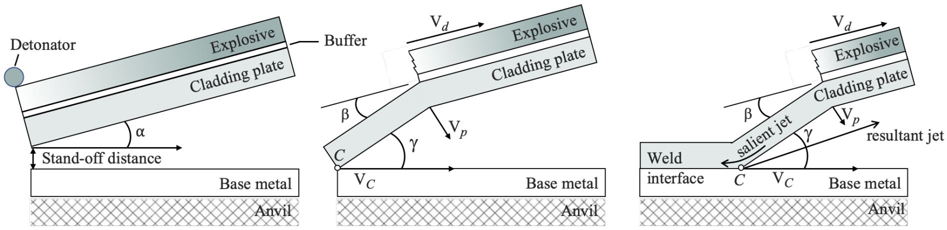

Figure 7.2: Schematic representation of the set-up of the explosion bonding process, where an explosive in sheet, granular or powder form is detonated from one end, rolling along the surface of the cladding plate while driving it into the base metal plate.

The to be bonded plates are extensively ground and cleaned to reduce impurities along the transition area. The subsequent positioning of the plates with a small intermediate spacing, the stand-off distance, determines the angle and velocity of the impact and the consistency of the running jet.

The imposed energy at the surface where the flyer meets the backer is a product of a variety of parameters, amongst which the impact angle, and the type and amount of explosive, determining the speed at which the explosion runs along the cladding's surface. The process depends on the oblique high-velocity impact between the two plates. The flyer plate is commonly placed at an angle, α, with respect to the backer, as can be observed from figure 7.2. With the passage of the explosive at the surface of the flyer plate (or buffer) at a velocity V_d, its impulse transmits a velocity V_p to the flyer plate, which the flyer plate holds until collision with the parent plate. From figure 7.2 we can derive that V_p stands to V_d in the form of $V_p = V_d \sin\gamma$, where γ is the resultant angle between the initial flyer angle, α and the effective angle of incidence of the impacting plates, β.

Upon impact of the flyer plate the pressure is of such high magnitude that the shear resistance of the two materials becomes negligible, resulting in a non-viscous compressible fluid behaviour of the materials in the vicinity of the point of impact, dividing the material into two jets. A main, salient jet develops in the direction pointing towards the initiation region, accompanied by a resultant, re-entrant jet in opposite direction. As the main jet divides, the highly energetic resultant jet at the interface between the backer and the flyer expels any oxides and small amounts of base material, thereby removing any bond-inhibiting surface films. The high pressure following from the impact results in a mechanical weld, which can exhibit intermetallic phases resulting from atomic diffusion. The intermetallic phases can be either beneficial or detrimental for the weld depending on their composition; i.e. of the brittle or ductile type.

Essential for a proper explosion bonding is the capability of the collision to create a sweeping resultant jet, where the velocity V_p is sufficiently high to generate the required pressure for the existence of the resultant jet. The resultant jet is required to ensure efficient removal of the surface film on either side of the to be bonded plane, realised by a hump formation leading the collision point. This hump is formed under the condition that ${}^{V_p}\!/_{\sin\beta}$ is smaller than the velocity of sound in the backer material [Crossland, 1982]. Moreover, the formation of the resultant jet is dependent on the angle of impact. A critical angle of impact exists below which a resultant jet is non-existing. Generally this angle is already initiated by the placement of the flyer plate under a starting angle (figure 7.2). However in the case of large plates, as is the case for our application, the parallel placement of the flyer plate with respect to the parent plate holds great advantages as is depicted in figure 7.3.

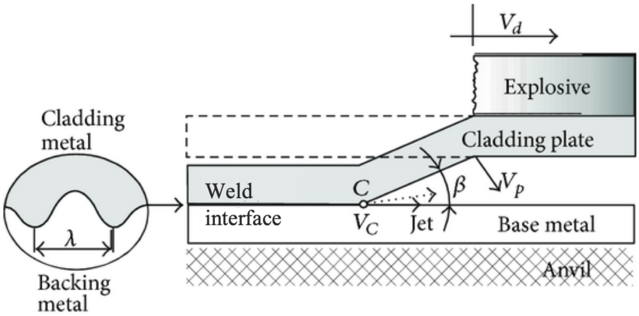

Figure 7.3: Schematics illustrating the parallel explosion bonding set-up as often used for larger plates, showing the situation at the impact zone during a rolling explosion [Wronka, 2014].

The effective angle β becomes equal to γ as α is eliminated, making the equation denoting the collapse of the flyer plate in the form of $^{V_P}/_{V_d} = \sin\beta$. From the latter we can derive that if the detonation velocity is less than the velocity of sound in the materials to be welded, and the values of V_d and V_p are such that the angle β becomes higher than the critical angle for the formation of a resultant jet, the plate can be welded in such a configuration. This condition is adjustable with the use of amount and type of explosive, together with a correct stand-off distance for the materials employed [Crossland, 1982; Bahrani et al., 1967].

The formation of the 'turbulent' interface region upon the formation of the hump in the parent material, and the salient and resultant jets can be observed in figure 7.4. The wave formation at lower impact angles, as is the case with parallel positioned plates, can be described analogous to the Von Kármán vortex shedding mechanism [Kowalick et al., 1971]. At higher velocities the resultant jet does not remain stably positioned between the two plates, but starts to oscillate. This oscillation at a certain magnitude, starts to interfere with the incoming flow, as can be observed from figure 7.4, resulting in alternating vortices in the flyer and base plates, respectively. The parent plate is deformed by the momentum of the resultant jet, generating this initial hump. Subsequently the resultant jet, when moving towards this hump, is redirected upward, until the moment exists when the resultant jet becomes completely entrapped. Following is the impact of the flyer on the top of the wave, from which a tail is formed, after which a re-entring jet will fill up some of the gap underneath the tail while starting to form the next hump and thus wave.

It was found by [Carton, 2004] that the existence of this analogy with the Von Kármán vortex shedding mechanism depends on employed materials and impact angle. In his study he discovered that for a stainless steel parent plate with a copper flyer a Von Kármán vortex street exists with increasing amplitude and wavelength at an impact angle up to some $20°$ after which wave formation disappears. The latter can be accounted for by the fact that the jet is able to fully escape the space between the flyer and parent plate, without hindering either.

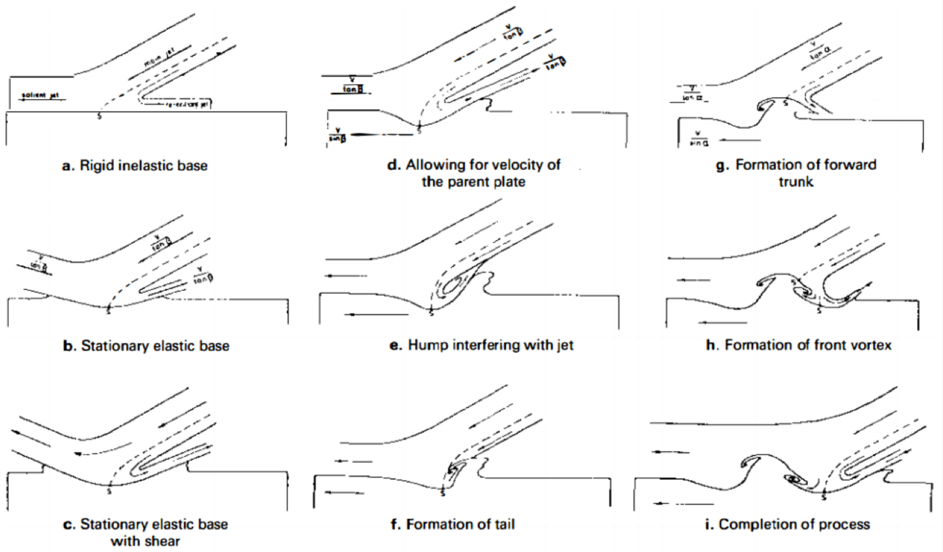

a. Rigid inelastic base

d. Allowing for velocity of the parent plate

g. Formation of forward trunk

b. Stationary elastic base

e. Hump interfering with jet

h. Formation of front vortex

c. Stationary elastic base with shear

f. Formation of tail

i. Completion of process

Figure 7.4: Schematics showing the wave formation as observed for a successful explosion bonding, resulting besides a connection via atomic diffusion in an interlocked mechanical connection in the form of waves. The formation of the waves is chronologically described from subfigures (a) to (i) [Wittman et al., 1975].

It can be concluded that an optimum exists at which an initial mechanical interlocking mechanism takes place, in the form of a wave pattern, possibly relevant for structural benefits. This leads to the notion that while explosion bonding is a reliable and repeatable process, a small adjustment in a fair set of parameters can result in major changes in weld characteristics. In the case of our application, and its stringent requirements under cryogenic and high vacuum conditions, a small weld imperfection resulting from small adjustments in weld parameters can result in a poor mechanical connection or a loss of helium leak tightness.

7.2.2 Materials in function of the welding process

The choice of a mechanical joining process results in added material requirements for either side of the bi-metal. A certain ductility of both materials is required as to promote ’hump’ formation without encouraging fracture. On the contrary, a too high level of ductility could result in a decreased resistance of the parent metal plate with respect to the jet, resulting in Kelvin-Helmholtz instability wave formation [Carton, 2004], with an accompanied reduction in mechanical linkage and resulting loss in atomic diffusion.

The austenitic stainless steels, 316L and 316LN generally show sufficient ductility for the purpose as parent plate in an explosion bonding process. The effect of explosion welding on the characteristics of the structural stainless steel side of the bi-metal is expected to be negligible, and is therefore be of less interest in the present study.

A significant effect of the welding process on the copper side of the bi-metal is foreseen. Heat input is reduced with respect to a fusion welding process, which results in limited behaviour-altering metallurgical processes. Nevertheless, the high deformation implied by the explosion can result in extensive local hardening in the case of a 'soft' material. Emphasis in this study therefore not only lies on the welded connection achieved but also its effect on the copper characteristics.

Table 7.1 shows the employed bi-metal plates for the current study, where the different copper materials, employed for the production of the plate, are listed. Not only the copper grades differ in purity, but also its initial temper state varies. Some copper plates are in an annealed, i.e. 'soft', temper (here O25 according to ASTM B601) prior to explosion bonding. Others were used in the welding process in an as hot-rolled (M20 according to ASTM B601) or half-hard (H02 according to ASTM B601) temper.

Table 7.1: Material characteristics of the explosion welded stainless steel to copper bi-metal plates.

Plate designation	Plate thickness SS [mm]	Cu [mm]	Explosion welding Company	Supplier Cu base plate	Material SS	Cu	Temper[a]
Plate 1	65	14	Company B	Supplier A	316L	C10100[b]	O25[c]
Plate 2	90	20	Company B	Supplier A	316L	C10100	O25
Plate 3	73	18	Company D	Supplier C	316L	C10100	O25
Plate 4	98	24	Company E	Supplier A	316L	C10100	H02[d]
Plate 5	90	25	Company F	Supplier C	316LN	C10200[e]	M20[f]
Plate 6	40	12	Company E	Supplier G	316L	C12200[g]	N.A.

---

[a] applying to the copper plate only
[b] OFE Cu; oxygen-free, electronic copper according to ASTM B224
[c] hot-rolled and annealed according to ASTM B601
[d] half-hard state according to ASTM B601
[e] OF Cu; oxygen-free copper according to ASTM B 224
[f] as hot-rolled according to ASTM B601
[g] DHP Cu; phosphor deoxidised, high residual phosphorus copper according to ASTM B224

Material suppliers and explosion welding companies are designated, allowing to compare material behaviour of essentially the same material with different processes like a variety of plate thickness employed, or a difference in parameters. For commercial reasons, explosion welding parameters are withheld and the company names are concealed. Note that even though some of the copper base plates are made from the same grade, and are produced by the same manufacturer, they do not originate from the same heat.

Structural characteristics of a copper-clad steel plate

8

From the two aspects covered in this study; the explosion weld as such, and its effect on the copper cladding, this chapter covers the former. The structural aspect of the achieved welded connection of the various plates as designated in table 7.1 is examined in terms of mechanical characteristics. To ensure a suitable mechanical performance of the copper-clad stainless steel plate, a void free bonding between the conductive copper sole and the structural stainless-steel is aimed for. This will secure the structural integrity of the joint when submitted to the varying loads during magnet operation. A metal-to-metal transition area showing a Von Kármán vortex street pattern is targeted, showing interlocking cladding upon parent metal waves, combined with some layer of intermetallic compound originating from atomic diffusion by high local deformation.

Shear- and tensile behaviour of the explosion welds is examined, thereby assessing the interlocked state of the welded region. Sensitive measurements are performed following specific design of application driven measurement procedures. Divergent mechanical behaviour observed for the various plates examined is subsequently rationalised with use of optical means, in which the effect of parametrisation becomes apparent.

8.1 Research methodology

In terms of structural requirements, welds are required to perform equally or better than the fused material of lowest mechanical strength. The measurement procedure targets the determination of the bonding quality, with a quantification factor directing towards the bonded region not being the weakest link in the chain.

8.1.1 Mechanical performance measurements

Performance of copper-clad plates is advised to be primarily measured in shear, as noted in the standard for copper and copper alloy clad steel plates ASTM B432. It establishes the requirements for a copper or copper-based alloy sheet integrally and continuously bonded to one or both sides of a carbon or low-alloy steel base plate.

Shear measurements are performed at room temperature, as its measurement procedure is not suitable for measurements at 4.2 K. Additional mechanical testing in tension is implemented to ensure the explosion weld's integrity also at liquid helium temperature.

Shear measurement method

A shear measurement set-up has been developed for the present study. The measurement set-up is based on guidelines available in the copper-cladding standard, demonstrated in figure 8.1. With use of the compression system of a universal tensile machine (UTS testsysteme GmbH, 200 kN maximum load) a shear load is exercised at the welded region. Tests are performed at a speed of 1 mm/min until failure, applying a custom-designed tooling constructed of pre-hardened sp300 steel according to the standard (figure 8.2).

Accurate measurement of the shear performance of the weld requires a delicate specimen extraction from the bulk. The measurement of shear at the copper to stainless steel interface requires precise machining at an interface with a varying position in the bulk.

The specimens were carefully machined following ASTM standard B 432 by electro-erosion as not to alter the individual and bonding interface characteristics. In some cases the electro-erosion machining was succeeded by a fine low-pressure milling to ensure the measurement of shear characteristics specifically at the bonded interface. Correct specimen extraction reveals the dissected characteristic wave-pattern as can be seen in figure 8.3. Specimens are machined with their loading axis nearly parallel to the main axis of explosion bonding (figure 8.3 right). In the cases where the availability of the material allowed, additional specimens were extracted with loading axis perpendicular to the main axis of welding (figure 8.3 left).

Cross-head displacement of the UTS machine is employed for displacement measurements as the ultimate shear strength τ_{max}, is the single leading parameter. When not specified otherwise, the minimum shear strength of a copper-clad, stainless steel interface holds 84 MPa following ASTM B432, however, preferably exceeding the shear strength of the weakest of the two welded materials.

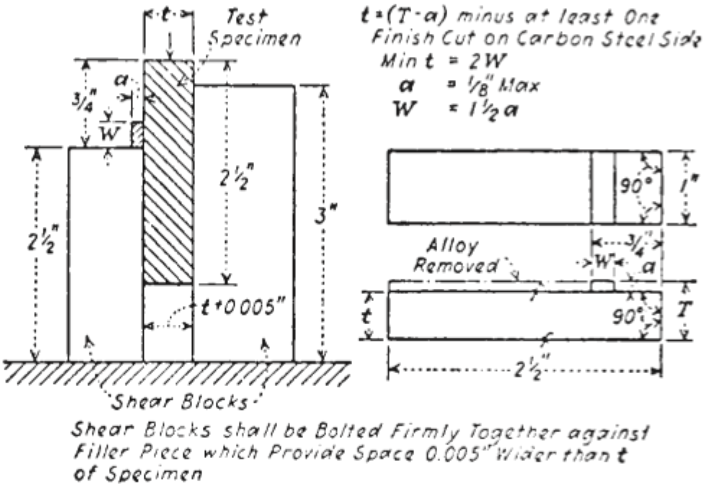

SI Equivalents

in.	mm	in.	mm
0.005	0.127	1	25.4
⅛	3.18	2½	63.5
¾	19.1	3	76.2

Figure 8.1: Schematic representation showing test specimen and method according to [ASTM, 2019] [1].

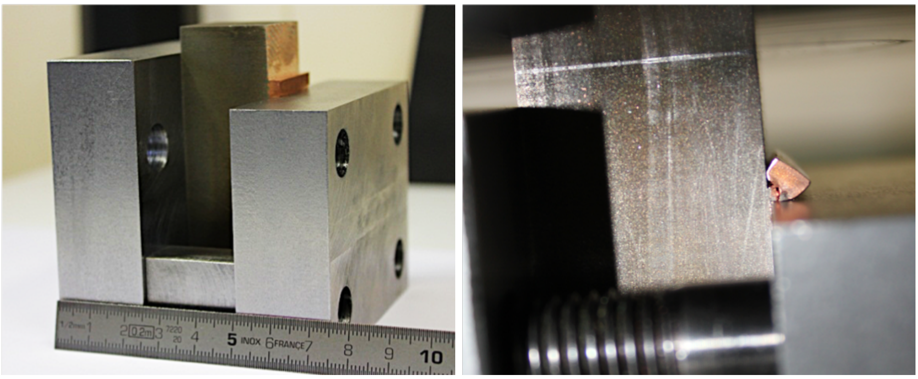

(a) Shear measurement tooling.

(b) Measurement set-up in operation.

Figure 8.2: Shear measurement set-up, constructed of sp300 pre-hardened steel (a). Shear is provoked at the copper to stainless steel interface, seen in (b).

---

[1] The shear test is not applicable when the specified minimum cladding is 1.9 mm or less, in this case an alternate bond strength test is recommended in the form of a three point bend test.

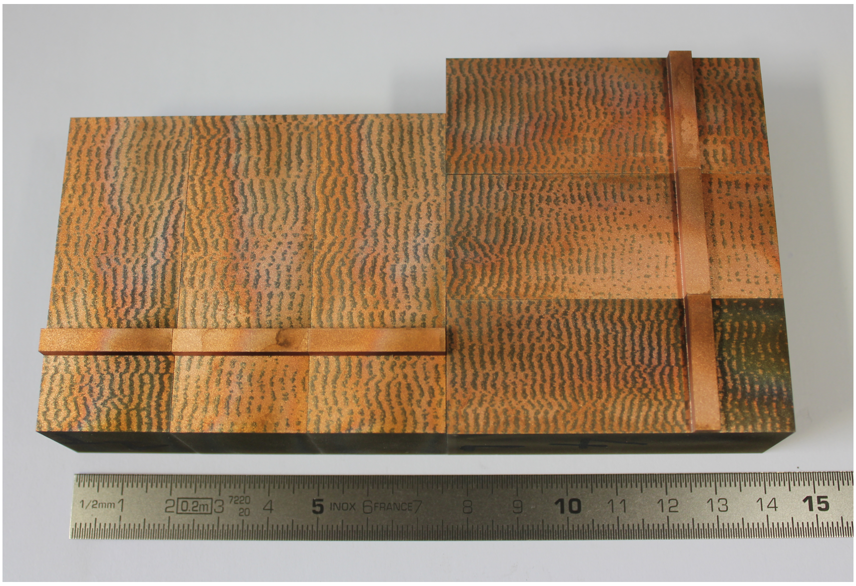

Figure 8.3: Machined shear specimens with loading axis perpendicular to (left), and parallel to (right) the direction of explosion welding. Specimens are carefully machined to ensure the shearing plane to coincide with the weld interface.

Tensile measurements as quality assessment

In the ASTM B432 standard for copper-clad stainless steel plate specification, tensile test are solely proposed on the base materials. Here presented are tensile measurements across the weld interface, at both ambient temperature as well as 4.2 K. Specimen dimensions and test method utilised can be revisited in figure 3.3 and section 3.2.1. The realisation of the sub-size specimens holds for the current study additional challenges. For an adequate measurement of the performance of the weld interface, the entire interface is required to lie within the gauge-length of the tensile specimen. For a copper-clad plate with only a 12 mm or 14 mm copper layer, additional copper strips were welded to the copper side of thin cross-cuts of the explosion welded plate, to guarantee the positioning of the original weld interface in the gauge length.

The added weld, however, shall not affect the measurements intended for the performance of the explosion weld. The secondary weld is placed in the head section of the specimen, leaving the reduced section unaltered. Electron-beam (EB) welding was applied to avoid modification of material characteristics in the gauge length. The electron beam has a very localised energy deposit. Little heat is dissipated throughout the rest of the material, resulting in a small heat affected zone, and thus no alteration of the earlier introduced explosion weld.

Specimens are removed with their long axis perpendicular to the explosion bonded plane. Initial machining of a slice, capable to facilitate the different specimens, was performed by spark-erosion to minimise work-hardening. The obtained 5 mm thick Cu - SS slice was then EB welded to an additional C10100 (OFE) copper strip with equal thickness to ensure the positioning of the explosion welded interface in

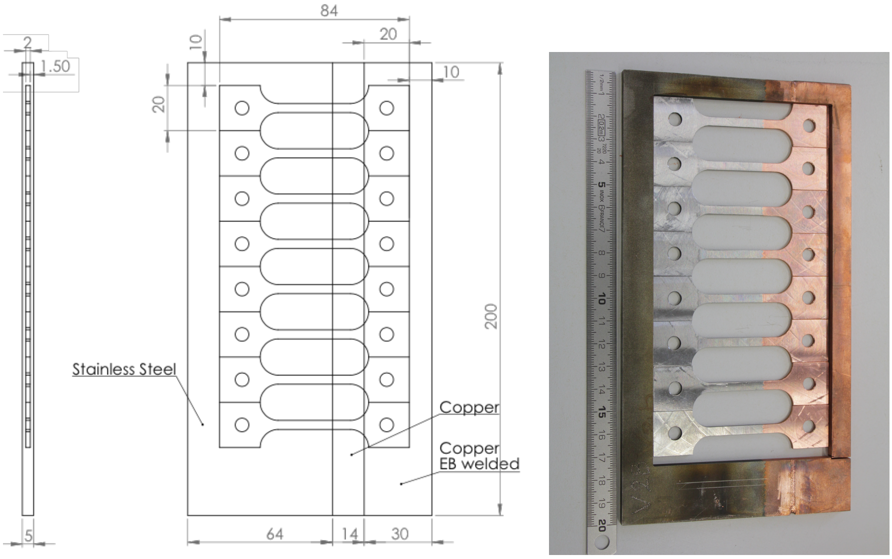

(a) Tensile specimen technical drawing. **(b)** Machined tensile specimens.

Figure 8.4: Tensile specimen extraction. Note the placement of the EB-weld in the larger portion of the head in order not to affect the material in the gauge length where the Cu - SS interface is inscribed.

the gauge length (figure 9.1). The welding process is then followed by a careful mechanical surface machining of the individual specimens, featuring the known 25 mm x 4 mm x 2 mm gauge.

Realising specimens by adding a copper strip to its head-end holds limitations. Plate 6, denoted in table 7.1, does not contain sufficient copper thickness for the additional EB-weld to stay clear of the reduced section while the original explosion weld remains included in the gauge length (here 25 mm, i.e. 12.5 mm to either side from the centre of the specimen). Measurements of such specimens could introduce misinterpretation resulting from either failure outside the gauge length, or the influence of the secondary weld seam. The reduced material availability has resulted in a mere optical quality assessment of this plate. A similar argument holds for Plate 3, where due to limited availability of testing material, mechanical testing could only be done in terms of tensile tests; for which the specimens are less voluminous. Shear tests were here omitted. Plate 5, on the contrary, was tested in shear, and not in tensile, as for the official qualification the latter was not required.

Even though not all plates were measured by all means, the ability existed to make a prediction of the behaviour based on the measured characteristics, in combination with the optical features observed.

The tensile test parameters implemented are comparable to those used for the measurements performed on the F XM-19 material presented in section 3.2.2, and are compliant with standards ASTM E8/E8M and ASTM E1450. Room temperature measurements are conducted using the electromechanical universal tensile machine presented in section 3.2.1 at a constant stress speed of 5 MPa/s up to one half of the expected yield strength, and subsequently slowed down to a strain rate of $1 \cdot 10^{-3}$ mm/mm/s according to ASTM standard E8/E8M. The setup developed by CERN for the high-precision tensile measurements at 4.2 K was utilised for cryogenic tensile testing (extensively described in section 3.2.1). The low-temperature stress-strain curves are subsequently determined by measuring at a strain rate of $3.3 \cdot 10^{-4}$ mm/mm/s consistent with ASTM standard E1450. At least three measurements are conducted in each series to guarantee minimum statistics, whereby three good measurements are required for the construction of a curve. 4.2 K measurements require the availability of at least five specimens to guarantee three representative measurements.

The measurement uncertainty for the ambient and liquid helium temperature tensile testing of the specimens of the explosion welded plates is analogous to the one established for the measurements performed on the F XM-19 material presented in section 3.2.3. The uncertainty in the measured R_m values is determined at an approximate 1.1% for the room temperature data, versus 1.2% for the liquid helium temperature measurements. The measured $R_{p0.2}$ data, however, is subject to an increased uncertainty in the sensitivity coefficient determining the permanent strain. Strain is a function of deformation over initial length, where here as initial length the full gauge length is assumed, even though deformation essentially takes place in its copper fraction. This leads to an additional uncertainty in force at $\epsilon_{p0.2}$ and thus $R_{p0.2}$. Uncertainty is estimated at 2.0% and 2.1% for $R_{p0.2}$ at room temperature and 4.2 K, respectively.

Measurement uncertainty for τ_{max}, obtained at ambient temperature is estimated at 1.6%, with the notion that the path of failure could heavily influence the uncertainty.

Note that the presented data is for qualitative assessment only as a result of the hybrid character of the specimens. Chosen here is to present the data in the tables including the measurement spread, in contrary to the mechanical data presented in Part I. This is resulting from the additional information the spread gives in these measurements. The measurement uncertainty as provided above is announced in the table notes.

8.2 Mechanical behaviour of a Cu-SS explosion weld

In table 8.1 the full mechanical characterisation of the studied plates is listed. The majority of plates exhibit room temperature and 4.2 K tensile properties, dominated by the copper. The results indicate a Cu - SS bonding strength of some 250 MPa to 275 MPa at room temperature, exceeding the strength of annealed C10100 copper of 220 MPa to 235 MPa at room temperature [Hardesty, 1980]. The specimens observed post measurement, shown in figure 8.5a, confirm a final failure located in the copper-end of the specimen. Moreover, its elongation is fully assigned to the copper half. The increase in ductility from an ambient measurement temperature to 4.2 K holds additional evidence of the strength of the weld being superior to its copper end, and the fact that copper characteristics are leading the overall clad-plate behaviour. Copper, containing an FCC structure, is known for retaining, or even demonstrating a rise in ductility when temperature is lowered [Reed et al., 1967].

Table 8.1: Mechanical properties of Cu-SS explosion welds at ambient temperature and 4.2 K.

	Temperature [K]	$R_{p0.2}{}^{a}$ [MPa]	$R_{m}{}^{b}$ [MPa]	$\tau_{max.}{}^{c}{}_{LD(TD)}$ [MPa]
Plate 1	RT	259 ± 3	261 ± 2	269 ± 22 (317 ± 21)
	4.2	311 ± 6	453 ± 6	
Plate 2	RT	239 ± 4	251 ± 1	378 ± 12 (294 ± 2)
	4.2	278 ± 12	459 ± 9	
Plate 3	RT	-	92 ± 73[d]	-
	4.2	-	193 ± 106[d]	
Plate 4	RT	268 ± 9	269 ± 8	210 ± 10
	4.2	350 ± 21	441 ± 12	
Plate 5	RT	-	-	186 ± 15 (187 ± 11)
	4.2	-	-	

---

[a] 0.2% yield strength; measurement uncertainty = 2.0% (2.1%) at RT (4.2 K)

[b] maximum tensile strength; measurement uncertainty = 1.1% (1.2%) at RT (4.2 K)

[c] maximum shear strength; measurement uncertainty = 1.6%

[d] premature failure

(a) Specimens of Plate 2, tested in tension, at 4.2 K (left) and RT (right).

(b) Specimens of Plate 5, tested in shear, in longitudinal direction (LD).

Figure 8.5: Selection of measurement specimens as tested in tensile (a), and shear (b). Notice that failure consistently takes place in the copper cladding.

Even when small imperfections are present at the weld interface (figure 8.6a), failure consistently occurs in the copper cladding, which is the case for all Plates 1, 2 and 4. In the case of Plate 3, besides a remarkably tensile strength, a large variation in the results can be noticed (table 8.1). Failure during traction measurements was observed to commence at the interface, denoting a weaker weld than the weakest of the two materials; e.g. the copper clad. In general, tensile behaviour of Plate 3 does not reach the characteristics of annealed C10100 copper; $R_m \leq 165$ MPa vs. 220 MPa $\geq R_m \leq 235$ MPa, respectively.

Figure 8.6b shows that specimen failure commences at extensive interface defects present at the weld interface, for which the anticipated material properties cannot be obtained. The measurement now reflects the mechanical behaviour of the system, i.e. the combination of stainless steel, explosion weld with voids, and copper. Material characteristics as the 0.2% yield point can not be established. Moreover, the value indicated in table 8.1 under the column of R_m merely represents the load at premature failure, divided over the initially machined cross-section. As the cross-sectional area is however reduced following from partial disconnection prior to the measurement, R_m does not provide a representative value for the individual materials (figure 8.6b).

The tensile measurements on the plate specimens showing inferior tensile strength of the copper with respect to the welded interface, reveal a hardened state of the C10100 copper. In these cases the state is comparable with C10100 copper in an H02 temper (half-hard) with an $R_{p0.2}$ of 250 MPa and an R_m of 290 MPa [Hardesty, 1980].

Macro-hardness measurements on the metallographic specimen performed in the region where failure by tensile testing is observed, presented later in table 9.1, confirm a local H02 temper. In the case of Plate 4, local hardness values even tend towards an H04 temper. Micro-hardness measurements indicate an increase in hardness towards the bonded interface, the region of the largest deformation. This holds for both the stainless steel base metal and the copper cladding.

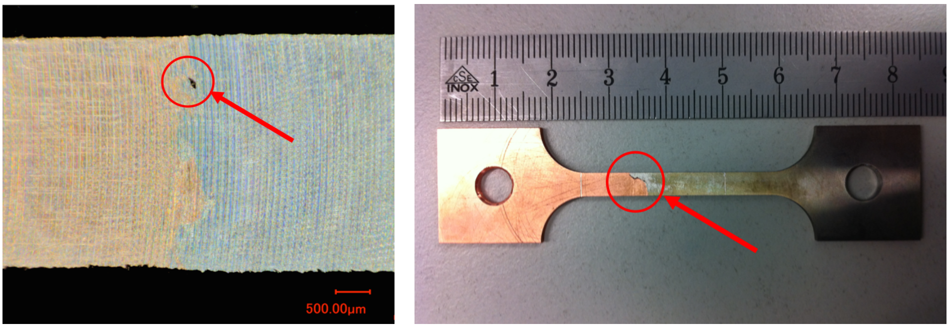

(a) Weld interface of a tensile specimen of Plate 2 prior to testing.

(b) Weld interface of a tensile specimen of Plate 3 prior to testing.

Figure 8.6: Tensile specimens of Plate 2 (a) and Plate 3 (b) prior to measurements at 4.2 K. Note the existence of interface defects in both specimens; in the case of Plate 2, subfigure (a), at micro-scale, and in the case of Plate 3, subfigure (b), at macro-scale. The nature and extent of the imperfection is found to significantly influence the mechanical characteristics of the weld.

High average shear strength was obtained for Plate 1 and Plate 2, both in longitudinal as well as transverse direction with respect to the main direction of explosion welding; some 270 MPa (380 MPa) and 315 MPa (295 MPa) for Plate 1 LD (TD) and Plate 2 LD (TD), respectively (table 8.1). The difference in shear strength between the two measured directions is quite significant, with a large spread in the individual results. Shear results are largely subject to the interlocked state of the stainless steel and copper at the sheared boundary, which can be observed from figure 8.5b where the measured specimens of Plate 5 are shown.

As the boundary covers a thickness of some 1 mm (figure 8.8b), the shear interface is located within this range. An interface machined slightly towards the stainless steel side (figure 8.5b, bottom specimen) will be sheared initially primarily in the stainless steel or the boundary region and will therefore exhibit higher shear properties than a specimen shearing mainly in the copper clad. This was observed for specimen A, with its shear stress - displacement diagram shown in figure 8.7b.

A comparison of Plate 1, presented in table 8.1 and figure 8.7a, with Plate 5, presented in table 8.1 and figure 8.7b, shows the absence of the distinct two-step shearing in the specimens of Plate 5. Whereas for Plate 5 (figure 8.7b), the ultimate shear strength already approaches that of a C10100/C10200 copper (150 MPa to 200 MPa, dependent on temper [Hardesty, 1980]), for Plate 1 initial values are far exceeding this. For Plate 1 it appears that where the shear plane commences at the weld interface, which exhibits superior shear characteristics with respect to the copper clad, the shear-plane later deviates towards the copper clad. This results in a second plateau in the diagram close to the shear strength of copper.

We can thus conclude that in the case of Plate 5 the shear characteristics of the weld interface do not deviate much from the shear characteristics of the copper clad.

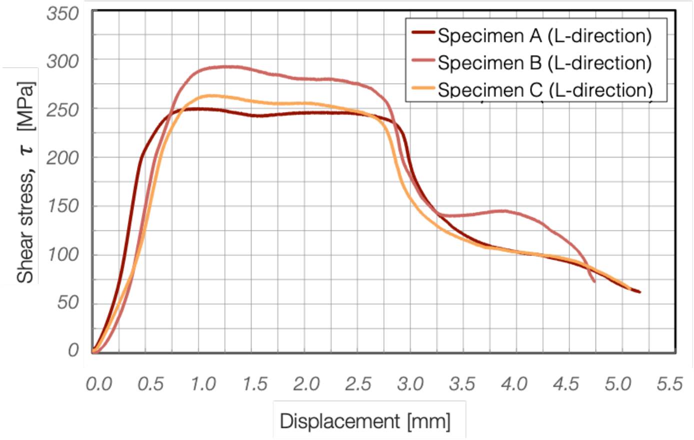

(a) Shear stress as function of cross-head displacement for the shear measurements performed on Plate 1.

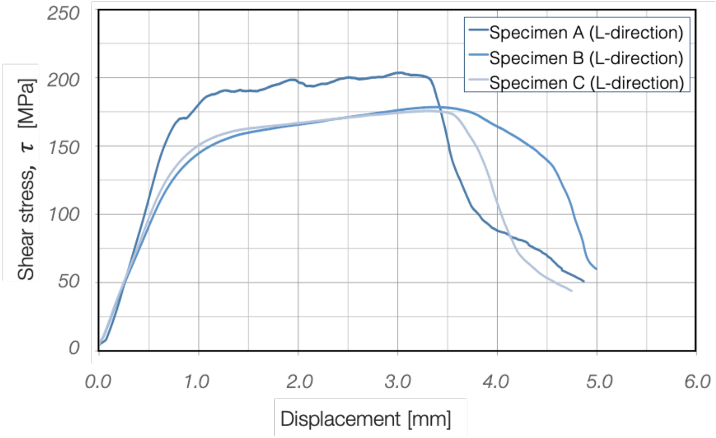

(b) Shear stress as function of cross-head displacement for the shear measurements performed on Plate 5.

Figure 8.7: Shear measurement results for Plate 1 (a) and Plate 5 (b). Note the two-step shear strength in the case of Plate 1, resulting from the deviation of the shear plane from the interface towards the weaker copper clad. For Plate 5 a lower, close to single step shear stress is obtained. A variety in maximum shear stress is observed for the different specimens, analogous with the initial shear plane as can be observed in figure 8.5b, where the specimens are ordered A, B, C, from bottom to top.

In all cases, the shear plane cuts through both materials leaving no clean stainless steel - copper separation. This indicates a shear strength of the interface beyond the one of the weakest of the two individual materials. The aforementioned is confirmed by the ultimate shear strength of all measured plates exceeding the common shear strength for C10100/C10200 copper alloys in H02 temper, i.e. about 180 MPa [Hardesty, 1980].

8.2.1 Structural observations at the weld interface

The most generic method of quality assessment of a welded connection is by optical means, either by macro-observations or by micro-observations. The macro-optical examination presented here is performed on the as-cut surfaces, following dissection by means of electro-erosion in order to limit its effect on the features of the explosion welded material, and to obtain a clean cut. Macro examinations were performed on a VHX 1000E by KEYENCE, a high dynamic range, 16-bit resolution, 18-54 million pixel ($\geq$ 4800x3600) digital microscope; a microscope with the advantage of extremely accurate measurement of material features in real-time.

Micro-optical examinations of the weld interface were performed in the longitudinal plane with respect to the main direction of explosion welding, aimed at the search for the characteristic wave pattern and evidence of atomic diffusion. It can provide a possible explanation for the observed mechanical behaviour of the different explosion welds presented.

Short samples were prepared by low-pressure mechanical polishing. Subsequent metallographic observations are achieved on the as-polished surface with the use of a variety of optical microscopes at different magnifications. Microscopes used are the LEICA Quantimet 600 and ZEISS Axio Imager with a resolution of up to 1296 x 968 pixels, with a wide range in field optics like Dark Field (DF), Bright Field (BF), Polarised Light (PL) and Differential Interference Contrast (DIC), for an adequate imaging of the various structures in the transitional area.

Figure 8.8 shows the characteristic interface structure observed for Plate 2, which shows high similarities with the structure observed for Plate 1, originating from the same company. The metallographic images show the limited, but present forward-rotating vortex, rich in stainless steel. Characteristic in the observed explosion weld is the exemplary counter-rotating vortex as described by the Von Kármán vortex shedding mechanism (figure 7.4). Some entrapped voids are visible, priorly designated as marginally influencing the mechanical integrity of the bond.

The wave pattern is equally observed in the weld interface of Plate 4, shown in figure 8.9, however, with reduced wave amplitude. This weld interface is showing even more clearly the stainless steel rich forward-rotating vortex. A similar entrapment of imperfections is here noted in the counter-rotating vortex. In both cases the presence of an interlocked material state is unmistakable, and atomic diffusion at the interface can be observed in the form of an intermetallic compound present.

(a) Micrograph of a weld interface section of Plate 2, unetched, magnification 50x.

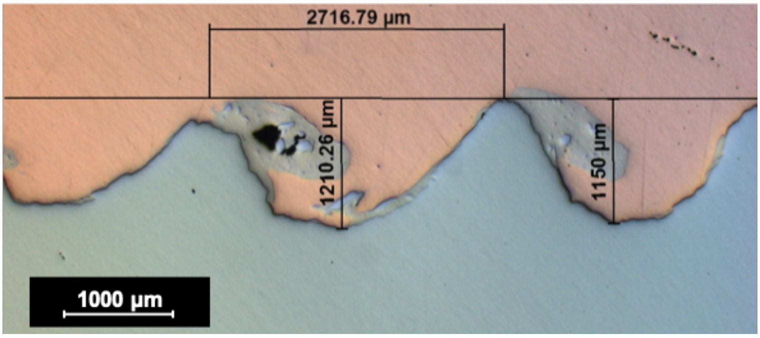

(b) Wave pattern of a weld interface section of Plate 2, unetched, magnification 50x.

Figure 8.8: Metallographic images of the characteristic wave pattern observed in the specimens of Plate 2, and its dimensions. The explosion welding direction is here from right to left.

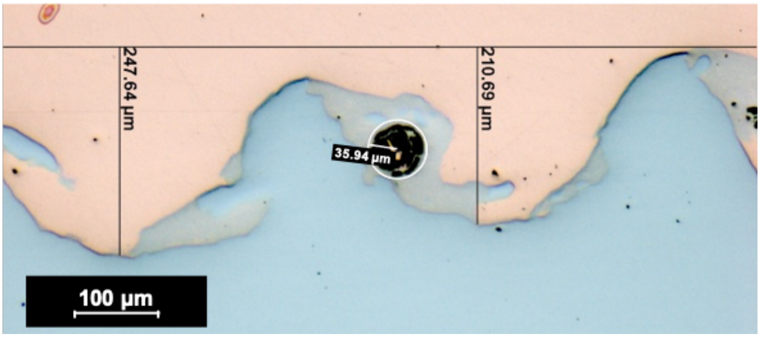

Figure 8.9: Metallographic image of the characteristic wave pattern observed in specimens of Plate 4, and its dimensions. Note the reduced wave amplitude with respect to the observation in specimens of Plate 2 (figure 8.8). The explosion welding direction is here from right to left. Original magnification 100x.

Such a high-quality stainless steel to copper connection is not observed in all cases. An extreme case, illustrating unadapted explosion welding parameters and their effect on the individual materials, is presented in figure 8.10. Here the macrostructure of the explosion bonded interface of Plate 3 is shown. Excessive local material deformation is observed, where the ductility of the stainless steel could not cope with the deformation imposed, thus resulting in material tearing.

(a) Macrograph of a weld interface section in specimens of Plate 3, unetched.

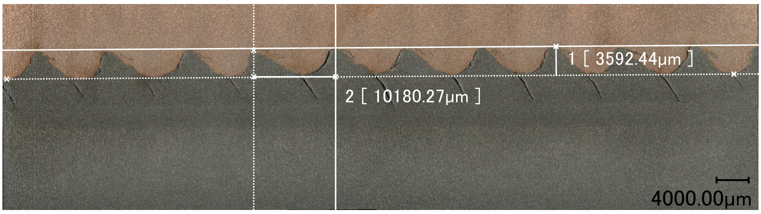

(b) Wave characteristics of a weld interface section in specimens of Plate 3, unetched.

Figure 8.10: Metallographic images of the characteristic wave pattern in specimens of Plate 3, and its dimensions. Notice the effect unadapted welding parameters have on the structural integrity of the individual materials. The explosion welding direction is here from right to left.

We can note from figure 8.10b that even though both material characteristics and process parameters play a role in the material behaviour at the weld interface, the latter is in this case leading. Explosion welds performed with suitable parameters should in general result in an amplitude of waves between 0.1 mm and 4.0 mm and a wavelength from 0.25 mm to 5.0 mm [Shrijit, 2019]. In the example of figure 8.10 we can observe a wavelength more than twice the general reported one, denoting an excessive collision velocity.

The copper cladding, when 'bumping' into the hump described in figure 7.4, realises a suitable compression in the down-going phase of the jet (subfigure (e)). However, while passing the base metal's hump the copper cladding contains a disproportioned speed which pulls on the weld too vigorously. The excessive tension on the developing weld behind the hump results in a loss of connection between the cladding and base material. The jet is subsequently pushed into the next hump, realising a large deformation in the stainless steel base material in the direction of the weld. The deformation is too excessive for stainless steel to cope with, with tearing of the parent material as a consequence.

The excessive collision velocity resulting from parametrisation has not allowed for the formation of an interlocked state, and the development of an intermetallic connection. Moreover, it has resulted in local damage of the parent material. The observation of the faulty weld interface of Plate 3 is fully consistent with its mechanical behaviour presented in section 8.2.

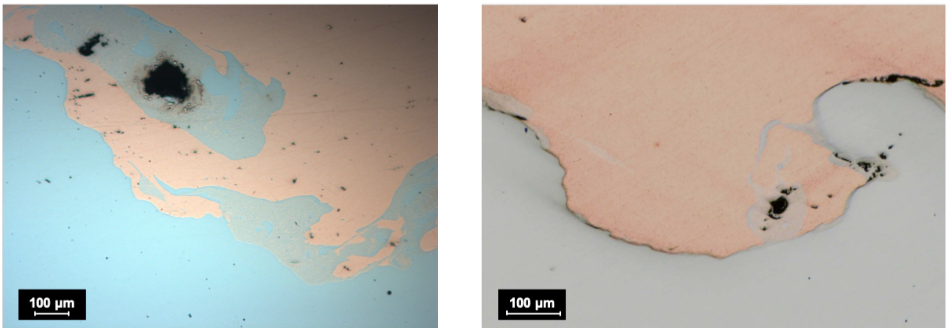

(a) Micrograph of counter-rotating vortex of the weld interface of Plate 1, unetched, magnification 100x.

(b) Micrograph of the forward-rotating vortex of weld interface of Plate 5, unetched, magnification 120x.

Figure 8.11: Metallographic weld interface images showing a single 'wave' in a specimen of Plate 1 (a) and Plate 5 (b). Note that even though for Plate 5 pores are smaller with respect to Plate 1, in Plate 5 elongated discontinuities are present at the weld interface, and atomic diffusion over the interface appears absent.

In the case of Plates 1, 2 and 4 the development of a diffusion layer is observed (figure 8.8 and figure 8.9). In figure 8.11a this diffusion layer of Plate 1 can be seen in detail, observed by the dispersion of a copper hue in the stainless steel. Plate 5 lacks the presence of such a layer, as can be seen in figure 8.11b. Limited diffusion is observed in the latter, accompanied with little counter- as well as the characteristic forward-shedding vortices as observed in a Von Kármán vortex street. The wave pattern is characteristic for a Kelvin-Helmholtz instability sequence, with a single ray of rather bulky vortices. The presence of Kelvin-Helmholtz instability could denote a large difference in horizontal velocity between the cladding and the base plate [Carton, 2004], whereby little shear is experienced at the interface, resulting in limited diffusion.

Even though both welds, i.e. the one of Plate 1 (figure 8.11a) and the one of Plate 5 (figure 8.11b), demonstrate some imperfections at the boundary, one can see that in case of Plate 1 the imperfection is merely gas cavity resulting from turbulence. In the case of Plate 5 not only gas entrapment has taken place, but also some elongated imperfections at the boundary between the two materials are observed. This confirms a difference in plate velocity, allowing for the plates to slide with respect to each other. Even though an interlocked state of the parent stainless steel plate and the copper flyer plate is observed, the weak bonding force during welding can account for the relatively limited shear strength of Plate 5.

9

Conductive properties of the copper following joint formation

The conductive properties of the copper side of the bimetallic box is of primary importance for its suitability as electrical component in the joint. The applicability of the explosion welding process, therefore, is not only determined by the quality of the achieved connection, but in equal degree by its effect on the properties of the copper.

For the stainless steel base metal, with as principle function a structural one, no immediate concerns are proclaimed, apart from the weld interface integrity. For the copper cladding, generally of high purity, additional attention is paid to the effect of explosion welding on its structural properties. Moreover, predicting the effect of local hardening on electrical conductivity and to some extent on thermal conductivity is of essence. No prior knowledge exists to which extent an explosion welding process influences clad materials at certain distance from the interface. Friction of the flyer plate with respect to the base plate could result in specific and localised changes in material properties.

In this chapter the suitability of the explosion welding process itself, and its effect on the base metal's behaviour following hardening and associated conductivity studies are presented. Moreover, the suitability of certain copper grades for specific applications is discussed, aiming at identifying optimal solutions for a range of joints.

9.1 Research methodology

The copper sole of the bi-metal has two main functions:

1. Provide adequate transport properties, depending on the coil system foreseen. For the PF coils the electrical resistivity requirement amounts 2.3 $n\Omega$m to 3.7 $n\Omega$m, relating to an RRR value of some 5 to 8 when considering a room temperature resistivity of 18 $n\Omega$m (section 7.1).

2. Feature an adapted temper suitable for cable compaction, whilst inhibiting strand movement. In the case of the PF coil joints a Vickers hardness HV, is targeted between 65 and 95, relating to a mechanical performance of some 180 MPa $R_{p0.2}$ and 240 MPa to 300 MPa R_m [Dalmut, G., 2005].

Hence, the assessment includes the measurement of transport characteristics, at 4.2 K, as well as an examination of the copper sole's hardness. Measurements are conducted both on specimens in the as-bonded state, as well as subsequent to thermal treatment, simulating the effect of processing treatment during joint formation hereafter explained. The results are examined against properties of the materials to be cladded as reported in a technical certificate, whenever available.

9.1.1 Method for RRR measurements at 4.2 K

The characteristic of a material's low temperature behaviour in terms of resistivity performance and implicitly its thermal response is the Residual Resistivity Ratio, or RRR. RRR is directly related to a material's purity and its temper state. A material's purity not only affects its electrical resistivity, but also its thermal conductivity, as impurities reduce the mean free path. A reduction in mean free path results in an increase of scattering points along the way and thus a decrease in both electrical and thermal conductivity. Scattering points not only consist of impurity elements; i.e. secondary phases formed in the material or for example interstitial or substitutional elements, but also other lattice distortions like dislocations (section 11.4).

The RRR of a superconductor is usually defined as the ratio between the electrical resistivity at room temperature, 293.15 K ($20\,^{\circ}\mathrm{C}$), and the temperature just above the critical temperature $\mathrm{T_c}$; for NbTi at about $10\ \mathrm{K}$. In the case of the copper cladding a critical temperature does not exist. Its resistance does level out and shows a plateau region for low temperatures, from which its RRR is calculated. Here the RRR is defined as the ratio of resistivity at room temperature over resistivity at 4.2 K. The measurement of electrical resistance is based on the determination of the voltage V, versus current I, curve measured for a material.

A specific experimental set-up has been employed, developed in view of the LHC [Charifoulline, 2006]. Specimens are fixed in a window frame fibreglass holder (130 mm x 100 mm), connected in series (figure 9.1a). The voltage drop over each specimen is determined during current ramp-up. The electrical resistance of each specimen is calculated by a least-square-fit regression analysis of the obtained VI-curves. The non-linearity of the VI-curve is used as a test quality criterion for the control of ohmic heating in the case of measurements at room temperature.

The maximum number of specimens mounted on the specimen holder is 20. The specimen length holds between 100 mm and 110 mm, relating to a voltage tap length of 80 mm, and a specimen cross-section of 2 mm x 2 mm. One to two specimen slots are used for a reference or calibration specimen (in figure 9.1a the two copper wires amidst the here aluminium specimens), and will remain mounted on the holder throughout all tests. The temperature is verified by a calibrated carbon-ceramic resistor fixed close to the reference specimen. During measurements the holder will remain in horizontal position in order to minimise the thermal non-uniformity along the specimens.

Specimens are measured in magnetic self-field of the specimens without the application of an additional external magnetic field.

The acquisition is performed with use of a KEITHLEY2182 nanovoltmeter, and KEITHLEY2001 and KEITHLEY2000 voltmeters, which are regularly calibrated according to Swiss national standards.

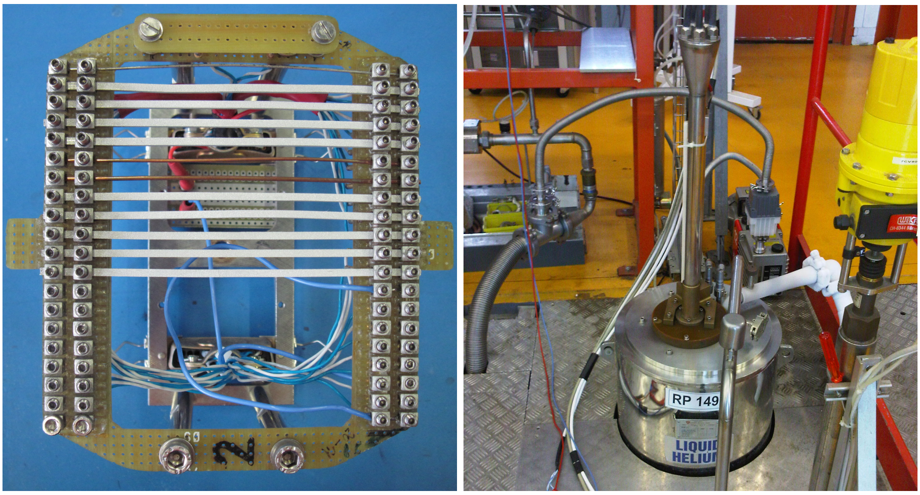

(a) RRR specimen holder.

(b) RRR measurement station.

Figure 9.1: Residual Resistivity Ratio, RRR, measurement set-up. A specimen holder (a) with 18(+2) specimens is lowered into a liquid helium cryostat (b) to measure voltage drops over the specimens at 4.2 K and intermediate temperatures towards ambient temperature when lifted out of the liquid helium medium.

Resistance measurements at room temperature

The room temperature measurements are performed in a specially developed 'RT test box' where the temperature is regulated at 20 ± $0.5\,^{\circ}\mathrm{C}$.

Excitation current is varied from 0 A to 1 A, resulting in a voltage drop in the range of 1 mV to 5 mV. This range of excitation satisfies the requirements of sufficient sensitivity and negligible ohmic heating.

Resistance measurements at 4 K to 10 K

For the cryogenic measurements a conventional 4.2 K liquid helium cryostat is used (figure 9.1b). Automatic ABB software controls the cryogenic operations including cooling to 4.2 K, liquid helium filling and station warm-up.

The resistance curve at low temperature is subsequently determined by warming up the specimens from 4.2 K to 8.5 K and subsequently 10 K. This condition is achieved by a heater situated on an intermediate vertical tube, heating up the helium gas around the specimens. The resistance of the reference specimen and the temperature near the specimens is monitored during the warm-up. This information is used to trigger the VI-curve scanning of all specimens.

The current is varied from 1 A up to 5 A, resulting in sample voltages of about 0.01 mV to 0.2 mV.

The VI-measurement takes a couple of minutes during which the temperature deviates by no more than 0.5 K. A servomotor located on top of the insert allows for the movement of the holder, i.e. can return the specimens to 4.2 K, allowing to repeat the test procedure if necessary.

Finally, an automatic analysis is applied on the measured data to determine the resistance from the VI-curves. The RRR values are calculated as the ratio:

$$\mathrm{RRR} = \frac{\rho_{\ 293.15\ \mathrm{K}}}{\rho_{\ 4.2\ \mathrm{K}}}, \tag{9.1}$$

where $\rho_{\ 293\ \mathrm{K}}$ and $\rho_{\ 4.2\ \mathrm{K}}$ are the resistivities at ambient temperature and 4.2 K, respectively. Measurement uncertainty is estimated at 1% [Charifoulline, 2006]. The obtained values are validated on the condition a linear VI-curves, the temperature spread and the data of the reference specimens.

Measurements are performed on specimens extracted from 2 to 3 positions in the copper sole depending on the thickness of the sole; in the vicinity of the bonded interface, towards the outer surface, and in between these two positions. Specimens are machined with use of electro-erosion in order not to alter the copper properties. The specimens are machined in the longitudinal direction (LD) with respect to the main direction of explosion bonding. During the mounting of the RRR specimens, care is taken not to deform the thin specimens to avoid additional work hardening effects; influencing the sensitive measurements.

9.1.2 Method for hardness testing

To relate the thermo-electrical behaviour of the copper sole material to its mechanical behaviour, hardness measurements are performed, generally equally dependent on the material's grade and temper.

Indentation hardness measurements are performed on samples, previously utilised for optical examination, with use of a Wolpert Wilson universal hardness tester. For the macro-hardness measurements (HV) a Vicker's pyramid diamond indenter is used at 10 kgf load (HV10), applied for 10 s - 15 s to obtain an approximate 0.8 mm diameter indentation in accordance with ISO standard 6507-1.

Hardness values are obtained for 2 to 3 positions corresponding to the RRR measurement positions, in order to assess a direct relation between mechanical and thermo-electrical performance, and the influence of the explosion bonded process on both. Micro-hardness (μHV) is measured along a line perpendicular to the explosion bonded plane with 1.0 kgf applied load (μHV1), running from the copper surface to beyond the Cu - SS interface, to assess any localised effect of the explosion bonding process on the copper sole.

The subsequently acquired and presented Rockwell hardness F-scale (HRF) values are converted from the collected HV data following ASTM E-140, to obtain the measurement data on a scale referred to in the ITER reference documents [ITER Organisation, 2015] referring to [ASTM, 2013]. Chosen is to perform the measurements in HV as a result of its recommendation in the standard for this type of material, and its related increased accuracy. Measurement uncertainty is estimated at 1.6% for the measurements performed in 3-fold, where a large fraction of the uncertainty follows from human error in the measurement of indentation dimensions.

9.1.3 Thermal treatments simulating joint formation

Pursuing the bimetallic block formation, the materials experience an extensive collection of manufacturing processes to arrive at the final product; i.e. the full electrical joint. During manufacturing the joints of the various coils pass through different heat involved processes. But along the range of joints present in the ITER Tokamak, a handful of thermal processes are equal or present a high level of similarities. Following joint box manufacturing, the two joint boxes of the twin-box concept are soldered together. This soldering process, where large surfaces are connected in a highly effective manner as to avoid additional electrical loss over the soldered connection, is accompanied by an increase in overall temperature of the two boxes. As a consequence of the high thermal conductivity of the copper, both the soldered surface, as well as the bulk will endure this temperature rise.

A thermal treatment was designed to simulate this soldering procedure endured by the copper of the previously explosion bonded bimetallic box. By applying thermal treatments one obtains a full view of the materials' performance, not only resulting directly from the explosion welding process, but also when the material reaches its final state. One can get a full picture of the overall material response, here for a certain range of copper alloys, along the manufacturing track, enabling predictability for future use.

For the soldering simulating thermal treatment, short sections of the Cu - SS explosion bonded plates were subjected to a primary vacuum furnace heat-treatment at fairly low temperature. A ramp-up is realised stretching over 1.5 h to simulate heating in 8 steps during the soldering process. The slow temperature increase results from the fact that during soldering heating power is maintained at every step until the joint temperature is stabilised. Temperature is subsequently held at 230 ± 10°C for 20 min with a threshold at 220°C. The thermal cycle simulating soldering treatment is shown in figure 9.2a. The internal holder of the set-up, exhibiting the positioning of the short bimetal sections and the location of the thermal sensors for monitoring and regulation of the temperature via an automated feedback loop, are presented in figure 9.2a.

For the correct operation of the electrical joint not only a sufficient connection is required between the two soles of the twin-box. Equally important is the connection between the superconducting strands of the CICC cable and the sole a groove is machined to accompany the superconducting cable (figure 1.8). In order to realise such a connection, the cable is compacted into the bi-metal in a mechanical manner, sometimes under the presence of an indium interlayer. The quality of the connection is studied under different process parameters, like for example a 'softening' treatment of the copper. This softening makes the material more susceptible for the compaction process, and generally realising a larger contact surface between the superconducting strands and the copper sole.

A vacuum furnace heat-treatment at elevated temperature is applied to certain specimens to simulate this final heat-treatment of the terminal box prior to cable insertion, facilitating cable compaction into the copper sole [Decool et al., 2003]. The temperature in this case is held at 400°C for 6 h, subsequent to a ramp-up at 20°C/h (figure 9.2c). The specimens are in this case treated inside a tube to avoid exposure to direct radiation.

An additional thermal treatment studied here is one concerning the superconducting cable in the joint. The poloidal field coils, the correction coils and the feeders to the coils make use of NbTi superconductor, which does not require a heat treatment for proper compound formation. However, in the case of Nb_3Sn, in the toroidal field coils and the central solenoid, such a heat treatment is needed (section 1.2.4). A selection of the bi-metals studied here are subjected to a thermal treatment simulating this Nb_3Sn reaction heat treatment. It concerns the bi-metals of Plate 4 and Plate 5, manufactured in view of future implementation in the toroidal and central solenoid coils, respectively. In the process of joint formation this treatment is not necessarily the last one, but resulting from its excessive heat input it is here last applied. As this thermal treatment outreaches those described above, it is assumed here that former treatments will not influence the final state of the material as it is fully driven by this heavy final heat-treatment.

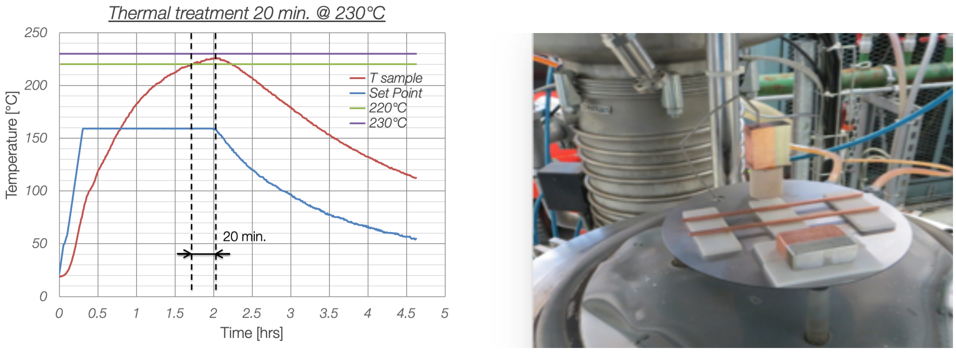

(a) TT simulating soldering operation.

(b) Layout applied for TT.

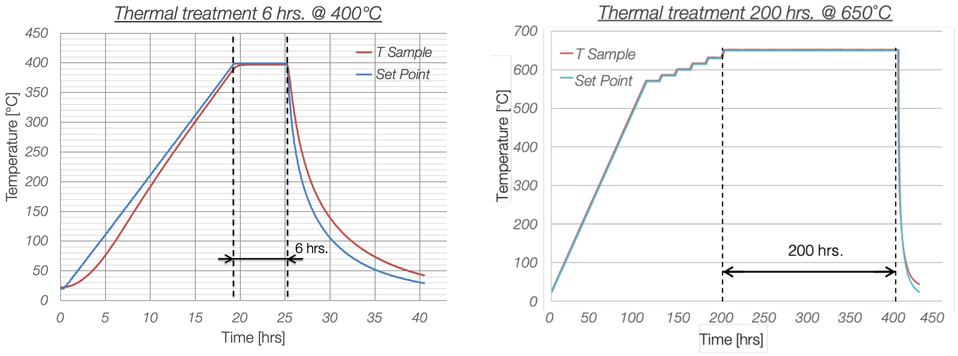

(c) TT simulating Cu softening operation.

(d) TT simulating Nb_3Sn reaction treatment.

Figure 9.2: Thermal treatments (TT) in vacuum applied for the simulation of further processing of the bimetals for the manufacturing of the twin-box electrical joint. Temperature measurements are taken both in a ’dummy’ specimen to monitor copper core temperature, as well as suspended in the furnace.

The Nb_3Sn reaction simulating heat treatment consists of a ramp-up to 650°C over 200 h to simulate the slow heating scheme realised during the reaction cycle. The temperature is then held at 650 ± 15°C for a total duration of 200 h. The reaction heat-treatment simulating cycle performed in the vacuum furnace can be observed in figure 9.2d.

All thermal treatments include an in-furnace cool-down in vacuum to avoid oxidation, as to prevent an effect on the highly sensitive RRR measurements. Note, however, that where reaction heat treatments in the process of the joint formation are equally done in vacuum, soldering processes are not.

9.2 Transport performance of an explosion welded copper sole

In table 9.1 the average results of the main copper cladding properties of the various copper-clad plates are listed. The RRR results, based on three positions, in the vicinity of the bonded interface (bottom), middle and towards the outer surface (top), show lower values in the vicinity of the explosion bonded interface where the plastic deformation during the explosion bonding process is largest. This finding is consistent with the earlier results during (μ)HV measurements.

Plastic strain increases towards the interface boundary resulting from load and deformation implied during the bonding process, even though the explosive lies on the top of the flyer, consistent with literature [Ghizdavu, 2011]. The sole plate where the influence of the explosive and its site can be denoted in the material characteristics, is in the case of Plate 4. Even though RRR values are lowest close to the interface, a minimum in electron scattering points is found at the center of the copper clad. Towards the top of the plate, i.e. distant from the welded interface, or closest to the explosive, a recurrent decrease in RRR is noted. The decrease in RRR observed is evidently resulting from plastic deformation, as here too an increase in hardness is apparent. Please note that the initial temper of the employed C10100 copper plate for this particular explosion bonded item (i.e. Plate 4) is elevated, i.e. H02 temper, with respect to the other plates studied.

In the cases where the heat-treatment simulating soldering, i.e. 20 min at 230°C, was applied, no significant effect on the hardness was observed. Even in the case of the highly-responsive high-purity copper in the form of the C10100 copper used for Plate 1, no apparent effect on the copper clad's hardness was revealed. An effect, however small, was though noted on the RRR of some 20 in the case of the high-purity copper of Plate 1, resulting from the highly sensitive measurement method of RRR for dislocations. Even little recovery in this case results in a reflection on dislocation dissolution.

Table 9.1: Resistivity vs. hardness results for the examined plates prior and subsequent to heat-treatments, simulating final joint formation.

	Distance from interface		Grade	State	HV	HRF	RRR
Plate 1	Top	at 11 mm	C10100	As-bonded	86 ± 1	78 ± 1	154 ± 2
				20 min at 230°C	86 ± 1	78 ± 1	176 ± 2
				6 h at 400°C	42 ± 1	31 ± 1	524 ± 5
	Bottom	at 5 mm	C10100	As-bonded	96 ± 2	84 ± 1	116 ± 1
				20 min at 230°C	98 ± 2	86 ± 1	134 ± 1
				6 h at 400°C	43 ± 1	32 ± 1	474 ± 5
			C10100 Certified plate (O25; 14 mm)		45	35	345
Plate 2	Top	at 17 mm	C10100	As-bonded	85 ± 1	77 ± 1	191 ± 2
	Middle	at 11 mm	C10100	As-bonded	94 ± 2	83 ± 1	146 ± 1
	Bottom	at 5 mm	C10100	As-bonded	99 ± 2	86 ± 1	126 ± 1
			C10100 Certified plate (O25; 20 mm)		40	28	365
Plate 4	Top	at 21 mm	C10100	As-bonded	110 ± 2	91 ± 1	69 ± 1
				200 h at 650°C	48 ± 1	39 ± 1	350 ± 4
	Middle	at 13 mm	C10100	As-bonded	102 ± 2	88 ± 1	72 ± 1
				200 h at 650°C	50 ± 1	42 ± 1	361 ± 4
	Bottom	at 5 mm	C10100	As-bonded	123 ± 2	96 ± 1	68 ± 1
				200 h at 650°C	46 ± 1	36 ± 1	354 ± 4
			C10100 Certified plate (H02; 24 mm)		96	84	-
Plate 5	Top	at 22 mm	C10200	As-bonded	79 ± 1	72 ± 1	80 ± 1
				200 h at 650°C + 77 K shock	40 ± 1	28 ± 1	150 ± 2
	Middle	at 14 mm	C10200	As-bonded	86 ± 1	78 ± 1	71 ± 1
				200 h at 650°C + 77 K shock	40 ± 1	28 ± 1	148 ± 1
	Bottom	at 6 mm	C10200	As-bonded	92 ± 1	82 ± 1	67 ± 1
				200 h at 650°C + 77 K shock	40 ± 1	28 ± 1	148 ± 1
			C10200 Certified plate (M20; 27 mm)		56	49	170
Plate 6	Top	at 9 mm	C12200	As-bonded	113 ± 2	92 ± 1	4.8 ± 0.1
				20 min at 230°C	112 ± 2	92 ± 1	4.8 ± 0.1
				6 h at 400°C	55 ± 1	48 ± 1	5.3 ± 0.1
	Bottom	at 5 mm	C12200	As-bonded	123 ± 2	96 ± 1	4.7 ± 0.1
				20 min at 230°C	117 ± 2	94 ± 1	4.8 ± 0.1
				6 h at 400°C	53 ± 1	46 ± 1	5.3 ± 0.1

The recovery or recrystallisation temperature depends on a variety of factors. The material's composition plays a large role. Additional factors are the initially prescribed deformation, i.e. dislocation density, and the duration at which the temperature is held, as can be seen in figure 9.3, in which the effect of the recrystallisation factors is illustrated. With the amount of introduced cold reduction, the recovery temperature decreases (figure 9.3a) [Bhargava et al., 2017]. In our case a typical half-hard state, i.e. H02, corresponds to a 15% to 20% cold reduction. The temperature hold results in a large range of temperatures to achieve recovery in a highly pure metal like C10X00 series (between 0.3 and 0.6 times the material's melting temperature). A longer holding time is required for lower applied temperatures (figure 9.3b) [Elmasry et al., 2017].

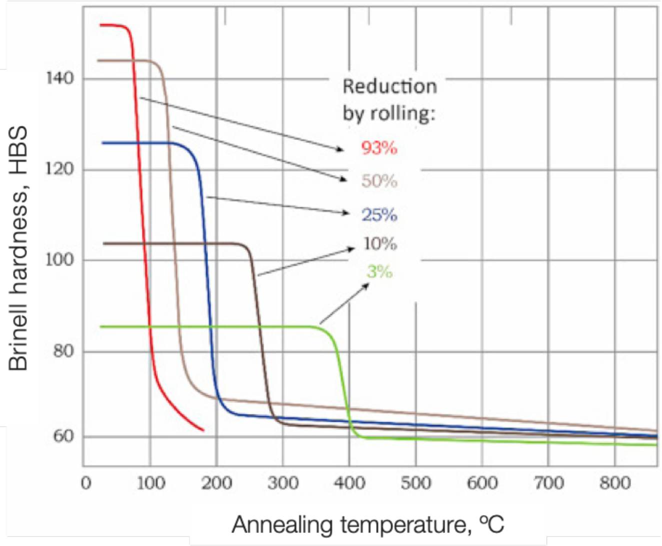

(a) Effect of the degree of the amount of introduced plastic deformation on the recovery characteristics of high-purity copper [Bhargava et al., 2017].

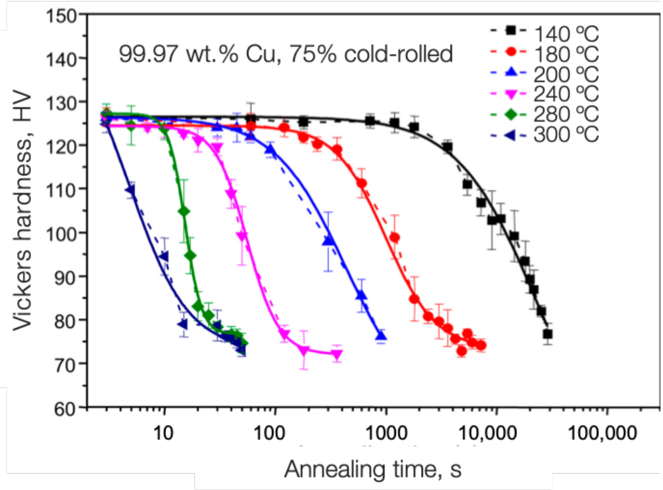

(b) Recovery as a result of annealing time of high-purity copper pre-deformed by equal channel angular pressing (ECAP) + cold rolling (CR) [Elmasry et al., 2017].

Figure 9.3: Diagrams illustrating the effect of initially introduced deformation (a) and applied annealing time with varying temperature (b), on the recovery characteristics of a highly pure copper alloy.

We can denote here, that in the case of a C10100 alloy in an approximate H02 temper, a temperature of 230°C stands at the initiation of recovery, whereby the holding time of 20 min provides to be insufficient for a full recrystallisation. The subsequent softening cycle at 400°C fully annealed the copper cladding beyond the initial state. This indicates a slightly hardened state of the initial copper plate, prior to explosion bonding, most likely as a result of coiling. Coiling of the plate in this case is performed on the initial state for storage and transportation.

In contrary, in the case of the less pure C12200 Cu of Plate 4, the heat-treatment simulating soldering did not have significant effect. The hardness but also RRR remained unaffected. The subsequent softening cycle annealed the C12200 copper cladding, similarly as for the C10100 Cu. For this low-purity grade Cu, RRR is mainly driven by impurity content. As expected, no significant increase of RRR is noticed with material annealing by a severe thermal cycle, while a large decrease in hardness is observed. The RRR of a fully annealed C12200 remains in the expected range of 3 to 5 [Ekin, 2006].

The softening cycle performed at 400°C for 6 h already results in a fully annealed state for both the C10100, and the C12200 alloys. No less is to be expected from the heat-treatment simulating the Nb_3Sn reaction cycle, with its extensive 200 h hold at 650°C. Applying this heat-treatment on Plate 4 and Plate 5 confirms this. A fully annealed state was achieved following its employment, to a softened state beyond the initial state of the copper plates used for bonding. Note that the initial state in both cases differ from a fully annealed state, i.e. H02 and M20, for Plate 4 and Plate 5, respectively. M20, designating a hot-rolled temper generally approaches the fully annealed temper in terms of hardness. Remarkable is the slightly hardened state of the C10200 plate prior to explosion bonding for Plate 5, for which a hardness of some 50 HRF is obtained, slightly higher than the 45 HRF reported for the M20 temper [Hardesty, 1980], which might imply an increased temper. Even more remarkable is the RRR value for this incoming plate of 170, as presented in its material certificate. Common RRR values for a fully annealed 99.95% to 99.97% purity copper, under which the C10200 copper falls, stretches towards 160 but generally not far beyond [Ekin, 2006]. With the RRR measurement procedure being a delicate one, we are confident of a fully annealed state for the C10200 grade following the heat-treatment cycle of 650°C for 200 h.

When the RRR results are presented as function of the HRF measurements a trend for the variety of materials employed in the clad-plates of this study is obtained. Figure 9.4 provides useful for the choice of materials for the electrical joint. Derived from the diagram is the relation between hardness, from which tensile characteristics can be deduced, and the material's (thermo-)electrical behaviour.

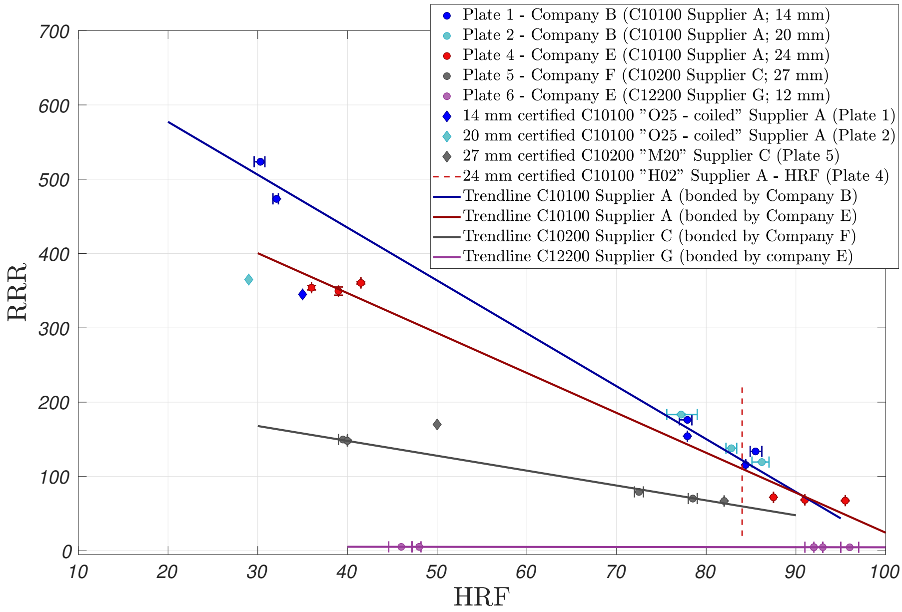

Figure 9.4: RRR as function of HRF for all examined copper-claddings. Notice the clear difference in resistivity behaviour between a highly pure, and a heavily alloyed copper. RRR shows to be driven by impurity content.

Figure 9.4 shows a very consistent trend-line for the highly pure C10100 copper, used in Plate 1 and Plate 2. The measurements confirm a lower purity copper, C10200, utilised for clad Plate 6. As expected, the purity of the copper as used in Plate 6, C12200, lies beneath the previously mentioned, and shows no noticeable dependence of RRR on hardness.

A clear extensively hardened initial state of the C10100 copper as employed for Plate 4 with respect to Plate 1 and Plate 2 can be noticed, leading back to its hardened state prior to explosion welding. When considering the results after annealing heat treatment, the highly sensitive RRR of the C10100 alloy of Plate 4 remains significantly lower than that of Plate 1. Even though both alloys fall under the denominator of a C10100 copper, the difference in sulphur and oxygen levels in the alloy; 6.5 ppm(S) & 1.2 ppm(O) vs. 5.2 ppm(S) & 1.0 ppm(O) for Plate 4 and Plate 1, respectively, could account for the reduced resistivity characteristics in a fully softened state of the former.

A hardened copper plate was applied for the fabrication of Plate 4 by explosion welding, denoted by the red dotted line in the diagram of figure 9.4. Nevertheless, the process introduces additional hardening as a result of the extensive deformation the plates endure during explosion welding.

10

Suitability of explosion welding in electrical joints

In the quest for a suitable, load-bearing metallic connection, which does not introduce any negatively altering properties in the conductive copper element, explosion welding was investigated. The extensive characterisation of post-welding features shows that the explosion bonding process is highly dependent on its parametrisation used. Furthermore a considerable effect is found on the characteristics of the main conductive element for the application; the copper sole. Additional research, aiming at the full understanding of the copper behaviour throughout the production process, has shown the reaction of the material on additional treatments. Based on the full study some insight is gained on the applicability of the explosion welding process, and the implementation of certain copper grades following varying manufacturing processes. This way a material solution, best suitable for the different joint applications can be targeted.

Explosion welding has shown its applicability in connecting a multitude of materials in a constructive way. Its execution, however, needs to be done with care. A large variety of factors play a role in the success of such a weld. When parameters are chosen well, its reliability can be commendable.

Following welding a large range of material treatments can still be applied without affecting the welded connection. The copper is malleable and can be designed as wished, providing the engineer with both advantages and disadvantages. Depending on the conductive material employed a simple post-welding treatment can render the material homogeneous and in the state as wished. The implication of joint fabrication treatments can also be detrimental for the material's properties as intended. Overall, with the provided materials comportment under a wide variety of post-welding treatments, a designer will be able to choose material and process characteristics in such a way to achieve the required effect.

In this chapter the main findings of the study are reviewed. Conclusions are drawn with respect to the performance of the welded connection and its effect on the various copper grades. Subsequently some recommendations are made for the improvement of welding conditions of the specific plates.

10.1 Conclusion regarding explosion welding for bi-metal joint fabrication

Explosion welding of an austenitic stainless steel to a large variety of copper grades was proven successful. Both materials show to be sufficiently ductile for the large deformations imposed by the explosion welding process. A single case demonstrated, however, that the ductility of the stainless steel base metal plate is not infinite. Unadapted welding parameters result in excessive collision velocity which results in the absence of vortices.

The explosion velocity is assumed exceeding 120% of the sonic velocity of the material being welded. 120% of the material's sonic velocity is the requirement for the collision point velocity to stay subsonic, resulting in a pressure wave to run in front of the collision point [Shrijit, 2019]. When the velocity of the detonated explosive exceeds this value a shock wave develops in the flyer plate, resulting in an extremely steep rise of the pressure. The material in front of the shock wave experiences no pressure, while the material behind the shock wave is compressed to high pressure. Significant plastic deformation takes place locally resulting in shock hardening and disintegration of the weld as a result of the high stress on the parent metal induced by the flyer. Interface defects are observed and local damage in the parent material with dimensions of 4 mm to 5 mm.

With optimised welding parameters 316 type austenitic stainless steel explosion welded to a copper alloy forms a Von Kármán vortex street at the interface, resulting in a favourable interlocking mechanism. The interlock structure originates from the presence of forward and counter-rotating vortices when a fluid turbulently flows around a blunt body. The Von Kármán vortex formation is accompanied by the forming of an intermetallic compound found in the counter-rotating vortex. Sufficiently large deformation takes place to allow for atomic diffusion. Mechanical measurements indicate intermetallics of non-brittle type as shear and tensile failure takes place in the copper cladding and not at the interface.

The formation of the counter-rotating vortex often leads to the entrapment of gas pockets, embedded in the welded structure as pores. Tensile and shear tests demonstrated that the properties of the clad plates, exhibiting a Von Kármán type interface wave pattern, are dominated by the individual materials. Independent of the imperfections described, the bi-metal fails consistently in the weaker C10100 copper cladding. This results in a tensile strength of the system of some 250 MPa(450 MPa) to 260 MPa(470 MPa) at room temperature (4.2 K), and a 0.2% yield strength of some 240 MPa(270 MPa) to 260 MPa(320 MPa) at room temperature (4.2 K), comparable to C10100 copper in a half-hard state (H02) with 250 MPa(290 MPa) for $R_{p0.2}(R_m)$.

In Plate 5 a different interface structure was observed. Explosion welding has led to the formation of a Kelvin-Helmholtz instability. This is commonly observed in fluid dynamics when there is a velocity difference between two constituents. Limited shear between the parent plate and the flyer plate results in limited diffusion. For Plate 5 no intermetallics were observed. The absence of intermetallics and a reduced interlocked state can account for its reduced shear strength with respect to Plate 1 and Plate 2 with a Von Kármán type interface holding a shear strength of 250 MPa to 390 MPa. However, with its shear strength of some 185 MPa it still scales with the shear strength of a C10100/C10200 copper alloy in an H02 temper, i.e. about 180 MPa. Furthermore, it exceeds the requirement of 120 MPa.

Mechanical measurements, on post explosion welding specimens, indicate increased hardening, beyond H02, towards the bonded interface layer, where the plastic deformation during the explosion welding is largest. Accordingly, copper RRR decreases towards the interface. This observation holds for all copper clad plates investigated, shown in table 10.1. The different heat-treatments applied in sequence, demonstrate little effect of the terminal soldering process on the RRR and mechanical characteristics of both high-purity (C10100) as well as low-purity (C12200) copper grade claddings (table 10.2). The final softening and heat-treatment simulating Nb_3Sn reaction treatment, however, results in the case of the high-purity C10100/C10200 Cu sole, in a high-RRR, low-hardness, fully-annealed state, in some cases beyond the initial state of the certified plates. On the other hand, for a low-purity copper, like the C12200 copper used for Plate 6, RRR values are driven mainly by impurity content. No significant increase of RRR is noticed with material annealing by the severe thermal cycle from some 4.5 to 5.5. Solely a large decrease in hardness is observed from about 95 HRF to 45 HRF.

Table 10.1: Summary of resistivity vs. hardness results at various positions in the copper claddings.

	Copper grade	State	Distance from interface		HRF	RRR
Plate 1	C10100	As-bonded	Top	at 11 mm	78 ± 1	154 ± 2
			Bottom	at 5 mm	85 ± 1	116 ± 1
Plate 2	C10100	As-bonded	Top	at 17 mm	77 ± 1	191 ± 2
			Middle	at 11 mm	83 ± 1	146 ± 1
			Bottom	at 5 mm	86 ± 1	126 ± 1
Plate 4	C10100	As-bonded	Top	at 21 mm	91 ± 1	69 ± 1
			Middle	at 13 mm	88 ± 1	72 ± 1
			Bottom	at 5 mm	96 ± 1	68 ± 1
Plate 5	C10200	As-bonded	Top	at 22 mm	72 ± 1	80 ± 1
			Middle	at 14 mm	78 ± 1	71 ± 1
			Bottom	at 6 mm	82 ± 1	67 ± 1
Plate 6	C12200	As-bonded	Top	at 9 mm	92 ± 1	4.8 ± 0.1
			Bottom	at 5 mm	96 ± 1	4.7 ± 0.1

Table 10.2: Summary of resistivity vs. hardness results of the copper claddings prior and subsequent to heat-treatments, simulating final joint formation.

	Copper grade	State	HRF		RRR	
Plate 1	C10100	As-bonded	78 - 85	(±1.6%)	116 - 154	(±1%)
		20 min at 230°C	78 - 86	(±1.6%)	134 - 176	(±1%)
		6 h at 400°C	31 - 32	(±1.6%)	474 - 524	(±1%)
		Certified plate (O25; 14 mm)	35		345	
Plate 2	C10100	As-bonded	77 - 86	(±1.6%)	126 - 191	(±1%)
		Certified plate (O25; 20 mm)	28		365	
Plate 4	C10100	As-bonded	88 - 96	(±1.6%)	68 - 72	(±1%)
		200 h at 650°C	36 - 42	(±1.6%)	350 - 361	(±1%)
		Certified plate (H02; 24 mm)	84		-	
Plate 5	C10200	As-bonded	72 - 82	(±1.6%)	67 - 80	(±1%)
		200 h at 650°C + 77 K shock	28	(±1.6%)	148 - 150	(±1%)
		Certified plate (M20; 27 mm)	49		170	
Plate 6	C12200	As-bonded	92 - 96	(±1.6%)	4.7 - 4.8	(±1%)
		20 min at 230°C	92 - 94	(±1.6%)	4.8	(±1%)
		6 h at 400°C	46 - 48	(±1.6%)	5.3	(±1%)

This implicates that for an electrical joint, connecting coils working in a pulsed regime, the use of a low-purity copper cladding serves. A low-RRR copper cladding reduces loop currents, hence reduces temperature rise, and increases the superconductor stability margin. Furthermore, this copper grade maintains its electrical properties while returning a softness suitable for cable compaction.

High-purity copper, in the form of a C10100 or C10200 grade is with its low resistivity suitable for (quasi-)stationary operating joints. Following reaction heat treatment these copper grades hardness, however, tend towards 40 HRF or below, relating to an approximate 0.2% yield point of 70 MPa at room temperature [Hardesty, 1980]. This could result in local yielding with the high forces introduced by the embedded superconducting cable, which needs to be taken into account.

For each individual application a copper purity needs to be identified, based on an optimum in electrical loss between alternating and direct current. An electrical joint positioned in a coil operated by alternating current, the use of a lower purity copper cladding, in combination with the severe thermal cycle implied by the reaction treatment of Nb_3Sn, results in a producible, low AC-loss electrical connection. Whereas for an electrical joint, only subjected to direct current, the use of a low-resistant, high-purity copper cladding shall be used, potentially omitting the softening treatment.

10.2 Recommendations for bi-metal improvement

Whereas for the Plates 1, 2, 4 and 6 profitable results were acquired in terms of interface characteristics, the welding process can be further adapted to reduce the possible entrapment of imperfections. An optimisation of the welding parameters suffices.

The formation of the counter-rotating vortex follows from the ’hump’ interfering with the jet (figure 7.4e),where the jet folds back onto itself. An air-pocket forms, later turning into the tail. The jet then needs to go up and over to reach the front vortex, after which the process repeats itself. A smaller impact angle can result in the formation of a smaller air-pocket at the hind-side of the ’hump’. A decreased angle in a parallel set-up means the reduction of the stand-off distance. One shall take into account, however, that generally a decrease of the impact angle is accompanied by a reduction in collision impact velocity, and thus the amplitude, wavelength and most importantly turbulence (thus interlocking) of the interface.

For Plates 3 and 5 an adjustment to the process parameters needs to be considered. For Plate 3 this involves the type and amount of explosive, possibly together with the stand-off distance used. For Plate 5 the Kelvin-Helmholtz instability is believed to be resulting from a too high difference in horizontal velocity between the flyer and the parent plate, or even between the re-entrant jet and the base plate [Carton, 2004]. This could indicate the usage of a too large impact angle, giving the flyer plate, and re-entrant jet, a relatively large forward component. Reduction of the stand-off distance can be sufficient in this case. This will simultaneously increase the shear at the surface where the two materials meet.

To summarise, explosion welding can be the perfect welding process for fusing joint members in the ITER type CIC conductor connections. Nevertheless, to realise a faultless weld, the process needs to be closely monitored, and specific welding campaigns to determine optimal parameters performed.

Part III

Customised high-purity aluminium as a structurally fit superconductor stabiliser

11

Challenging structural strength of a high-purity aluminium stabiliser

> ***What do you call that nice, shiny white metal they use to make slidings and air planes out of? Aluminum, right? Aluminum, pronounced 'uh-LOO-mih-num', right? Anybody knows that! But do you know how the British spell it? 'Aluminium', pronounced 'Al-yoo-MIH-nee-um'. Ever hear anything so ridiculous? The French and Germans spell it 'aluminium', too, but they're foreigners who don't speak Earth-standard. You'd think the British, however, using our language, would be more careful***
>
> — **Isaac Asimov**
> (American writer and biochemist)

High-purity aluminium, with a purity of 99,999% or more, or five-nine aluminium (from now on denoted as 5N aluminium) is used as a stabiliser material in many composite NbTi superconductors for high-energy physics detector magnets, rather than copper [Ten Kate, 2008]. Pure aluminium compares favourably with copper as a result of its better transparency to particles, its excellent thermal and electrical conductivity at 4.2 K, and its reduced mass and cost.

High-purity aluminium is characterised by its high RRR value, however, unfortunately also by its relatively low mechanical strength. From section 1.1.2, where the simultaneous requirements of increasing magnetic field and large bores results in stringent requirements for the superconducting coil, we note that the necessity for a large-size, reinforced aluminium stabilised conductor is essential.

In this introductory chapter concepts of reinforced aluminium for conductive purposes are introduced. The current state-of-the art is presented including a historical overview. Different methods of mechanical strengthening are discussed, amongst which the use of lattice modifications to hinder running dislocations. The main focus lies on the deliberate introduction of precipitates and dislocations as blocking points for running dislocations. In the last section the influence of lattice modifications on the electro-thermal transport properties is described in order to determine the best trade-off between mechanical and conducting behaviour.

11.1 Introduction

Over the years it has become increasingly apparent that high-purity aluminium is no longer sufficing for superconductor stabilising purposes. Where for a wide range of detector magnets aluminium in its purest form was still satisfactory, and the stabiliser's role was limited to thermal and electrical transport, in some cases local or global plasticity became worrisome. The mechanical load on the stabilised superconductors in combination with the request to maintain a highly radiation transparent conductor while maintaining structural integrity of the coil (i.e. a self-supporting structure), led to the investigation of reinforced stabiliser solutions.

The evolution of reinforced stabilisers commenced in the nineties of last century with the Solenoid Detector Collaboration, SDC, prototype solenoid, for which a light aluminium alloy was introduced to withstand hoop stress in the coil [Yamamoto et al., 1995]. In the further development for the LHC, where collision energies were foreseen of up to 14 TeV, this research was continued. With operating currents up to 20 kA, magnetic fields towards 4 T, and bore diameters reaching 6 m, reinforcement became essential. Hoop stress in operating condition here reaches almost 100 MPa on the conductor cross-section. Note that in this extreme case an additional external structure was employed.

Two alternative strategies were developed. The first is based on boundary strengthening, by separating the mechanical purpose of the stabiliser from its electrical/thermal one. The second one targets an integral solution, by integrating the mechanical function into the material directly surrounding the superconductor, thereby coupling its mechanical and conducting function.

CMS, the Compact Muon Solenoid, adapted the former solution. A 20 kA superconductor is wound inside a 50 mm thick external support cylinder. The conductor consists of a 32-strand superconducting Rutherford cable (section 1.2.3), stabilised with high-purity aluminium, and subsequently mechanically reinforced with two continuous sections of an aluminium alloy specifically selected for the application [Sgobba et al., 2006; Martin et al., 1996]. A continuous electronbeam (EB) welding technique was developed, connecting the reinforcement bands to the 2.6 km long conductor units. Figure 11.1 shows a representation of the specific aluminium-stabilised conductors, illustrating the evolution of the conductors for detector magnets over the past years. On the far right is a representation of the CMS conductor, with its high-purity (in this case 4N) aluminium stabiliser coupled to the high-strength aluminium alloy EN AW 6082.

In this boundary-strengthening solution, the 4N aluminium stabiliser, directly surrounding the Rutherford cable, acts as the electrical and thermal stabiliser. The EN AW 6082-alloy carries the mechanical load thanks to its exceptionally high yield strength with an $R_{p0.2}$ of 258 MPa at the operating temperature of 4.2 K, following a customer's heat-treatment (i.e. magnet coil curing cycle, which results in peak-aged properties). The effect of the processing that is required for this type 'boundary reinforcement' on the RRR of the high-purity stabiliser is considered negligible. The RRR is primarily influenced by the co-extrusion of the insert and not necessarily by the EB-welding process. Since the electrical resistivity of EN AW 6082 is a factor 1000 higher than the 4N Al stabiliser, its effect on the overall electrical resistivity is estimated to be less than 1% [Curé et al., 2004].

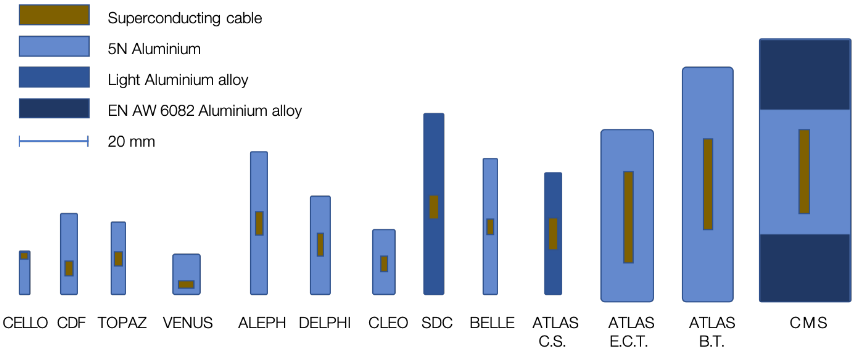

Figure 11.1: Schematic of the history in aluminium stabilisers used in detector magnets over the past years, chronologically ordered [Yamamoto et al., 1999]. Note the advancement in the use of aluminium alloys with time, coincident with the increase in magnetic field strength and magnet bore size.

For the ATLAS central solenoid (CS), operating at a nominal field of 2 T at a current of 7.6 kA, with a free bore diameter of 2.4 m, a volume-strengthened aluminium stabiliser is used. Since the magnetic-field configuration in the ATLAS detector is relatively complex (section 1.1.2), load composition is fairly complicated, with local and global loads intertwined. To stabilise the central solenoid coil its design features two specific characteristics: a uniformly reinforced, high-purity stabiliser, combined with the use of a pure aluminium strip to ensure uniform energy absorption and quench protection [Yamamoto et al., 2008]. The use of a low-alloyed high-purity aluminium stabiliser (as depicted in figure 11.1), has as two major advantages: the preservation of high particle transparency, and the ability to avoid local plasticity.

The Nb-Ti/Cu superconductor is directly co-extruded with the low-alloyed high-purity stabiliser (section 1.1.2), reducing further processing steps. Note that the elimination of an additional element, such as the reinforced sections for the CMS conductor, also reduces locations where failure could initiate.

In the integral strategy, applying volume strengthening, concessions need to be made since RRR is exponentially related to impurity content. Particularly in high-RRR materials, like 5N aluminium, a low alloying addition will cause a significant decrease in RRR, i.e. the electrical and thermal resistivity of the material will rise, making this a delicate process (figure 11.2). The high-purity reinforced aluminium stabiliser used in the ATLAS CS, features an $R_{p0.2}$ of $\sim$100 MPa at 4.2 K, following cold-drawing and coil-curing cycle, while its RRR value remains above 500 [Tonogi et al., 1999].

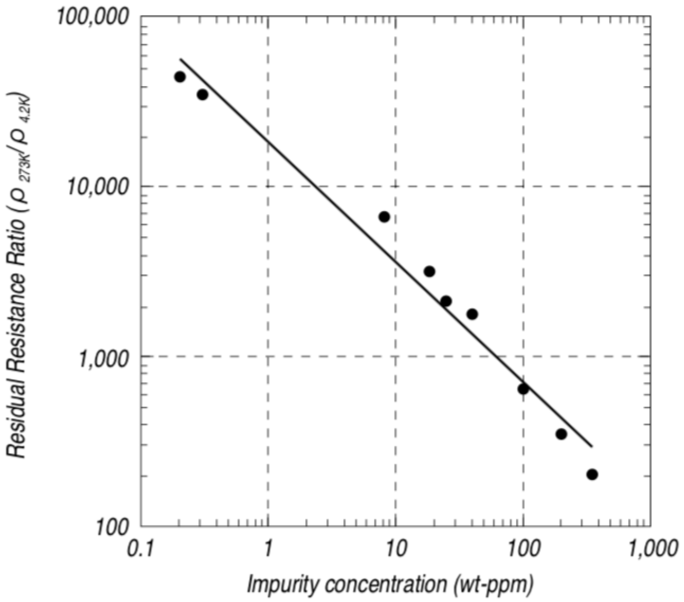

Figure 11.2: Influence of impurity concentration on the Residual Resistivity Ratio (RRR) of high-purity aluminium [Tonogi et al., 1999]. Notice the exponential behaviour, only 100 ppm impurity content reduces the RRR to less than 1000.

In this study a reinforced stabiliser scale-up is proposed based on volumetric strengthening by adjusting the chemical composition of the entire stabiliser. This choice is made because, like in the ATLAS case, in future detector magnets local plasticity can be expected to play a major role. However, in the future one could also consider a hybrid solution, where boundary strengthening is applied alongside a volume-strengthening solution.

11.2 Lattice imperfections for mechanical strength

All crystalline materials contain lattice imperfections. Lattice imperfections may be introduced deliberately during the production process, by adjusting the chemical composition (e.g. ATLAS CS stabiliser), or by dedicated post-production material treatments. Lattice imperfections can, however, also be introduced unintentionally during application-based material processing.

Obtaining a virtually perfect material, with absence of any lattice imperfections, is challenging. Often though a 'perfect' material is not suitable for a given application. Lattice imperfections are known to 'pin' other growing defects, resulting in an enhanced strength of the material. Although dislocations are generally the dominant carriers of plasticity, they can also serve as a hardening mechanism by pinning others.

Here we will describe specific methods to introduce mechanical strengthening by lattice modification. In table 11.1 the crystalline imperfections treated are summarised, together with their associated strengthening effect, and the section in which they are discussed.

Table 11.1: Strengthening mechanism of crystalline imperfections.

0D	1D	2D	3D
Solid-solution strengthening	Work-hardening	Hall-Petch strengthening	Precipitate strengthening
vacancies	*edge dislocations*	*external surfaces*	*secondary phases*
interstitials	*screw dislocations*	*grain boundaries*	*inclusions*
	mixed dislocations	*twin boundaries*	*pores*
		phase boundaries	*cracks*
section 11.3.2	section 11.2.1	section 11.2.2	section 11.2.3

11.2.1 Dislocations

Dislocations, one-dimensional defects along which the atoms in the crystalline structure are misaligned, are commonly introduced during material production and post-treatment. They generally result from internal stress introduced during material solidification or from plastic deformation under thermal stress, and are often associated with fast cooling processes. Dislocations can also be introduced by external loads resulting in material plasticity. Dislocations result in a rearrangement of the lattice that propagates through the microstructure. The dislocations create weaker, strained, lattice bonds than the bonds in a regular crystal lattice, making them a typical origin of failure as a result of plastic deformation.

This kind of lattice distortion is found in a variety of sorts, depending on the type of slip-plane they form. One can distinguish edge-, screw- and mixed dislocations, where the latter is, as suggested, a mix of the former two. An edge dislocation, often resulting from normal stress, exists along the line where an additional half-plane of atoms is present. A screw dislocation on the other hand is thought to be resulting from internal shear forces, and relates to the lateral shift by one atomic distance of the upper front region of the crystal with respect to its bottom region [Callister et al., 2009].

A Burgers vector can be associated with a dislocation to describe its direction and magnitude [Callister et al., 2009]. The direction of a pure edge dislocation is perpendicular, that of a true screw dislocation parallel to the Burgers vector. For metals, the topic of this thesis, the Burgers vector points in a close-packed crystallographic direction, and its magnitude is equal to the atomic spacing.

Hardening by dislocations

Work-hardening, also called strain-hardening or cold work, is a process involving the intentional introduction of plastification, i.e. dislocations on an atomic scale, with the purpose of hardening the material, by dislocation pinning.

The mechanism of dislocation pinning can be described by a thermodynamic process. A crystal lattice tends to the lowest energy state by formation of bonds between its constituents. Similarly, dislocations interact to achieve the most favourable energy condition of the crystal. As a result of lattice rearrangement, local strain fields are present around dislocations. Negatively strained bonds next to a dislocation generate a compressive strain field, whereas positively strained bonds beyond the end of a dislocation generate a neighbouring tensile strain field. The interaction with the strain fields of neighbouring dislocations can be described by the general principle of charged fields, where opposite charge attracts.

As a result from this obstructed dislocation movement, higher stress levels are required for plastic deformation. In a work-hardened material at moderate stress levels only elastic deformation occurs, leaving it with an increased yield point. Lattice bonds are strained and released upon load according to the original modulus of elasticity. Plasticity simply shifts to higher stress levels, with a decreased ductility since the ultimate tensile strength classically[1] remains unchanged [Callister et al., 2011].

Work-hardening can be described by:

$$\sigma = \sigma_y + \kappa(\epsilon_0 + \epsilon_p)^n, \tag{11.1}$$

where σ denotes the new yield stress, κ the strength index, ϵ_p the introduced plastic strain, ϵ_0 the plastic strain prior to processing, and n the strain-hardening index. The latter is defined as:

$$n = \frac{dlog(\sigma)}{dlog(\epsilon)} = \frac{\epsilon}{\sigma}\frac{d\sigma}{d\epsilon}, \tag{11.2}$$

where $\epsilon = (\epsilon_0 + \epsilon_p)$. Rearrangement of equation 11.2 results in the determination of the rate of strain-hardening at a given stress and strain:

$$\frac{d\sigma}{d\epsilon} = n\frac{\sigma}{\epsilon}. \tag{11.3}$$

Work hardening is especially effective in materials with a high ductility and a reasonably high melting point. Plastic deformation is introduced at a relatively low temperature, typically ambient temperature; i.e. well below the recrystallisation temperature.

11.2.2 Interface imperfections

With interface imperfections we denote all crystal imperfections that are two-dimensional and separate regions of the material that have different crystal structures and/or crystallographic orientations. This label covers external surfaces, grain boundaries, twin boundaries and phase boundaries. Such boundaries are accompanied by a surface energy, increasing the overall energy of the system. At the external boundaries, atoms are not bound to the full number of neighbours,

---

[1] In basic quasi-static elastic-plastic deformation. Some higher-order effects can result in a slight change of R_m with work-hardening, this is however not its main purpose.

which means that some bonds of atoms are not satisfied, which rises their energy with respect to atoms well inside the lattice.

At grain boundaries this higher energy state results from differing crystallographic orientation along the boundary. Across the boundary an atomic mismatch is found, resulting in a local energy rise, analogous with the surface atoms prior discussed.

A twin boundary involves a similar mismatch as a result of a discontinuity in lattice regularity, with atoms positioned in mirror positions with respect to each other at either side of the boundary.

Similarly a higher energy state exists at a phase boundary, in materials composed of a multitude of phases, where a variation in physical and/or chemical composition results in a comparable lattice mismatch [Callister et al., 2009].

Hall-Petch strengthening

Hall-Petch strengthening makes use of this increased energy associated with the strain field at the grain boundaries. The disorder found at the border between two adjacent grains results in an 'arresting' point for a propagating dislocation, which would need to pass the region of increased strain energy. Moreover, a local change in grain orientation leads to a deceleration of dislocation movement as it also has to change direction. A dislocation pile-up generally occurs, resulting in an energy barrier. The dislocation pile-up is suddenly release when dislocation force exceeds the energetic barrier.

Decreasing the grain size increases the probability and frequency that a dislocation encounters such a barrier. This reduces pile-up as dislocations are better distributed. The maximum Hall-Petch strengthening is achieved when grain size approaches the dislocation size. At this point grain boundary sliding starts to occur, resulting in a decrease in material strength [Callister et al., 2011].

Grain size decrease can be achieved by a variety of processes, amongst which mechanical processing such as the aforementioned cold working. Also specific thermal treatments can result in a reduction of grain size.

11.2.3 Volume imperfections

Under volume imperfections or three-dimensional imperfections, we denote pores, cracks, foreign inclusions and all other secondary phases.

Precipitation hardening

Precipitates are volume imperfections that are introduced intentionally with the purpose of increasing mechanical strength. Precipitates are generally formed from an oversaturated solid-solution by using the temperature dependence of solubility of the element in the host material. This technique is used to increase the yield strength of materials, in a similar manner as the introduction of dislocations or interfacial defects by impeding the movement of other lattice defects.

A wide range of elements are frequently used in aluminium alloys for precipitation strengthening. The process generally commences by a solid-solution heat treatment to reach the maximum practical concentration of the hardening constituent in solid-solution. This involves heating the aluminium alloy close to the eutectic temperature, maintaining the temperature for a certain period to effect the desired solution, followed by a quench to retain this solution [Walsh, 1994]. Quenching in material-processing refers to a cool-down, which is rapid enough to not leave time for phase transformations.

The following 'ageing' treatment, named after the length of time required to achieve the optimal effect, can produce varying sizes and types of precipitates in the host solid. Depending on their size and type, precipitates can have different effects on the materials properties. The diffusion required for the ageing process depends highly on temperature, making it a fairly delicate process. Too little diffusion, 'under-ageing', will result in precipitates that are too small to impede running dislocations. 'Over-ageing', i.e. too much diffusion, will result in large precipitates, too dispersed to interact with the majority of the propagating dislocations.

An optimum exists in precipitation size, for the dispersion and blocking mechanisms. This optimum reflects the different ways a propagating dislocation may interact with a precipitate with radius r. A dislocation may 'cut' through the precipitate, leaving a locally increased surface strain-energy, but it can also 'bow' around it. The impact on the material strength of these two mechanisms can be quantified as:

$$\tau = \frac{r\gamma_s\pi}{bL}, \tag{11.4a}$$

$$\tau = \frac{Gb}{L-2r}, \tag{11.4b}$$

where equation 11.4a gives a simplified description of dislocation cutting and equation 11.4b of dislocation bowing. τ here denotes the material strength, r the precipitate radius, γ_s the initial surface energy, b the magnitude of the Burgers vector, L the spacing between adjacent pinning points, and G the shear modulus. Note that the mechanism of 'cutting' is directly proportional to the radius of the precipitate. This simply reflects that smaller precipitates require less effort to cut through.

When the precipitates grow, they become increasingly difficult for the dislocations to cut through. Precipitates increasingly impede the movement of the dislocations until the 'bowing' mechanism takes over. This is referred to as Orowan strengthening, which becomes more important when precipitates become larger, and dislocations take the path of least resistance. This is reflected by the presence of L and r in the denominator. Precipitate radius r and their spacing L are proportionally related via the volume fraction of the secondary phase in the host material. Figure 11.3 demonstrates the crossing point in the strength versus precipitation size relation, where bowing takes over from cutting with increasing precipitate radius.

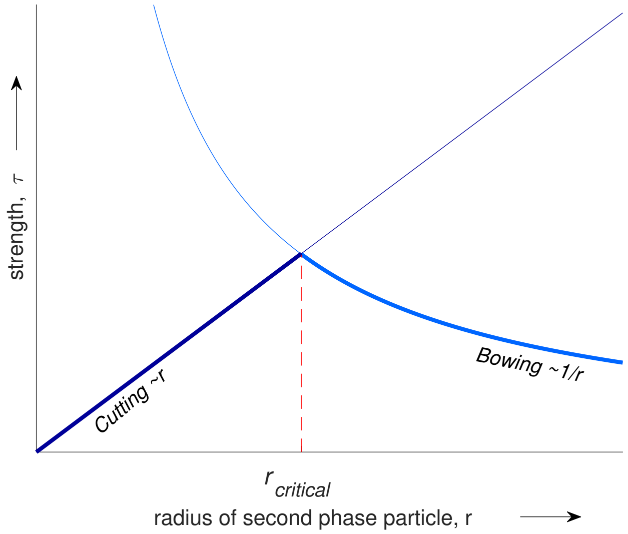

Figure 11.3: Precipitation strengthening mechanisms with increasing secondary phase particle size. An optimum, $r_{critical}$, exists where precipitation bowing (or looping) takes over from precipitation cutting, or in other words; slip-planes running though the secondary phase particle [Callister et al., 2011].

11.3 Introducing impurities

Lattice discontinuities and stress fields that arrest dislocations during slip are of great interest to the tailor-made aluminium stabiliser material. Introduction of secondary phase particles can be realised in a variety of ways. Precipitates can be formed following from metallic alloying additions. However, also recent development of light metals for structural applications by powder metallurgy processes provide possibilities. Powder metallurgy can be used to introduce inclusions of any nature in the metal matrix.

11.3.1 Metal matrix composites

For the design of light metals for structural applications, strengthening by ceramic fibres or particles has received a lot of attention [Kainer, 1996]. The metal matrix composites, or MMCs, are modern materials, which can theoretically be tailored to perfection. Most often used are discontinuous particulate or whisker (short fibre) reinforcements (figure 11.4), which can drastically increase yield point, fatigue strength and creep resistance. The obvious advantage of discontinuous reinforced (as compared to continuous fibre reinforced) MMCs is that it renders the material isotropic. Furthermore, standard shaping methods such as extrusion, forging and rolling of the ready-made material can be used, which is a necessity for the application envisaged here.

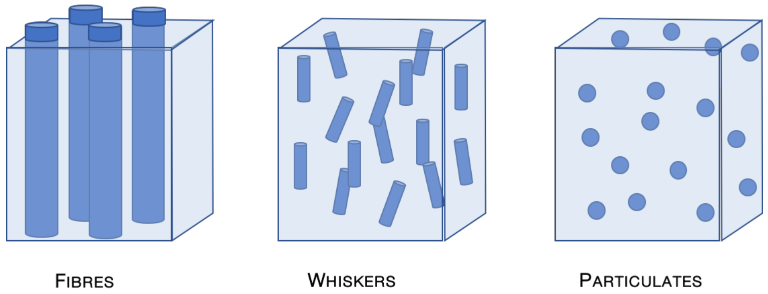

Figure 11.4: Schematics of the reinforcements adopted in MMC structures, where an obvious advantage can be recognised from whisker and mainly particulate additions in terms of manufacturability and isotropy [Clyne et al., 1995].

With the adaptation of powder-metallurgy production techniques, a multitude of ceramic reinforcement options is possible, all of which are known for stability during thermal processing as no solubility or segregation issues are encountered. The most commonly used discontinuous reinforcement particles in an aluminium matrix are alumina particles; specific carbides such as SiC or B_4C; and carbon in various forms such as graphite. Recently carbon particulates known as ’buckyballs’ and ’nanotubes’ are being developed, enabling low added material density.

Powder-metallurgy processes generally involve extrusion and/or forging of metal powder - particle mixtures. In some cases spray-forming or 3D-printing techniques are used. The disadvantage of these processes, to date, is the relatively limited cleanliness of the process. Specifically in the context of this thesis a significant amount of additional impurities will be introduced in the highly-pure metal matrix, degrading its transport characteristics.

New deposition and in-situ processes nonetheless show great promise, and are currently being studied. This could make MMCs potentially very interesting for future use.

11.3.2 Mechanical alloying

Mechanical alloying, or alloying for mechanical purposes, is the most common way to enhance the structural strength of a material. In fact, even though highly-pure aluminium is the 4th best electrical conductor, it is hardly ever used in its 5N form for electrical purposes, let alone when structural strength is required. High-conductivity commercial aluminium alloys like Al 1350 EC (Electrical Conduction) already contains and impurity content of 0.5 wt.%. Despite this ’reinforcement’, its $R_{p0.2}$ in the annealed state, i.e. Al 1350-O, is constrained to some 30 MPa, limiting its applications. 5N Al in its pure form will barely reach an $R_{p0.2}$ of 10 MPa, and is thus almost malleable by hand [Kaufman, 1999]. Alloying is an efficient means to increase the structural potential of an electrical conducting materia, but can also be to a high degree, detrimental for its transport properties, as will be discussed in section 11.4.

Low impurity content alloying is generally advisable, here designated as ’doping’. With doping we denote alloying additions up to a maximum of 2 wt.%. To achieve the necessary $R_{p0.2}$ of 120 MPa of our tailor-made aluminium solely by alloying is challenging. Additional strength shall therefore come from supplementary lattice imperfections as described in section 11.2. Precipitation alloying, however, is well adapted for strengthening here as it inhibits recrystallisation in post-processing thermal treatments. Precipitates have an additional advantage over MMCs as their formation tends to start in the vicinity of present dislocations, where their presence thus most effectively reduces the number of mobile dislocations [Reed, 1972].

In the future MMC structures could provide an answer for further enhancement of a high-strength, high-RRR aluminium stabiliser, for now we will focus on the possibilities of a ’doped’ alloy.

11.4 Reduced transport properties due to lattice imperfections

In the previous paragraphs we discussed how material strengthening involves the inhibition of propagating dislocations by some form of densely spaced foreign ’phase’. However, it is this same inter-phase spacing, which is critical when discussing the metal’s transport characteristics. As soon as the inter-phase spacing approaches the mean free path of the moving electrons, resistivity will increase as a result of interface scattering.

11.4.1 Mean free path concession

Electrical resistivity is known to originate from electron scattering as a result of thermal vibrations of the crystal lattice (phonons), and the presence of imperfections in the structure [Kasap, 2005]. The relative effect of each of the imperfections described in section 11.2 on the transport characteristics varies with material system, impurity type and degree of grain refinement and cold work applied. The rule of Nordheim states that in general, in a dilute state, the residual resistivity at low temperature is directly proportional to the impurity concentration [Hall, 1959]. This has been shown to be also valid for aluminium [Cook et al., 1997].

A ’phase’ is defined as a more-or-less homogeneous region in the system with uniform chemistry and physical characteristics. Full solubility of one element into another results in a single-phased system and the resulting material therefore has uniform characteristics over the volume (leaving micro-structural alterations out of consideration). When more than one phase is present in a given system, each will have its own properties and the boundary between them will give rise to an abrupt change in characteristics. Different phases can result from either (or both) different physical or chemical characteristics.

Elements in solid-solution are known for their impact on electrical resistivity. As a result of the homogeneity of the single phase structure, electron conduction needs to run through this phase, inherently defining the conductivity. The new atomic structure results in the change of mean free path. In the case of a secondary phase, or particulate, in a highly-conductive low-strength matrix electrons take the path of least resistance, here the conductive matrix. Precipitate alloying can increase mechanical properties while reducing its effect on the electrical conductivity.

11.4.2 Adapting solubility to application

Choosing a reinforcement addition or impurity concerns the assessment of mechanical strengthening that follows from compositional changes, and the effect of the alloying addition following from further processing. Specifically the alloyed material's work-hardening susceptibility and its compatibility with later heat treatments is of concern.

Co-extrusion of a superconducting cable with an aluminium stabiliser leaves little margin for later thermal treatments, and makes precipitation-hardening challenging. The aluminium stabiliser alloy must allow for a temporary temperature increase during the co-extrusion process (described in section 12.2.1), and the coil-curing treatment (described in Section 13.4). The processes shall not detrimentally affect sought-for material properties below their required value. Designed for application, the material shall be thermally stable throughout processing.

By targeting a low solid-solubility of the reinforcement element for a wide range of temperatures these detrimental effects can be avoided. By choosing wisely one can introduce a low quantity of impurities in a precipitate state without relying on thermal ageing. The secondary phase atoms will provide a recrystallisation resistance against annealing in the process of coil curing.

Alloying elements

In the design of the material a minimum influence of the impurities on the transport characteristics is targeted, with a maximum mechanical effect. Additive elements like chromium or iron are known for their low solubility in aluminium. However, even at low concentrations Cr and Fe greatly impact the electrical resistivity table 11.2. Elements such as magnesium, copper and zinc are known for their increased solubility in aluminium. Nevertheless, in solid-solution Mg, Cu and Zn have relatively less influence on the alloy's electrical resistivity. The correct alloying addition therefore not directly follows from its solubility in aluminium, but also its additional electrical resistivity it brings in either state (i.e. in solid-solution or precipitated state).

Electrical resistivity, and in particular the resistivity increase due to solute impurities, is often denoted in percent International Annealed Copper Standard %IACS, where the conductivity of annealed copper is taken as a reference. The conductivity of annealed copper is $5.8 \cdot 10^7\ S/\mathrm{m}$, measured at $20°\mathrm{C}$ [United States National Bureau of Standards, 1914]. Note that this standard dates from the year 1914. With the current production techniques this reference is slightly outdated, but is still used as definition of 100% IACS. We can express the electrical conductivity of a metal as:

$$\sigma_{\%IACS} = \frac{\sigma_{S/\mathrm{m}}}{5.8 \cdot 10^7 S/\mathrm{m}} \cdot 100, \tag{11.5a}$$

$$\sigma_{\%IACS} = 172.41 \cdot \sigma_{\mu S/\mathrm{cm}}, \tag{11.5b}$$

where $\sigma_{S/\mathrm{m}}$ and $\sigma_{\mu S/\mathrm{cm}}$ denote the electrical conductivity in siemens per meter and microsiemens per meter, respectively.

Since conductivity σ, and resistivity ρ are inversely proportional, we can describe %IACS also as:

$$\sigma_{\%IACS} = \frac{172.41}{\rho_{\mu\Omega\cdot\mathrm{cm}}}. \tag{11.6}$$

High-purity aluminium, with a resistivity of $2.65\ \mu\Omega \cdot \mathrm{cm}$ at $20°\mathrm{C}$ (figure 11.5), then has conductivity of 65% IACS. If we would introduce in this high-purity aluminium matrix 1 wt.% titanium, at its solubility limit, the electrical conductivity reduces with 31% IACS, bringing the resulting conductivity of this 'doped' alloy down to 33% IACS.

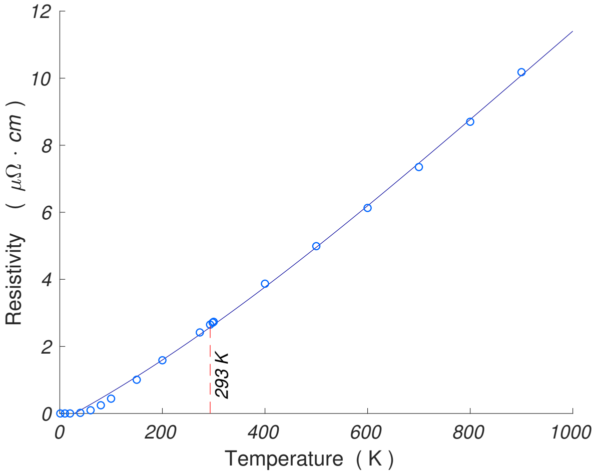

Figure 11.5: Electrical resistivity of polycrystalline, annealed 5N aluminium as a function of temperature. The reference resistivity value at 20°C, i.e. 293 K, is shown by means of the red dashed line, and measures $2.65\ \mu\Omega \cdot \mathrm{cm}$[Lide, 1994].

In table 11.2 a selection of possible solutes is listed from which high-purity aluminium could benefit in terms of mechanical properties. The effect of the individual solutes depends on their valency, atomic size and other differences from the aluminium solvent material. These binary alloys have been selected either because of their high influence on the mechanical properties by developing intermetallic compounds, or due to their low influence on the electrical conductivity. Note that low compatibility of the solute and solvent creates higher strain fields, and thus better dislocation impedance. Note that from table 11.2 the negative effect of precipitates on the electrical performance is far less than that of impurities present in solid-solution. As discussed in section 11.2.3 the advantage of precipitates in the solvent matrix is their high interference with running dislocations.

Table 11.2: Impurity solutes and their effect on the electrical conductivity of aluminium [Cook et al., 1997; Takahashi et al., 1997; Wada et al., 2000a; Yamamoto et al., 1999; KB Alloys Inc., 2007; Wang et al., 2002].

Element	**At. weight**	**Density**	**Temperature**[a]	**Solid**	**Conductivity loss per wt.%**	
				Solubility	in solid solution	precipitated
	[u]	[g/cm^3]	[°C]	[wt.%]	[%IACS]	[%IACS]
B	10.811	2.34	600	<0.001[b]		2.1
Mg	24.305	1.74	450	14.90	11.0	5.0
Si	28.086	2.33	580	1.650	14.5	2.1
Ti	47.867	4.54	665[c]	1.000	31.0	2.5
V	50.942	6.11	665[c]	0.600	34.0	5.5
Cr	51.996	7.19	660[c]	0.770	40.6	4.1
Mn	54.938	7.43	660	1.820	37.0	7.4
Fe	55.845	7.87	655	0.052	34.3	1.4
Ni	58.693	8.90	640	0.050	15.3	1.5
Cu	63.546	8.96	550	5.670	7.6	0.7
Zn	65.390	7.13	380	82.80	2.4	0.6
Ga	69.723	5.91	30	20.00	3.0	
Sb	121.76	6.68	660	0.100	4.8	
Ce	140.12	6.77	640	0.050	0.2	

[a] eutectic unless stated otherwise
[b] in effect value to be treated as if in precipitated state
[c] peritectic

The quest for a reinforced aluminium stabiliser based on a precipitation 'doped' material is therefore legitimate. Table 11.2 brings certain solutes to attention, with boron showing high potential. Because of its extremely low solid-solubility in aluminium, any increase in resistivity is accounted for by precipitates. Boron, or BORAL master alloys, AlB_2 and AlB_{12} are often used in the initial production of high-purity aluminium. When boron is added in sufficient quantities, it reacts to form insoluble boron compounds with trace elements like chromium, titanium, zirconium and vanadium present in the aluminium ingots. The insoluble diborides formed from AlB_{12}, however, tend to settle out of the metal, leaving little to no reinforcement impurities. On the other hand, the insoluble diborides formed from AlB_2 remain entrained but introduce significant grain refining response. Since excessively small grains significantly enhance the electrical resistivity, boron is considered unfit for the application.

A few solutes have been left out of the table, despite their low solid-solubility in Al, because of the nature of the application, i.e. the possibility of nuclear reactions taking place. Reactions with certain trace elements will give rise to additional nuclides, which can be radioactive and thus undesired, especially if they are long-lived. An example is ^{60}Co, produced by thermal-neutron capture by traces of cobalt in aluminium or iron. This nuclide can dominate the radioactivity many years after irradiation, when most other nuclides have already decayed. A similar issue is found with trace elements of sodium, giving rise to the nuclide ^{22}Na, with a 2.6 year half-time [Forkel-Wirth et al., 2013].

Tin is similarly omitted, because of the binary alloy's low eutectic temperature, which complicates post production thermal treatments (i.e. coil-curing cycles).

The remainder of low-soluble impurity elements presented in the table has been extensively studied in the search for a stabiliser material for the ATLAS central solenoid [Yamamoto et al., 1999; Wada et al., 2000a; Wada et al., 2000b]. Not only the suitability of nickel, antimony and the rare earth cerium have been studied, but also the effect of their concentration, the fabrication method and post processing (i.e. cold work and coil-curing). Measurements have shown the suitability of all three solutes in the precipitation-strengthening of the highly pure aluminium. A slight preference for Sb and Ce was identified when concentrating on their low effect on the residual resistivity, while Ni was found to have a greater effect on the mechanical properties at low concentrations. Table 11.3 shows a summary of these studies.

When reading this table we should keep in mind that these are material characteristics of the bulk. The measurements were performed on specimens extracted from worked material, however, they were not obtained from the fully processed application. The yield strength of these alloys will generally further increase when processed on a production scale, however consequently, their transport properties will deteriorate.

Table 11.3: Mechanical and transport properties of selected precipitation Al-alloys at different stages of cold-working (i.e. cross-section reduction) [Yamamoto et al., 1999; Wada et al., 2000a; Wada et al., 2000b].

	15% reduced[a]		20% reduced		25% reduced	
	RRR	$R_{p0.2}$[b] [MPa]	RRR	$R_{p0.2}$ [MPa]	RRR	$R_{p0.2}$ [MPa]
Al-0.05wt.%Ni	620	57	583	64	564	67
Al-0.1wt.%Ni	522	61	530	68	517	70
Al-0.2wt.%Ni			625	64		
Al-0.5wt.%Ni			400	78		
Al-1.0wt.%Ni			250	82		
Al-2.0wt.%Ni			200	106		
Al-0.2wt.%Ce	1393	48				
Al-0.5wt.%Ce	739	56	724	65	642	67
Al-1.0wt.%Ce	394	68				
Al-0.3wt.%Sb	1120	49				
Al-0.8wt.%Sb	745	56	775	65	782	67

[a] prior to measurements the material has been cured for 15 h at 130°C

[b] mechanical measurements performed at ambient temperature

The relatively small influence of Ce and Sb on the RRR follows from their low solubility in aluminium as predicted by table 11.2. Cerium is despite being a 'rare earth element' a relatively plentiful element in the earth's crust, at 68 ppm (similar to copper). However, due to its geochemical properties, rare earth elements are generally very dispersed and not often found sufficiently concentrated to be economically exploitable. This makes Ce a very expensive solute, and thus less suitable for large-scale applications. The same holds for Sb, which is a less abundant element. Sb is used in the semi-conductor industry, although in small quantities because of its elevated price.

The choice was therefore to explore the possibilities of a nickel 'doped' aluminium, a material with higher production possibilities, and moreover a proven concept in the current ATLAS central solenoid. Supersaturated nickel atoms already precipitate in aluminium at some 0.005 wt.% addition at 500°C, due to a change in solid-solubility with temperature similar as observed in precipitation hardening, i.e. ageing [Fink et al., 1934; Tsubakino et al., 1996]. Furthermore, the precipitated nickel atoms form intermetallic compounds with aluminium during subsequent heat-treatment, allowing the electrical resistivity to decrease even further. Finally, the small nickel that remains in solid-solution, has a relatively small impact on the overall electrical resistivity.

When considering the scale-up towards a 60 kA, 5 T class conductor at 4.2 K, for which we reckoned to need an $R_{p0.2}$ of 120 MPa, and an RRR of some 500, we can deduce from table 11.3 that the highest potential lies in a nickel concentration of 1000 ppm to 2000 ppm, in other words between 0.1 wt.% and 0.2 wt.%.

12

Effect of mechanical alloying on 5N-Al characteristics

In sections 11.3.2 and 11.4.2 it was introduced that a precipitation-type alloy, obtained by dilute-alloying of high-purity aluminium with a suitable additive like Ni, cold-drawn (20% reduction) and finally subjected to partial annealing, can feature a yield strength of some 70 MPa at ambient temperature (in bulk). Simultaneously this process retains a relatively high-purity aluminium matrix by preventing the impurity solute atoms to enter into solution state, allowing for a RRR as high as about 500.

Specifically, the precipitation-type alloy studied here is a 5N aluminium doped with 0.1 wt.% nickel, selected based on its proven track-record.

This chapter deals with the mechanical improvement made when adopting a dilute-alloyed aluminium with respect to a 5N aluminium for a scaled-up stabilised superconductor. The large-scale co-extrusion process is described with the specific materials and process parameters used. Mechanical versus transport properties of the co-extruded dilute-alloyed aluminium is compared to those of an extruded 5N-aluminium. Effects in the microstructure resulting from both dilute-alloying as well as the production process are assessed, thereby reasoning possible additional mechanical strengthening effects. Finally a translation to 4.2 K material characteristics is made, following 4.2 K tensile testing, whereby an improvement of mechanical characteristics at 4.2 K with respect to ambient temperature is observed to be high.

12.1 Precipitation-type alloy as workhorse for superconducting solenoids

The ATLAS central solenoid is wound with a Nb-Ti/Cu cable, co-extruded with the precipitation type Al-0.1wt.%Ni alloy. The ATLAS conductor with a critical current of 20 kA at a nominal operating magnetic field of 2 T, features a cross-section of 130 mm^2. This reduced cross-section compared to the 700 mm^2 envisaged for a 60 kA at 5 T class conductor, is mechanically advantageous. The lower amount of mechanical reinforcement needed simultaneously results in better transport characteristics (section 11.4). Smaller cross-sections lead to the more straightforward processing of composite structures, with less material to be displaced and/or thermally treated (seen in Part I of this thesis). Material properties of the bulk are not representative for the same material following specific production processes. Furthermore, as production processes scale-up, material characteristics will change.

Here the first step in conductor scale-up is described, focussing on material behaviour after large-scale co-extrusion. To demonstrate the feasibility of using Al-0.1wt.%Ni as stabiliser material, a large 40-strand Nb-Ti/Cu superconducting cable was co-extruded with a precipitation type Al-0.1wt.%Ni alloy, to a significant larger cross-section size of 57 mm x 12 mm, than previously realised (figure 12.1).

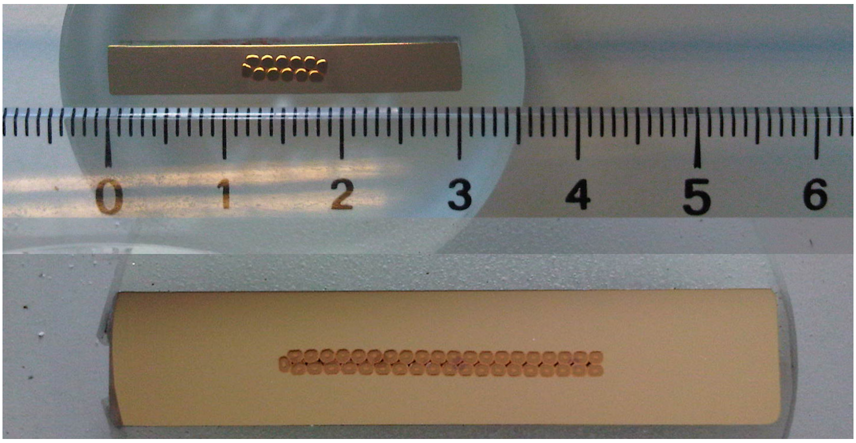

Figure 12.1: Cross-section of the ATLAS central solenoid conductor, 30 mm x 4.3 mm (top), and the 57 mm x 12 mm scaled-up conductor consisting of a 40-strand Nb-Ti/Cu SC cable co-extruded with an Al-0.1wt.%Ni alloy stabiliser (bottom).

12.2 Research methodology

For this study an experimental extrusion was set up at Nexans, Cortaillod (CH), using the extrusion die of the ATLAS barrel toroid conductor [Ten Kate, 2008], with the desired scale-up towards some 700 mm^2 conductor cross-section. Rough billets of as-cast Al-0.1wt.%Ni and 5N-grade high-purity Al (as reference material) were made available by KEK.

To obtain a sufficient length for all required material- and process characterisations, a total of 15 billets of some 36.5 kg each were used in a billet-on-billet continuous extrusion process. A Rutherford cable remainder, previously employed for the ATLAS End Cap Toroid (E.C.T., figure 11.1), was used as a ’dummy’ for the co-extrusion process. This cable comprises 40 strands, with a strand diameter of 1.3 mm. The goal of this study is to achieve a genuine application-relevant material characterisation, allowing for experimental data and conclusions that are representative for future conductors.

12.2.1 Billet-on-billet co-extrusion process

Billet reshaping by forging is realised by CERN prior to the billet-on-billet continuous extrusion process. The co-extrusion is performed in a 3800 t press normally employed for the production of aluminium sheathed power cables and seamless tubes. During the process the heated aluminium billets are introduced from the top, while simultaneously the Rutherford cable is entered from the posterior of the machine, resulting in a material flow around and along the cable. This process encases the cable into the aluminium stabiliser.

For the stabiliser to be effective, the cable and stabilising material must bond properly. Thermal stability as well as possible current transfer between cable and stabiliser depends on a clean and defect free bond. Furthermore, mechanical integrity must be conserved when internal stress strains the material connection. The choice of co-extrusion pressure, temperature and speed aims for a reliable diffusion bonding between the copper matrix of the cable strands and the aluminium, while avoiding both current degradation of the cable, and microstructural alteration of the stabiliser. With the limited process duration, the realisation of such well-controlled diffusion is challenging.

A specific cable cleaning and preheating station has been developed, essential for the diffusion bonding, positioned in-line with the extrusion press. The cable is de-scaled mechanically, focussing on oxide removal, and subsequently preheated under a protected atmosphere to avoid any oxidation, potentially degrading the transport characteristics. During preheating, the peak temperature of the cable is held below 350°C. During the actual co-extrusion, a temperature of the cable in excess of 350°C is limited to a maximum duration of 30 s, followed by an in-line water quench.

Aluminium billets were introduced in sets of five. Co-extrusion commenced with five billets of high-purity 5N-Al, to tune the correct extrusion parameters using a known material. This was followed by five billets of Al-0.1wt.%Ni, and finally a repeated five billets of 5N-Al for press cleaning. Effectively (with 3.5 billets remaining in the press from a previous extrusion), this resulted in a volume of 8.5 billets prior to the first exit of co-extruded Al-0.1wt.%Ni with a volume equivalent to 5 billets,

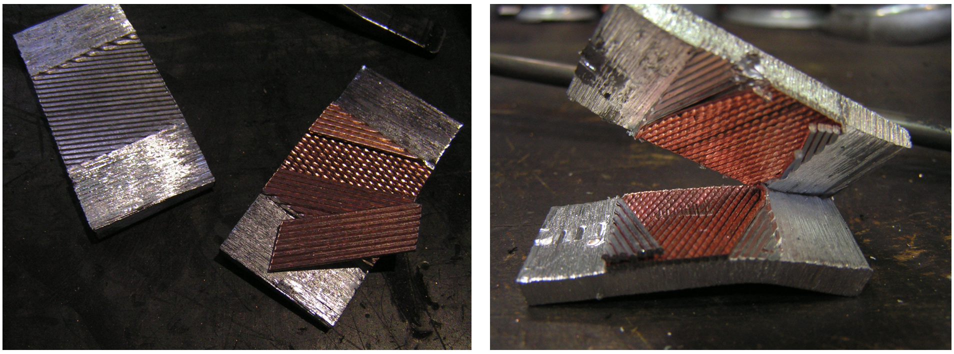

(a) Peel-off witness sample showing inadequate bonding.

(b) Peel-off witness sample showing satisfactory bonding.

Figure 12.2: Peel-off samples demonstrating the quality of bonding during the co-extrusion process. Subfigure (a) taken right after the start of co-extrusion, both cable and stabiliser surface are 'clean'. In subfigure (b) the sample is extracted after parameter adjustment; a metallic aluminium 'stain' is left on the cable surface. The width of the Rutherford cable in the images is some 26 mm.

followed by a final 1.5 billets extruded of 5N-Al. The last 3.5 billets 5N-Al remained in the press upon cool down.

The extrusion temperature is set at 400°C, comparable to the simulated co-extrusion between 430°C and 360°C used in the development of the ATLAS central solenoid conductor [Wada et al., 2000a; Wada et al., 2000b; Tonogi et al., 1999]. The extrusion temperature is kept constant with the introduction of the Al-0.1wt.%Ni billets, but the extrusion pressure is increased with 20% - 25%, which is still well within the working margins of the 3800 t press. Extrusion speed was reduced slightly to 1.5 m/min when introducing the reinforced Al-0.1wt.%Ni material. Note that the speed has to be larger than 0.8 m/min to avoid cable overheating [Blau et al., 2002]. The parameters chosen, subject to minor adjustments during the process, resulted in adequate cable-stabiliser bonding. This is shown in figure 12.2, where peeled-off witness samples are presented. Witness samples were taken regularly along the initiation of the co-extrusion to determine the setting of the parameters. Indication of proper bonding can be deduced from the metallic remainder on the cable after peel-off, denoting aluminium present on the copper outer shell of the cable. This is indicative of a superior bonding strength between the copper and the aluminium than the aluminium's intrinsic strength, i.e. it is evidence of a form of diffusion taking place.

The co-extrusion process resulted in a total conductor length of some 335 m, stored on a spool. As a result of the continuous billet-on-billet extrusion process, we have to account for transitional areas along the length of the conductor. This incorporates not only the volume it takes for the changed material to arrive at the die (from 5N-Al to Al-0.1wt.%Ni and back), but also results from the specific material flow in the press. Figure 12.3a shows one of the transitional areas. In this length of the co-extruded conductor a pattern of material flow can be observed.

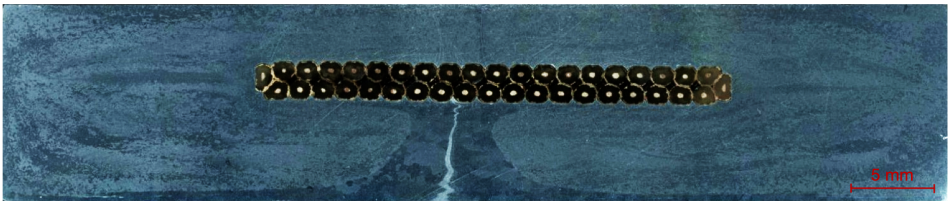

(a) Image of the conductor cross-section, showing the transition from 5N-Al to Al-0.1wt.%Ni.

(b) Image of the conductor cross-section (without cable), showing the transition from Al-0.1wt.%Ni to 5N-Al.

Figure 12.3: Micrograph images demonstrating material flow observed during the transition to a ’new’ material. The highly pure 5N-Al appears in a darker hue due to its coarser grain structure. The newly introduced material flows in centrally, while the to be phased out material is pushed around towards the bottom of the extruded product.

The newly introduced material in the press, here Al-0.1wt.%Ni, appears to enter directly centrally in the die with a direct flow towards and around the cable, here seen in the lighter hue. The ’old’ 5N-Al material, being phased-out, is forced around the cable towards the bottom realising a sort of ’weld’ at the bottom, seen in a darker hue. This phenomenon is even better observed in a sample taken towards the finish of the extrusion (figure 12.3b), where the Rutherford cable is absent, and a transition is made from Al-0.1wt.%Ni to 5N-Al. One can see, from the coarser microstructure (with a darker hue) that the 5N-Al enters from the center, and the to be phased-out Al-0.1wt.%Ni is pushed towards the outer rim, merging in the bottom.

The extrusion process with a wide range of variables, and a particular succession of materials both with and without cable, resulted in a usable co-extruded Al-0.1wt.%Ni conductor of 15 m. This length was largely sufficient for the envisaged experiments. Concurrently, a fair amount of reference material became available in the form of pure 5N-Al co-extruded with cable, and of both materials extruded without cable. This allows for the determination of the effect of the cable on the properties of the further processed material.

Three sections of the extruded conductor were used for the optical, mechanical, and electrical field characterisations: 1) a section of 5N-Al stabiliser extruded without Rutherford cable, as reference material; 2) a section of Al-0.1wt.%Ni alloy stabiliser extruded without cable; and 3) a section of Al-0.1wt.%Ni alloy stabiliser co-extruded with Rutherford cable. These three extruded material variants are referred to as 5N-Al and Al-Ni, for the stabilisers extruded without cable, and as Al-Ni^c for the co-extruded conductor.

12.3 Transport characteristics vs. mechanical strength of diluted alloys

All measurements discussed in this chapter were conducted on the bulk section of the extruded conductor, shown in figure 12.4. This was done to ensure representative results for the future increased-size stabilised conductors, and to eliminate any deviations in the material characteristic resulting from surface effects. During extrusion the external surface, as well as the interface between the stabiliser and the cable, experience work-hardening. This results in a material temper that is not representative for the bulk. Specimens are taken at a distance at least 1 mm from the aforementioned interfaces. Note that this is a conservative approach as far as local mechanical properties are concerned, while the inverse is true for the local conductivity. While designing a stabilised superconductor these local effects need to be considered.

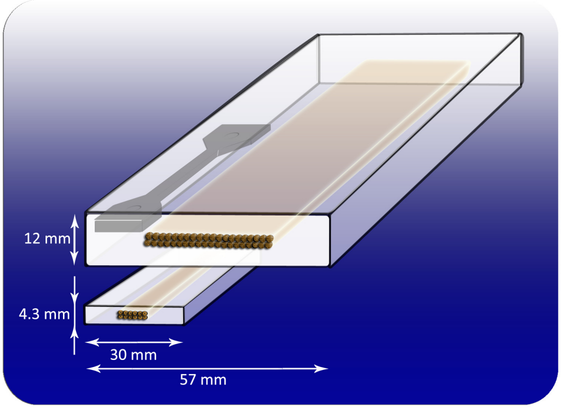

Figure 12.4: Schematic representation of the new co-extruded Al-Ni stabilised conductor, 57 mm x 12 mm (top). For comparison, the 30 mm x 4.3 mm ATLAS CS conductor is shown to scale (bottom). The shaded area indicates where measurement specimens are taken from the bulk section of the conductor.

With the co-extruded conductor presented here we need to make use of sub-sized tensile samples, as was the case for the measurements performed on the bi-metallic plates in Part II. The same mechanical measurement procedure is used (in detail described in section 3.2.1) with a similar specimen size holding a 25 mm gauge length and a 3 mm x 3 mm cross-sectional area. As depicted in figure 12.4, the specimens are machined with their longitudinal axis parallel to the extrusion direction, in order for the tensile force direction to correspond directly with the direction of hoop stress during magnet operation. The specimens are machined by spark erosion, as with the bi-metallic material, in order to avoid strain-induced hardening in the as-extruded material.

At least three measurements were carried out on each material variant and condition, at a constant stress rate of 5 MPa/s up to one-half the specified yield strength, and subsequently slowed down to a deformation rate of 1.5 mm/min (i.e. following standard ASTM E8/E8M).

Figure 12.5a shows the tensile properties of the three extruded stabilisers; 5N-Al , Al-Ni and Al-Ni^c. The results are shown for the as-extruded state. The error bars reflect the spread in the results, which is typically $\leq$6%. The measurement uncertainty is equivalent to the uncertainty estimated in the F XM-19 study (section 3.2.3) and holds 1.4% for $R_{p0.2}$ at RT and 1.1% for R_m at RT.

At ambient temperature, the 5N-Al exhibits in the as-extruded state, an average $R_{p0.2}$ of 22 MPa. The Al-Ni alloy shows for the as-extruded state an average $R_{p0.2}$ of 27 MPa. The Al-Ni^c alloy shows for the as-extruded state a similar average $R_{p0.2}$ of 26 MPa. The differences in the ultimate tensile strength R_m, between the co-extruded and the plain extruded Al-Ni are slightly more elevated. Note that the mechanical properties for the co-extruded material are slightly inferior to the plain extruded case, against expectations. This is thought to be a result of a different material flow in the presence of a cable. This caused a lower extrusion speed, and implicates an increased material heating time inside the die. Longer heating times generally result in a reduction of lattice imperfections, as discussed in section 11.2, accompanied by the slight reduction in mechanical properties.

The inverse relationship in dilute alloys between mechanical and transport properties, as predicted in section 11.1, becomes apparent when we inspect the RRR results shown in figure 12.5b. Note that already a small alloying addition of 0.1wt.% nickel reduces RRR by half, while increasing the mechanical properties only marginally. Where a large cross-sectional extrusion of 5N-Al results in an RRR of 2814, a similar extrusion of Al-0.1wt.%Ni exhibits an RRR of only 1153, with a limited spread in results. The same experimental RRR measurement methodology was adopted as for the copper cladding, discussed in section 9.1.1. 2 mm x 2 mm cross-sectional specimens were extracted from the bulk of the conductor by spark-erosion with their longitudinal axis parallel to the extrusion direction. The results presented here are subject to the same 1% measurement uncertainty as reported for the measurements of the copper cladding section 9.1.1, established by [Charifoulline, 2006].

Furthermore, in line with our hypothesis, not only volume imperfections but also dislocations and interface imperfections can have an influence on the transport properties in highly-pure materials (section 11.4). This can be inferred from the increase in RRR value of the co-extruded Al-Ni material (RRR 1191) compared to the plain extruded Al-Ni material (RRR 1153). This is consistent with the earlier observed slight decrease in mechanical properties, thought to be related to increased heating time in the die.

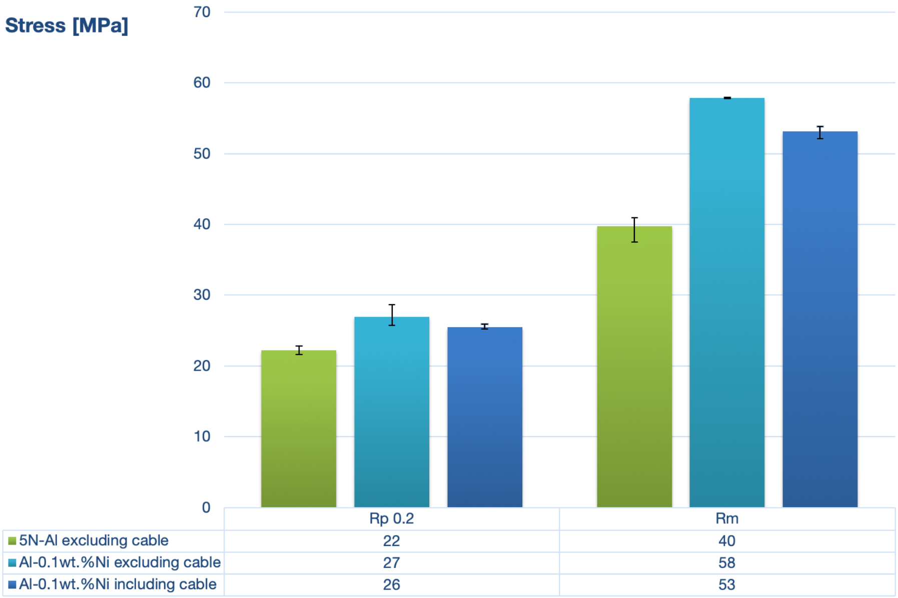

(a) Mechanical properties $R_{p0.2}$ and R_m obtained at ambient temperature for various sections of the as-extruded conductor.[1]

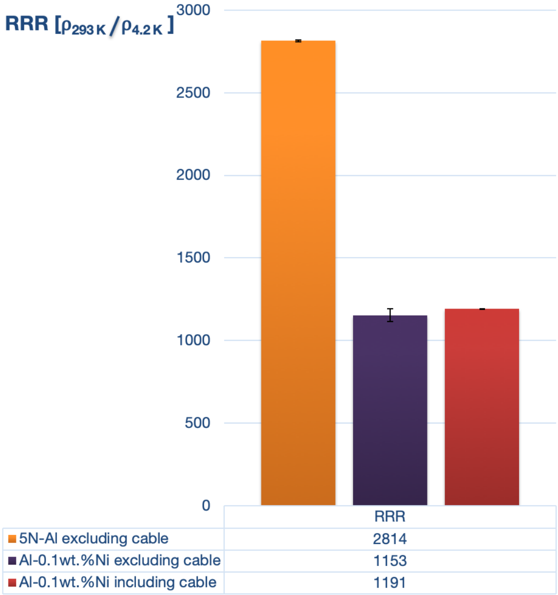

(b) Transport property RRR here defined as $\rho_{293\ K}/\rho_{4.2\ K}$ obtained at for various sections of the as-extruded conductor.

Figure 12.5: Overview of the prominent properties as obtained for the co-extruded Al-Ni alloy with respect to the reference materials Al-Ni simply extruded without cable, and the original 5N-Al material in equivalent state. Note the curious decrease in mechanical properties with co-extrusion of the Al-Ni alloy.[1]

---

[1] The error-bars denote the measurement spread, additional measurement uncertainties are estimated at 1.4% for $R_{p0.2}$, 1.1% for R_m, and 1% for RRR.

12.3.1 Microstructural effects clarifying additional strengthening effects

The microstructural observations presented here are equally representing the bulk of the material, to ensure a direct and general relation between the mechanical, transport and microstructural characteristics of the material. Specimens for microstructural analysis are taken in a plane perpendicular to the extrusion direction, resulting in conductor cross-sectional specimens. The specimens are prepared according to ASTM standard E3 by low-pressure mechanical polishing to reduce pitting and tailing in the soft materials. Specimens without Rutherford cable are electro-chemically etched following ASTM E407 with a 1 g/40 mL HBF_4/H_2O solution to reveal grain structure. Specimens containing copper (i.e. the specimens with cable) are chemically etched with a 3 mL/100 mL HF/H_2O solution to limit chemical deposition of copper on the aluminium.

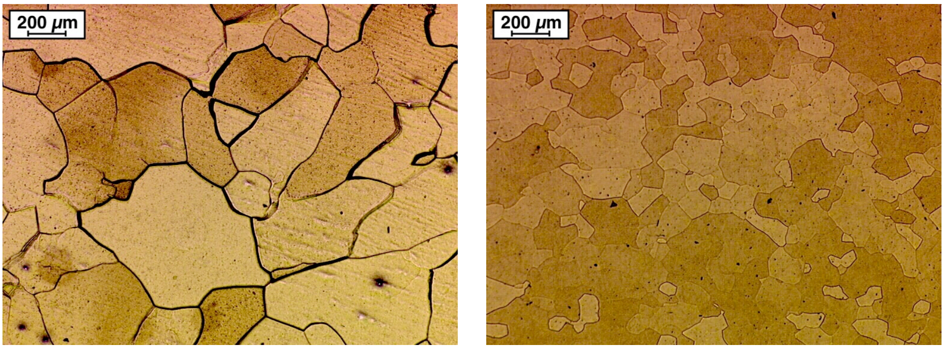

(a) Micrograph of an as-extruded 5N-Al specimen, original magnification 50x.

(b) Micrograph of an as-extruded Al-Ni specimen, original magnification 50x.

Figure 12.6: Microstructure images of 5N-Al, subfigure (a), compared with Al-Ni, subfigure (b), in the as-extruded case. The images are taken in the conductor cross-sectional plane, in the bulk section of the stabiliser.

Grain size decrease is a well-known effect with precipitate formation in a crystal structure Callister et al., 2009. This effect can be seen in figure 12.6, when comparing the microstructure of the two stabiliser materials. The images show a clear grain size reduction going from the 5N-Al extruded stabiliser (figure 12.6a, G 0.5) to the Al-Ni extruded stabiliser (figure 12.6b, G 3.5). This confirms the hypothesis drawn in section 12.3 that the mechanical and transport characteristics obtained are not solely dependent on volumetric impurities, but result from a variation of lattice imperfections.

The relationship between grain size, introducing grain boundary strengthening, and mechanical properties is, however, not observed in figure 12.7. Here the microstructure of the co-extruded Al-Ni material (figure 12.7b) is compared with the extruded variant without cable (figure 12.7a). The mechanical data presented higher values for the extruded variant without cable, compared to the co-extruded variant, from which one would expect a coarser grain structure for the latter.

The contrary is however true, shown in figure 12.7. The grain structure of the co-extruded variant is marginally finer (G 4.0) than the grain structure of the extruded Al-Ni stabiliser (G 3.5). This supports the assumption that additional recovery could take place in the co-extruded variant Al-Ni^c, due to a longer elevated temperature hold, thereby reducing dislocation density introduced by mechanical work during the extrusion process. Recrystallisation and grain growth take place at higher temperatures, grains can therefore be smaller in the co-extruded variant whilst mechanical strength is higher. The presence of the cable during the extrusion process can induce the compaction of grains observed here.

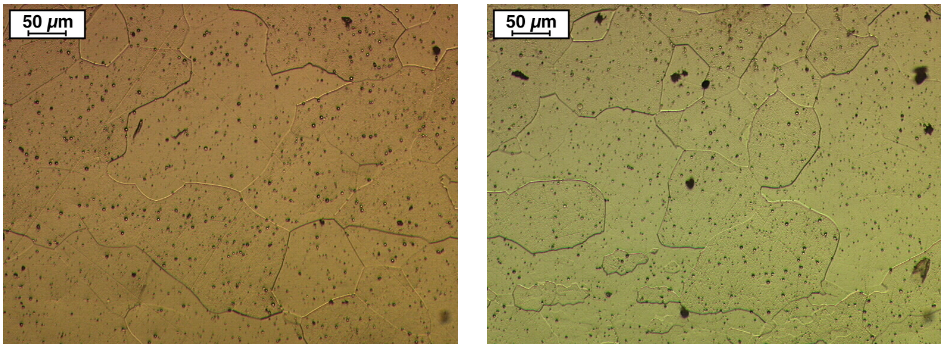

(a) Micrograph of an as-extruded Al-Ni specimen, original magnification 200x.

(b) Micrograph of a co-extruded Al-Ni^c specimen, original magnification 200x.

Figure 12.7: Microstructure images of Al-Ni without cable, subfigure (a), compared to the co-extruded Al-Ni^c, subfigure (b). The images are taken in the conductor cross-sectional plane, in the bulk section of the stabiliser.

12.3.2 Mechanical characteristics at 4.2 K

The ratio between $R_{p0.2}$ at 4.2 K and at ambient temperature is reported to be 1.35 for dilute Al-alloys in as-extruded state [Hansen et al., 1958]. Note that this would not satisfy the target of an $R_{p0.2}$ of 120 MPa for the intended conductor scale-up. The reported ratio would result in an $R_{p0.2}$ of some 35 MPa at 4.2 K, far from the stringent target.

To determine the low-temperature effect of dilute alloying in application-relevant samples, the co-extruded Al-0.1wt.%Ni material was mechanically tested at 4.2 K. Analogous specimens to the ones used at ambient temperature, were tested immersed in a liquid helium cryostat, using the same low-temperature measurement method as described in section 3.2.1. Stress-strain curves were initially determined by measuring at a stroke rate of 0.5 mm/min (congruent with a strain rate of $\sim 3.3 \cdot 10^{-4}$ s^{-1}), for subsequent specimens stroke rate was decreased to 0.15 mm/min (strain rate $1 \cdot 10^{-4}$ s^{-1}), both consistent with ASTM standard E1450-09. The measurement speed was decreased during testing to determine a possible effect of strain-rate sensitivity on the material's behaviour, treated in section 13.3.2. Five specimens are extracted from the Al-Ni^c conductor to obtain satisfactory data on at least three of them.

The measurement uncertainty is identical to the 4.2 K measurement uncertainty determined in the F XM-19 study (section 3.2.3) and holds 1.5% for $R_{p0.2}$ and 1.2% for R_m. Measurement uncertainty is here included in the table, denoted by the ±.

Similar to what was remarked for copper at low temperatures (section 1.2.4), we determine a successful measurement at 4.2 K as one where the Al-alloy exhibits serrated yielding. This guarantees the correct local measurement temperature, relevant for the application.

The increase in tensile properties is found to be quite significant going from an ambient measurement temperature down to 4.2 K. The improvement of mechanical properties at 4.2 K is reflected by an average $R_{p0.2}$ of 75 MPa for the as-extruded state. The ratio between $R_{p0.2}$ at 4.2 K and at room temperature is therefore determined to be 2.9. A much elevated ratio with respect to the anticipated ratio of about 1.35, which is beneficial for its purpose.

Table 12.1: Evolution of mechanical properties of Al-Ni^c going from room temperature down to 4.2 K.

	Temperature	**RRR**	**R$_{p0.2}$**	**R$_m$**
	[K]	-	[MPa]	[MPa]
Al-Ni^c as-extruded (incl. cable)	RT	1191 ± 12	26 ± 1	53 ± 1
	4.2		75 ± 1	303 ± 4

13

Effect of work-hardening on an Al-0.1wt.%Ni-stabilised conductor

The process of cold-working, i.e. plastic deformation in a limited temperature range to avoid recovery during the process, is a very efficient means to enhance mechanical properties.

In order to determine the workability of the tailor-made stabiliser solution, and to confirm the effect on the mechanical and transport properties, cold-work is applied to increase the mechanical properties of the as-extruded temper. The goal is to bridge the gap towards the required $R_{p0.2}$ *of 120 MPa while maintaining an RRR of* $\geq$*500.*

In this chapter the workability of the Al-0.1wt.%Ni-alloy is presented. The first section describes the two methods employed to introduce work-hardening, one on a laboratory scale, the other on a scale suitable for production. The results of the laboratory-scale work-hardening process is used to compare the workability of the Al-Ni (co-)extrusion with the 5N-Al extrusion, and it is subsequently used to define the parameters for the production-scale process. In section 13.2 the outcome of the laboratory-scale work-hardening process is presented, showing a doubling of the 0.2% yield strength with 30% cold reduction. The changes in microstructure observed with the cold-work is discussed in section 13.2.1, after which in section 13.3 the switch is made to a production-scale process.

The production-scale process, being more forceful and two-dimensional, needs less passes to arrive at the same cross-section reduction as the laboratory-scale process. The material reaction to this demanding process is presented in section 13.3, and its difference on the material properties compared with the laboratory-scale process is discussed. The impact of the production-scale process on the integrity of the stabilised-conductor is treated, followed by the measurement of its effect on the material's 4.2 K characteristics.

To finish, this chapter holds a section discussing the thermal stability of the material in section 13.4, where a recovery temperature is found between 470 K and 530 K.

13.1 Work-hardening of a conductor section

In the run-up of the production of the ATLAS central solenoid [Wada et al., 2000a] found that the workability of AlNi-stabilised superconducting cables has an upper limit. In order to preserve full functionality of the NbTi cable, the area reduction is limited to some 25%. They confirmed that both a 26% cold-drawn short sample and a 23% cold-drawn sample of 50 m showed no cable deterioration. Mechanical and transport characteristics for the central solenoid conductor were examined following cold-worked cross-section reductions of 15%, 20% and 25%/, from which 20% to 25% was considered optimal [Wada et al., 2000b]. Subsequently, for the manufacturing of the ATLAS solenoid a reduction of 21% was applied.

To compare the present work with the work of K. Wada et al., a similar range in cross-section reduction is retained, specifically between 0% and 35%. This study aims at: 1) observing the effect of various cold reductions, 2) comparing the effect resulting from a large-size co-extrusion process, and 3) to determine the limit for such large-size extrusions in terms of cable-stabiliser integrity. The previous studies on Al-0.1wt.%Ni as stabiliser material in the development of the ATLAS central solenoid conductor [Yamamoto, 2004; Wada et al., 2000a; Wada et al., 2000b; Yamamoto et al., 1999] and of the CMS solenoid conductor [Sgobba et al., 2006] are used as a reference.

The study here comprises two phases; an initial phase on a laboratory scale, reducing the cross-section in a single direction; and a second phase on a production scale, applying load to realise cross-section reduction in two directions.

In the initial phase short conductor sections (50 cm to 200 cm) were subjected to work-hardening using actively driven rollers. Load is exclusively applied in the short transverse direction (ST), while rolling parallel to the extrusion direction. A maximum thickness reduction of 30% is realised with intermediate sample extractions after 15%, 20%, and 25%. This process is designed to give results in a laboratory scaled environment that are relevant for the production-scale. Here, the workability of the co-extruded Al-Ni^c is compared with the Al-Ni and 5N-Al extruded reference state.

Subsequently a production-scale experiment was performed using 1.5 m long sections of the co-extruded Al-Ni^c stabilised superconductor. The aim was to confirm the properties of cold-rolled co-extruded Al-Ni^c on a production-scale, to determine the optimal area reduction, and to assess the workability by bi-directional rolling as function of the amount of passes.

The production-scale experiment was performed on a 50 ton, actively driven, four-roll Turks-head mill from DEM SpA. (figure 13.1) at Criotec, Chivasso (I). This is an installation also used for production of the ITER cable-in-conduit conductors [Corte et al., 2012; Corte et al., 2013]. Force is applied mainly in the short transverse direction (ST), while the wide transverse direction (TD) is constrained to preserve cable integrity and to maintain a realistic aspect ratio (width/thickness). The samples are rolled in contra-extrusion direction to account for spooling and de-spooling in the case that the work-hardening takes place at a different location as during extrusion. Cold-rolling was applied either in a single step or in multiple steps, to determine the influence of the work-hardening sequence on the material characteristics. Moreover, one sample was subjected to a homogeneous reduction, i.e. by applying an equal reduction in ST-direction and TD-direction, to evaluate the effect of the direction of applied load on the cable-stabiliser bonding characteristics.

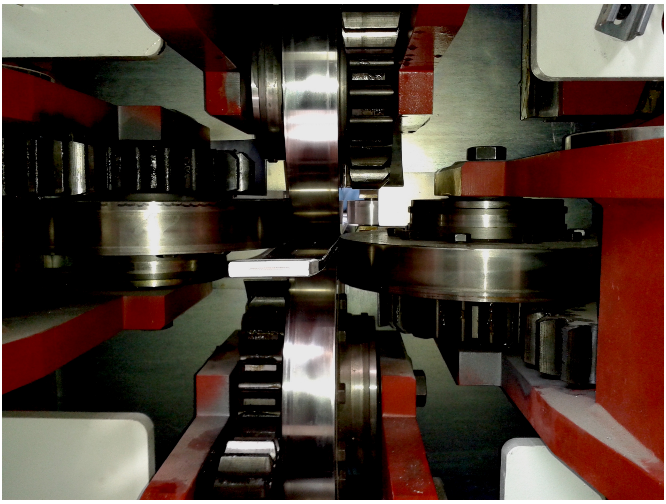

Figure 13.1: Image of the Turks-head rolling process of the large-size, co-extruded Al-Ni^c stabilised conductor. Plastic deformation is induced in the short-transverse direction (ST), here vertical, while in the gross of measurements the wide transverse direction (TD) is simply constrained to maintain the correct $^{TD}/_{ST}$ aspect ratio.

13.2 Workability of the Al-0.1wt.%Ni-alloy

Figure 13.2 shows the tensile properties of the three extruded stabilisers: 5N-Al, Al-Ni, and Al-Ni^c, resulting from the laboratory-scale experiment. The results are shown for the as-extruded state (0% thickness reduction), and for the 15%, 20%, 25% and 30% thickness-reduced cases. The error-bars in the graph indicate measurement spread. Measurement uncertainty holds, analogous to the measurements performed on the conductor prior to work-hardening, 1.4%(1.1%) for $R_{p0.2}(R_m)$ at RT, and 1.5%(1.2%) for $R_{p0.2}(R_m)$ at 4.2 K.

At ambient temperature we remind that the 5N-Al in the as-extruded state exhibits an average 0.2% yield strength, $R_{p0.2}$, of 22 MPa. Single-direction multi-pass rolling of this extruded material results in an average $R_{p0.2}$ of 49 MPa in the 30% cold-rolled state. The Al-Ni alloy showed for the as-extruded state an average $R_{p0.2}$ of 27 MPa, increasing to an average 60 MPa for the 30% cold-worked state. The Al-Ni^c alloy showed for the as-extruded state a similar value of 26 MPa. In line with the aforementioned plain-extruded case the co-extruded material shows for the 30% cold rolled state a somewhat lower value of 58 MPa. This difference is slightly higher than in the as-extruded case, which may indicate a diminishing effect of the Rutherford cable on the work-hardening process. During the rolling process, the cable carries a large portion of the stress due to its relatively large strength compared to the Al-based stabiliser, making it difficult to work the latter. Furthermore, due to the high strength of the cable, stabiliser-material flow does not only occur in the longitudinal direction, as it does during the cold-rolling of the plain-extruded Al-Ni, but also in the transverse direction. This results in an equal thickness reduction between the two cases (Al-Ni and Al-NI^c), but a differing cross-sectional area reduction.

Notice furthermore how $R_{p0.2}$ gradually approaches R_m, and how R_m starts to increase once $R_{p0.2}$ exceeds the original R_m value that was found for the non-work-hardened material, which are both characteristics of cold-worked materials [Kaufman, 1999].

As discussed in section 11.4, RRR values tend to decrease with increased work-hardening as a result from a decreased mean free path with dislocation density. This phenomenon can indeed be seen in figure 13.3, where the relationship between $R_{p0.2}$ at room temperature and RRR are presented for each work-hardening increment. In the as-extruded state, we have seen that the 5N-Al shows an average RRR value as high as 2814 related to an average $R_{p0.2}$ of 22 MPa. The RRR drops to an average of 1464 for the 30% CW case, which corresponds to an average $R_{p0.2}$ of 49 MPa; a large drop in the RRR value with respect to a relatively small increase in $R_{p0.2}$.

The Al-Ni alloy shows an average RRR value of 1191 in the as-extruded state at an average $R_{p0.2}$ of 26 MPa. For the 30% cold-worked state an average RRR value of 673 is obtained. Both materials lose half of their RRR with 30% work hardening, but this constitutes a larger overall decrease for the 5N-Al material than for the Al-Ni alloy. In this sense, the results confirm the superior properties of the Al-Ni alloy over the conventional high-purity Al. Increasing the mechanical properties with use of work-hardening has a less detrimental effect on the transport properties of the Al-Ni stabiliser. However, a clear trade-off between the $R_{p0.2}$ and the RRR value remains.

When comparing the Al-Ni and the Al-Ni^c data in figure 13.3, it can be seen how the overall behaviour of the Al-0.1wt.%Ni alloy follows a general trend, i.e. the relation between RRR and $R_{p0.2}$ evolve in the same manner with increasing cold-work. It appears, however, that the starting point is somewhat shifted. The as-extruded case for the plain and for the co-extruded variant differ slightly in terms of temper, which undoubtedly needs to be considered in a production-line application.

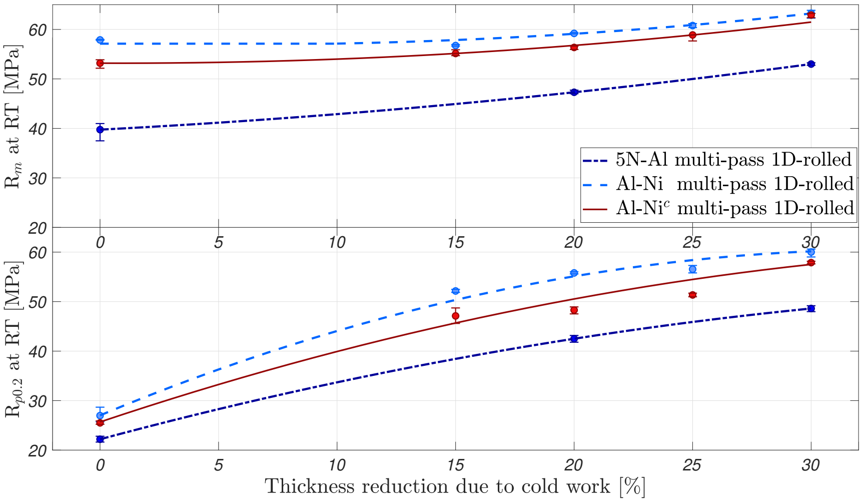

Figure 13.2: Tensile properties of the 5N-Al conductor, the Al-Ni conductor, and the Al-Ni^c conductor in five different work-hardened tempers. Mechanical properties increase in an almost linear manner with thickness reduction due to cold work. Notice the slightly lower mechanical properties of the Al-Ni^c alloy with respect to the alloy without cable for higher work-hardened states.

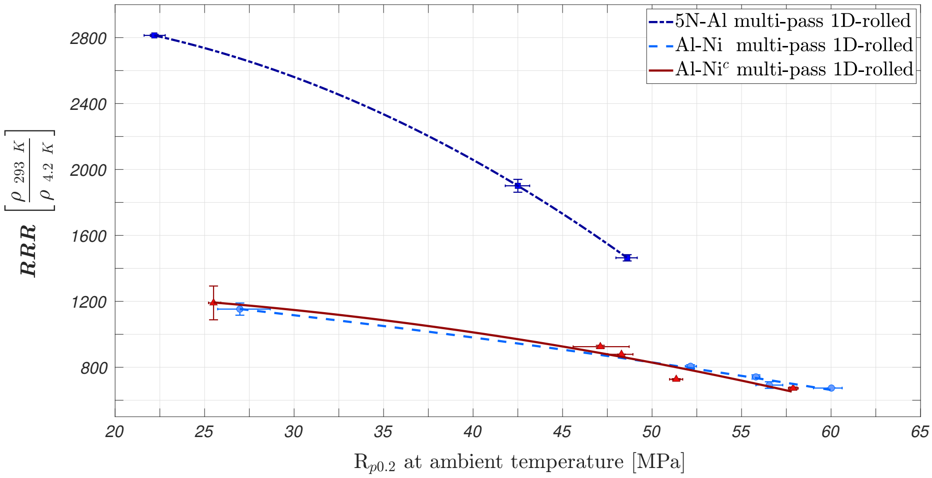

Figure 13.3: RRR plotted as a function of for the different material variants at various stages of cold-work. Increasing $R_{p0.2}$ by work-hardening has a less detrimental effect on the RRR of the Al-Ni alloy as it does on the RRR of the high-purity Al.

13.2.1 Changes in the microstructure

Figure 13.4a and figure 13.4b were shown before in section 12.3.1 when discussing the difference in microstructure between the as-extruded Al-0.1wt.%Ni and the well-known 5N-Al. These images are now compared with the microstructure both materials after various levels of cold-work (figure 13.4). Note the typical evolution of the materials' microstructure with cold-work by rolling where only one direction is constrained. A flattening of the grains in the direction of the load; the short-transverse or ST-direction (here vertical) is observed, while the transverse direction, TD (here horizontal) is unrestrained. A clear grain-size difference between the 5N-Al extruded stabiliser (left in figure 13.4) and the Al-Ni extruded stabiliser (right in figure 13.4) was already observed. Here we also observe a decrease of grain-size with increasing cold work. In figure 13.5 the grain-size as a function of thickness reduction by cold work is presented, quantifying the latter effect. The grain decrease with work-hardening appears more apparent for the 5N-Al stabiliser than for the Al-Ni stabiliser.

A similar trend in grain-size appears to be present for the Al-Ni extruded material as was observed for the transport behaviour as a function of the mechanical characteristics (figure 13.3). In essence an equivalent relationship exists in grain-size with respect to cold-worked state for both the plain- as well as the co-extruded case, with a discrepancy in as-extruded temper. A smaller grain-size here does not directly relate to increased mechanical behaviour as a result of a difference in the as-extruded temper. This strengthens our earlier presumption of this discrepancy to have origin in dislocation-density in the two as-extruded tempers. An enhanced hardened state of the as-extruded temper of the plain-extruded case is to be expected. Note that nevertheless the material behaves in a similar manner independent of it's as-extruded temper.

13.2.2 Al-0.1wt.%Ni's workability: comparison with literature

When comparing the mechanical properties found here with those of the Al-0.1wt.%Ni stabiliser material, published in the frame of the development of ATLAS and CMS solenoid conductors, some discrepancies in the data show up. Where we find a maximum 0.2% yield strength of 56 MPa for the Al-Ni alloy in 20% cold-worked state, in [Sgobba et al., 2006] an $R_{p0.2}$ of 59 MPa at room temperature is reported of the Al-0.1%Ni alloy in the same cold-worked state. However, [Wada et al., 2000a] and [Yamamoto et al., 1999] report an $R_{p0.2}$ value as high as 79 MPa at room temperature for the same cold-worked state. It should be noted also that they obtained divergent results for the same Al-Ni alloy temper. In earlier measurements they found $R_{p0.2}$ values of 71 MPa and 55 MPa (all at room temperature and 20% cold-worked) [Wada et al., 2000b]. The differences could be explained by slightly different material processing in the early stages of

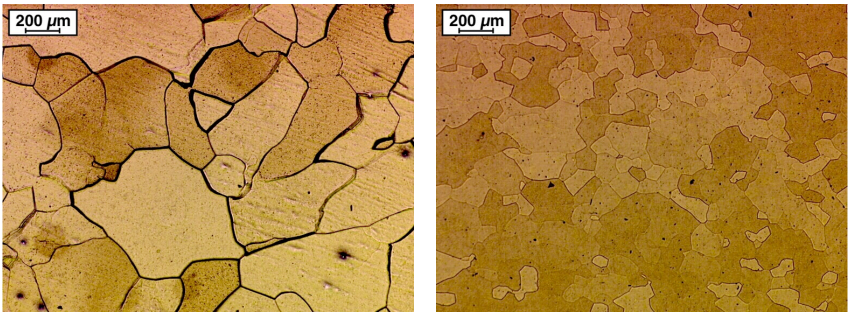

(a) 5N-Al 0% CW **(b)** Al-Ni 0% CW

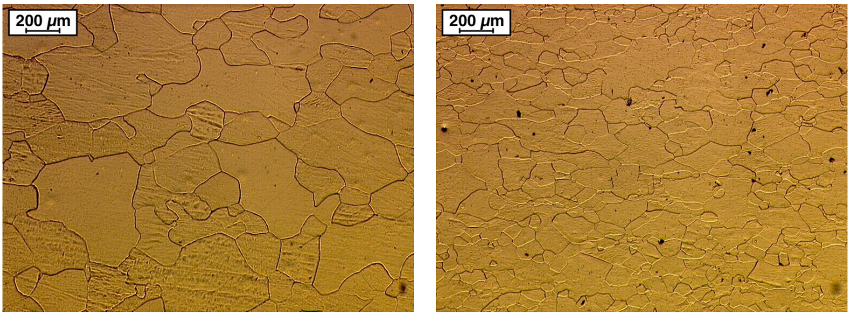

(c) 5N-Al 20% CW **(d)** Al-Ni 20% CW

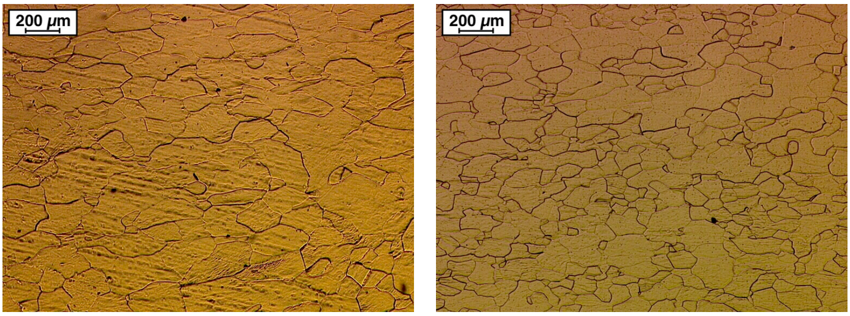

(e) 5N-Al 30% CW **(f)** Al-Ni 30% CW

Figure 13.4: Microstructure images of the 5N-Al extruded stabiliser (left) and Al-Ni extruded stabiliser (right) at various thickness reductions. Thickness reduction is applied in the ST-direction, here vertically. The micrographs are taken at the same position as the tensile and RRR specimens (figure 12.4) at an original magnification of 50x. Notice the close to equi-axed grains in the 0% CW case and the increased $^{TD}/_{ST}$ aspect ratio in the case where thickness reduction has taken place.

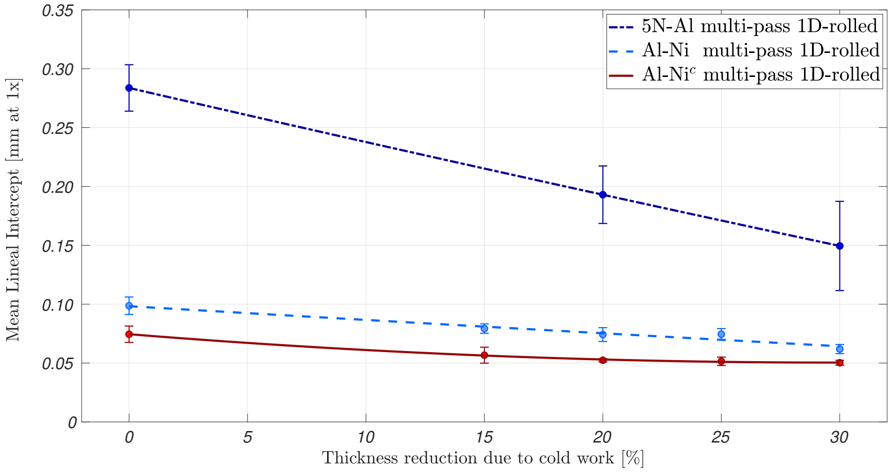

Figure 13.5: Grain size as function of work-hardened state for the three extruded variants. Grain sizes show to decrease with work-hardening extent.

conductor production, as suggested in [Wada et al., 2000b]. Moreover, the fact that the conductor sections used for the workability experiment for the ATLAS and CMS solenoid conductors have a considerably lower cross-sectional area may be of importance. Smaller extrusion cross-sections can very well result in smaller grain sizes, and thus in higher mechanical strength due to grain-boundary strengthening [Callister et al., 2009]. Grain-size measurements showed an average grain-size G 5 (at 1x magnification) for the Al-Ni alloy, whereas the ATLAS specimen gives a slightly finer grain structure with G 5.5. However, such a small difference by itself can not explain the differences in tensile results observed. G scales to the mean lineal intercept (following the Heyn mean lineal intercept method in ASTM E112), by the empirical relation $G = (-6.6457\ log(L_3)) - 3.298$, where L_3 is the mean lineal intercept length.

In larger extruded sections a surface effect may arise during work-hardening (section 12.3.1), resulting in extensively worked surface regions and a less-worked bulk region. As described in section 12.3, the tensile tests in this study are all conducted on the bulk section of the stabiliser, by extracting the specimens at $\geq$1 mm under the surface to avoid that the results are influenced by this so-called skin effect. This assures predictive results for future larger-size stabilised-conductor extrusions. The skin effect is less important in smaller cross-sections, where work-hardening is distributed more evenly as a result of a decreased volume to deform. ATLAS' conductor tensile measurements conducted on either the entire conductor or the extracted specimens could therefore show different results with respect to those presented in this study.

13.3 Properties of Al-0.1wt.%Ni following production-scale work-hardening

Since the values presented in section 13.2, that were obtained after mechanical hardening by rolling on a laboratory-scale, were slightly lower than the gross of measurements results reported on the Al-0.1wt.%Ni stabiliser material in the development of the CMS and ATLAS solenoid conductor, we need to have a closer look at the work-hardening process itself. The implementation of a production-scale work-hardening, realising a cross-section reduction in a single pass, providing us with a more realistic determination of material characteristics for future use.

The observation of the relatively low mechanical strength obtained in our study previously led to the cautious conclusion that increased cross-sectional areas result in decreased work-hardening effects. In comparing here a multi-pass, laboratory-scale work-hardening with a production-scale limited- and single-pass work-hardening, an additional answer is found for the relatively low tensile strength found in section 13.2.

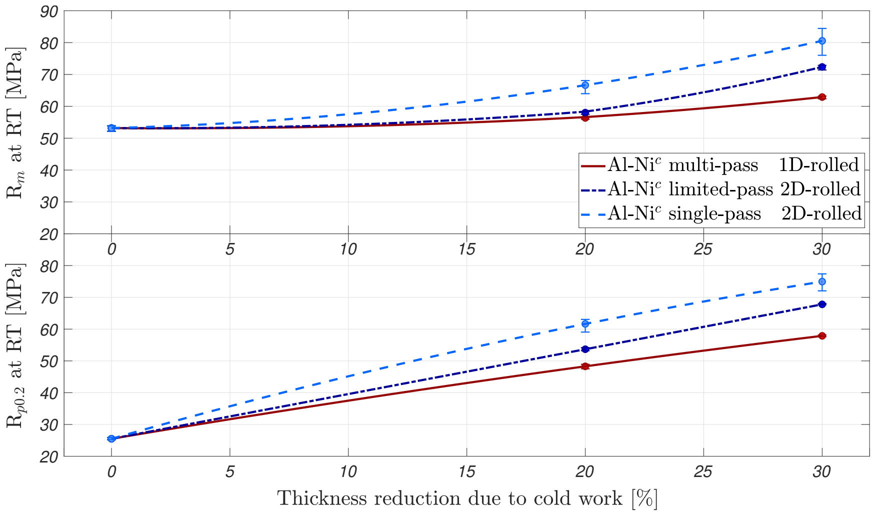

Figure 13.6: Room temperature tensile properties of the co-extruded conductor in three different cold-worked states. Data is shown for the multi-pass, flat-rolled conductor, and for the limited- and single-pass, bi-directionally rolled conductor. Notice the decrease in tensile properties with amount of cold-roll passes.

In figure 13.6, presented are the $R_{p0.2}$ and R_m values from the laboratory-scale, as well as the ones for the production-scale study. A distinct increase is visible from the laborarory-scale manually-driven flat rolling by two rolls, to the production-scale bi-directional rolling by four rolls. In the laboratory-scale case a certain reduction was achieved by multiple passes, whereas in the production-scale case the same reduction was achieved in a limited- or single-pass. The limited-pass case represents the cold-rolled conductor on a production-scale, where the reduction was achieved in an amount of passes with steps of 10% of the initial cross-sectional area, i.e. 2 passes and 3 passes, for the 20% and 30% reduced state, respectively.

Clearly the mechanical properties decrease with the amount of passes. The explanation may relate to the phenomenon of age-softening; a phenomenon that is well-documented for high-purity aluminium, aluminium alloys with a high-purity aluminium matrix, and other light alloys [Leu et al., 2010]. Age-softening is the loss of strength and hardness that occurs at room temperature due to the spontaneous decrease of residual stress in the strain-hardened structure. Age-softening in-between passes might be responsible for the observed decreased effect of cross-section reduction on the mechanical properties of the Al-Ni stabiliser material.

Figure 13.7 displays the relationship between $R_{p0.2}$ and RRR, this time for the multi-pass, single-pass and limited-pass cold-rolled cases. Although the corresponding curves in figure 13.7are shifted with respect to each other, a similar relationship exists between RRR and $R_{p0.2}$ at room temperature for the various work-hardening processes. This illustrates how RRR does depend on how exactly the lattice imperfections are in introduced in the material, but just on their type, presence and quantity.

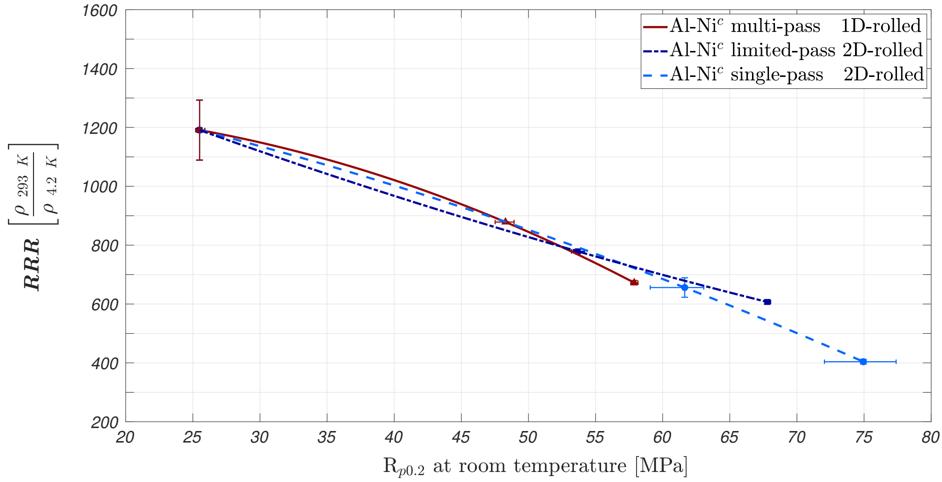

Figure 13.7: RRR plotted against $R_{p0.2}$ for various cold-worked states obtained with the three work-hardening processes. Although the evolution of strength with size reduction is different for each process, the relationship between RRR and $R_{p0.2}$ remains equal.

Promising is that the trend tends to an $R_{p0.2}$ value of some 70 MPa at an RRR value of 500. With the earlier obtained 4.2 K to ambient temperature ratio ($R_{p0.2}$ at 4.2 K / $R_{p0.2}$ at RT) of >2 (section 12.3.2), these room temperature values would bring us towards an $R_{p0.2}$ value of at least 140 MPa, exceeding the aim of 120 MPa. We will come back to this in section 13.3.2.

13.3.1 Impact on quality of bonding

For adequate performance of the conductor, a proper void-free bonding between the copper matrix of the Rutherford cable strands and the aluminium-based stabiliser must be ensured. This will provide the superconducting cable with an effective channel for heat- and current transfer in the case of a running normal zone, and will also ensure mechanical stability. In the co-extrusion process, cable cleaning by brushing and cable preheating were adopted to assure the best quality of bonding [Blau et al., 2002]. In section 12.2.1 it was discussed that in the initial length of the co-extrusion, the bonding quality was monitored and adjusted by conducting regular peel-off tests. Prior to the continuous co-extrusion of the full length of conductor, the peel-off tests revealed a residue of aluminium on the Rutherford cable, indicating rupture inside the aluminium and thus suggesting a relatively strong metallographic bond between the Rutherford cable and the aluminium-based stabiliser.

However, with the introduction of cold-work and the accompanying redistribution of stabiliser material, this metallographic bond is stressed. This is especially the case when the mechanical deformation and the resulting material flow (incompressible), is applied in a single-step process such as the production-type work-hardening presented.

Bonding inspection by ultrasonic means

Following co-extrusion and work-hardening extensive studies on the quality of bonding were performed at the Swiss Federal Laboratories for Materials Science and Technology (Empa), on both sides in the TD-LD plane of the conductor over short lengths (200 mm). Mechanical C-scanning, an ultrasonic pulse-echo immersion technique, is used to reveal detailed information on the bond-quality [Neuenschwander et al., 1998]. A 20 MHz ultrasonic probe scans the surface of the short sample while it is immersed in demineralised water. The resulting C-scan is a two-dimensional plot of the echo amplitudes, scaled between 0 V and 1 V, reflected by the stabiliser-superconductor interface. Various amplitudes are indicated by a different color. The quality of bonding is deduced from the amplitude, with a small amplitude empirically corresponding to a 'good' bonding and a large amplitude to a 'poor' bonding.

Bonding inspection by radiographic means

In addition to ultrasonic testing, the samples were also measured with an X-ray micro computed tomography (CT) setup installed at Empa. For the initial radiographic images a Viscom XT9160-TDX source was operated at 140 kV and 0.07 mA. The emitted spectrum was hardened with a 0.1 mm thick lead filter and detected by a Perkin Elmer XRD 1621 CN3 ES detector. Subsequent measurements were done by using a Viscom XT9225-TEP X-ray source with an acceleration voltage of 200 kV and a 1 mm thick copper hardening filter to improve the contrast of the Rutherford cable.

The ultrasonic measurements on the short samples turned out to give important information of the influence of the work-hardening process on the quality of bonding of the Al-Ni to the copper matrix of the cable. Representative sections of the short samples measured by UT are shown in figure 13.8, accompanied by X-ray radiography images of the same sections. In the ultrasonic images a1, b1, c1, d and e, delamination of the Al-Ni based stabiliser is marked by a high amplitude echo, i.e. the bright colored areas. In the X-ray radiography images a2, b2 and c2, a light hue indicates strand breakage. Images a1 and a2 of figure 13.8 show a section of a short sample of the 15% reduced conductor. In the center of this short sample, the here displayed section, no delamination is revealed by the UT, and also no strand breakage is indicated by radiography. On the contrary, for the 35% cold-reduced case, major delamination can be observed (figure 13.8b1). This delamination is accompanied by strand breakage, as witnessed in image b2 of figure 13.8. It appears that, by not having the support of the attached stabiliser material, delaminated strands are strained more and eventually break. The locations of strand breakage were consistent with concave ripples present on the Al-Ni based stabiliser surface, indicating flow of stabiliser material into the void where no strand is present.

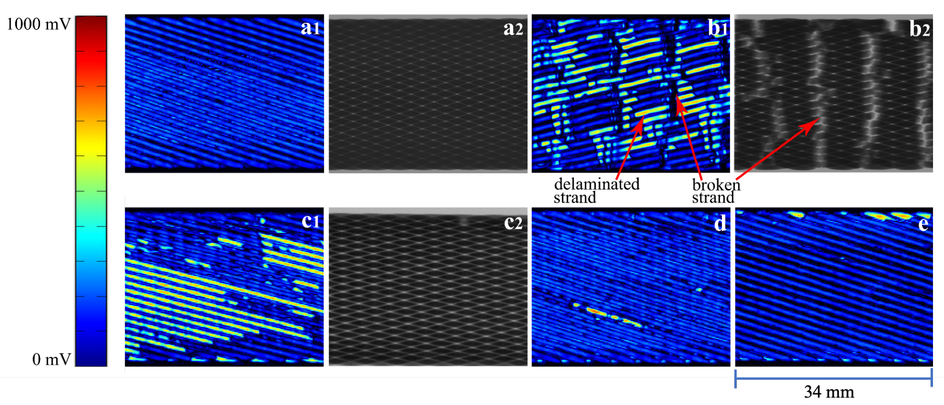

Figure 13.8: Ultrasonic C-scans and radiography images of the co-extruded, cold-rolled Al-Ni stabilised conductor. Subfigures *a1*, *b1*, and *c1* show C-scans of selected sections of the 15%, 35% and 20% single-pass cold-rolled conductor, respectively. Subfigures *a2*, *b2* and *c2* show the corresponding X-ray images. Subfigures *d* and *e* show C-scans of selected sections of the 20% cold-rolled conductor in two passes (limited-pass), and the homogeneously reduced, respectively.

In image c1 of figure 13.8 a C-scan of a selected section of the 20% cold-worked sample is presented, accompanied by its radiographic image in image c2. Major delamination is visible in the C-scan, as well as some minor indications of strand breakage (top right) in the radiography images. Further study on longer lengths should indicate whether a reduction of 20% by single-pass cold-rolling results in only delamination or if significant strand breakage occurs as well.

When we compare the delamination of the 20% cold-rolled conductor that was reduced in a single pass (figure 13.8c1) with the delamination of the 20% cold-rolled conductor, which was reduced in two passes (figure 13.8d), we observe a distinct difference. Limited-pass rolling, as performed on the sample corresponding to image d, clearly holds promise. A decrease in delamination intensity is apparent, showing that the load reduction associated with this two-step rolling reduces the risk of problems at strand level. The relief of internal stress in-between cold-work passes has a clear influence on the bonding quality of the conductor.

Furthermore, homogeneously reducing the cross-section results in an even more optimised situation (figure 13.8e). The homogeneous reduction, here done in a single pass, leads to a cross-section reduction in two directions. Load is applied in ST- and TD-direction with respect to the rolling direction (LD), whereas the TD-direction in all other cases presented in this study are either left free (laboratory-scale), or merely constrained (production-scale limited- and single-pass). The bi-directional reduction of this homogeneously reduced case limits the force applied per direction to achieve at the same cross-sectional area reduction. This implies a reduction of the material flow at the position of the cable. The only delamination observed in this case is concentrated at the edges of the Rutherford cable, most likely due to the concentrated stabiliser material flow in this area. The result is remarkable and could, with some additional research, lead to a credible work-hardening method that results in the desired mechanical properties as well as maintaining conductor integrity.

13.3.2 Mechanical characteristics at 4.2 K

Table 13.1 shows the average results of the main properties for Al-Ni^c at different cross-section reductions, providing a full picture of the material in an application relevant setting. Results are reported for the as-extruded temper (0% cold-worked), and for the 20% and 30% cold-reduced states. The data represents the results obtained in a single pass, with load applied in ST-direction, and the TD-direction is constrained (figure 13.1). Besides the ambient temperature results discussed above, here also 4.2 K results are shown. The measurement uncertainty is denoted by the ± values presented in the table.

At room temperature, the evolution of $R_{p0.2}$ of the Al-Ni^c in as-extruded state, to the 20% cold-worked state exhibits a quite significant increase from an average of 26 MPa to an average of 62 MPa. The subsequent increase in $R_{p0.2}$ from 20% cold-work to 30% (average of 75 MPa) is less distinct.

The evolution of the ultimate tensile strength R_m, of Al-Ni^c follows a more continuous behaviour from an average of 53 MPa in the as-extruded state, over an average of 67 MPa for the 20% cold-worked case, to an average of 81 MPa for the 30% cold-worked case. Following work-hardening $R_{p0.2}$ approaches R_m. In our application, $R_{p0.2}$ is the leading property for the success of the conductor. The strong increase in $R_{p0.2}$ of the cold-worked states compared with the as-extruded state confirms the high workability of the Al-0.1wt.%Ni material, also in a production-scale work-hardening sequence.

Table 13.1: Properties of Al-Ni^c as a result of various production-scale cross-section reductions.

	Temp. [K]	**RRR** -	**R$_{p0.2}$** [MPa]	**R$_m$** [MPa]
As-extruded	RT	1191 ± 12	26 ± 1	53 ± 1
	4.2		75 ± 1	303 ± 4
20% single-pass cold-rolled	RT	656 ± 7	62 ± 1	67 ± 1
	4.2		127 ± 2	376 ± 5
30% single-pass cold-rolled	RT	404 ± 4	75 ± 1	81 ± 1
	4.2		174 ± 3[a]	496 ± 6

[a] deduced from only two measurements

The increase in tensile yield- and ultimate strength is quite significant from room temperature 293 K to 4.2 K for the various cold-worked states (table 13.1 and figure 13.9). Both cold-worked tempers exhibit an $R_{p0.2}$ above 100 MPa at 4.2 K, as well as an R_m above 350 MPa. The ratio between $R_{p0.2}$ at 4.2 K and at room temperature varies lightly between the different tempers, ranging from a maximum of 2.9 for the as-extruded state to a minimum of 2.1 for the 20% reduced temper. Note that these ratio's lie well above those reported in literature (section 12.3.2).

Figure 13.9 shows the deterioration of RRR with increasing cross-section reductions obtained with single-pass, production-scale cold-rolling. RRR falls from an average of 1191 for the as-extruded state to an average of 404 for the 30% cold-reduced state. A roughly linear relation between RRR and $R_{p0.2}$ at room temperature is reported for the co-extruded Al-0.1wt.%Ni stabiliser material. A linear relationship also holds at 4.2 K, although here a less steep descent of RRR with increase in $R_{p0.2}$ is visible.

From the average results in figure 13.9, it can be noticed that the mechanical and transport properties of Al-0.1wt.%Ni can be modified by a work-hardening process to fit the requirements for a 60 kA, 5 T class conductor, which requires an $R_{p0.2}$ at 4.2 K beyond 120 MPa , while preserving an RRR value of more than 500. We can deduce from the mechanical results, that an Al-0.1wt.%Ni stabiliser, which is cold-worked to a cross-section reduction of some 18% will exhibit an $R_{p0.2}$ of approximately 120 MPa at 4.2 K, while preserving an RRR of about 700.

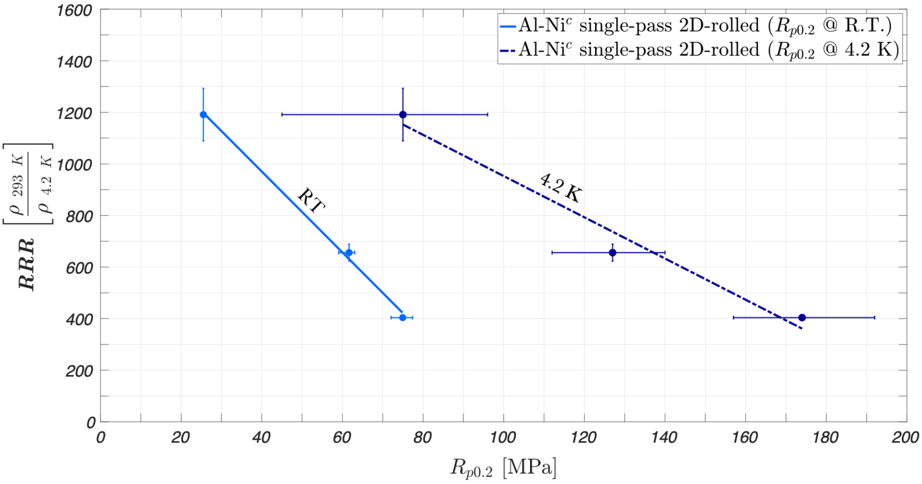

Figure 13.9: RRR plotted against $R_{p0.2}$, for the various cold-worked states, at both room temperature and 4.2 K. Notice the large increase in $R_{p0.2}$ at 4.2 K compared to room temperature.

Strain rate sensitivity

At room temperature, the deviation of the individually measured values from their mean value is minimal. However, as illustrated by the error-bars in figure 13.9, at 4.2 K the deviation from the average is quite significant. A factor that could account for the relatively large spread in obtained values is a significant strain-rate sensitivity of the Al-0.1wt.%Ni alloy at 4.2 K. Tensile specimens were tested at two strain rates of $3.3 \cdot 10^{-4}\ \mathrm{s}^{-1}$ and $1 \cdot 10^{-4}\ \mathrm{s}^{-1}$ (section 12.3.2). A higher strain rate results in slightly higher mechanical properties, i.e. the Al-0.1wt.%Ni material is strain-rate sensitive at 4.2 K. An example is shown in figure 13.10 where the raw data of three specimens of 20% single-pass cold-worked Al-Ni^c, measured with varying strain rates, is presented. Note that besides a small variation within a single strain rate, not unusual for 4.2 K measurements, a fairly large spread is observed when considering two different strain rates (i.e. between sample 1 and sample 2 & 3). This positive impact of strain rate on a material's behaviour is well known for aluminium and it's alloys [Karnes et al., 1966].

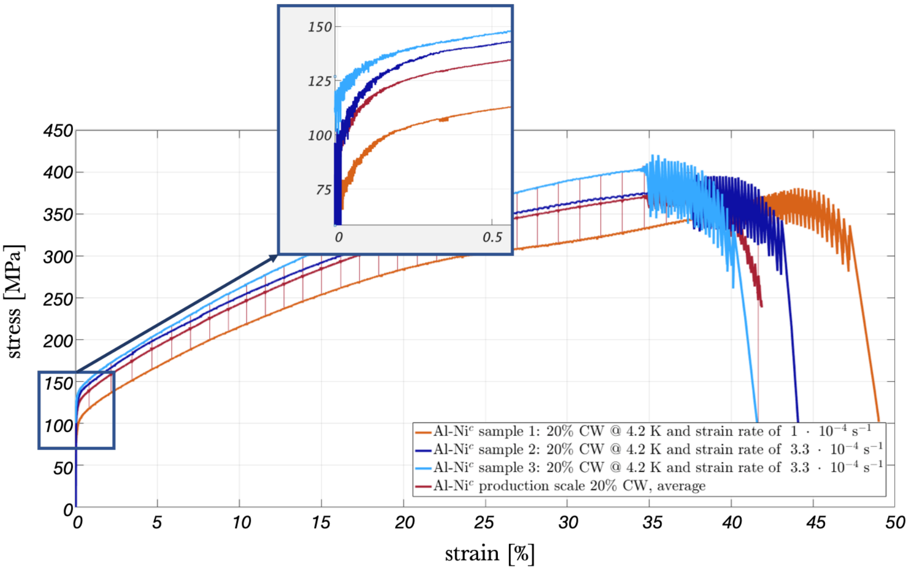

Figure 13.10: Stress-strain curves at 4.2 K for co-extruded Al-0.1wt.%Ni subjected to 20% work hardening by single-pass cold-rolling. Note the shift in mechanical properties with applied strain rate, indicating the well-known phenomena of strain-rate sensitivity in aluminium alloys. Observed here is furthermore the 'nice' serrated yielding, indicative of a liquid helium measurement temperature section 1.2.4.

This aspect has to be taken into account when considering the material's formability, but also in the application itself. Further cryogenic tensile characterisation at a strain rate similar to the one expected in an operational situation could give a more decisive insight in this issue.

13.3.3 Scaling electrical resistivity with dislocation density

The effect of dislocations on the resistivity of a highly-conductive material is know to be smallest at liquid helium temperature, whilst increasing rapidly with increasing temperature between 20 K and 80 K and to saturate above this range [Endo et al., 1988].

Measuring accurately a concentration of dislocations in a metal is very difficult. Here an attempt is made to estimate the increase in dislocation density with 20% and 30% cold-reduction. The increase in dislocation density is made with use of the observed resistivity increase at 4.2 K. The increment in dislocation density ΔD follows from the increment in electrical resistivity resulting from introduced dislocations $\rho_{\Delta D}$ divided by the dislocation resistivity ρ_d, which is the increase in resistivity per dislocation unit:

$$\Delta D = \frac{\rho_{\Delta D}}{\rho_d}. \tag{13.1}$$

The unit of dislocation density is total dislocation length per unit of volume, here m/m^3. In annealed aluminium or copper, for example, the dislocation density tends to be some 10^{10} m/m^3. For a ultrahigh-purity single-crystal aluminium subjected to cyclic annealing dislocation density levels are reported as low as 10^7 m/m^3 [Mizuno et al., 2005]. After severe deformation dislocation density in a high-purity aluminium or copper may, however, reach 10^{16} m/m^3 [Fickett, 1982].

Experimental dislocation resistivity in aluminium tend to be in the order of $3 \pm 1 \cdot 10^{-19}$ $\mu\Omega$ m^3, with the lower limit applying at 4.2 K [Fickett, 1982]. With a resistivity increment measured at 4.2 K of some $1.8 \cdot 10^{-5}$ $\mu\Omega$ m from the Al-Ni^c material in as-extruded state to the 20% cold-reduced state, we can derive an increment in dislocation density of $9.1 \cdot 10^{13}$ m/m^3. Following additional cold-work, resulting in a subsequent 4.2 K resistivity increment of about $2.5 \cdot 10^{-5}$ $\mu\Omega$ m, the additional increment in dislocation density is estimated at $1.3 \cdot 10^{14}$ m/m^3.

13.4 Thermal stability against coil curing

After winding a coil a heat-treatment is performed to cure the polyamide resin insulator. This coil-curing is performed under pressure in order to give the coils their basic shape and to position the conductors as near as possible to their ideal location. This heat treatment may also affect the mechanical and transport properties of the stabiliser material. It can, as a partial annealing, dissolve some of the lattice imperfections earlier introduced during work-hardening. Annealing occurs by the diffusion of atoms within the solid, driving the crystal lattice back towards its equilibrium state. The movement of atoms redistributes and destroys the dislocations in the solid. A partial annealing, dissolving only dislocations, but not extending towards recrystallisation and grain growth is generally denoted as 'recovery'.

A heat treatment on the other hand, could also induce ageing; creating precipitates that impede the movement of dislocations and additionally strengthen the material section 11.2.3. [Wada et al., 2000a] and [Wada et al., 2000b], however, reported that the heat treatment referred to here; i.e. the ATLAS coil-curing cycle, results in a slightly lower yield strength and higher residual resistivity ratio, indicating that the annealing effect dominates.

For a full characterisation of the stabiliser material, and its suitability for the application, the properties are here also established after coil curing. Additional material characterisation is performed following a partial annealing corresponding to the ATLAS coil curing process ($130^\circ\mathrm{C}$ for 15 h, also used in [Wada et al., 2000a]) and after a partial annealing approaching the more severe CMS coil-curing process ($100^\circ\mathrm{C}$ for 145 h followed by $135^\circ\mathrm{C}$ for 50 h).

13.4.1 Thermal treatment methodology

Short lengths of cold-rolled Al-Ni^c were submitted to various thermal treatments in an SNOL 9/1100 furnace, and mechanically tested in order to assess the stability of the mechanical properties against different resin curing cycles. 20% and 30% cold-rolled short samples were subjected to 15 h-long thermal cycles, consistent with the ATLAS resin curing cycle. Temperatures were chosen between 373 K and 630 K (100°C to 360°C), to determine the recovery temperature while staying within a reasonable temperature range related to resin curing. The temperature near the samples was monitored with a SEFRAM 7337 multimeter, showing a variation of ± 4.5 K at the lowest temperature, and only ± 1 K at the highest temperature.

Indentation hardness measurements were performed on the thermally treated samples with a Wolpert Wilson universal hardness tester. The HV hardness measurements employed a Vicker's pyramid diamond indenter at 10 kgf load (HV10), applied for 10 s to 15 s, to obtain an approximate 0.8 mm diameter indentation, in accordance with ISO standard 6507-1. Hardness values were obtained from the center of the aluminium-based stabiliser, to eliminate possible surface effects due to extrusion and cold rolling, in accordance with all other measurements performed so far. The hardness values reported here were determined from at least six individual measurements for each material condition. The spread between the measurements is denoted by the error-bars in the graph. Measurement uncertainty is here estimated at 1.1% for the measurements performed in 6-fold.

13.4.2 Work-hardening dependent recovery

In figure 13.11 the effect of a thermal curing cycle on 20% and 30% cold-rolled conductor specimens is shown. The curves report the hardness measurements on short specimens subjected to 8 different thermal treatments for 15 h in the range between room temperature and 630 K. The diagram clearly indicates a temperature range where recovery of lattice defects takes place, reversing the work-hardening effect, and resulting in degraded mechanical properties.

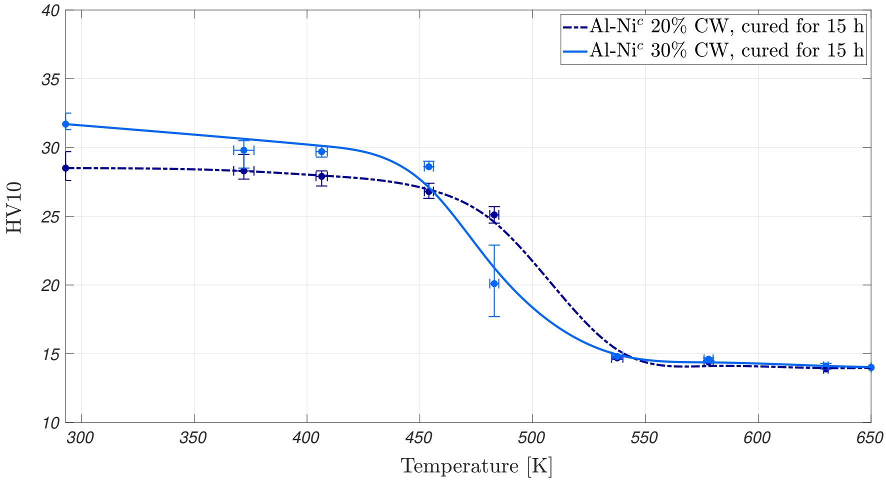

Figure 13.11: Vickers hardness, HV10, plotted as function of thermal treatment temperature. The data presents HV10 values of 20% and 30% single pass cold-rolled short samples subjected to various thermal treatments with a duration of 15 h.

One can observe a small but significant difference in recovery temperature for the different cold-rolled states. Recovery is mainly situated between 470 K and 530 K (some 200°C to 260°C) for the 20% cold-worked state, whereas for the 30% cold-worked state the recovery already takes place between 450 K and 510 K (about 180°C to 240^{circ}C). This indicates a slight influence of the level of mechanical work on the process of recovery. Note though that this observation is performed based on merely two cold-worked cases, from which a trend cannot be determined. For both states, no indication of precipitation hardening effects is observed. Precipitation hardening due to artificial ageing is in fact unlikely to occur due to the fact that diffusion of nickel in aluminium only takes place as from a temperature of 632 K [Du et al., 2003].

We can clearly conclude that a resin curing cycle for NbTi superconducting coils, with a temperature of about 400 K, is not likely to reach the recovery temperature when the curing duration remains below 15 h.

14

Al-0.1wt.%Ni candidate material for a high-energy magnet stabiliser

With the test results that were presented for the application-designed Al-0.1wt.%Ni, processed in a production-scale setting, we can make a verified statement of the alloy's suitability. The post-extrusion thermo-mechanical treatments carried out on a large-size co-extruded stabilised superconductor provides with additional information about the material's behaviour and possible shortcomings.

The main conclusion is that Al-0.1wt.%Ni as a co-extruded stabiliser, has a clear potential. The increase in yield strength with dilute nickel alloying that was earlier reported for smaller conductors is here confirmed for large-size extrusions, and the enhancement of the mechanical properties at 4.2 K is promising for the low-temperature application.

In this chapter, besides the conclusions drawn from the study on Al-0.1wt.%Ni for stabiliser purposes, also some recommendations for its optimisation are discussed. The Al-Ni alloy could benefit from adjusted process parameters in the post-production treatments, both in terms of the mechanical treatments as well as the thermal ones.

14.1 Conclusion based on the Al-Ni alloy's performance

With the already respectable track-record of the Al-0.1wt.%Ni alloy in the development of stabilised superconductors for the ATLAS detector central solenoid, we can confirm the positive evaluation of the performance of the dilute Ni alloy for larger conductors.

Co-extrusion of the tailor-made material was proven successful up to a large size of 57 mm x 12 mm, with processing techniques resumed ten years after the production of the ATLAS and CMS conductors in 1998 to 2003 [Baccaglioni et al., 2001; Blau et al., 2002]. Extrusion parameters were slightly adjusted to accommodate for the tougher stabiliser material, but all remained well within the working margins of the 3800 t press. The chosen parameters resulted in a proper cable-stabiliser bonding. With this co-extrusion process a demonstration of a new, 60 kA I_c at 5 T, 4.2 K class conductor was successfully realised.

The Al-0.1wt.%Ni alloy shows for the as-extruded state an $R_{p0.2}$ value of some 25 MPa, which can be compared to a reference 5N-Al extruded variant exhibiting an $R_{p0.2}$ value of some 20 MPa. The inverse effect of dilute alloying on the mechanical properties versus the transport once anticipated, was confirmed. The relatively small alloying addition of 0.1wt.% nickel, increases the mechanical properties only marginally but easily reduced the RRR by half. Where large cross-sectional extrusion of 5N-Al results in an RRR value of about 2800, a similar extrusion of Al-0.1wt.%Ni exhibits an RRR value of only some 1150.

However, while the margin in transport characteristics with respect to the aimed-for RRR of 500 is still fairly large, Ni doping by itself only makes a small step in mechanical properties towards the envisaged $R_{p0.2}$ value of 120 MPa at 4.2 K.

The increase in mechanical properties is found to be favourable from an ambient measurement temperature to 4.2 K, resulting in an $R_{p0.2}$ of some 75 MPa for the as-extruded state. The ratio between $R_{p0.2}$ at 4.2 K and at room temperature ($R_{p0.2}$ at 4.2 K / $R_{p0.2}$ at 293 K), is therefore determined to carry a ratio of about 2.9. This is a higher ratio than the expected ratio of about 1.35, and is beneficial for its purpose. The as co-extruded variant of the Al-0.1wt.%Ni alloy, however, does not yet have the mechanical characteristics required for the specific scale-up. The as-extruded temper however still has some margin in transport properties to accommodate for further processing.

Further processing in this research consisted of a wide range of work-hardening studies, determining the Al-0.1wt.%Ni alloy's workability on a production scale. Data has been obtained for the co-extruded Al-0.1wt.%Ni alloy cold reduced in a range of 0% to 30%, while varying work-hardening parameters. As anticipated, a deterioration of RRR with increasing cross-section reductions was observed as a result of the production-scale cold-rolling, while $R_{p0.2}$ improved significantly.

Although the initial as-extruded temper was found to be somewhat different, a similar relation exists between RRR and $R_{p0.2}$ at room temperature for the various work-hardening processes for the co-extruded alloy. The evolution of RRR does not depend on the way dislocations are introduced in the material by work-hardening, it just correlates with their shear presence and quantity.

Promising is that this trend tends to an $R_{p0.2}$ value of about 70 MPa at ambient temperature at an RRR of 500. With the earlier obtained 4.2 K to ambient temperature ratio of >2, this was expected to result in a 4.2 K $R_{p0.2}$ of at least 140 MPa, exceeding the aim of 120 MPa.

When actually measuring the mechanical properties at 4.2 K, we denote that the increase in tensile properties from room temperature to 4.2 K is, just like for the as-extruded case, remarkable also for the various cold-rolled states. All work-hardened tempers present an $R_{p0.2}$ value above 100 MPa at 4.2 K, accompanied by an R_m above 350 MPa. The improvement of mechanical properties at cryogenic temperature results in an average $R_{p0.2}$ of 75 MPa for the as-extruded state, and an average of some 125 MPa and 175 MPa for the 20% and 30% cold-reduced cases, respectively. The ratio between $R_{p0.2}$ at cryogenic temperature and at room temperature for the different material states varies slightly, ranging from a maximum of 2.9 for the as-extruded state to a minimum of 2.1 for the 20% reduced temper; far above the 1.35 reported in literature.

With RRR remaining well above 500 for a 20% cold-reduced temper, we conclude that the mechanical and resistivity properties of Al-0.1wt.%Ni can be modified by mechanical processing to fit the requirements for a 60 kA, 5 T class conductor, exhibiting an $R_{p0.2}$ value of $\geq$120 MPa at 4.2 K, while preserving an RRR of more than 500. An Al-0.1wt.%Ni stabiliser, which is cold-worked to a cross-section reduction of some 18% following a production-scale, single-pass work-hardening process, will exhibit an $R_{p0.2}$ value of approximately 120 MPa at 4.2 K, while preserving an RRR of about 700. This proves its suitability for future use in high-energy magnets.

14.2 Optimising the co-extruded Al-0.1wt.%Ni-stabilised conductor

The comparison of various work-hardening processes (flat-roll multiple-pass, bi-directional single-pass and bi-directional limited-pass) demonstrated a distinct increase of mechanical properties with a decrease in number of cold-roll passes. This suggests that there exists a process of recovery of dislocation pinning points by age-softening in between cold-work passes for these very dilute aluminium alloys. We do, however, notice a single and nearly linear relation between RRR and $R_{p0.2}$, independent of the number of passes. From the above, the conclusion can be drawn that the mechanical and resistivity characteristics of Al-0.1wt.%Ni not only depend on the amount of work-hardening, but also to distinct parameters of the work-hardening process.

To make a final step towards the full predictability of the Al-Ni alloy in a production-based setting, an understanding of this process of age softening is desired. In order to design an optimised work-hardening process for production line purposes, a comprehensive study of age-softening effects with work-hardening parameters is essential, and therefore recommended.

In this quest for the optimal work-hardening sequence, further advances in conductor integrity need to be made. The results of ultrasonic and radiographic characterisations of the quality of bonding give rise to concern. Measurements conducted on conductor short samples that were cold-rolled to a cross-section reduction of more than 20% show clear indications of both delamination of the stabiliser material from the Rutherford cable, and of outright cable damage. Ultrasonic images of various 20% cold-reduced conductor sections show evidence of a distinct relation between bonding quality and cold-work procedure. Reduction in several passes is favourable for the bonding quality compared to a reduction in a single pass. Moreover, homogeneously compressing to a 20% reduced state results in a far lower extent of delamination, which is furthermore located differently. X-ray radiography showed some minor indications of strand damage, revealing that this high-force bi-directional rolling on large size co-extruded Al-0.1wt.%Ni superconductors can only be performed without introducing defects, in the specific manner presented in this study, up to a cross-section reduction of 15%. This value notably depends on conductor aspect ratio and on the amount of work-hardening passes.

In designing future production lines for an Al-Ni co-extruded conductor, also the design of the post-processing needs to be taken into account. The hardness of the various thermally treated 20% and 30% cold-reduced specimen, showed no indication of precipitation-hardening due to artificial aging. A recovery of the earlier applied work-hardening did arise between a temperature of some 450 K and 530 K for the 20% and 30% reduced conductor subjected to a thermal treatment of 15 h, respectively. This implicates that the coils resin-curing temperature, when applied for some 15 h, should not exceed 450 K for the 30% cold-worked, and 470 K for the 20% cold-worked conductor. When envisaging a longer coil-curing heat treatment, additional study will be needed.

In view of the observed relation between the mechanical and transport properties at 4.2 K of the co-extruded Al-0.1wt.%Ni alloy, and taking into account the requirements, a next step to a cross-sectional size conductor of some 1500 mm^2 can be envisaged. Equally, with the margin observed in transport properties, one could explore the possibility of enhancing the Ni alloying quantity to 2000 ppm to boost the mechanical properties further. Obviously, when taking these steps, one should carefully monitor RRR to safeguard the essential function of the alloy; its performance as a stabiliser.

Conclusion

15

> *I think and think for months and years.*
> *Ninety-nine times the conclusion is false.*
> *The hundredth time I am right.*
>
> — **Albert Einstein**
> (German theoretical physicist)

In this thesis the focus lies on the selection, production and testing of application-tailored structural materials for large-scale superconducting magnets. Its aim is to enhance the understanding of the controlling factors to determine the suitability of these materials and to explore the possibility of further optimisation.

Large-scale magnets for nuclear fusion or high-energy physics form a highly demanding environment that poses a wide range of strict requirements on key components such as load-bearing structural elements (Part I), electrical joints (Part II), and thermally stabilising superconducting cable reinforcements (Part III).

For the three parts of the thesis separate conclusions were formulated and presented in chapters 6, 10 and 14, respectively. In this final concluding chapter, we synthesise the main points and make a comparison between the different tailored solutions, highlighting both similarities and differences.

15.1 Compositional challenges

The success of a material-based solution always depends strongly on composition, not just in terms of its direct relation to the final properties, but also in view of processing. Conferring the properties by the appropriate thermo-mechanical route is essential for its performance. This importance is apparent in all three parts of this thesis:

- a purpose-designed material like the structural steel F XM-19 only reaches its envisaged performance when responding correctly to the manufacturing route, both in terms of steelmaking (ESR) as well as the forging process. A high level of ductility is required, with limited phase transformation with temperature change;

- in the case of the explosion-welded stainless steel and copper bi-metal for the terminal joints, careful control of the ductility of both components is key. Some degree of ductility is needed for the correct vortex formation at the interface, but a too-similar ductility of the flyer- and parent-metal plates results in a too large velocity difference at the interface and thus an improper weld. This holds regardless of the standoff distance. A fitting shear condition between the two components of the bi-metal is essential;

- a similar conclusion holds for the aluminium stabiliser throughout its processing from co-extrusion to cold-working into its final shape and temper. For the application material toughness is needed, while for material processing in the early stages material flow under relatively low thermal conditions is required to achieve the appropriate bonding with the superconducting cable.

These points illustrate how in any tailored material solution, control over physical processes in the material during fabrication is key. For a low-alloyed aluminium, the formation of precipitates in the high-purity matrix is essential for its use as an electro-thermal stabiliser with the desired mechanical properties. In the case of a stainless steel-to-copper explosion weld, the formation of intermetallic compounds at the interface is necessary for its mechanical strength. On the contrary, when employing a stainless steel such as F XM-19 as a structural element in a magnetic environment, secondary-phase formation needs to be prevented. A full austenitic structure without any ferromagnetic phases must be achieved.

To promote, or prevent, (in)appropriate physical processes in the material, the fabrication process must be carefully monitored *and* the chemical composition must be well-chosen. A proper low-solubility alloying element such as nickel in a high-purity aluminium avoids excessive inhibition of electrical- and thermal conduction resulting from solute atoms. The precipitated state of the alloying addition on the other hand will strain the matrix sufficiently to allow for mechanical enhancement. Also in a structural steel subjected to a range of thermal processes and finally used in a magnetic environment, the composition needs to be balanced to promote an austenite structure over the full processing range, thereby minimising embrittlement and magnetisation.

Chemical composition not just influences the mechanical behaviour of the material, but even more so its thermo-electrical properties. The residual resistivity ratio (RRR) strongly depends on the material's purity. This was confirmed for both aluminium- and copper-alloys. Even the minor addition of 0.1 wt.% nickel in high-purity aluminium reduces the RRR by half. Similarly, while depending on its temper, C10100 copper features RRR values ranging from 70 to 400, whereas C12200 exhibits an RRR value of not even a tenth of this due to the presence of alloying elements.

The key observation is that over the full range of tailored material solutions examined in the frame of this thesis, the chemical composition is the first factor to be considered. In the case of a stainless steel with selected for its mechanical function, chemical composition drives its easy-of-fabrication as well as its mechanical and magnetic behaviour. For materials employed not just for strength but also for thermal- and/or electrical transport, the initial chemical composition plays an even larger role in the latter.

15.2 Mechanical work and its effect on material behaviour

Optimising a material in terms of its chemical composition alone does not bring out its full potential. Additional processing can also enhance material characteristics, either 'accidentally' from necessary manufacturing routes or by design. However, post-processing must be done with care, since it can also induce a degradation of the desired properties. One of the material treatments employed in the investigations in this thesis is mechanical work. In all three cases considered, the application of work-hardening was found to have signification effect on the material properties:

- in the case of the Al-0.1wt%Ni stabiliser, work-hardening was applied specifically to enhance the yield strength to the level required for future large-size detector magnets. While alloying involves a clear trade-off between improved mechanical strength through added dislocation pinning against reduced conductivity due to enhanced scattering, mechanical work, when done at ambient temperature, balances more favourably in the direction of mechanical enhancement. Dilute alloying with 0.1 wt.% nickel was found to increase the yield strength of the as-extruded temper from 22 MPa to 25 MPa, but degraded the RRR value to more than half, from 2800 down to 1150.

  In contrast, subsequent cold-work (some 25% cross-section reduction done in multiple passes) can double the yield strength while only reducing the RRR to about ${}^{2}/{}_{3}{}^{th}$ of its value in the as-extruded temper. This indicates a more favourable scaling between dislocation and mean free path with cold-work compared to dilute alloying. However, the method and severity of cold-work also have an influence, in particular in a composite structure such as the Al-0.1wt%Ni stabilised Rutherford cable. One should also note that the observed scaling does not necessarily apply to every alloy.

- work-hardening may also be a side-effect of the processing, illustrating how, when designing an application-tailored material, one needs to keep in mind the full production sequence up until the final state. This was the case with the F XM-19 heavy-gauge forgings. Even though the production process involves a full annealing cycle after forging, distinct traces of the work applied remained. The traces can follow from the forging process, but also from successive straightening operations. Not only can excessive mechanical work lead to material flaws, but even when during the process no apparent difficulties are observed, mechanical work can lead to material alterations. Extensive elongation resulted in some anisotropy of the material, reflecting on the mechanical behaviour of the steel. In this particular case the resulting directionality proved to be beneficial for the application, but in general such effects should be born in mind and, if necessary, one should take precautions.

- a similar observation was made for the copper sole of the copper-to-stainless steel bi-metal. When employing explosion welding for ease-of-bonding and to avoid excessive applied heat as applied in a regular welding process, considerable work-hardening is introduced. Generally, any method that promotes a solid-state process involves large forces and deformations. Such plastic deformation generates dislocations that impede the motion of running dislocations, i.e. it leads to work-hardening. This also holds for explosion bonding, where large forces and deformation are essential to the formation of the interlocked state and intermetallic-phase formation for a mechanically sound weld.

  The deformation at and around the interface was also found to have an effect on the properties of the copper sole, which is intended primarily as a conductive element. In the as-welded state, a clear hardness gradient was observed over the copper sole, with the highest values at the interface. As the superconducting cable is embedded in the bi-metal, with its current carrying interface towards the far end of the copper sole and opposite side to the explosion weld, this unintended hardening effect is likely to be beneficial. The end where mechanical stability is required, i.e. where the cable needs to be held in place, is the strongest. At the other end a less hard copper is preferred for cable compaction and for adequate electrical current transfer.

We can conclude that work-hardening, whether it is a side-effect of the fabrication process or intentionally introduced, needs to be taken into account when designing a tailored material solution. The efficiency of work-hardening has shown to depend on various parameters, such as method of application, initial chemical composition and the degree of deformation. This implies that when designing an application-specific material one shall not merely ’apply a chemical recipe’, but must also optimise the ’cooking method and duration’.

15.3 Influence of thermal processing

Arguably the most pronounced conclusions in this thesis involve the materials' response to thermal influences. Thermal stability is a property needed at cryogenic temperature for large-scale superconducting magnet systems, but is also essential at elevated temperatures during fabrication.

- For a stainless steel, thermal stability is always of major importance, but even more so when it is to be employed in a low-temperature, high magnetic field environment. The F XM-19 material intended for the tie plates of the pre-compression structure of the ITER tokamak needs to maintain a fully austenitic microstructure throughout processing and application. We showed how chemical composition and thermal processing are closely intertwined in realising the desired final configuration.

  Suitability of the stainless steel is related to its tendency to phase changes during thermal processing, i.e. following from its chemical composition. With the forged F XM-19 structures, thermal processing can be adapted, although to a limited extent. Elevated temperatures, both during forging and post-processing, are essential for the release of internal stress and material inhomogeneity that may result from the forging. Where additional thermal processing may improve homogeneity, the total heat input cannot be diminished, which needs to be taken into account when targeting a specific chemical composition.

- Stability against thermally induced modification is highly important in high-purity metals, where a limited amount of phase transformation is generally targeted in the processing temperature range. In high-purity materials for electrical or thermal transport, thermal processes target material recovery, where the previously discussed work-hardening is reversed. Such recovery involves relatively long dwells at elevated temperature, which implies the decrease of dislocation density, and can be succeeded by recrystallisation and grain growth in function of its severity.

  For both the copper sole in the electrical joint box as for the high-purity aluminium stabiliser in a superconducting coil, one aims for a thermally stable material. Both are exposed to thermal processes during manufacturing, such as superconductor reaction heat-treatments or coil-curing treatments. In either case, the material composition and post-processing are designed to induce a certain combination of material characteristics, which has to be maintained during thermal treatments, or at least kept within ranges suitable for the application.

  The copper employed for the copper-to-stainless steel explosion welds was found to exhibit limited stability against annealing. With thermal processing the material returns fully to its annealed state, or in some cases even beyond. For the Al-0.1wt%Ni alloy, the presence of AlNi intermetallics allows the material to retain some of its work-hardening induced mechanical properties. More importantly, during coil-curing or, similarly, at the extrusion temperature, the diffusion of nickel in aluminium is limited and the intermetallics, which are dispersed in the high-purity aluminium matrix remain present. This makes the

Al-0.1wt%Ni alloy highly stable with respect to thermal processing.

In contrast, a high-conductivity copper that is thermally stable, which is beneficial e.g. for electrical joints operating in quasi-stationary condition, still needs to be identified. A solution could be a non heat-treatable copper alloy that is dispersion-strengthened, making use of the same type of reinforcement as the Al-0.1wt%Ni alloy, i.e. on a fine dispersion of precipitated 'impurities' that leaves the highly conductive matrix mostly unaffected. In the current copper solution, post-welding treatments render the material back to its initial state, recovering full homogeneity of the copper sole and releasing all the mechanical work that could in fact be beneficial for the application. Just like with the aluminium stabiliser, a dispersion-strengthened copper system might well maintain a certain degree of mechanical strength while not jeopardising its quasi-stationary current conductivity.

As a final and general conclusion, we note that in order to develop an application-tailored material, one has to take into account a large variety of interlinked factors. Often materials are studied in their bulk form to determine their potential, but here we intentionally chose to examine the materials' properties following a full manufacturing cycle, in order to understand and predict their true behaviour in the application.

The conclusions presented above illustrate how the analysis of tailored materials in a production setting is essential to understand their suitability for highly-demanding applications such as the ones envisaged in this work. One can not merely depend on the general behaviour of the raw material.

Bibliography

Abada, A., M. Abbrescia, S. S. AbdusSalam, et al. (2019). „FCC-hh: The Hadron Collider. Future Circular Collider Conceptual Design Report Volume 3“. In: *European Physical Journal - Special Topics* 228.4, pp. 755–1107 (cited on page 5).

Ambrosino G .and Ariola, M .and De Tommasi G. (2009). „Design of the plasma position and shape control in the ITER tokamak using in-vessel coils“. In: *IEEE Transactions on Applied Superconductivity* (cited on page 3).

Anderson, T. L. (2005). *Fracture Mechanics*. Fundamentals and Applications, Third Edition. CRC Press (cited on page 58).

Arauzo, A. (2014). *Physical Characterization of Nitronic-50 ITER samples*. Tech. rep. SMF-2014.08.29-IXX (cited on page 85).

ASTM (2013). *ASTM B152/B152M - 13: Standard Specification for Copper Sheet, Strip, Plate and Rolled Bar* (cited on page 129).

– (2019). *ASTM B432 - 19: Standard Specification for Copper and Copper Alloy Clad Steel Plate* (cited on page 113).

Aurubis (2013). *Cu-ETP*. URL: `https://finland.aurubis.com/fileadmin/media/pdf/EN/industiral-products-specifications-2013fall/CU_ETP.pdf` (cited on page 101).

Baccaglioni, G., B. Blau, G. C. Cartegni, et al. (2001). „Production and qualification of 40 km of Al-stabilized NbTi cable for the ATLAS experiment at CERN“. In: 12.1, pp. 1215–1218 (cited on page 194).

Bahrani, A. S. and B. Crossland (1967). „Explosive welding of tubes to tube-plates“. In: *Welding and Metal Fabrication* 35.3, pp. 88–94 (cited on page 107).

Begley, J. A. and J. D. Landes (1972). „The J Integral as a Fracture Criterion“. In: *Fracture Toughness: Part II*. 100 Barr Harbor Drive, PO Box C700, West Conshohocken, PA 19428-2959: ASTM International, pp. 1–23 (cited on page 61).

Bhargava, A. K. and M. K. Banerjee (2017). „Heat-Treating Copper and Nickel Alloys“. In: *Comprehensive Materials Finishing* (cited on pages 133, 134).

Blakely, M. (2010). „Explosion welding and bimetal transitions for weight management“. In: *International Conference on Mass Properties* 69 (cited on page 105).

Blau, B., D. Campi, B. Curé, et al. (2002). „The CMS conductor“. In: *IEEE Transactions on Applied Superconductivity* 12.1, pp. 345–348 (cited on pages 164, 183, 194).

Bonhomme, S. (2003). *Modernisation des essais de traction a basse temperature et mesure de l'effet de serration*. Tech. rep. (cited on page 47).

Bottura, L. and C. Luongo (1999). *Superconductors, Stability in Forced Flow*. Vol. 12. Hoboken, NJ, USA: American Cancer Society (cited on page 17).

Callister, W. D. and D. G. Rethwisch (2009). *Materials Science and Engineering: An Introduction*. 8th ed. Wiley (cited on pages 33, 149, 151, 169, 180).

– (2011). *Fundamentals of Materials Science and Engineering*. An Integrated Approach. Wiley (cited on pages 150, 151, 153).

Carton, E. (2004). „Wave Forming Mechanisms in Explosive Welding". In: *Materials Science Forum* 465-466, pp. 219–224 (cited on pages 107, 108, 124, 141).

CERN (1997a). *ATLAS central solenoid: Technical Design Report*. TDR ATLAS CS. Geneva: CERN (cited on pages 5, 14).

– (1997b). *ATLAS muon spectrometer: Technical Design Report*. TDR ATLAS MS. Geneva: CERN (cited on page 14).

– (2019). *CLIC detector images*. URL: `https://clicdp.web.cern.ch/content/clic-detector` (cited on page 6).

Charifoulline, Z. (2006). „Residual resistivity ratio (RRR) measurements of LHC superconducting NbTi cable strands". In: *IEEE Transactions on Applied Superconductivity*. CERN, AT Dept, CH-1211 Geneva 23, Switzerland, pp. 1188–1191 (cited on pages 127, 128, 167).

Ciazynski, D., B. Bertrand, P. Decool, A. Martinez, and L. Bottura (1996). „Results of the European study on conductor joints for ITER coils". In: *IEEE Transactions on Magnetics* 32, pp. 2332–2335 (cited on page 13).

Ciazynski, D., J. L. Duchateau, P. Decool, P. Libeyre, and B. Turck (2001). „Large superconducting conductors and joints for fusion magnets: from conceptual design to test at full size scale". In: (cited on page 11).

Ciazynski, D. and A. Martinez (2002). „Electrical and thermal designs and analyses of joints for the ITER PF coils". In: *IEEE Transactions on Applied Superconductivity* 12.1, pp. 538–542 (cited on page 100).

Clyne, T. W. and P. J. Withers (1995). *An Introduction to Metal Matrix Composites*. Cambridge University Press (cited on page 154).

Collings, E. W. (1980). „The Magnetic Character of Austenitic Stainless Steels". In: *Advances in Cryogenic Engineering Materials*. Boston, MA: Springer, Boston, MA, pp. 37–47 (cited on page 91).

Cook, R., M. A. Kearns, and P. S. Cooper (1997). „Effects of residual transition metal impurities of electrical conductivity and grain refinement of EC grade aluminum". In: *TMS Light Metals*, pp. 809–814 (cited on pages 155, 158).

Copper Development Association Inc. (2020). *Datasheet CuOFE*. URL: `https://alloys.copper.org/alloy/C10100` (cited on pages 102, 103).

Corte, A. della, L. Affinito, U. Besi Vetrella, et al. (2012). „A New European Production Line for CIC Conductors". In: *IEEE Transactions on Applied Superconductivity* 22.3, pp. 4804504–4804504 (cited on page 174).

Corte, A. della, A. Di Zenobio, L. Muzzi, et al. (2013). „ITER and JT-60SA Conductor Production at ICAS“. In: *IEEE Transactions on Applied Superconductivity* 23, pp. 4200904–4200904 (cited on page 174).

Corthesy, J. (1995). *Realisation d'un dispositif experimental pour la qualification des proprietes mecaniques a 4.2 K d'aciers inoxydables speciaux pour le grand collisionneur protonique*. Tech. rep. (cited on page 47).

Crossland, B. (1982). *Explosive welding of metals and its application*. Oxford University Press, USA (cited on pages 106, 107).

Curé, B. (2010). *Study of a 5-Tesla large aperture coil for the CLIC detector*. Tech. rep. LCD-Note-2011-007 (cited on page 9).

Curé, B., A. Blau B .and Herve, P. Riboni, S. Sequeira Tavares, and S. Sgobba (2004). „Mechanical properties of the CMS conductor“. In: *Ieee Transactions on Applied Superconductivity*. CERN, CH-1211 Geneva 23, Switzerland, pp. 530–533 (cited on page 147).

Dalmut, G. (2005). „Vacancy generation mechanism at high temperatures in ultrahigh-purity aluminum single crystals with a low dislocation density“. In: *Journal of Crystal Growth* 275.1-2, e1697–e1702 (cited on pages 100, 126).

Davis, J. R. (1994). *Stainless Steels*. ASM International (cited on pages 28, 80).

– (2001). *Copper and Copper Alloys*. ASM International (cited on page 101).

De Tommasi, G. (2018). „Plasma Magnetic Control in Tokamak Devices“. In: *Journal of Fusion Energy* 38.3-4, pp. 406–436 (cited on page 3).

Decool, P., D. Ciazynski, P. Libeyre, et al. (2003). „Design and manufacture of a prototype NbTi full-size joint sample for the ITER poloidal field coils“. In: *Fusion Engineering and Design* 66-68, pp. 1165–1169 (cited on page 130).

Degitz, L. (2013). *ITER's central magnet requires a powerful support cage*. URL: `https://www.usiter.org/news/iters-central-magnet-requires-powerful-support-cage` (cited on pages 29, 32).

DeLong, W. T., G. A. Ostrom, and E. R. Szumachowski (1956). „Measurement and calculation of ferrite in stainless steel weld metal“. In: *Welding Journal* 35.11, 521s–528s (cited on page 43).

Devred, A., I. Backbier, and D. Bessette (2012). „Status of ITER conductor development and production“. In: *IEEE Transactions on Applied Superconductivity* 22.3, p. 4804909 (cited on page 17).

Drexler, E. S., N. J. Simon, and R. P. Reed (1994). „Strength and Toughness at 4 K of Forged, Heavy-Section 316LN“. In: *Advances in Cryogenic Engineering Materials*. Boston, MA: Springer, Boston, MA, pp. 1199–1206 (cited on page 38).

Du, Y., Y. A. Chang, B. Huang, et al. (2003). „Diffusion coefficients of some solutes in fcc and liquid Al: critical evaluation and correlation“. In: *Fusion Engineering and Design* 363.1-2, pp. 140–151 (cited on page 191).

Dulon, K. (2010). *Packing a punch*. URL: `https://www.iter.org/fr/newsline/-/182` (cited on page 10).

Ekin, J. W. (2006). *Experimental Techniques for Low-Temperature Measurements : Cryostat Design, Material Properties, and Superconductor Critical-Current Testing*. Oxford Univ. Press (cited on page 135).

Elmasry, M., F. Liu, Y. Jiang, et al. (2017). „Negative Temperature Dependence of Recrystallized Grain Size: Formulation and Experimental Confirmation on Copper." In: *Materials (Basel, Switzerland)* 10.3, p. 308 (cited on pages 133, 134).

Endo, T. and T. Kino (1988). „Logarithmic Temperature-Dependence of the Electrical-Resistivity Due to Dislocations in Metals". In: *Journal of Physics F: Metal Physics* 18.10, pp. 2203–2210 (cited on page 189).

Espy, R. H. (1982). „Weldability of nitrogen-strengthened stainless steels". In: *Welding Journal*, pp. 149–156 (cited on pages 43, 44).

Fickett, F. R. (1982). *Electrical Properties of Materials and Their Measurement at Low Temperatures - NBS Technical Note 1053*. Tech. rep. Tech. Note 1053 (cited on page 189).

Fink, W. L. and L. A. Willey (1934). „Equilibrium Relations in Aluminium-nickel Alloys of High Purity". In: *New York Meeting* (cited on page 160).

Forkel-Wirth D.and Roesler, S., M. Silari, M. Streit-Bianchi, et al. (2013). „Radiation protection at CERN". In: *arXiv.org*, pp. 415–436 (cited on page 159).

Foussat, A., P. Libeyre, N. Mitchell, et al. (2010). „Overview of the ITER Correction Coils Design". In: *IEEE Transactions on Applied Superconductivity* 20.3, pp. 402–406 (cited on page 4).

Freudenberg, K. D. and R. L. Myatt (2011). „ITER Central Solenoid support structure analysis". In: *2011 IEEE/NPSS 24th Symposium on Fusion Engineering*, pp. 1–6 (cited on page 10).

Gabauer, W. (2000). *Manual of Codes of Practice for the Determination of Uncertainties in Mechanical Tests on Metallic Materials -The Determination of Uncertainties in Tensile Testing-*. Tech. rep. UNCERT COP 07:2000 (cited on page 51).

Ghizdavu, V. (2011). „Explosive welding of copper to steel". In: *International Conference Proceeding AFASES* (cited on page 132).

Hall, G. L. (1959). „Nordheim's Theory of the Resistivity of Alloys". In: *APS Physical Review Journal* 116.3, pp. 604–605 (cited on page 155).

Hamada, K., H. Nakajima, K. Matsui, et al. (2008). „Development of jacketing technologies for ITER CS and TF conductor". In: *AIP Conference Proceedings* 986.1, pp. 76–83 (cited on page 38).

Hamada, K., T. Saito, and K. Kawano (2011). *Stainless Steel Mechanical Testing for Conductor Jacket of ITER Central Solenoid and Poloidal Field Coils*. Tech. rep. 3 (cited on page 38).

Hansen, M. and K. Anderko (1958). *Constitution of binary alloys; 2nd ed.* Metallurgy and metallurgical engineering. New York, NY: McGraw-Hill (cited on page 171).

Hardesty, F. (1980). *ASM handbook. Volume 2, properties and selection: Nonferrous alloys and pure metals*. 9th ed. Vol. 2. American Society of Metals (cited on pages 117–119, 121, 135, 140).

Herve, A., D. Campi, and B. Curé (2008). „Experience gained from the construction, test and operation of the large 4-T CMS coil“. In: *IEEE Transactions on Applied Superconductivity* 18.2, pp. 346–351 (cited on page 9).

Hull, F. C. (1973). „Delta ferrite and martnesite formation in stainless steels“. In: *Welding Journal* 52.5, pp. 193–203 (cited on page 43).

International Atomic Energy Agency (2001). *Summary of the ITER Final Design Report* (cited on page 3).

Irwin, G. R. (1957). „Analysis of Stresses and Strains near the End of a Crack Traversing a Plate“. In: *Journal of Applied Mechanics - Transactions of the ASME* E24, pp. 351–369 (cited on page 58).

ITER Organisation (2013a). *ITER plant design specification*. Tech. rep. (cited on pages 4, 10).

– (2013b). *ITER System Design Description (DDD)*. Tech. rep. (cited on page 12).

– (2014). *Technical Specification for Clad Plate for SULTAN Test*. Tech. rep. US ITER 1010102-PD0049-R01 (cited on page 100).

– (2015). *Joint Box Bi-Metal Plate Acceptance Specification*. Tech. rep. DR-030 (cited on page 129).

– (2016). *Procurement Specification for CS Conductor Conduit Development*. Tech. rep. ITER-D-2LTKVM (cited on page 37).

– (2017). *Procurement Specification for CS Structure Tie Plate*. Tech. rep. LX8EGP (cited on pages 12, 30, 31, 33, 39, 51, 91).

Janssen, M., J. Zuidema, and R. Wanhill (2004). *Fracture Mechanics, Second Edition*. Fundamentals and Applications. CRC Press (cited on pages 58, 64, 65).

Kainer, K. U. (1996). *Aluminium and magnesium based metal matrix composites*. Kovine, zlitine, tehnologije (cited on page 153).

Kapiza, P. and E. Rutherford (1929). „The Change of Electrical Conductivity in Strong Magnetic Fields“. In: *Proceedings of Royal Society London* 123.791 (cited on page 102).

Karnes, C. H. and E. A. Ripperger (1966). „Strain Rate Effects in Cold Worked High-Purity Aluminium“. In: *Journal of the Mechanics and Physics of Solids* 14.2, pp. 75–88 (cited on page 188).

Kasap, S. O. (2005). *Principles of Electronic Materials and Devices*. McGraw-Hill Education (cited on page 155).

Kaufman, J. G. (1999). *Properties of Aluminum Alloys*. Tensile, Creep, and Fatigue Data at High and Low Temperatures. ASM International (cited on pages 154, 176).

KB Alloys Inc. (2007). „BORAL: Aluminium Boron Master Alloys | KB Alloys“. In: pp. 1–6 (cited on page 158).

Kowalick, J. F. and D. R. Hay (1971). „A Mechanism of Explosive Bonding“. In: *Metallurgical Transactions* 2, pp. 1953–1958 (cited on page 107).

Langeslag, S. A. E., L. Lain Amador, and Z. Zhang (2014). *Qualification of 316LN welded plates for ITER Magnet Supports*. Tech. rep. CERN-1360369 (cited on page 38).

Larbalestier, D. (2011). „Superconductivity at 100 - what materials will serve us in the next century?“ In: *American Physical Society* Volume 56, Number 4, J2.002 (cited on page 14).

Launey, J. de (1959). „Magnetoresistance of Copper“. In: *Journal of Physics and Chemistry of Solids* 11.1-2, pp. 37–42 (cited on page 102).

Leu, J-S., C-T. Chiang, S. Lee, Y-H. Chen, and C-L. Chu (2010). „Strengthening and Room Temperature Age-Softening of Super-Light Mg-Li Alloys“. In: *Journal of Materials Engineering and Performance* 19.9, pp. 1235–1239 (cited on page 182).

Libeyre, P., N. Dolgetta, and P. Decool (2003). „Mechanical tests of the ITER toroidal field model coil“. In: *IEEE Transactions on Applied Superconductivity* (cited on page 4).

Libeyre, P., C. Cormany, and N. Dolgetta (2015). „Status of design and manufacturing of the ITER Central Solenoid and Correction Coils“. In: *IEEE Transactions on Applied Superconductivity* (cited on page 4).

Lide, D. R. (1994). *CRC Handbook of Chemistry and Physics, 73rd Edition*. CRC Press (cited on page 157).

Lim, B., F. Simon, Y. Ilin, and C-Y. Gung (2010). „Design of the ITER PF coils“. In: *IEEE Transactions on Applied Superconductivity* 21.3, pp. 1918–1921 (cited on pages 4, 13).

Marcinek, D. J. (2016). „Model of discontinuous plastic flow at a temperature close to absolute zero“. PhD thesis (cited on page 17).

Martin, G. and S. Sgobba (1996). *Mechanical Properties of Aluminium Alloy DS-Al-550 at Low Temperatures*. Tech. rep. Geneva (cited on page 146).

Martovetsky, N., R. Manahan, R. Jayakumar, et al. (1998). „Development and Test of the ITER Conductor Joints for the central solenoid“. In: *Fusion technology* 34.3, pp. 808–814 (cited on page 11).

Matula, R. A. (1979). „Electrical Resistivity of Copper, Gold, Palladium, and Silver“. In: *Journal of Physical and Chemical Reference Data* 8.4, pp. 1147–1298 (cited on page 101).

McRae, D. M., R. P. Walsh, E. N. C. Dalder, et al. (2014). „Fatigue and fracture properties of a super-austenitic stainless steel at 295 K and 4 K“. In: *Transactions of the International Cryogenic Materials Conference ICMC Volume 60*. AIP Publishing LLC, pp. 59–66 (cited on page 39).

McRae, D. M., S. Balachandran, and R. P. Walsh (2017). „Fatigue and fracture of three austenitic stainless steels at cryogenic temperatures“. In: *IOP Conference Series: Materials Science and Engineering* 279, p. 012001 (cited on page 38).

Mitchell, N., A. Devred, P. Libeyre, B. Lim, and F. Savary (2012). „The ITER Magnets: Design and Construction Status“. In: *IEEE Transactions on Applied Superconductivity* 22.3, pp. 4200809–4200809 (cited on pages 10, 11).

Mizuno, K., S. Yamamoto, K. Morikawa, et al. (2005). „Vacancy generation mechanism at high temperatures in ultrahigh-purity aluminum single crystals with a low dislocation density“. In: *Journal of Crystal Growth* 275.1, e1697–e1702 (cited on page 189).

Morris, J. W. (1993). „Steels for low temperature applications“. In: (cited on page 36).

Nakajima, H., K. Hamada, K. Takano, K. Okuno, and N. Fujitsuna (2004). „Development of low carbon and boron added 22Mn-13Cr-9Ni-1Mo-0.24 N steel (JK2LB) for jacket which undergoes Nb3Sn heat treatment“. In: *IEEE Transactions on Applied Superconductivity* 14.2 (cited on page 37).

Neuenschwander, J., T. Lüthi, I. L Horvath, and V Pasquer (1998). *Ultrasonic Testing of Aluminium Stabilized High-Current Superconducting Cables*. ECNDT. Swiss Federal Laboratories for Materials Testing and Research (EMPA) & Swiss Federal Institute of Technology (ETH) (cited on page 183).

Nobelclad (2020). *Explosion welding process*. URL: `https://www.nobelclad.com/process` (cited on page 105).

Nyilas, A. (2010). *Fatigue Crack Growth Rate and Fracture Toughness Properties of Type 316LN Extruded Jacket Materials at 7 K having undergone two Different Solution Annealing Treatments*. Tech. rep. CEME-060741-1 (cited on page 38).

– (2014). „Estimation of Uncertainty for Fatigue Growth Rate at Cryogenic Temperatures“. In: *Advances in Cryogenic Engineering* 60, pp. 8–15 (cited on pages 70–72).

Nyilas, A. and H. Krauth (1982). „Use of Heavy Section Austenitic Welds for 4-K Service“. In: *Advances in Cryogenic Engineering Materials*. Boston, MA: Springer, Boston, MA, pp. 853–863 (cited on page 44).

Nyilas, A. and S. Sgobba (2011). *Fracture Mechanics tests on JK2LB material Jacket compacted and aged*. Tech. rep. (cited on page 38).

Obst, B. and A. Nyilas (1991). „Experimental evidence on the dislocation mechanism of serrated yielding in fcc metals and alloys at low temperatures“. In: *Fusion Engineering and Design* 137, pp. 141–150 (cited on page 17).

Peckner, D. and I. M. Bernstein (1977). *Handbook of stainless steels*. McGraw-Hill Companies (cited on page 33).

Pequenao, J. (2008). „Computer generated image of the whole ATLAS detector“. In: (cited on page 6).

Plaza, L. M. (2000). *Manual od Codes of Practice for the Determination of Uncertainties in Mechanical Tests on Metallic Materials -The Determination of Uncertainties in Plane Strain Fracture Toughness (KIC) Testing-*. Tech. rep. UNCERT COP 03:2000 (cited on page 70).

Rawers, J. and A. M. Grujicic (1996). „Effects of metal composition and temperature on the yield strength of nitrogen strengthened stainless steels“. In: *Fusion Engineering and Design* 207.2, pp. 188–194 (cited on page 35).

Reed, R. P. (1972). „Aluminium 2. A review of deformation properties of high purity aluminium and dilute aluminium alloys“. In: *Cryogenics* 12.4, pp. 259–291 (cited on page 155).

Reed, R. P. and R. P. Mikesell (1967). „Low temperature mechanical properties of copper and selected copper alloys; a compilation from the literature“. In: *NBS Monograph 101* (cited on pages 18, 117).

Rice, J. R. (1968). „A Path Independent Integral and the Approximate Analysis of Strain Concentration by Notches and Cracks“. In: *Journal of Applied Mechanics - Transactions of the ASME* 35, pp. 379–386 (cited on page 59).

Rolando, G., A. Foussat, J. Knaster, Y. Ilin, and A. Nijhuis (2013). „Performance assessment and optimization of the ITER toroidal field coil joints“. In: *Superconductor Science and Technology* 26.8, p. 085004 (cited on page 13).

Schaeffler, A. L. (1947). „Constitution diagram for stainless steel weld metal“. In: *Metal Progress* Data sheet, 680 B (cited on pages 34, 35).

Sgobba, S., L. R. Bacher, M. Couach, and S. Marque (1995). „Cryogenic Properties of special Welded Stainless Steels for the Beam Screen of the Large Hadron Collider“. In: *Proceedings of the 4th European Conference on Advanced Materials and Processes* 153, pp. 1–7 (cited on page 46).

Sgobba, S., D. Campi, B. Curé, et al. (2006). „Toward an improved high strength, high RRR CMS conductor“. In: *IEEE Transactions on Applied Superconductivity*. ETH, CH-8092 Zurich, Switzerland, pp. 521–524 (cited on pages 146, 174, 178).

Sgobba, S., J-M. Dalin, P. Libeyre, D. J. Marcinek, and A. Nyilas (2012). „Progress in Production and Qualification of Stainless Steel Jacket Material for the Conductor of the ITER Central Solenoid“. In: *IEEE Transactions on Applied Superconductivity* 22.3 (cited on page 38).

Sgobba, S., P. Libeyre, D. J. Marcinek, and A. Nyilas (2013). „A comparative assessment of metallurgical and mechanical properties of two austenitic stainless steels for the conductor jacket of the ITER Central Solenoid“. In: *Fusion Engineering and Design* 88.9-10, pp. 2484–2487 (cited on page 38).

Sgobba, S., S. A. E. Langeslag, A. Arauzo, P. Roussel, and P. Libeyre (2016). „Physical Properties of a High-Strength Austenitic Stainless Steel for the Precompression Structure of the ITER Central Solenoid“. In: *IEEE Transactions on Applied Superconductivity* 26.4, pp. 2535388–4 (cited on page 42).

Sgobba, S., J-M. Dalin, S. A. E. Langeslag, et al. (2017). „Qualification of structural stainless steel products for the ITER correction coil cases“. In: *Fusion Engineering and Design* 124, pp. 980–984 (cited on page 38).

Sharma, R. G. (2015). *Superconductivity*. Basics and Applications to Magnets. Springer (cited on page 15).

Sherborne Sensors (2013). *Series U2000 Miniature tension/compression load cell for force measuring*. URL: `http://www.alliantech.com/pdf/capteurs_force_jauges/U2000.pdf` (cited on page 48).

Shrijit, G. (2019). *Explosion welding: Applications and variants*. URL: `http://www.yourarticlelibrary.com/welding/explosive-welding/explosive-welding-applications-and-variants-metallurgy/97287` (cited on pages 123, 138).

Smart, J. S. and A. A. Smith (1943). „Effect of certain fifth-period elements on some properties of high-purity copper“. In: *Transactions AIME* 152, p. 103 (cited on page 102).

Takahashi, A., L. C. McDonald, H. Yasuda, and K. T. Hartwig (1997). „Micro-Alloyed High-Purity Aluminum for Low-Temperature Conductor Applications“. In: *Physica Status Solidi (A)* 160.2, pp. 413–418 (cited on page 158).

Ten Kate, H. H. J. (2008). „The ATLAS superconducting magnet system at the Large Hadron Collider“. In: *Physica C: Superconductivity and its applications* 468.1, pp. 2137–2142 (cited on pages 145, 162).

Tobler, R. L., A. Nishimura, and J. Yamamoto (1997). „Design-relevant mechanical properties of 316-type steels for superconducting magnets“. In: *Cryogenics* 37.9, pp. 533–550 (cited on pages 36, 52).

Tonogi, T., G. Iwaki, S. Inaba, et al. (1999). „Aluminum Stabilized Superconductor for the ATLAS Central Solenoid Magnet.“ In: *Hitachi Cable Review* 18, pp. 87–92 (cited on pages 147, 148, 164).

Tsubakino, H., U. Ishihara, and A. Yamamoto (1996). „Precipitation of Ni in Al-0.02 at% Ni alloy“. In: *Materials Science Forum* 217, pp. 901–906 (cited on page 160).

Turck, B., D. Bessette, D. Ciazynski, and J. L. Duchateau (1993). „Design methods and actual performances of conductors for the superconducting coils of tokamaks“. In: *15th IEEE/NPSS Symposium. Fusion Engineering*. IEEE, pp. 667–670 (cited on page 16).

Unified Alloys (2017). *Stainless Steel Grades and Families: Explained - Unified Alloys*. URL: `https://www.unifiedalloys.com/blog/stainless-grades-families/` (cited on page 36).

United States National Bureau of Standards (1914). *Copper Wire Tables*. Washington Government Printing Office (cited on page 157).

US ITER project (2013). *ITER Tie Plate drawing 008367* (cited on page 30).

Vander Voort, G. F. (1991). *Atlas of Time-temperature Diagrams for Irons and Steels*. ASM International (cited on page 34).

Wada, K., S. Meguro, H. Sakamoto, et al. (2000a). „Development of high-strength and high-RRR aluminum-stabilized superconductor for the ATLAS thin solenoid“. In: *IEEE Trans. Appl. Supercond.* 10.1, pp. 373–376 (cited on pages 158–160, 164, 174, 178, 190).

Wada, K., S. Meguro, H. Sakamoto, A. Yamamoto, and Y. Makida (2000b). „High-strength and high-RRR Al-Ni alloy for aluminum-stabilized superconductor“. In: *IEEE Transactions on Applied Superconductivity*. Furukawa Elect Co Ltd, Nikko, Japan, pp. 1012–1015 (cited on pages 159, 160, 164, 174, 178, 180, 190).

Walsh, R., D. McRae, E. Dalder, et al. (2015). „Welded tie plate feasibility study for ITER central solenoid structure“. In: *AIP Conference Proceedings* 1574.1, pp. 16–22 (cited on page 44).

Walsh, R. A. (1994). *McGraw-Hill Machining and Metalworking Handbook*. First edition. McGraw-Hill Professional Publishing (cited on page 152).

Wang, G-Q., S. H. Liu, S-H. Liu, C-M. Li, and Q. Gao (2002). „Reaction of boron to transition metal impurities and its effect on conductivity of aluminum“. In: *Transactions of Nonferrous Metals Society of China* 12.6, pp. 1112–1116 (cited on page 158).

Weijers, H. W., W. D. Markiewicz, and A. V. Gavrilin (2016). „Progress in the development and construction of a 32-T superconducting magnet“. In: *IEEE Transactions on Applied Superconductivity* 26.4, pp. 1–7 (cited on page 2).

Wilson, M. N. (1987). *Superconducting Magnets*. Oxford University Press (cited on pages 9, 16).

Wittman, R. H., S. H. Carpenter, and R. A. Huggins (1975). „Explosion Welding“. In: *Annual Review of Materials Science* 5, pp. 177–199 (cited on page 108).

Wronka, B. (2014). „Ultrasonic Flaw Detection for Quality Assessment of Explosively Clad Plates“. In: *Advances in Materials Science and Engineering* 2014, p. 171279 (cited on page 107).

Yamamoto, A. (2004). „Advances in Superconducting Magnets for Particle Physics“. In: *IEEE Transactions on Applied Superconductivity* 14.2, pp. 477–484 (cited on page 174).

Yamamoto, A., O. Araoka, Y. Doi, et al. (1995). „Development of a prototype thin superconducting solenoid magnet for the SDC detector“. In: *IEEE Trans. Appl. Supercond.* 5.2, pp. 849–852 (cited on page 146).

Yamamoto, A., Y. Makida, K-I. Tanaka, et al. (1999). „Development towards Ultra-thin Superconducting Solenoid Magnets for High Energy Particle Detectors“. In: *Nuclear Physics B (Proceedings Supplements)*. High Energy Accelerator Research Organization (KEK) 1-1 Oho, Tsukuba, Ibaraki, 305-0801, Japan, pp. 565–570 (cited on pages 15, 147, 158–160, 174, 178).

Yamamoto, A., T. Taylor, Y. Makida, and K. Tanaka (2008). „Next Step in the Evolution of Superconducting Detector Magnets“. In: *IEEE Transactions on Applied Superconductivity* 18.2, pp. 362–366 (cited on page 147).

Zheng, J. and B. E. Powell (1997). „a Method to Reduce the Scatter in Fatigue Crack Growth Rate Data“. In: *Fatigue & Fracture of Engineering Materials & Structures* 20.9, pp. 1341–1350 (cited on page 70).

List of Figures

1.1 Brief outline of the thesis. 1

1.2 Schematic depicting the magnetic control system to form, contain and drive the highly energetic plasma required for nuclear fusion. The image displays only the primary magnet system, which is accompanied by correction coils to absorb any deviations from the required resulting magnetic field [De Tommasi, 2018]. 3

1.3 Schematic representation of the ATLAS detector, indicating besides the main particle tracking systems also the main magnet systems. Note the position of the solenoid magnet around the inner tracker, leaving particles to pass through the conductor prior to arriving in the calorimeters [Pequenao, 2008]. 6

1.4 Schematic representation of the foreseen CLIC detector, denoting its main particle-tracking systems, but moreover the positioning of its solenoid. Note the increase in bore diameter with this new-generation detector magnets [CERN, 2019]. 6

1.5 Ratio of structural aluminium in the proposed conductor versus hoop strain for a range of $^{E}/_{M}$ ratios [Curé, 2010]. 9

1.6 Operating current in the 6 CS modules throughout the 15 MA plasma scenario foreseen to be the primary operating scenario of the ITER tokamak. The six modules are magnetised together until plasma initiation, and are subsequently discharged according to individual current profiles to sustain the plasma [Dulon, K., 2010]. 10

1.7 Schematic image showing the ITER central solenoid, consisting of its six (6) modules, and its related pre-compression structure. The tie plates are the vertical elements containing the central solenoid module stack, and measure some 15 m in height [ITER Organisation, 2013b; ITER Organisation, 2017]. 12

1.8 Image representing an electrical joint and its positioning in the PF coils. Inter-pancake connection requires the use of an electrical joint, here in the form of a twin-box joint, consisting of two cables compacted into a bimetallic box and subsequently soldered [Rolando et al., 2013; Lim et al., 2010]. 13

1.9 Image demonstrating the function and positioning of the aluminium stabilised superconductor, requiring to exhibit besides excellent conductive properties also decent mechanical properties as the structure is enforced to be self-supportive [CERN, 1997a; CERN, 1997b; Larbalestier, 2011]. 14

1.10 Critical current density J_c of two commercial superconductors, NbTi and Nb_3Sn, as a function of magnetic field B and temperature T. A critical surface exists above which the superconductor returns to its 'normal' resistive state. 16
1.11 Cross sectional image of the Cable In Conduit Conductor for the Toroidal Field coil of the ITER magnet system, and its components explained [Devred et al., 2012]. 17
1.12 Characteristic stress - strain curve of a C10200 copper, extensively studied in Part II. Measurements performed in tension are presented for a wide range of temperatures, where one can note the discontinuous yielding to be present solely at a temperature as low as 4.2 K [Reed et al., 1967]. 18
1.13 Schematic representation of the thesis build-up. 23

2.1 Photograph showing the 15 m tie plate forging from a single piece. Note that this image is taken during an intermediate forging step, is indicative, and thus not contain the full length of the end-piece. The image illustrates the manipulation of the piece on the one end, and the challenges to maintain dimensions and straightness [Degitz, 2013]. 29
2.2 Pictures denoting the build-up of the tie plate welded structure, consisting of three smaller but still sizeable forgings; two head forgings (a) and one slab forging (b), joined by three heavy double-V bevel welds (c). The weld close-up in image (d) provides some perception of the complexity and heaviness of the weldment [Degitz, 2013]. . . 32
2.3 Iron-carbon binary phase diagram, showing already its complexity with temperature without the addition of other alloying elements, known for their promotion or inhibition of austenite, i.e. the γ-phase. *From:* [Vander Voort, 1991]. 34
2.4 Original Schaeffler constitution diagram for the prediction of ferrite formation in austenitic stainless steel welds [Schaeffler, 1947]. . . . 35
2.5 Schematic representation of austenitic stainless steel grades and families [Unified Alloys, 2017]. 36

3.1 Schaeffler-Espy modified constitution diagram for stainless steel (weld) metal, for high manganese, high nitrogen containing heats [Espy, 1982]. 44
3.2 Specimen extraction scheme for the welded solution (a) and the single piece forged solution (b). 45
3.3 Specimen design for both liquid helium and ambient temperature tensile tests. 46
3.4 Photograph of the employed tensile cryostat as developed by CERN in the preparation of the LHC. The cryostat, with its male (right) an female (left) part can house the sub-size specimens of figure 3.3 for cryogenic tensile testing. 47
3.5 Cryogenic tensile set-up employed for the presented study. Photograph of the set-up (a) and a schematic representation (b). 48

3.6 Stress-strain monitoring systems as employed for low temperature tensile tests. Load-cell for accurate measurement of applied load (a) and a spring type extensometry system (here photographed while being calibrated) for the on-specimen measurement of material deformation (b). 49

3.7 Overview of the prominent tensile properties as obtained for the F XM-19 alloy, forged and in welded state, with respect to the reference technical requirement of ASTM A965 (denoted with the horizontal line). Note the remarkable behaviour of the XM-19 material for a sizeable forged product. 54

3.8 Micrographs obtained at a magnification of 100 x following mechanical polishing succeeded by electrolytic etching at 6 V for 1 minute with a 10 g/100 ml oxalic acid/H_2O solution according to ASTM E407, to reveal the microstructure of the slab (a), and head (b) region of the SPF forging. Direction of maximum flow (i.e. longitudinal direction) is vertical in this view. Notice the difference in grain structure between the slab and head region; a finer structure is observed for the slab region, however containing a greater severity of strain lines. 56

3.9 Micrographs obtained at an original magnification of 100 x following mechanical polishing succeeded by electrolytic etching at 6 V for 1 minute with a 10 g/100 ml oxalic acid/H_2O solution according to ASTM E407, to reveal the microstructure of the top (a), and bottom (b) region of forged head of the SPF solution. Direction of maximum flow (i.e. longitudinal direction) is vertical in this view. Notice the finer grain structure observed for the top head region, the region adjacent to the slab, with respect to the bottom head region. 56

4.1 Load-displacement graphs for bodies of a non-linear elastic material (a) and a plastically deformable material (b). 60

4.2 P-v curve, showing the plastic work U_{pl}, which at the onset of crack extension is otherwise named U_{cr}. Load-point displacement denotes the displacement observed at the axis where load is applied, from which v_{el} and v_{pl} are its elastic and plastic parts, respectively. 61

4.3 Characteristic J resistance curve, determined from J versus Δa data points obtained for different crack extensions for a single material. . 62

4.4 CT specimen design as employed for the J_Q tests described in this document. All dimensions are in mm. Specimen design is chosen for comparison reasons; no geometrically independent material property can be deduced from this geometry as a result of its reduced thickness. 64

4.5 Illustration of the unloading compliance method, reducing the amount of tests to be performed. 65

4.6 Characteristics of a fatigue crack growth rate curve ${}^{da}/_{dN} = f(\Delta K, R)$. 67

4.7 Dynamic and static fracture mechanics set-up employed for low temperature analysis of fracture toughness and fatigue crack growth rate. 68

4.8 Two specimens representing the FCGR + J_Q measurement of the WS weld, denoting the actual position of the notch [Nyilas, 2014]. Note that the onset of crack extension will be highly influenced by the physical position of the notch, the weld to base metal ratio, and additional material effects introduced by the welding process. 71

4.9 Fatigue Crack Growth Rate vs. Stress Intensity at liquid helium temperature for the two tie plate prototypes at various positions and in various crack growth directions. 72

4.10 Photograph indicating the 90° crack growth during the J_Q test in specimen LS2 of the SPF tie plates slab piece (a), and a corresponding micrograph showing the fibrous microstructure of the SPF tie plate slab (b). 74

4.11 Micrographs showing the microstructure of the WS slab (a) and head (b) forging, both containing to some extent micro strain lines as a result from the material processing. 75

4.12 Compliance diagram based on the numerically obtained compliance for the $0°$ and the subsequent $90°$ crack propagation in an E = 200 GPa type steel, compared to the general ASTM E1820 compliance function at E = 200 GPa. Note the nice agreement between the ASTM compliance function and the numerical compliance for the $0°$ crack plane, whereas for the $90°$ crack plane the curve flattens. 77

4.13 Compliance specimen design, here with a 4 mm out of plane machined artificial crack extension, as employed for the measurements in view of determining a valid compliance function. All dimensions are in mm. 78

4.14 Photograph of all produced and measured compliance specimens with different artificial machined out of plane crack extensions for the determination of a correct compliance function for $90°$ crack extension. 78

4.15 Calculated compliance at a $90°$ crack plane plotted against the compliance obtained for the same crack plane in an experimental manner. The ASTM compliance function is added as a reference. Data is represented for a material exhibiting an E-modulus of 200 GPa. Note that the data for the numerical and experimental cases agree very well. A small deviation could be accounted for by a small discrepancy in E-modulus. The $90°$ fit line represents the newly adopted compliance function for the tested specimens featuring crack-plane deviation. . . 80

4.16 Fracture toughness K_Q vs. 0.2$\%$ yield strength $R_{p0.2}$ at 4.2 K for the F XM-19 forged material and its weld. For comparison grain size numbers are also displayed. 81

5.1 Characteristic magnitisation curves, demonstrating magnetisation response for a non-magnetic, soft-magnetic and hard-magnetic material. 85

5.2 Specimen holder for the magnetic measurements performed by VSM technique, in dismounted (a) and mounted (b) state. Magnetic field, H, is indicated in red, to denote applied magnetic field direction with respect to the specimen orientation. 86

5.3 Magnetisation curves. Magnetisation, M, as function of the external field, H, for the three measured zones of the WS and the SPF forgings, respectively. 87

5.4 Micrographs of the central area M of the WS slab, following Murakami etching (a), staining for the presence of particular secondary phases like δ-ferrite (yellow), and following Oxalic acid etching (b). In both cases δ-ferrite stringers appear to be present in the WS slab's central region. 88

5.5 Magnetic permeability as function of temperature for the WS prototype (a), and the SPF prototype (b). Note that the y-axis values differ, and that where for the SPF prototype values well below the required limit ($\mu_r \leq 1.030$) are measured, for the WS prototype most of the regions present values exceeding this limit. 90

7.1 Influence of impurity additions on the electrical conductivity of oxygen free electrolytic refined copper. The second y-axis represents the remaining conductivity following impurity additions in IACS[1] [Smart et al., 1943]. 102

7.2 Schematic representation of the set-up of the explosion bonding process, where an explosive in sheet, granular or powder form is detonated from one end, rolling along the surface of the cladding plate while driving it into the base metal plate. 105

7.3 Schematics illustrating the parallel explosion bonding set-up as often used for larger plates, showing the situation at the impact zone during a rolling explosion [Wronka, 2014]. 107

7.4 Schematics showing the wave formation as observed for a successful explosion bonding, resulting besides a connection via atomic diffusion in an interlocked mechanical connection in the form of waves. The formation of the waves is chronologically described from subfigures (a) to (i) [Wittman et al., 1975]. 108

8.1 Schematic representation showing test specimen and method according to [ASTM, 2019] [2]. 113

8.2 Shear measurement set-up, constructed of sp300 pre-hardened steel (a). Shear is provoked at the copper to stainless steel interface, seen in (b). 113

8.3 Machined shear specimens with loading axis perpendicular to (left), and parallel to (right) the direction of explosion welding. Specimens are carefully machined to ensure the shearing plane to coincide with the weld interface. 114

8.4 Tensile specimen extraction. Note the placement of the EB-weld in the larger portion of the head in order not to affect the material in the gauge length where the Cu - SS interface is inscribed. 115

8.5 Selection of measurement specimens as tested in tensile (a), and shear (b). Notice that failure consistently takes place in the copper cladding. 118

8.6 Tensile specimens of Plate 2 (a) and Plate 3 (b) prior to measurements at 4.2 K. Note the existence of interface defects in both specimens; in the case of Plate 2, subfigure (a), at micro-scale, and in the case of Plate 3, subfigure (b), at macro-scale. The nature and extent of the imperfection is found to significantly influence the mechanical characteristics of the weld. 119

8.7 Shear measurement results for Plate 1 (a) and Plate 5 (b). Note the two-step shear strength in the case of Plate 1, resulting from the deviation of the shear plane from the interface towards the weaker copper clad. For Plate 5 a lower, close to single step shear stress is obtained. A variety in maximum shear stress is observed for the different specimens, analogous with the initial shear plane as can be observed in figure 8.5b, where the specimens are ordered A, B, C, from bottom to top. 120

8.8 Metallographic images of the characteristic wave pattern observed in the specimens of Plate 2, and its dimensions. The explosion welding direction is here from right to left. 122

8.9 Metallographic image of the characteristic wave pattern observed in specimens of Plate 4, and its dimensions. Note the reduced wave amplitude with respect to the observation in specimens of Plate 2 (figure 8.8). The explosion welding direction is here from right to left. Original magnification 100x. 122

8.10 Metallographic images of the characteristic wave pattern in specimens of Plate 3, and its dimensions. Notice the effect unadapted welding parameters have on the structural integrity of the individual materials. The explosion welding direction is here from right to left. 123

8.11 Metallographic weld interface images showing a single 'wave' in a specimen of Plate 1 (a) and Plate 5 (b). Note that even though for Plate 5 pores are smaller with respect to Plate 1, in Plate 5 elongated discontinuities are present at the weld interface, and atomic diffusion over the interface appears absent. 124

9.1 Residual Resistivity Ratio, RRR, measurement set-up. A specimen holder (a) with 18(+2) specimens is lowered into a liquid helium cryostat (b) to measure voltage drops over the specimens at 4.2 K and intermediate temperatures towards ambient temperature when lifted out of the liquid helium medium. 127

9.2 Thermal treatments (TT) in vacuum applied for the simulation of further processing of the bimetals for the manufacturing of the twin-box electrical joint. Temperature measurements are taken both in a 'dummy' specimen to monitor copper core temperature, as well as suspended in the furnace. 131

9.3 Diagrams illustrating the effect of initially introduced deformation (a) and applied annealing time with varying temperature (b), on the recovery characteristics of a highly pure copper alloy. 134

9.4 RRR as function of HRF for all examined copper-claddings. Notice the clear difference in resistivity behaviour between a highly pure, and a heavily alloyed copper. RRR shows to be driven by impurity content. 136

11.1 Schematic of the history in aluminium stabilisers used in detector magnets over the past years, chronologically ordered [Yamamoto et al., 1999]. Note the advancement in the use of aluminium alloys with time, coincident with the increase in magnetic field strength and magnet bore size. 147
11.2 Influence of impurity concentration on the Residual Resistivity Ratio (RRR) of high-purity aluminium [Tonogi et al., 1999]. Notice the exponential behaviour, only 100 ppm impurity content reduces the RRR to less than 1000. 148
11.3 Precipitation strengthening mechanisms with increasing secondary phase particle size. An optimum, $r_{critical}$, exists where precipitation bowing (or looping) takes over from precipitation cutting, or in other words; slip-planes running though the secondary phase particle [Callister et al., 2011]. 153
11.4 Schematics of the reinforcements adopted in MMC structures, where an obvious advantage can be recognised from whisker and mainly particulate additions in terms of manufacturability and isotropy [Clyne et al., 1995]. 154
11.5 Electrical resistivity of polycrystalline, annealed 5N aluminium as a function of temperature. The reference resistivity value at 20°C, i.e. 293 K, is shown by means of the red dashed line, and measures $2.65\ \mu\Omega \cdot$ cm[Lide, 1994]. 157

12.1 Cross-section of the ATLAS central solenoid conductor, 30 mm x 4.3 mm (top), and the 57 mm x 12 mm scaled-up conductor consisting of a 40-strand Nb-Ti/Cu SC cable co-extruded with an Al-0.1wt.%Ni alloy stabiliser (bottom). 162
12.2 Peel-off samples demonstrating the quality of bonding during the co-extrusion process. Subfigure (a) taken right after the start of co-extrusion, both cable and stabiliser surface are 'clean'. In subfigure (b) the sample is extracted after parameter adjustment; a metallic aluminium 'stain' is left on the cable surface. The width of the Rutherford cable in the images is some 26 mm. 164
12.3 Micrograph images demonstrating material flow observed during the transition to a 'new' material. The highly pure 5N-Al appears in a darker hue due to its coarser grain structure. The newly introduced material flows in centrally, while the to be phased out material is pushed around towards the bottom of the extruded product. 165
12.4 Schematic representation of the new co-extruded Al-Ni stabilised conductor, 57 mm x 12 mm (top). For comparison, the 30 mm x 4.3 mm ATLAS CS conductor is shown to scale (bottom). The shaded area indicates where measurement specimens are taken from the bulk section of the conductor. 166

12.5 Overview of the prominent properties as obtained for the co-extruded Al-Ni alloy with respect to the reference materials Al-Ni simply extruded without cable, and the original 5N-Al material in equivalent state. Note the curious decrease in mechanical properties with co-extrusion of the Al-Ni alloy.[1] 168
12.6 Microstructure images of 5N-Al, subfigure (a), compared with Al-Ni, subfigure (b), in the as-extruded case. The images are taken in the conductor cross-sectional plane, in the bulk section of the stabiliser. . 169
12.7 Microstructure images of Al-Ni without cable, subfigure (a), compared to the co-extruded Al-Ni^c, subfigure (b). The images are taken in the conductor cross-sectional plane, in the bulk section of the stabiliser. . 170

13.1 Image of the Turks-head rolling process of the large-size, co-extruded Al-Ni^c stabilised conductor. Plastic deformation is induced in the short-transverse direction (ST), here vertical, while in the gross of measurements the wide transverse direction (TD) is simply constrained to maintain the correct $^{TD}/_{ST}$ aspect ratio. 175
13.2 Tensile properties of the 5N-Al conductor, the Al-Ni conductor, and the Al-Ni^c conductor in five different work-hardened tempers. Mechanical properties increase in an almost linear manner with thickness reduction due to cold work. Notice the slightly lower mechanical properties of the Al-Ni^c alloy with respect to the alloy without cable for higher work-hardened states. 177
13.3 RRR plotted as a function of for the different material variants at various stages of cold-work. Increasing $R_{p0.2}$ by work-hardening has a less detrimental effect on the RRR of the Al-Ni alloy as it does on the RRR of the high-purity Al. 177
13.4 Microstructure images of the 5N-Al extruded stabiliser (left) and Al-Ni extruded stabiliser (right) at various thickness reductions. Thickness reduction is applied in the ST-direction, here vertically. The micrographs are taken at the same position as the tensile and RRR specimens (figure 12.4) at an original magnification of 50x. Notice the close to equi-axed grains in the 0% CW case and the increased $^{TD}/_{ST}$ aspect ratio in the case where thickness reduction has taken place. 179
13.5 Grain size as function of work-hardened state for the three extruded variants. Grain sizes show to decrease with work-hardening extent. . 180
13.6 Room temperature tensile properties of the co-extruded conductor in three different cold-worked states. Data is shown for the multi-pass, flat-rolled conductor, and for the limited- and single-pass, bi-directionally rolled conductor. Notice the decrease in tensile properties with amount of cold-roll passes. 181
13.7 RRR plotted against $R_{p0.2}$ for various cold-worked states obtained with the three work-hardening processes. Although the evolution of strength with size reduction is different for each process, the relationship between RRR and $R_{p0.2}$ remains equal. 182

13.8 Ultrasonic C-scans and radiography images of the co-extruded, cold-rolled Al-Ni stabilised conductor. Subfigures *a1*, *b1*, and *c1* show C-scans of selected sections of the 15%, 35% and 20% single-pass cold-rolled conductor, respectively. Subfigures *a2*, *b2* and *c2* show the corresponding X-ray images. Subfigures *d* and *e* show C-scans of selected sections of the 20% cold-rolled conductor in two passes (limited-pass), and the homogeneously reduced, respectively. 184

13.9 RRR plotted against $R_{p0.2}$, for the various cold-worked states, at both room temperature and 4.2 K. Notice the large increase in $R_{p0.2}$ at 4.2 K compared to room temperature. 187

13.10 Stress-strain curves at 4.2 K for co-extruded Al-0.1wt.%Ni subjected to 20% work hardening by single-pass cold-rolling. Note the shift in mechanical properties with applied strain rate, indicating the well-known phenomena of strain-rate sensitivity in aluminium alloys. Observed here is furthermore the 'nice' serrated yielding, indicative of a liquid helium measurement temperature section 1.2.4. 188

13.11 Vickers hardness, HV10, plotted as function of thermal treatment temperature. The data presents HV10 values of 20% and 30% single pass cold-rolled short samples subjected to various thermal treatments with a duration of 15 h. 191

List of Tables

1.1 Main parameters of the superconducting coils of the ITER tokamak magnet structure. 4
1.2 Main parameters of the superconducting central solenoid of ATLAS vs. CLIC_SiD. 7

2.1 Chemical composition in wt.% of the different heats presented in table 2.2. 37
2.2 Selected 4.2 K mechanical data of recent austenitic stainless steel development. 38
2.3 Chemical composition of F XM-19 as per ASTM A182 by weight percent. 39

3.1 Chemical composition of F XM-19 heats employed for this study. . . . 42
3.2 Chemical composition of the 316LMN filler as employed for the welded structure. 45
3.3 Tensile measurements; sample designation. 51
3.4 Summary of test results comprising all traction data. 52

4.1 Fracture mechanics; sample designation. 69
4.2 Summary of test results, comprising both tensile and fracture mechanics data. 73
4.3 Details and numerical values as obtained for the FEM analysis of 0° crack extension and subsequently 90° crack diversion of CT specimens as employed for this research. 77
4.4 Details and experimental values obtained for the physical analysis of 0° crack extension and subsequently 90° crack diversion of CT specimens. 79

5.1 Specimen characteristics as employed for the magnetic measurements, essential for the calculation of the magnetic properties of the F XM-19 material. 86
5.2 Characteristic relative magnetic permeability for F XM-19 [Collings, 1980]. 91

7.1 Material characteristics of the explosion welded stainless steel to copper bi-metal plates. 109

8.1 Mechanical properties of Cu-SS explosion welds at ambient temperature and 4.2 K. 117

9.1 Resistivity vs. hardness results for the examined plates prior and subsequent to heat-treatments, simulating final joint formation. . . . 133

10.1 Summary of resistivity vs. hardness results at various positions in the copper claddings. 139
10.2 Summary of resistivity vs. hardness results of the copper claddings prior and subsequent to heat-treatments, simulating final joint formation.140

11.1 Strengthening mechanism of crystalline imperfections. 149
11.2 Impurity solutes and their effect on the electrical conductivity of aluminium [Cook et al., 1997; Takahashi et al., 1997; Wada et al., 2000a; Yamamoto et al., 1999; KB Alloys Inc., 2007; Wang et al., 2002].158
11.3 Mechanical and transport properties of selected precipitation Al-alloys at different stages of cold-working (i.e. cross-section reduction) [Yamamoto et al., 1999; Wada et al., 2000a; Wada et al., 2000b]. 160

12.1 Evolution of mechanical properties of Al-Ni^c going from room temperature down to 4.2 K. 171

13.1 Properties of Al-Ni^c as a result of various production-scale cross-section reductions. 186

P r o
p o s
i t i
o n s

Propositions

Accompanying the Thesis:

Tailored Structural Material Solutions for Large-Scale Superconducting Magnets

1. The ease of jumping though a hoop strongly depends on its internal field and the person's aura.

2. De oplossing voor het stiktof-probleem is vloeibaar helium.

3. To properly interpret low-temperature mechanical measurement results one should personally perform the measurements.

4. Dispersion-strengthening can be the answer to mechanical enhancement of high-purity materials when high residual transport properties are required (this thesis).

5. Mechanical work introduced during the product forming process largely affects the material behaviour post final treatment (this thesis).

6. The ASTM compliance function cannot straightforwardly be applied in the calculation of J without assessing the fractured specimen (this thesis).

7. Whereas international standards require certain measurement techniques and specimen dimensions, adequate quality assessment of application-specific material solutions demands deviation from these standards.

8. The deficiency of low-temperature measurement standardisation results in the misinterpretation of their results.

9. The advancement of non-destructive examination techniques is jeopardising the applicability of welded connections.

10. Heavy-gauge forging is not only the solution to avoid weld defects, it is also the most exciting, forceful, and well choreographed dance performed by humans.

- Stefanie Langeslag